Modélisation des suies par méthode sectionnelle pour la simulation RANS des moteurs Diesel

Damien Aubagnac-Karkar

THÈSE

présentée par

Damien AUBAGNAC-KARKAR

pour l'obtention du

GRADE de DOCTEUR

NUMERO D'ORDRE : 2014ECAP0061

Formation doctorale :
Énergétique

Laboratoire d'accueil :
IFP Énergies Nouvelles, Division : Techniques d'Applications Énergétiques
et
Laboratoire d'Énergétique Moléculaire
et Macroscopique, Combustion (EM2C)
du CNRS et de l'ECP

Sectional soot modeling for Diesel RANS simulations

Composition du jury:

Pr. Bénédicte CUENOT	CERFACS	Rapporteur
Pr. Fabian MAUSS	BTU Cottbus	Rapporteur
Pr. Pascale DOMINGO	CORIA	Examinateur
Dr. Jérôme HELIE	Continental	Examinateur
Pr. Christine ROUSSELLE	Université d'Orléans	Examinateur
Dr. Olivier COLIN	IFP Énergies Nouvelles	Examinateur
Pr. Nasser DARABIHA	EM2C	Examinateur
Dr. Jean-Baptiste MICHEL	IFP Énergies Nouvelles	Examinateur

Remerciements

Mes premiers remerciements vont à mes encadrants de thèse, Nasser Darabiha de l'école Centrale Paris, Olivier Colin et Jean-Baptiste Michel d'IFP Energies Nouvelles, qui m'ont guidé et m'ont permis de découvrir les joies et les peines du métier de chercheur durant ces trois années. Merci Nasser pour ta patience, tes conseils toujours avisés et les opportunités que tu m'as offertes pour completer ma formation. Merci Olivier pour tes idées aussi nombreuses que pertinentes, pour m'avoir aidé à exprimer la rigueur de ma pensée en mots. Enfin, merci Jean-Baptiste pour ta présence régulière, pour la rigueur scientifique que tu caches sous ton style détaché et pour l'aide que tu as su apporter à chaque fois qu'il fallait finir des viennoiseries dans mon bureau.

Je souhaiterais aussi remercier les membres de mon jury de thèse pour avoir accepté d'évaluer mon travail et pour avoir partagé avec moi leurs opinions à son sujet. Merci à Madame Cuénot et Monsieur Mauss pour avoir pris le temps de relire mon manuscrit en détail et avoir rédigé les rapports. Merci à Mesdames Domingo et Rousselle ainsi qu'à Monsieur Hélie pour avoir pris le temps d'étudier mon travail.

Je remercie également Antonio Pires da Cruz qui m'a accueilli dans le département qu'il dirigeait durant mes trois années de thèse, ainsi que Christian Angelberger; tous deux m'ont fait confiance pour mener à bien cette thèse. Je suis aussi reconnaissant envers l'ensemble des ingénieurs et experts du département qui ont partagé avec moi leurs savoir-faire et ont permis à ma thèse d'avancer au-delà de certains points bloquants. Je remercie particulièrement André Nicolle dont l'expertise en chimie a débloqué quelques situations. Et bien sûr, je dois mentionner la patience et la compétence de Nicolas Gillet et Anthony Velghe, gardiens des temples que sont les codes du département. Aurais-je pu compiler C3D ne serait-ce qu'une fois si je n'avais pas payé mon tribut en pain au chocolat à Anthony Velghe?

Ce travail n'aurait pas été possible sans l'aide des équipes d'expérimentateurs de la direction R10. La base moteur fournie par l'équipe de Ludovic Noël a facililité la validation de mon modèle. La connaissance des méthodes expérimentales de l'ECN que l'équipe de Gilles Bruneaux a partagé avec moi a été d'une grande aide.

Enfin, je vais parler du troisième étage du bâtiment Claude Bonnier. Ma thèse aurait clairement été très différente si elle ne s'était pas déroulée à cet étage. Les soutiens et les moqueries d'une troupe de thésards tous dans le même bateau ont rythmé mes journées pendant ces trois années. Je remercie les anciens pour leur accueil : Pauline dont je poursuivais les travaux, mais aussi Yohann, Alexis, Julien, Carlo, Sullivan ou encore JB le tueur de cerfs ... Ensuite, je me dois de mentionner spécialement le bureau CB308, haut lieu de culture, de débat politique, philosophique et scientifique

animé durant ces trois années par Sophie, Guillaume, Oguz, Jan, Bejoy et Betty, avant son départ pour la lointaine contrée du bureau voisin. Je remercie les autres thésards qui ont rendu ces trois années agréables avec quelques verres, parties de football ou autre sorties pour couper entre deux calculs plein de bugs. Ainsi, merci à Haifa, Lama, Federico, Emre, Elias, Benjamin, Karl, Anthony, Stéphane, Adam, Nicolas ...

Enfin, je remercie ma famille qui m'a supporté avant cette thèse, durant ces trois années et qui va devoir continuer encore quelques temps. J'ai toujours été soutenu dans mes projets aussi étranges soient-ils (une thèse? quelle iée!), merci.

Abstract

Soot particles emitted by Diesel engines cause major public health issues. Car manufacturers need models able to predict soot number and size distribution to face the more and more stringent norms. In this context, a soot model based on a sectional description of the solid phase is proposed in this work. First, the type of approach is discussed on the base of state of the art of the current soot models. Then, the proposed model is described. At every location and time-step of the simulation, soot particles are split into sections depending on their size. Each section evolution is governed by:

- a transport equation;
- source terms representing its interaction with the gaseous phase (particle inception, condensation surface growth and oxidation);
- source terms representing its interaction with other sections (condensation and coagulation).

This soot model requires the knowledge of local and instantaneous concentrations of minor species involved in soot formation and evolution. The kinetic schemes including these species are composed of hundreds of species and thousands of reactions. It is not possible to use them in 3D-CFD simulations. Therefore, the tabulated approach VPTHC (Variable Pressure Tabulated Homogeneous Chemistry) has been proposed. This approach is based on the ADF approach (Approximated Diffusion Flame) which has been simplified in order to be coupled with the sectional soot model.

First, this tabulated combustion model ability to reproduce detailed kinetic scheme prediction has been validated on variable pressure and mixture fraction homogeneous reactors designed for this purpose. Then, the models predictions have been compared to experimental measurement of soot yields and particle size distributions of Diesel engines. The validation database includes variations of injection duration, injection pressure and EGR rate performed with a commercial Diesel fuel as well as the surrogate used in simulations. The model predictions agree with the experiments for most cases.

Finally, the model predictions have been compared on a more detailed and academical case with the Engine Combustion Network Spray A, a high pressure Diesel spray. This final experimental validation provides data to evaluate the model predictions in transient conditions.

Keywords : Combustion, Simulation, Pollutant, Soot, Diesel, Tabulated chemistry

Résumé

Les particules de suies issues de moteur Diesel constituent un enjeu de santé publique et sont soumises à des réglementations de plus en plus strictes. Les constructeurs automobiles ont donc besoin de modèles capables de prédire l'évolution en nombre et en taille de ces particules de suies. Dans ce cadre, un modèle de suies basé sur une représentation sectionnelle de la phase solide est proposé dans cette thèse. Le choix de ce type d'approche est d'abord justifié par l'étude de l'état de l'art de la modélisation des suies. Le modèle de suies proposé est ensuite décrit. A chaque instant et en chaque point du maillage, les particules de suies sont réparties en sections selon leur taille et l'évolution de chaque section est gouvernée par :

- une équation de transport;
- des termes sources modélisant l'interaction avec la phase gazeuse (nucléation, condensation, croissance de surface et oxydation des suies);
- des termes sources collisionnels permettant de représenter les interactions entre suies (condensation et coagulation).

Ce modèle de suies nécessite donc la connaissance des concentrations locales et instantanées des précurseurs de suies et des espèces consommées par les schémas de réactions de surface des suies. Les schémas fournissant ces informations pour des conditions thermodynamiques rencontrées dans des moteurs Diesel comportant des centaines d'espèces et des milliers de réactions, ils ne peuvent être utilisés directement dans des calculs de CFD. Pour pallier cela, l'approche de tabulation de la chimie VPTHC (Variable Pressure Tabulated Homogeneous Chemistry) a été proposée. Cette approche est basée sur l'approche ADF (Approximated Diffusion Flame) qui a été simplifiée pour permettre son emploi couplé au modèle de suies sectionnel.

Dans un premier temps, la capacité du modèle tabulé à reproduire la cinétique chimique a été validée par comparaison des résultats obtenus avec ceux de réacteurs homogènes avec loi de piston équivalents. Finalement, le modèle VPTHC, couplé au modèle de suies sectionnel, a été validé sur une base d'essais moteur dédiée avec des mesures de distribution en taille de suies à l'échappement. Cette base comporte des variations de durée d'injection, de pression d'injection et de taux d'EGR à la fois pour un carburant Diesel commercial et pour le carburant modèle utilisé dans les calculs. Les prédictions des débits horaires de suies et des distributions à lâéchappement obtenues sont en bon accord avec les mesures.

Ensuite, les résultats du modèle ont été comparés avec les mesures plus académiques et détaillées du Spray A de l'Engine Combustion Network, un spray à haute pression et température. Cette seconde validation expérimentale a permis l'étude du comportement du modèle dans des régimes transitoires.

Mots-clefs : Combustion, Simulation, Polluants, Suies, Diesel, Chimie Tabulatée

Contents

Chapter 1

Introduction

1.1 Motivations

1.1.1 Combustion in the world

The mastery of combustion led to the industrial revolutions by providing the energy required for mass production and transportation. Providing energy by combustion is a foundation of our current society. Indeed, this process is currently involved in 90% of the energy production on Earth [1] and is the most used process in the energy industry. This situation is illustrated in Fig. 1.1 which shows the origin of primary energy used on Earth according to U.S. Energy Information Administration [2]. Combustion is used to release the chemical energy contained in liquid fuels (oil mostly), coal, natural gas and part of the renewable fuels (wood), showing its importance in our society. The importance of hydrocarbon fuels, which are coal, gas and oil, also appears clearly. Figure 1.1 also shows the current growth of the energy consumption. This growth exists since the beginning of the industrial revolution around the world but the data of Fig. 1.1 show that it does not seem to stop. Facing a constantly increasing demand induces several challenges for energy and transportation industries.

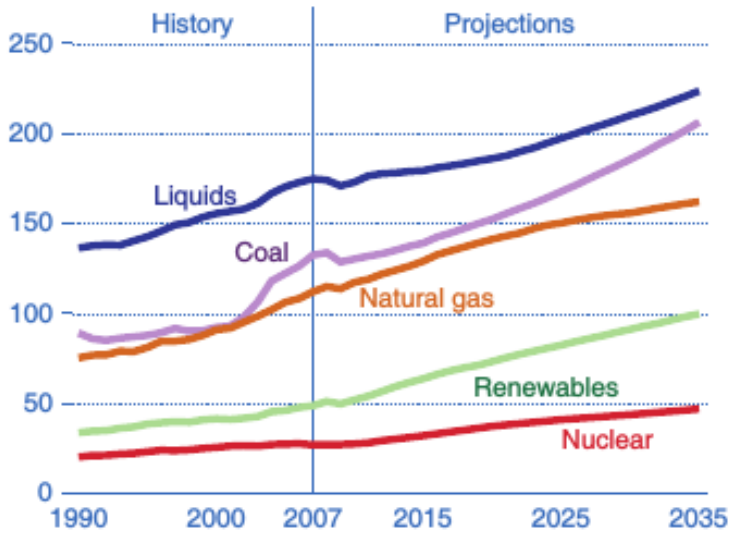

Figure 1.1: World energy consumption by fuel type from 1990 through 2035 (projection) [2]

This constantly increasing demand in energy causes strong stresses to both the ability of producers to respond to it and to the environment. On the one hand, the scarcity of fuels becomes a major economical and social issue with uncertain evaluation of hydrocarbon resources [2]. On the other hand, one of the main combustion products, the carbon dioxide CO_2, has a strong impact on global warming. Incomplete combustion products, such as unburned hydrocarbons, carbon monoxide and soot particles, are considered as pollutants and have an impact on climate as well as they cause health issues. Finally, the high temperatures reached during combustion also lead to nitrogen oxides production, involved in tropospheric ozone creation which is very noxious to human beings.

1.1.2 Automotive industry context

Liquid fuels are one of the resources concerned by scarcity. Their consumption by sector is given in Fig. 1.2, according to the U.S. Energy Information Administration [2]. The transportation domain appears to be one of the largest energy consumers. It is also the domain where the use of different sources of energy seems to be the more complicated. Indeed, many transportation devices, such as cars or planes, have to transport their energy sources. In this context, the high energetic density of liquid fuels is required. The number of vehicles is also constantly growing. For cars, it goes from 126 millions in 1960 to 1 billion in 2010 according to the US Department of Energy [3]. This trend should not stop in the future because of the demand from the industrializing countries. Thus, the car industry faces a challenge with a larger public to reach with less and less resources and emissions that have to be controlled.

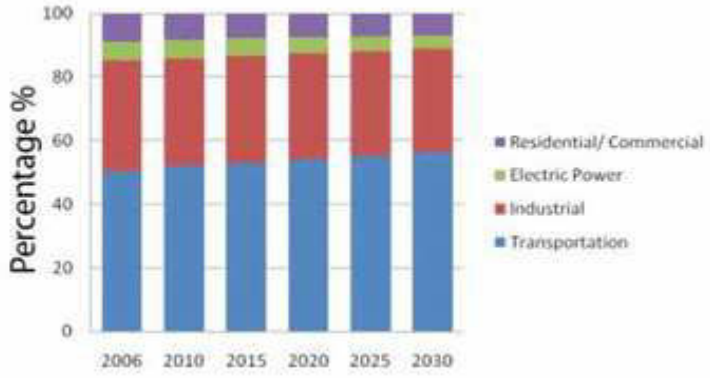

Figure 1.2: Consumption of liquid fuel in the world by sector from 2006 through 2030 (projection) [2]

In this context, the transformation of the fuel latent energy into mechanical energy has to be understood, mastered and controlled. This results in constant work to improve current engines design.

1.2 Automotive industry context

Current car engines are internal combustion engines, most of them are piston engines, also known as reciprocating engines. The release of the fuel energy as well as the pollutants emissions come

from the combustion inside these engines. The way this combustion is realized is also the main way to classify cars.

1.2.1 Reciprocating engines basics

Most of the modern car engines are four-stroke engines. This means that they provide energy by completing a five steps thermodynamical cycle realized during four strokes. They differ in the fact that they can be either Compression Ignition (CI) engines, also called Diesel engines, or Spark Ignition (SI) engines. Figure 1.3 shows the five functioning steps of a four-stroke reciprocating engine which can be either a Diesel or a SI engine:

- Intake: the first stroke is dedicated to the gas intake in the cylinder. A first difference appears at this step since the intake gas can be either air (for Diesel engines or direct injection SI engines) or a premixed fuel/air mixture (for indirect injection SI engines).
- Compression: during the second stroke, the piston is compressing the air or fuel/air mixture to reach a high enough temperature and pressure for the combustion to occur in good conditions.
- Combustion: the main difference between Diesel and SI engines lies in this step. In Diesel and direct injection SI engines, the fuel is generally injected slightly before the end of the second stroke and slightly after the beginning of the third one. SI engines ignitions are triggered by a spark plug, leading to a propagating flame in a premixed fuel/air mixture. Diesel engines ignitions depend on the fuel ability to auto-ignite at high temperature and pressure, leading to a diffusion flame between a region very rich in fuel around the fuel spray and the air region in the cylinder.
- Expansion: this is the step where the energy released by the combustion is converted into mechanical energy thanks to the pressure work on the piston.
- Exhaust: the last step of a four-stroke cycle is dedicated to the exhaust of the burned gases before the next cycle begins.

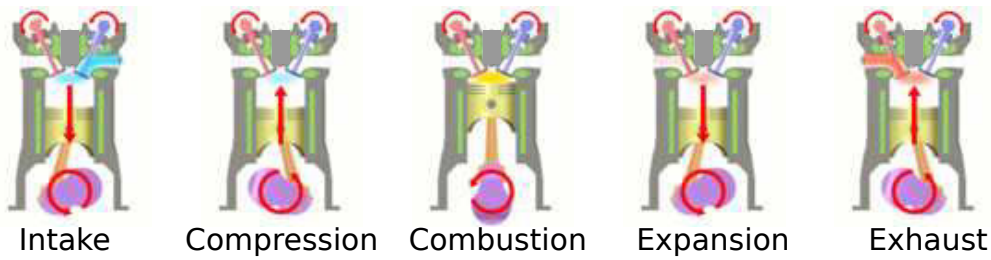

Figure 1.3: Scheme of the five functioning steps of a four-stroke engine.

Figure 1.4 shows the ideal thermodynamical cycle occurring in a piston engine. It is the thermodynamical trajectory followed during a four-stroke cycle. This p-V diagram is idealized, with:

- isobaric intake (point 0 to point 1);
- adiabatic compression (point 1 to point 2);

- an instantaneous (and thus isochoric) heat release from combustion (point 2 to point 3);
- adiabatic expansion (point 3 to point 4);
- instantaneous pressure decrease at the expansion end to reach exhaust pressure (point 4 to point 5);
- isobaric exhaust process (point 5 to point 0).

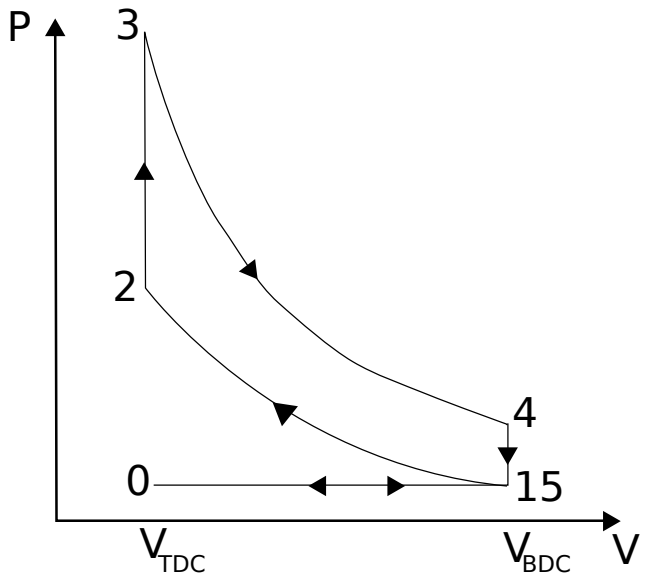

Figure 1.4: Idealized thermodynamical cycle realized in a piston engine.

It points out the importance of the compression ratio τ which is the volume ratio between the volume at Bottom Dead Center (BDC) and Top Dead Center (TDC). Indeed, the theoretical cycle efficiency η appears to be dependent on the compression ratio:

$$\eta = 1 - \tau^{1-\gamma} \tag{1.1}$$

where γ is the ratio of the constant pressure specific heat and the constant volume specific heat of the gas.

1.2.1.a Flame regimes

The description of SI and Diesel engines included mentions to two different ways to burn fuel. The fuel chemical energy is released through a propagating premixed flame in SI engines and through a non-premixed flame in Diesel engines. These differences are detailed next with a short introduction to combustion. Generally, a combustion reaction writes:

$$\nu_{Fuel} Fuel + \nu_{Ox} Oxidizer + \nu_{Dil} Diluant \rightarrow \nu_{Pr} Products \tag{1.2}$$

where ν_{Fuel}, ν_{Ox}, ν_{Dil} and ν_{Pr} are the stoichiometric coefficient of the reaction.

The exothermic reaction occurs when fuel and oxidizer are mixed with a ratio Φ (equivalence ratio) not too high or too low with respect to the stoichiometric conditions and when the temperature and pressure are high enough to trigger the reaction. The equivalence ratio writes:

$$\Phi = \frac{\frac{Y_{Fuel,0}}{Y_{Ox,0}}}{\left(\frac{Y_{Fuel,0}}{Y_{Ox,0}}\right)_{st}} = \frac{Y_{Fuel,0}}{Y_{Ox,0}} \frac{\nu_{Ox} M_{Ox}}{\nu_{Fuel} M_{Fuel}} \tag{1.3}$$

where $Y_{Fuel,0}$ and $Y_{Ox,0}$ are the initial mass fractions of fuel and oxidizer, M_{Fuel} and M_{Ox} are the molar fractions of fuel and oxidizer and the subscript st refers to the value at the stoichiometric conditions. The mixture is considered rich if $\Phi > 1$ and lean if $\Phi < 1$.

The ability of a mixture to burn is not only function of its equivalence ratio, temperature and pressure but it also strongly depends on the fuel. Moreover, the fraction of dilutant gases which can absorb heat and damper the ignition or propagation processes is also an important parameter.

These chemical reactions are realized in flows of fuel and oxidizer (usually air) which can be mixed or not prior to combustion. The previously introduced two types of combustion differ in this sense and the methods to define the flames vary in each case.

Premixed flames

Premixed flames are defined as a flame front separating a region of fresh premixed gases and a region of burned gases. As illustrated in Fig. 1.5, this flame front can be separated in two zones. A pre-heat zone where the fresh gases temperature is increased by thermal diffusion. In this region, the fuel and oxidizer begin to react to create radicals required to complete the combustion reaction. The reaction zone is the zone of the flame front where, when the temperature and quantity of radicals are high enough, the reaction intensity increases and chemical heat is released.

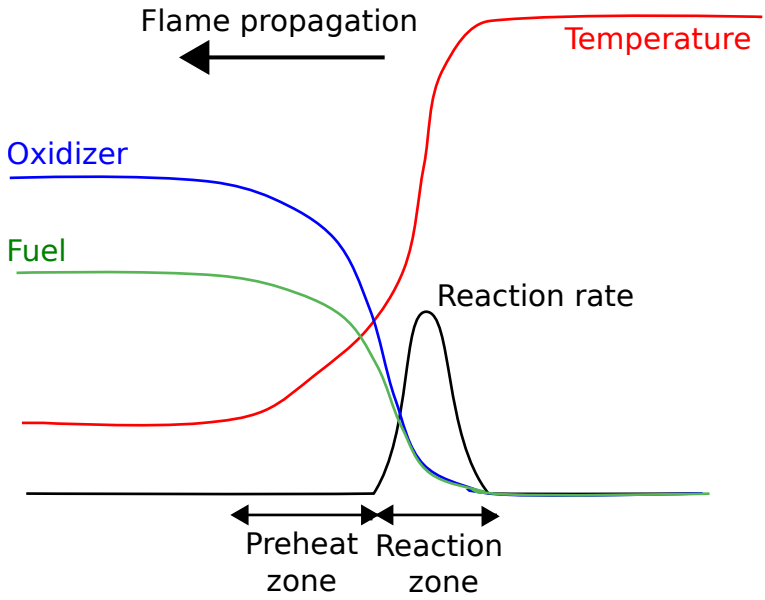

Figure 1.5: Scheme of a premixed flame structure.

The evolution from the fresh gases to the burned ones can be described by a progress variable. This progress variable can be defined from local temperature or species mass fractions. The main characteristics defining a premixed flame will be its propagating speed and its thickness.

Non-premixed flames

Non-premixed (or diffusion) flames are defined as a reacting zone between a fuel region and an oxidizer region. The structure of a non-premixed flame is shown in Fig. 1.6. The flame is controlled by the mixing between fuel and oxidizer and is located at a position where the local equivalence ratio is equal to unity. However, reactions take place in regions close to this location with high and low equivalence ratios. This method is safer than premixed combustion because it prevents accidental ignition or propagation. Indeed, most of the fuel is located in regions too rich for combustion reactions to occur.

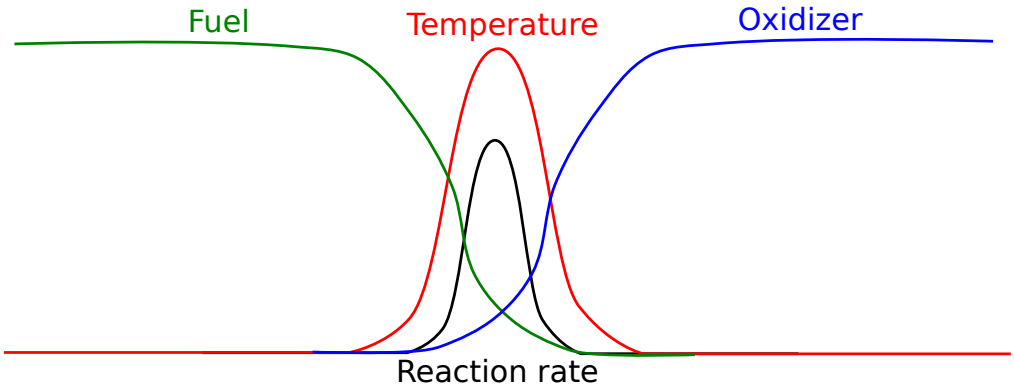

Figure 1.6: Scheme of a non-premixed flame structure.

To describe these flames, a mixture fraction Z can be defined. This mixture fraction is equal to 1 in the pure fuel region, 0 in the oxidizer region and evolves continuously in between without effect due to the chemical reaction. Various definitions of the mixture fraction can be found in the literature. The most used one is:

$$Z = \frac{1}{\Phi + 1}\left(\Phi \frac{Y_{Fu}}{Y_{Fu,0}} - \frac{Y_{Ox}}{Y_{Ox,0}} + 1\right) \tag{1.4}$$

where Y_{Fu} and Y_{Ox} are respectively the local fuel and oxidizer mass fractions. $Y_{Fu,0}$ and $Y_{Ox,0}$ are taken outside of the flame in their respective regions.

In this study, the mass fraction of the fuel tracer, which is a virtual species driven by the transport equation of fuel without the chemical source term, is considered as the mixture fraction. Such a species can be used as a mixture fraction because it is only convected and diffused by the flow.

1.2.1.b Main differences

SI and Diesel engines face different limitations and issues. Standard SI engines efficiency is limited by the possible auto-ignition of its mixture. This type of event, called knock, can destroy engines. To avoid it, the compression ratio has to be lower and processes increasing the intake pressure (such as turbochargers or superchargers, providing more torque and a better fuel efficiency) also have to be used with caution. These limits do not exist on Diesel engines because the auto-ignition is used to trigger the combustion. Auto-ignition can be used in Diesel engines because the fuel and air are not premixed, unlike in SI engines. The energy release is then controlled by the fuel injection rate and it is possible to build pistons able to resist the pressure and thermal strains it imposes.

1.2.2 Number of Diesel powered cars

These design differences make Diesel engines more efficient than standard SI Engines. The fact that Diesel fuel has a higher calorific value per unit-volume than Gasoline (and users buy volumes of fuel) increases this difference from an user point of view. These aspects are illustrated in Fig. 1.7.

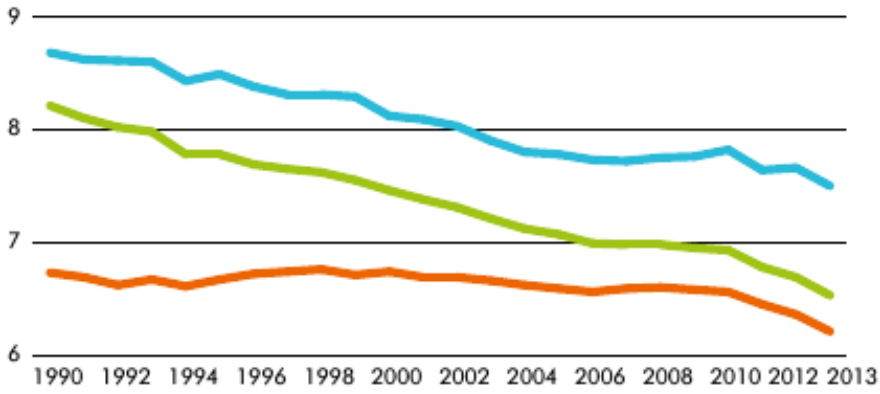

Figure 1.7: Average fuel consumption in liter for 100 km for cars using Diesel engines (orange), SI engines (blue) and all cars (green) in France from 1990 to 2013 [4].

These reasons made Diesel engines more and more used in European Union during the three last decades as illustrated in Fig. 1.8. The current situation with more than half of the new cars sold in Europe being Diesel powered places the understanding of Diesel engines combustion and pollutants emissions as a major issue for the car industry. The proportion of Diesel engines in new cars sales is even superior to 66% in Spain, France, Ireland, Luxembourg and Portugal in 2013 according to the latest data of the French Car Manufacturer Committee (CCFA) [4].

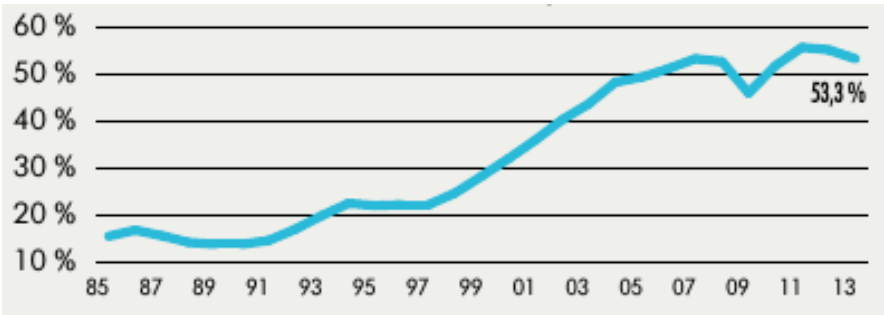

Figure 1.8: Proportion of Diesel powered cars among the new cars sales in Europe from 1985 to 2013 [4].

1.2.3 Norms

In this context, the non-premixed combustion used by Diesel engines has to be studied and controlled. The separation of fuel and air in diffusion flames induces combustion phenomena in regions with very high fuel to air equivalence ratios. The global production of pollutants depending on

equivalence ratio and temperature has been summarized by Pischinger *et al.* [5]. The diagram given in Fig. 1.9 shows the different local conditions in temperature and equivalence ratio Φ required for soot production and oxidation as well as NO_x production. The conditions required to produce soot particles are locally met in non-premixed flames. Accordingly, soot particles emissions are higher in Diesel engines than in SI engines.

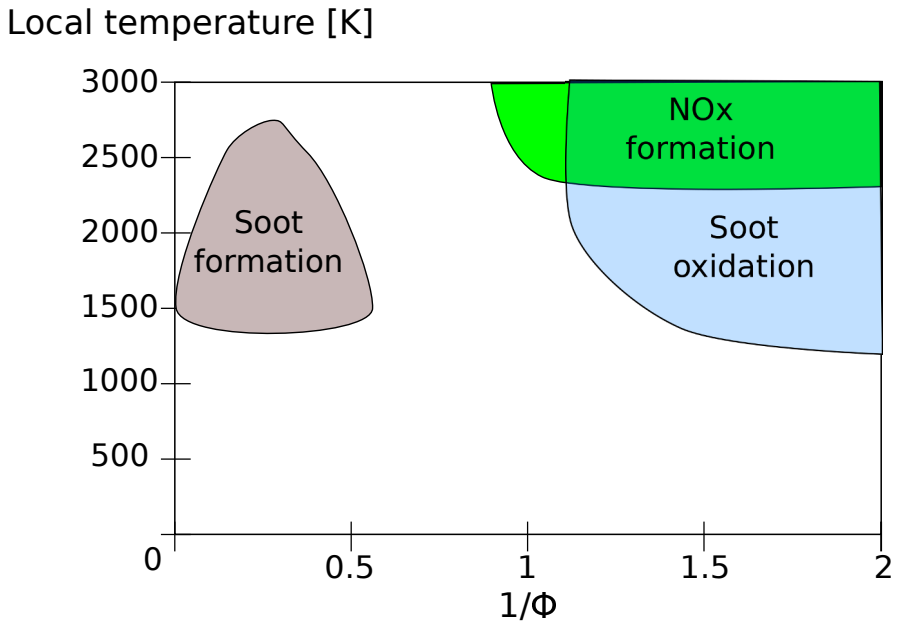

Figure 1.9: Diagram of soot and NO_x formation and oxidation conditions depending on temperature and equivalence ratio [5].

With a constantly growing number of Diesel cars in Europe and the soot emissions they generate, soot particles became a major concern for the car industry. Indeed, the amount of soot particles emitted grew larger as did the responsibility of the car industry for their emissions. In 2000, 25% of the PM2.5 particles (particles with a diameter smaller than 2.5 μm) emitted in France were due to road transportation [6] and 87% of it were emitted by Diesel engines [7]. In 2005, approximately 25% of the PM10 (particles with a diameter smaller than 10 μm) in France had their source in road transportation [8].

These large emissions of soot particles due to Diesel engines raise public health issues. Indeed, O'Connor *et al.* [9] have shown that exposing children to PM2.5 increases the risks of the children to develop asthma or other pulmonary diseases. Globally, exposition to solid carbon particles increases the risk of cancer and pulmonary inflammations [10, 11]. Moreover, the thinest particles, PM0.1 (particles with a diameter smaller than 100 nm), can infiltrate deep into the lungs according to Donaldson *et al.* [11].

Solid particles in air also have an impact on the environment. PM2.5 are thin enough to be transported by atmospheric events instead of deposing on the ground because of their weight. Thus, they infect atmosphere and damage stratospheric ozone by reacting with it [12, 13]. Moreover, solid particles also have an impact on greenhouse effect and are mentioned as the second cause of global warming by Jacobson *et al.* [14]. Physical phenomena driving the interaction between particles and the atmosphere are complex and depend on the particles aggregate structures according to Adachi

et al. [15]. This complexity and its uncertainties prevent the development of controls on particles for climatic reasons as there are already for public health reasons. However, Diesel engines (as well as residential burners) produce thin soot particles which are very probably involved in global warming as shown by Bond *et al.* [16].

These concerns about public health led the European Union to adapt its norms for cars emissions. Indeed, the EURO norms (European emission standards), limit the mass of soot emitted by Diesel powered cars with lower and lower value from the EURO1 in 1992 to the EURO4 in 2005. This trend was confirmed with the EURO5 in 2009 which required a soot yield five times lower than EURO4 and added a particle number limit for particles larger than 23 nm. The EURO norms for Diesel cars are presented in Fig. 1.10 including the others regulated pollutants such as the carbon monoxide (CO), hydrocarbons (HC) and nitrogen oxides (NO_x).

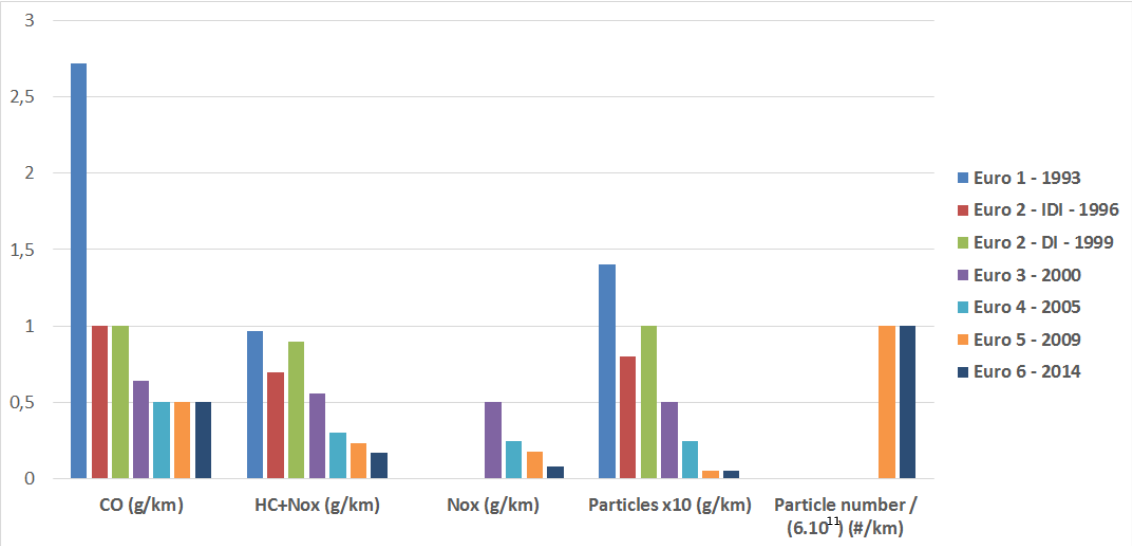

Figure 1.10: EURO norms for Diesel engines grouped by pollutant and colored by standard [17].

Latest design of SI engines, mostly using direct injection, also face issues related to soot emissions even if they allow to increase fuel efficiency of SI engines. Indeed, direct injection implies a combustion in a mixture stratified in equivalence ratio thus meeting the conditions of soot productions. This evolution has also been taken into account in EURO norms with more stringent recent norms concerning the soot emissions of SI engines as illustrated in Fig. 1.11 also adding the non-methane hydrocarbons (NMHC).

1.2.4 Control of emissions

To meet these requirements, pollutant emission control strategies have already been applied by the car manufacturers. These strategies can be split into two groups, the post-treatment strategies which aim to treat the pollutants after the engine in the exhaust system and the combustion control strategies which aim to limit the pollutants formation during the combustion. Most of the modern cars combine the two approaches to reach the low standard imposed by current norms.

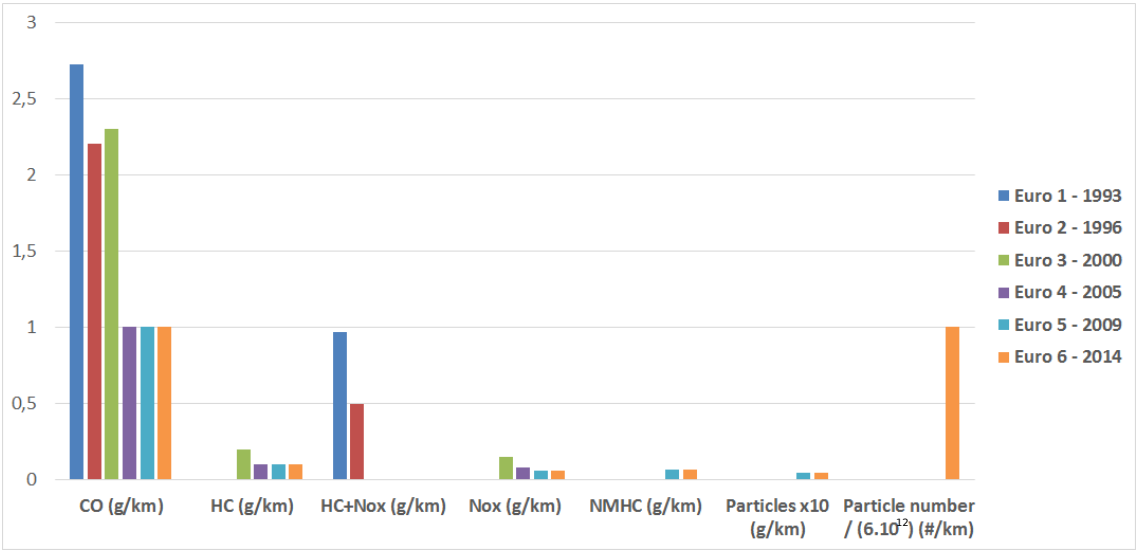

Figure 1.11: EURO norms for SI engines grouped by pollutant and colored by standard [17].

1.2.4.a Post-treatment

Most current SI engines use three-way catalyst (TWC) as their post-treatment system. It completes the combustion reaction by:

- reducing nitrogen oxides into nitrogen and oxygen;
- oxidizing carbon monoxides to complete its transformation into carbon dioxide;
- oxidizing unburnt hydrocarbons (HC) to complete their reaction into carbon dioxide and water.

However, this method requires the mixture to be quasi-stoichiometric since it reduces and oxidizes at the same time. The average mixture in Diesel engines is usually lean which cancels the ability to reduce NO_x.

To face this limit, Diesel engines can be equipped with several post-treatment systems. Most Diesel engines use an Oxidation Catalyst (usually called DOC for Diesel Oxidation Catalyst) to oxidize CO and HC into CO_2 and water. DOC can also oxidize some soot particles. Nitrogen oxides can be treated by NO_x traps or using Selective Catalytic Reduction (SRC).

Finally, the soot particles are treated with a Particulate Filter (PF) in Diesel engines. This step is optional in SI engines which produce less soot particles. However, new SI engines designs could use PF since they produce more soot because of a combustion in a more stratified environment. PF trap soot particles and oxidize them during their regeneration phases. These phases have to be done regularly to keep the filter active between them. PF can reduce the soot emissions in mass of two orders of magnitude. However, they have some limits:

- their use is complicated with regular regeneration phases which have to be done, otherwise the PF can become unusable;
- they are expensive;
- they do not filter small particles smaller than a given diameter (usually 50 nm [18])

1.2.4.b Combustion control

Pollutant emissions can be limited at the engine exhaust by using some methods to optimize the combustion. For instance, the use of Exhaust Gas Recirculation (EGR) reduces the NO_x formation by reducing the temperature inside the cylinder. Indeed, a larger fraction of non-reactive gases with high specific heat (mostly water and CO_2) absorbs the heat release. However, this method also increases the mixture equivalence ratio by reducing the quantity of oxygen inside the cylinder. This leads to an increase of the soot formation.

Some other methods are specific to Diesel engines. For instance, multiple injections can be done in the same cycle. This method uses the heat released by small injections before or after the main one to reach better thermodynamical conditions either for the main combustion to occur or to oxidize soot particles.

However, these methods are empirical and not yet fully understood. More studies have to be done to improve their efficiency, including numerical studies which require models able to predict the evolution of soot inside an engine cylinder.

1.3 Objectives of the present work

This study addresses the new issue of soot particle number in Diesel engines. The more and more restrictive norms create a need of new engine designs among the car manufacturers. To develop these new engines, soot formation and evolution models able to predict soot yield and size distribution in 3-D configurations are required. Indeed, numerical prediction of these data would help the design process to converge to better engine geometries and settings to improve the combustion conditions and reduce the raw-engine soot emissions. The 3-D aspect is also very important because of the very heterogeneous conditions in Diesel engines combustion chambers.

In this context, the objective is to develop a soot model able to predict soot particles yield and soot number density function (SNDF) in 3-D simulations of Diesel engines combustion chamber. This model should:

- provide good enough predictions of soot yield and SNDF to allow the evaluation of parametric variations from simulations;
- be adaptable to industrial 3-D CFD codes without too large cpu costs which would lower its interest.

1.4 Turbulent flows modeling

1.4.1 Different types of simulations

The fuel and air flows in Diesel engines combustion chambers are turbulent. The codes used to perform 3-D simulations of such engines require to represent or to model the turbulence effects. Depending on the size of the domain and the objectives, different methods exist to model turbulence. An illustration of the turbulence spectrum also showing which part of it are modeled by each method is given in Fig. 1.12, along with an illustration of a typical simulated signal in each case. These different approaches are:

- Direct Numerical Simulation (DNS): DNS represents all the scales of the turbulence spectrum by directly solving the Navier-Stokes equations. It requires a very refined mesh to represent

effects down to the Kolmogorov scale. The time step and numerical methods needed to perform a correct DNS are also very expensive in term of cpu cost. This method is not used for combustion chambers simulations yet because of its high computational cost. It is mostly used to study very local phenomena and to develop models for less accurate approaches.

- Large Eddy Simulation (LES): In LES, the smaller scales of turbulence are modeled and turbulence is resolved down to scale Δ (or up to a wavelength κ_c in the turbulence spectrum). Even if part of the turbulence spectrum is modeled, LES allows to simulate variabilities due to turbulence such as engine cycle to cycle variabilities [19]. The computational cost of LES is still very high but combustion chambers simulations using LES can be performed.

- Reynolds Averaged Navier Stokes simulation (RANS): In RANS simulations, the complete turbulence spectrum is modeled. This reduces strongly the computational cost but limits the simulated data to averaged data. However, averaged data taking into account the effects of turbulence is enough for many applications. Thus, RANS simulations are the most used for combustion chambers and industrial applications generally. In these simulations, the influence of the turbulence model as well as the coupling of other models (two-phases flows, combustion ...) is the most important compared to LES or DNS because everything is modeled.

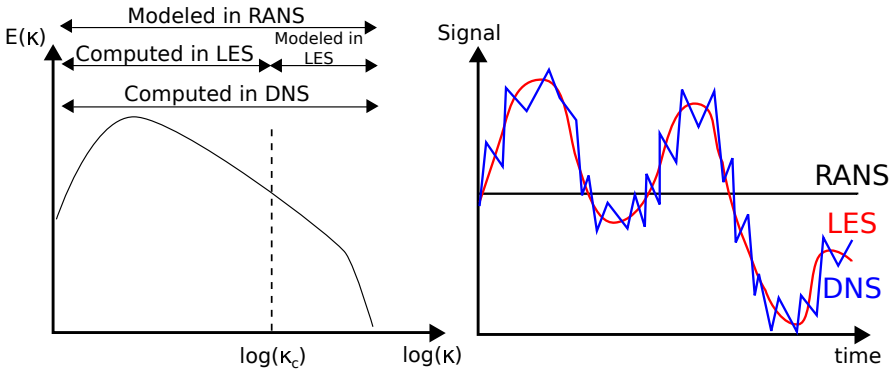

Figure 1.12: Schematic presentation of the modeled and computed part of the turbulence spectrum in RANS, LES and DNS (left) given with example of typical signal in time for the three methods (right).

To perform 3-D simulations of Diesel engines using advanced combustion models coupled to a detailed soot model, only RANS approach appears to be usable at this time. The progress of High Performance Computing coupled to the implementation of advanced combustion models in LES codes could make the use of LES possible in the near future.

1.4.2 RANS simulations basics

1.4.2.a Averaged equations

Any scalar X transported in a turbulent flow can be split into:

- a mean value $\overline{X}$ (Reynolds average)
- a fluctuation X' about its mean value, verifying $\overline{X'} = 0$

Then, the scalar X writes:

$$X = \overline{X} + X' \tag{1.5}$$

To simplify the turbulence equations in compressible flows, Favre average $\widetilde{X}$ can be introduced [20]:

$$\widetilde{X} = \frac{\overline{\rho X}}{\overline{\rho}} \tag{1.6}$$

where ρ is the gas density. Fluctuation about $\widetilde{X}$ writes X'' and verifies $\widetilde{X''} = 0$.

The Navier-Stokes equations can then be averaged [1]. The averaged equations describe the evolution of averaged values affected by turbulence. They read:

- Mass conservation:

$$\frac{\partial \overline{\rho}}{\partial t} + \frac{\partial \overline{\rho}\tilde{u}_j}{\partial x_j} = 0 \tag{1.7}$$

- Momentum:

$$\frac{\partial \overline{\rho}\tilde{u}_i}{\partial t} + \frac{\partial \overline{\rho}\tilde{u}_i\tilde{u}_j}{\partial x_j} = -\frac{\partial \overline{p}}{\partial x_i} + \frac{\partial}{\partial x_j}\left(\overline{\tau_{ij}} - \overline{\rho u_i'' u_j''}\right) \tag{1.8}$$

  where τ_{ij} is the viscous stress tensor and $\overline{\rho u_i'' u_j''}$ is the Reynolds tensor which has to be modeled in RANS. Boussinesq proposed a model which is usually used [21]:

$$-\overline{\rho u_i'' u_j''} = \mu_t\left(\frac{\partial \tilde{u}_i}{\partial x_j} + \frac{\partial \tilde{u}_j}{\partial x_u} - \frac{2}{3}\frac{\partial \tilde{u}_k}{\partial x_k}\delta_{ij}\right) - \frac{2}{3}\overline{\rho}k\delta_{ij} \tag{1.9}$$

  where μ_t is the turbulent viscosity and k is the turbulent kinetic energy defined as $k = \widetilde{u_i'' u_i''}$. Both μ_t and k have to be modeled.

- Species mass fraction:

$$\frac{\partial \overline{\rho}\widetilde{Y_i}}{\partial t} + \frac{\overline{\rho}\widetilde{Y_i}\tilde{u}_j}{\partial x_j} = -\frac{\partial}{\partial x_j}\left(\overline{V_{i,j}Y_i} + \overline{\rho u_j'' Y_i''}\right) + \overline{\rho}\widetilde{\dot{\omega}}_i \tag{1.10}$$

  where Y_i is the i^{th} species mass fraction, $\widetilde{\dot{\omega}}_i$ is the i^{th} species production rate, $\overline{V_{i,j}Y_i}$ is the laminar diffusion flux modeled by a Fick law:

$$\overline{V_{i,j}Y_i} \approx -\overline{\rho}D_i\frac{\partial \widetilde{Y_i}}{\partial x_j} \tag{1.11}$$

  where D_i is the species i diffusion coefficient. Usually, these diffusion coefficients are considered equal for all species and written D. This approximation can be done because the turbulent diffusivity is very dominant over the molecular diffusivity of all species. Finally, a closure is required for the turbulent transport term:

$$\overline{\rho u_j'' Y_i''} = -\frac{\mu_t}{Sc_t}\frac{\partial \widetilde{Y_i}}{\partial x_j} = -D_t\frac{\partial \widetilde{Y_i}}{\partial x_j} \tag{1.12}$$

where Sc_t is the turbulent Schmidt number and $D_t = \frac{\mu_t}{Sc_t}$ the turbulent diffusion. Then, the transport equation of the i^{th} species mass fraction writes:

$$\frac{\partial \overline{\rho}\widetilde{Y_i}}{\partial t} + \frac{\overline{\rho}\widetilde{Y_i}\tilde{u}_j}{\partial x_j} = \frac{\partial}{\partial x_j}\left((D + D_t\frac{\partial \widetilde{Y_i}}{\partial x_j}\right) + \overline{\rho}\widetilde{\dot{\omega}_i} \tag{1.13}$$

- Enthalpy:

$$\frac{\partial \overline{\rho}\widetilde{h_s}}{\partial t} + \frac{\overline{\rho}\widetilde{h_s}\tilde{u}_j}{\partial x_j} = \frac{\partial}{\partial x_j}\left(\frac{\mu_t}{Pr_t}\frac{\partial \widetilde{h_s}}{\partial x_j}\right) + \widetilde{\dot{\omega}}_h \tag{1.14}$$

where Pr_t is the turbulent Prandtl number and $\widetilde{\dot{\omega}}_h$ is the enthalpy source term.

Similar transport equations can be written to represent variance $\widetilde{X''^2}$ of any scalar X.

1.4.2.b Turbulence modeling

Various models exist to compute turbulence effects in RANS simulations [1]. The ones used in this study are two variations of the k-ϵ model: the standard one and the Re-Normalization Group (RNG). Both models are based on two transport equations and a set of constants. First, the turbulent viscosity, μ_t, writes:

$$\mu_t = C_\mu \rho \frac{k^2}{\epsilon} \tag{1.15}$$

where C_μ is a model constant.

The turbulent kinetic energy k is given by the following transport equation:

$$\frac{\partial \overline{\rho}k}{\partial t} + \frac{\overline{\rho}k\tilde{u}_j}{\partial x_j} = \frac{\partial}{\partial x_j}\left[\left(\mu + \frac{\mu_t}{\sigma_k}\right)\frac{\partial k}{\partial x_j}\right] + P_k - \overline{\rho}\epsilon \tag{1.16}$$

where σ_k is a modeling constant, $P_k = -\rho\overline{u_i''u_j''}\frac{\partial u_j}{\partial x_i}$. The turbulent energy dissipation rate ϵ is deduced from a transport equation:

$$\frac{\partial \overline{\rho}\epsilon}{\partial t} + \frac{\overline{\rho}\epsilon\tilde{u}_j}{\partial x_j} = \frac{\partial}{\partial x_j}\left[\left(\mu + \frac{\mu_t}{\sigma_\epsilon}\right)\frac{\partial \epsilon}{\partial x_j}\right] + C_{\epsilon 1}\frac{\epsilon}{k}P_k - C_{\epsilon 2}\overline{\rho}\frac{\epsilon^2}{k} \tag{1.17}$$

where σ_k and $C_{\epsilon 1}$ are model constants. $C_{\epsilon 2}$ is a model constant in the standard model and deduced from an equation in the RNG model [22].

The constants for the standard k-ϵ model are taken from Jones and Launder [23]. The equivalent set of constants as well as the relation giving $C_{\epsilon 2}$ are taken from Yakhot *et al.* [22] for the k-ϵ RNG model.

1.5 Thesis outline

This thesis is split into two parts, each one separated in two chapters:

- First, the soot formation and evolution is studied. A study of the physical phenomena involved in soot life cycle and the existing methods to model soot particles is given in Chapter 2. It is concluded by a definition of the modeling approach proposed in this study and an explanation of its novelties with respect to the models existing in the literature. Then, the solid phase soot model is detailed in Chapter 3. Finally, a first validation on academical cases is presented.

- Then, two validation cases of the sectional soot model coupled with detailed chemistry turbulent combustion models are presented with 3-D RANS simulations compared to experimental measurements. In Chapter 4, Diesel engine cases are studied using an experimental database of various operation points which have been simulated. The Chapter 5 contains a similar study for Diesel sprays in a constant volume vessel with more detailed diagnostics and combustion model. This vessel allows more measurements to be performed for validations than an actual engine case would. The respective combustion models which are coupled with the soot model are presented with each validation.

Global conclusions about the present work are given in the last chapter.

Chapter 2

Soot modeling background

Introduction

Soot particles are low diameter compounds (from nanometer to micrometer) of reactive flows usually composed of aggregated elementary particles. They are created by the condensation of carbonic species in the rich regions of flames. Although they are used since prehistory for Cave Art [24, 25], their structures and the physical phenomena driving their evolutions are still open topics. Indeed, soot formation is based on several phenomena strongly depending on local thermodynamic conditions and gaseous composition which make them difficult to model.

In this chapter, the main phenomena of soot formation understood or predicted so far are presented first. Then, the existing soot modeling approaches are presented. Finally, the proposed model, which will be presented in Chapter 3, and its situation among the different approaches is clarified as well as the soot modeling objectives of this study.

2.1 Soot formation mecanisms

Soot formation is a very complex phenomenon of conversion from gaseous hydrocarbon molecules to solid agglomerates containing thousands of carbon atoms. The different phases of soot formation are still uncertain but the global path leading to these agglomerates is known. These steps are illustrated in Fig. 2.1 and detailed in this section.

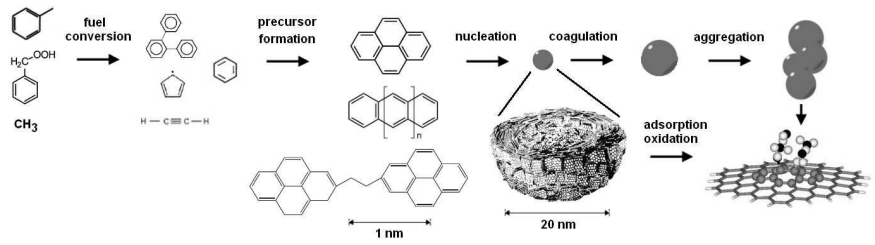

Figure 2.1: Illustration of the main pathways for soot formation and evolution.

2.1.1 Gaseous precursor formation

Polycyclic Aromatic Hydrocarbons (PAH) are considered as the main soot precursors. They are reaction intermediates of combustion and their evolutions are still open topics. However, their growth is usually based on single ring aromatic species such as benzene (C_6H_6), phenyl group (C_6H_5) and cyclopentadienyl (cC_5H_5).

2.1.1.a First aromatic cycle formation

The representation of the first aromatic cycles formation is then a crucial step towards soot modeling since they are the base of PAH block in kinetic schemes. Three main pathways have been identified in the litterature to lead to the first benzene ring [26]:

- The $C_4 + C_2 \rightarrow C_6$ reactions:
  A first way to create a benzene ring (C_6H_6) was proposed by Cole *et al.* [27] and Frenklach *et al.* [28]:

$$C_2H_3 + C_2H_2 \rightarrow C_4H_5 \tag{2.1}$$
$$C_4H_5 + C_2H_2 \rightarrow C_6H_6 + H \tag{2.2}$$

  However, Miller and Melius [29] have shown that these reactions cannot explain the amount of benzene measured experimentally in some cases.

- The $C_3 + C_3 \rightarrow C_6$ reactions:
  Kern and Xie [30] proposed a second way to form a benzene ring from smaller hydrocarbons. This reaction, also mentioned by Miller and Melius [29], is the recombination of two propargyl radicals (C_3H_3) into a benzene ring:

$$C_3H_3 + C_3H_3 \rightarrow C_6H_6 \tag{2.3}$$
$$C_3H_3 + C_3H_3 \rightarrow C_6H_5 + H \tag{2.4}$$

- The $C_5 + C_1 \rightarrow C_6$ reaction:
  Another reaction has been proposed later by Melius *et al.*[31] and also validated by Ikeda *et al.* [32]. This reaction is the addition of a methyl group on cyclopentadiene:

$$C_5H_5 + CH_3 \rightarrow C_6H_6 + 2H \tag{2.5}$$

There are still studies to predict single ring aromatic species with more accuracy. Lamprecht *et al.* [33] showed that the balance of the three proposed reactions to form benzene depended strongly on thermodynamical conditions in acetylene and propene flames. A similar study of Gueniche *et al.* [34] led on methane flames doped by unsaturated compounds also shows the sensitivity of benzene formation to the different pathways.

Rasmussen *et al.* [35] studied the dominance of $C_3H_3 + C_3H_3 \rightarrow C_6H_5 + H$ reaction in the propargyl recombination way. The $C_3 + C_3$ reactions rate constants are also evaluated in recent works [36, 37].

Recently, Nawdiyal *et al.* [38] studied rich 1-hexene flames showing a dominance of the $C_5 + C_1 \rightarrow C_6$ reactions over the propargyl recombination, the $C_4 + C_2 \rightarrow C_6$ pathway being the less important one. However, Bierkandt *et al.* [39] showed that the propargyl recombination is dominant in acetylene flames. These recent results illustrate the importance of fuel for the first step leading to soot formation.

2.1.1.b Polycyclic Aromatic Hydrocarbons formation

PAH formation models are still very uncertain due to the very low concentration and lifetime of these species, making experimental measurements very complicated. However, the recent progress in optical diagnostic could offer new possibilities and data to modelers [40].

Some pathways already exist to represent the growth from single ring aromatic species to Polycyclic Aromatic Hydrocarbons. The two main pathways are presented in the following:

- Cyclopentadiene to naphthalene [31]:
  The growth to PAH could begin with the cyclopentadiene recombination to naphthalene which can be presented either in one or multiple step rearranging atoms to add a second aromatic ring on the first cyclopentadiene:

$$C_5H_5 + C_5H_5 \rightarrow \text{Naphthalene} + 2H \tag{2.6}$$

  This pathway is shown to be not dominant in the growth of larger aromatic species [41, 42]. However, Lindstedt and Rizos [43] also showed that this direct reaction would overpredict naphthalene and a two-step sequence could not explain the amount of naphthalene experimentally measured.

- The HACA cycle [26, 28, 44]:
  The Hydrogen Abstraction Carbon Addition (HACA) cycle is a usual representation of growth from benzene to larger PAH. The HACA cycle described by Francklach and co-workers [26, 28, 44] is based on two reactions occurring repetitively: Hydrogen Abstraction by a radical hydrogen and Carbon Addition from acetylene, as illustrated in Fig. 2.2. This cycle is consid-

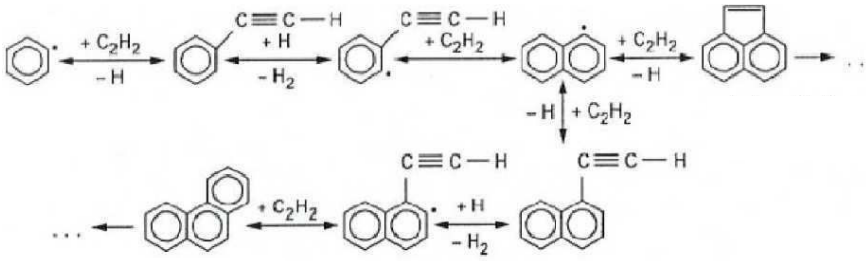

Figure 2.2: Illustration of the HACA cycle reactions

ered dominant for PAH growth by Appel *et al.* [45] but Böhm *et al.* [46] showed its limit to predict some PAH species. Even if it is commonly used, the physical details of the reaction represented in this cycle are still uncertain. This cycle is then used as a reference and a base to develop growth cycle either by adding reactions or by using various sets of reaction rate constants [47, 48]. Moreover, similar cycles are proposed such as the "phenyl addition/cyclization" (PAC) and the "methyl addition/cyclization" (MAC) are studied [49].

Frenklach [26] also mentioned the cyclopentadiene way as an addition to the HACA cycle. In recent models, the two approaches are mixed with creditable results [50, 51]. However, the growth of PAH is also still an open topic as explained by Wang [52], as well as the nascent soot physics based on PAH.

2.1.2 Smallest solid particles: particle inception

The actual conditions on which carbon condenses into solid particles are not yet known [26, 53, 54]. Usually, the first solid particles correspond to a dimer PAH larger than pyrene [45]. This way to model particle inception is usually used in soot models [55, 56, 57, 58]. Coronene is taken as a reference by Richter *et al.* [59], leading to a similar size for the smallest solid particles. Another approach exists, based on atomic mass unit *amu*, considering that carbon compounds are solid when their atomic mass unit is larger than a constant criterion, varying from 800 to 2000 [60, 61].

For all considered sizes of the smallest solid particles, most of the representations of particle inception are based on two phenomena:

- Solid particles formation from colliding precursors [26, 53] described by the Smoluchowski equation [62],
- Growth of large enough carbon-based compounds from the HACA cycle [28].

In this context, two situations are isolated by Frenklach [26]. At low temperatures, chemical bond can be created from collisions because there are only little thermodynamical limits to it. At higher temperatures, the growth is controlled by the HACA cycle which is based on acetylene, a thermodynamically stable species.

Recently, Eaves *et al.* [54] study also stressed the importance of taking into account the reversibility of the particle inception process. These results agree with the measurements of Sabbah *et al.* [63] observing a too strong dissociation of pyrene dimerization for it to be a liable reaction of particle inception. Accordingly, pyrene should only be used as an indicator of where particles inception occurs and how it varies with respect to standard combustion parameters (equivalence ratio, temperature, pressure...).

2.1.3 Collisional phenomena

2.1.3.a Light particle collisions

Two main phenomena are usually modeled as collisional phenomena:

- Condensation: PAH colliding with a solid soot particle;
- Coagulation: collision between two solid soot particles.

Condensation increases soot mass and size without impacting on the particle number, while coagulation increases particle size and decreases particles number without impacting on soot mass. Particle inception can also be considered as a collisional phenomenon [53, 55, 56]. The most common approach has been proposed by Seinfeld [64] and also applied to the soot formation context by Kazakov and Frenklach [65]. It describes collisional phenomena using the Smoluchowski equation:

$$\dot{N}_{a,t} = \frac{1}{2}\int_0^a \beta_{a-b,b} N_{b,t} N_{a-b,t} db - \int_0^\infty \beta_{a-b,b} N_{a,t} N_{b,t} db \tag{2.7}$$

This equation provides the collisional source term for particles of size a: $\dot{N}_{a,t}$. $\beta_{x,y}$ represents the collision frequency between particles of sizes x and y. It should be noticed that even if a represents the size of solid particles, $a-b$ and b can represent:

- two sizes of gaseous soot precursors leading to a solid particle of size a (particle inception)
- a gaseous soot precursor and a solid soot particle (condensation)
- two solid soot particles (coagulation)

The collision frequency $\beta_{x,y}$ depends on the Knudsen number Kn and thermodynamical conditions. The Knudsen number reads:

$$Kn(x) = \frac{\lambda_{gas}}{d} \tag{2.8}$$

where d is the diameter of the considered particle and λ_{gas} is the mean free path, written:

$$\lambda_{gas} = \frac{RT}{\sqrt{2} d_{gas}^2 \mathcal{N}_A P} \tag{2.9}$$

where P is the pressure, T is the temperature, $\mathcal{N}_A$ is the Avogadro number, R the universal gas constant and d_{gas} the mean diameter of gas molecules.

Depending on the Knudsen number, three collision regimes can be established [64, 65]:

- If $Kn \gg 1$ ($Kn > 10$ in [55, 56, 57]), the pressure is low enough and the particles are small enough with respect to the temperature driven agitation for a free-molecular regime of collision to be established. The particles can be considered as randomly moving spheres which can collide within a very large free space between each of them. In this case, the collision frequency $\beta_{x,y}$ writes:

$$\beta_{x,y}^{fm} = \left(\frac{3}{4\pi}\right)^{\frac{1}{6}} \sqrt{\frac{6k_bT}{\rho_{soot}}} \sqrt{\frac{1}{x}+\frac{1}{y}} \left(x^{\frac{1}{3}} + y^{\frac{1}{3}}\right)^2 \tag{2.10}$$

  where k_b is the Boltzmann constant, ρ_{soot} is the solid soot density, x and y are the colliding particles volume and T the gaseous temperature.

- If $Kn \ll 1$ ($Kn < 0.1$ in [55, 56, 57]), the pressure is high enough and the particles are large enough with respect to the temperature driven agitation for a continuum regime of collision to be established. The amount of space taken by particles and their motions is large with respect to the available space and collisions are more likely to occur. In this case, the collision frequency $\beta_{x,y}$ writes:

$$\beta_{x,y}^{c} = \frac{2k_bT}{3\mu} \left(\frac{C(x)}{x^{\frac{1}{3}}} + \frac{C(y)}{y^{\frac{1}{3}}}\right) \left(x^{\frac{1}{3}} + y^{\frac{1}{3}}\right) \tag{2.11}$$

  where μ is the gaseous dynamic viscosity and $C(x) = 1 + 1.257Kn$ is the Cunningham slip correction factor [66, 67].

- For intermediary cases, the collision frequency is written as the harmonic mean of the limit values [65, 67, 68]:

$$\beta_{x,y} = \frac{\beta_{x,y}^{fm}\beta_{x,y}^{c}}{\beta_{x,y}^{fm} + \beta_{x,y}^{c}} \tag{2.12}$$

2.1.3.b Agglomeration

When the primary particles growth step is over, the particles grow by a collisional phenomenon called agglomeration. They collide and bound to each other in order to form large chain structures [26]. These agglomerates are the large particles measured at the exhaust of Diesel engines. However, the agglomeration mechanisms are still unknown and defining their structure is a current research topic [69, 70]. These structures are also studied for soot-in-oil to evaluate the effect of soot particles over lubricant as in La Rocca *et al.* [71].

The collision rates are modeled as coagulation ones in most models models [57, 72, 73] but multiple variables models can predict agglomerates structures [73].

2.1.4 Soot surface chemistry

Soot particles evolutions also depend on chemical phenomena. The gaseous phase composition and thermodynamical conditions as well as the available soot surface and its ability to react are parameters which lead to an increase or a decrease of the soot mass due to surface chemistry.

Frenklach proposed a soot surface chemistry controlled by the HACA cycle. This approach is very commonly used to represent soot surface chemistry [52, 55, 56, 61, 74, 75, 76, 77, 78, 79, 80]. It is based on the assumption that $C-H$ bounds are present on soot surface. The HACA cycle could then occur at soot surface as it does for the gaseous PAH growth [26]. The HACA cycle constants are not yet well defined [52] and various studies propose different sets of constants as the one proposed by D'Anna and Kent [74, 75]. A version of the HACA cycle including a reverse reaction on the carbon addition, named HACA Ring Closure (HACA-RC), has also been proposed by Mauss [81] and used for soot modeling [55, 77, 78].

It has been shown that the chemical reaction rate of particle decreases with particle size [26, 82]. Two main causes have been identified to explain this phenomenon [26, 82]:

- Reaction sites at soot surface might not be active due to surface state.
- Gaseous hydrogen concentration could decrease, stopping the first step of the HACA cycle to occur for most of the soot surface reactive sites.

The evaluation of soot surface composition is a major aspect of soot surface modeling [52]. Recent studies of Dworkin and co-workers [83, 84] proposed a representation of the proportion of active sites depending on the thermal history of particles. This topic is also a source of research in the field of atmospheric sciences [85].

2.2 Soot modeling approaches

To design engines able to match the more and more stringent norms of the 21^{th} century, the car manufacturers need models able to predict soot production of real engines. To reach these current industrial targets for soot predictions, the previously introduced physical phenomena have to be integrated into advanced numerical models. The complexity of these models depends on which type of prediction is needed and on the tool it has to be implemented in.

There are three main types of soot models [86]: empirical models, semi-empirical models and phenomenological models (or detailed models). These three different types of models are presented in this section.

2.2.1 Empirical correlations

Empirical correlations are very often used by the car industry. These models are based on correlations between the soot mass production and the engine operating conditions. These correlations were the first step towards soot modeling. For instance, Calcote and Manos [87] defined a Threshold Soot Index (TSI) that ranks fuel from 0 to 100 depending on their soot production and proposed a correlation between this TSI and the fuel molecular structure for premixed and diffusion flames. This correlation has been studied by Olson *et al.* [88], providing a large database of case to widen its possible applications.

More recent correlations can depend on more parameters such as the one proposed by Mehta and Das [89], commonly used for engine simulations. They obtained a correlation depending on six parameters: the spray mixing rate, the swirl mixing rate, the compression ratio, the injection temperature, the injection velocity and the engine speed. As illustrated in Fig. 2.3, this correlation gives decent predictions of soot production when compared to experimental measurements.

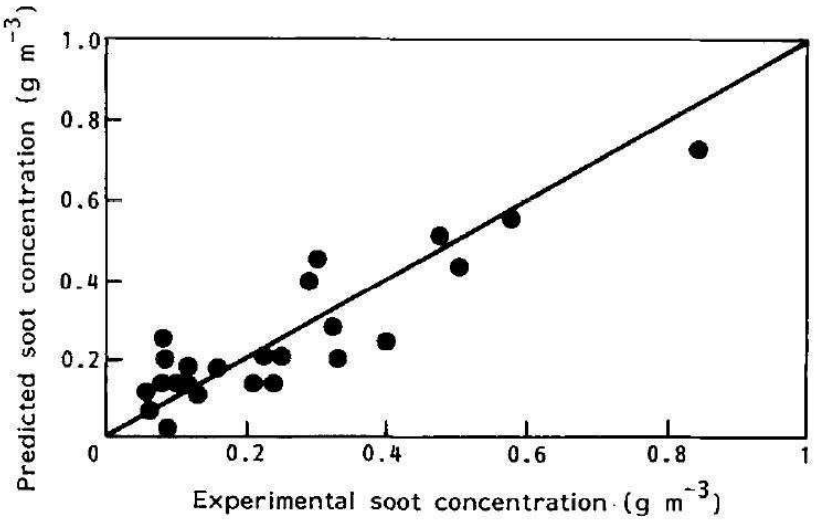

Figure 2.3: Prediction of a Diesel engine soot yield using Mehta and Das correlation [89] compared to experimental measurements [89].

However, these correlations can only be used in conditions close to the one they were established on. They also only provide global soot values, either mass or volume fraction. It is not possible to describe the soot distribution in size using this type of correlation.

These correlations are also not usable in 3-D CFD code because they do not predict a time-evolution of soot particles. Instead, they only predict a final value at exhaust for engine correlations, or a value such as the TSI for flames correlations.

The use of these approaches is limited to global system simulations.

2.2.2 Semi-empirical models

Semi-empirical models attempt to represent some physical phenomena driving soot time-evolution. However, the different sizes of soot particles are not represented and global formation and oxidation rates are applied to values representing the whole range of modeled particles. These global source terms are usually applied to one or two variables and are designed to be applicable to turbulent flames simulations as the model proposed by Leung *et al.* [90] which was recently used to model soot evolution in Diesel sprays simulations by Bolla *et al.* [91] using a Conditional Moment Closure approach. These models can also be coupled with detailed PAH modeling as proposed by Sukumaran *et al.* [58].

The modeled variables can be different from one model to another. Three examples are given to illustrate the different types of semi-empirical models from the more empirical to the more phenomenological one:

- Said *et al.* [92] model: In this model, two transported variables are used to describe the soot time-evolution. The first variable is an intermediary soot species mass fraction Y_I equivalent to a soot precursor. The second variable is the total mass fraction of soot Y_S. These two species are coupled as shown in their respective transport equations:

$$\dot{\omega}_{Y_I} = k_A Y_F Y_{Ox}^{\alpha} exp\left(-\frac{T_A}{T}\right) - k_B y_I Y_{Ox}^{\beta} \exp\left(-\frac{T_B}{T}\right) - k_I(T) Y_I \tag{2.13}$$

$$\dot{\omega}_{Y_S} = k_1(T) Y_I - \frac{k_O}{\rho_S d_S} Y_{Ox} Y_S P T^{-1/2} \exp\left(-\frac{T_C}{T}\right) \tag{2.14}$$

  where k_A, k_B, k_O, α, β, T_A, T_C and T_B are experimentally-obtained constants, k_I and k_S are experimentally-correlated reaction rates, d_S is an arbitrary-guessed particle diameter, ρ_S is the density of solid soot, P is the pressure, T is the temperature and Y_{Ox} and Y_F are the mass fraction of oxidant and fuel respectively.

  The intermediary soot species I is created by the fuel cracking and consumed by oxidation and the creation of actual soot S. Here, the soot variable S is only formed from the intermediary species and consumed by oxidation.

  This model predicts a soot mass time-evolution in the context of a 3-D simulation but does not include the representation of different phenomena such as coagulation, particle inception or surface growth.

- Moss *et al.* [93] model: In this model, the two variables representing the soot time-evolution are the soot number density N and the soot volume fraction f_v. The evolutions of these two variables are controlled by the following source terms included in standard transport equations:

$$\dot{\omega}_{\frac{N}{\mathcal{N}_\mathcal{A}}} = \alpha - \beta \left(\frac{N}{\mathtt{N_A}}\right)^2 \tag{2.15}$$

$$\dot{\omega}_{\rho_S f_v} = \gamma N + \delta \tag{2.16}$$

  where $\mathcal{N}_\mathcal{A}$ is the Avogadro number, β is a variable representing coagulation, γ is a variable representing surface growth, α and δ are variables representing particle inception. These

variables write:

$$\alpha = C_\alpha \rho^2 T^{1/2} X_C \exp\left(-\frac{T_{alpha}}{T}\right) \quad (2.17)$$

$$\beta = C_\beta T^{1/2} \quad (2.18)$$

$$\gamma = C_\gamma \rho^2 T^{1/2} X_C \exp\left(-\frac{T_{gamma}}{T}\right) \quad (2.19)$$

$$\delta = C_\delta T^{1/2} \quad (2.20)$$

where ρ is the gas phase density, X_C the fuel mole fraction and the C_i and T_i are prescribed numerical constants.

The model of Moss *et al.* [93] represents particle inception and its effect on the soot volume and number. The surface growth is also represented and its source term couples the soot number density and volume fraction. Finally, the coagulation effect is only to reduce the soot number density.

This model provides data on the soot volume fraction and number, thus also giving an average particle size. It also takes into account most phenomena involved in soot evolutions but does not include oxidation.

- Phenomenological Soot Kinetics (PSK) model [80]: In the PSK model, the evolution of two variables, an intermediary soot variable "PR" and a soot species "Soot" evolutions are driven by a set of ten reactions:

$$\begin{aligned}
\mathrm{C}_n\mathrm{H}_m &\overset{R1}{\leftrightarrow} \frac{n}{2}\mathrm{C}_2\mathrm{H}_2 + \frac{m-n}{2}\mathrm{H}_2 \\
\mathrm{C}_2\mathrm{H}_2 &\overset{R2}{\leftrightarrow} \frac{2}{n_{C,PR}} PR + \mathrm{H}_2 \\
PR + PR &\overset{R3}{\leftrightarrow} soot \\
soot_i + \mathrm{C}_2\mathrm{H}_2 &\overset{R4}{\leftrightarrow} soot_{i+2} + \mathrm{H}_2 \\
soot_i + PR &\overset{R5}{\leftrightarrow} soot_{i+n_{C,PR}} \\
soot_i + soot_j &\overset{R6}{\leftrightarrow} soot_{i+j} \\
PR + \frac{n_{C,PR}}{2}\mathrm{O}_2 &\overset{R7}{\leftrightarrow} n_{C,PR}\mathrm{CO} \\
\mathrm{C}_2\mathrm{H}_2 + \mathrm{O}_2 &\overset{R8}{\leftrightarrow} 2\mathrm{CO} + \mathrm{H}_2 \\
\mathrm{H}_2 + \frac{1}{2}\mathrm{O}_2 &\overset{R9}{\leftrightarrow} \mathrm{H}_2\mathrm{O} \\
soot_i + \mathrm{O}_2 &\overset{R10}{\leftrightarrow} 2\mathrm{CO} + soot_{i-2}
\end{aligned} \quad (2.21)$$

where $n_{C,PR}$ is the number of carbon atoms in a precursor, $soot_i$ is the soot species and $soot_{i+j}$ does not represent a different soot species but indicates the fact that the reaction will add or take the mass of j carbon atoms from the soot species.

This model represent all phenomena from fuel pyrolysis (R1) to soot oxidation (R10), including PAH formation (R2), particle inception (R3), surface growth from precursors (R5) and acetylene (R4), coagulation (R6) and oxidation of precursors (R7) and acetylene (R8,R9).

The PSK model has been used for 3-D RANS modeling of engine cases [94, 95]. It provides a prediction of the soot mass in 3-D RANS simulations by taking into account all phenomena involved in soot formation and oxidation.

The use of only two variables at most in these semi-empirical approaches makes them unable to predict soot size distributions. This limit is also a limit to their prediction of soot mass and number time-evolution because many phenomena depend on particle size.

2.2.3 Detailed soot models

In order to predict the soot time-evolution with a better accuracy and to also predict SNDF, detailed soot models have been developed. These models represent the dynamics of soot formation from the smallest solid particle to large primary particles or agglomerates. They split into three main types, described in the following.

2.2.3.a Stochastic approach

Stochastic approaches model molecules and particles structures and their evolutions using Monte-Carlo method usually. The modeled particles structures evolve by the addition or abstraction of atoms according to probabilistic considerations. Using presumed trajectories to represent the input of their stochastic model, Balthasar and co-worker predicted complete SNDF with credible results [96, 97]. The method has been used by Singh *et al.* to predict SNDF including data on particle age, allowing to study numerically the evolution of some soot modeling parameter dependence to soot aging [98].

These approaches also permit the modeling of molecular structures of soot precursors or particles. Violi and co-workers modeled the physical properties of soot precursors and predicted characteristic time for particle inception using these approaches [99, 100, 101]. Stochastic approaches also allow the description of the type and number of available sites at PAH and nascent particles surface [102, 103].

However, it is very complicated to direclty couple a gas phase solver and this type of soot model [104]. Moreover, some of the features provided by these approaches, such as the site description, are not directly usable with a complete population balance equation solver [103]. Some recent works have been done to conceive this type of coupling in simple flows, mostly focusing on the issue of coagulation modeling [105, 106, 107].

2.2.3.b Method of moments

The method of moments is a mathematical method used to describe dispersed phases in flows. Based on an assumption on the dispersed phase distribution shape, the method of moment allows to describe the distribution using its first characteristic moments. The dispersed phase can be described by more than one variable, usually two variables are used to describe soot distributions [73, 108, 109, 110] In this context, the order x in volume and y in surface moment of a distribution writes:

$$\mathcal{M}_{n,y} = \sum_i V_i^x S_i^y N_i \tag{2.22}$$

where V_i, S_i and N_i are respectively the volume, surface and particle number density of size class i. More complex closure can also be used to describe moments of soot distribution [108]. The physical

phenomena are then represented by their effects on the different moments of the distribution as detailed by Mueller *et al.* [108].

Balthasar and co-workers [97, 111] used a single variable method to describe soot volume fraction evolutions in partially-stirred plug flow reactor and laminar flames. Single variable method has also been used to model turbulent jet by Mauss *et al.* [112] showing good prediction of soot volume fraction. This method has even been applied to 3-D RANS Diesel sprays simulations by Karlsson *et al.* [113] and full engine simulations by Priesching *et al.* [114] but without quantitative comparisons against the experimental measurements.

Laminar flames and counterflow diffusion flames have also been studied using a two variable approach by Mueller *et al.* [108, 109]. Thanks to its low computation cost, the method of moments have been used in 3-D CFD simulations, including LES [110, 115, 116] and DNS [73, 117, 118]. Flames simulated using a method of moments in a LES code show various results qualities in terms of soot volume fraction with respect to the experimental measurements [110, 115]. However, Mueller and Pitsch presented a complete LES simulation of an aircraft combustor, without experimental comparison though [116].

Using an infinity of moments would describe the distribution totally. However, this is practically impossible. A limited number of moments is then used to represent the distribution and this leads to the assumption made on the distribution shape. Moreover, the data of the predicted SNDF is rarely given and compared to experiment yet.

2.2.3.c SNDF resolution

In these approaches, the distribution in size of soot particles is split into different classes. Both sectional dispersed phase models and chemical models representing soot particles as species are included in this discussion. Indeed, these two approaches share the splitting in size of the SNDF and only express it in different ways. The main difference between the two approaches lies on the way the source terms are written.

- Chemical representation [72, 74, 119]: In this type of model, a detailed kinetic mechanism describes the evolution of gaseous species during the combustion as well as large PAH species which represent the solid phase. Usually, the switch from the standard gaseous reactions to the solid phase reaction occurs for species constituted of more than 30 carbon atoms. The different processes driving soot formation and evolution will all be written as chemical reactions. For instance, in the model proposed by Richter *et al.* [119], the growth of the tenth size class soot particles (called $BIN10$) by acetylene addition reads:

$$\mathrm{BIN10J} + \mathrm{C_2H_2} \rightarrow 0,9998408\ \mathrm{BIN10} + 0,0001592\ \mathrm{BIN11} + 0,5414\ \mathrm{H} \tag{2.23}$$

  where $BIN10J$ is a species representing the radical aromatic of size class 10, $BIN10$ and $BIN11$ are the aromatic of size classes 10 (representing particles with mass from 102401 to 204800 amu) and 11 (representing particles with mass from 204801 to 409600 amu) respectively.

  This model has been used to simulate soot number density and average particle size in laminar premixed benzene flames [119]. D'Anna and Kent also used this type of approach to simulate soot volume fraction and mass in ethylene premixed and non-premixed laminar flames [74, 76] and soot volume fraction in methane, ethylene and butene premixed laminar flames [75].

These models require large computational resources because both the detailed kinetic scheme has to be solved, including all the reactions between every "BIN". However, it has been used for 3-D RANS Diesel simulations by Fraioli *et al.* [72] with decent results but a very high computation cost as planned.

- Sectional method [55, 61, 77]: The sectional method describes the SNDF as a distinct dispersed phase interacting with the gaseous phase. This dispersed phase is composed of a given amount of scalars, representing the size classes of the distribution. Introduced by Gelbard *et al.* for atmospheric aerosol studies [120], it has also been used to describe spray droplets by Tambour and co-workers [121, 122]. The relevance of this method for spray simulations has been contested by Laurent and Massot [123] because the various velocities and temperature of same size droplets at the same locations cannot be represented. However, the method has been applied to soot formation and is still considered relevant for these cases because these issues are neglectable compared to soot formation and oxidation processes.

  This method has been applied to ethylene laminar premixed flames [57, 124], to ethylene nonpremixed laminar flames [79, 84] and to ethylene turbulent diffusion flames by Netzell *et al.* [78]. A single Diesel engine case has also been simulated by Marchal *et al.* [125] showing the method can be applied to complete engine simulations.

  The source terms description can be very similar to the ones used with chemical representation of soot as in Blacha *et al.* [61]. This study also includes a sectional representation of PAH growth between the gaseous phase and the solid soot phase sectional model. This approach shows good results on ethylene, propylene, kerosene surrogate and toluene premixed and nonpremixed laminar flames [61] for soot volume fraction and SNDF predictions. It has also been applied to turbulent nonpremixed flames [126] with encouraging results.

  Finally, the computation cost of this method can be high because of the large number of scalars to transport (one per section) but its numerical implementation is simple. Moreover, this method is not based on an assumption concerning the SNDF shape.

2.3 The proposed approach

In the present study, the proposed model only aims to represent the solid soot phase as the models presented in Section 2.2. Empirical and semi-empirical models cannot be used in this study because the industrial requirements include the concept of particle size to match norms past EURO 5. Moreover, the target model has to be implemented in a 3-D CFD code in order to represent the composition heterogeneities, which could not be done with an empirical model. However, most of the detailed soot models currently developed have not been validated against experimental measurements on 3-D cases. The few of them which have been validated, mostly with a sectional approach, usually are only presented with one 3-D case. Moreover, all the referenced turbulent flames were simulated with light fuels.

Accordingly, a detailed soot model has been developed. Among the different approaches to model soot size distributions, only the sectional method and method of moments were suitable for this study. Indeed, stochastic approaches can hardly be coupled to codes including spatial heterogeneities and the chemical approach would require either to solve a complete kinetic scheme or to tabulate every species representing solid soot particles which is practically impossible. Even

if the computation cost is higher for sectional models, this approach has been preferred over the method of moments for three reasons:

- to avoid the presumption of the soot size distribution shape;
- because the method of moments requires specific numerical schemes to ensure moments realizability [127];
- because its numerical implementation does not require a reconstruction of the SNDF, thus allowing a direct and easier study of the different locations of soot particles with respect to their sizes in 3-D simulations.

However, similar works using the method of moments could be done in the future as a perspective of the present study.

The gaseous phenomena described in Section 2.1.1 (growth of PAH) will not be studied and are included in kinetics schemes taken from literature to represent the gaseous phase. A major aspect of this work is to introduce the predictions of these kinetic schemes into 3-D RANS simulations with a reasonable computation cost. The tabulated turbulent combustion models used to do so are described in Chapter 4 and 5 prior to the description of the validation case they were used with.

In this context, the main objectives of this study are:

- to adapt a sectional soot model to Diesel conditions;
- to couple it with turbulent combustion models able to model heavy fuels combustion;
- to validate both the model and its coupling to a turbulent combustion model against experimental data.

This leads to three main novelties presented in this study:

- the confirmation that tabulated approaches can be coupled to detailed soot solver, their ability to reproduce the gaseous chemistry required by this type of soot model being shown;
- the validations of a detailed 3-D soot model against experimental data on 3-D turbulent cases (engine cases and spray cases in a constant volume vessel);
- the validation of a detailed 3-D soot model on heavy fuels turbulent flames or engine cases.

Chapter 3

The Sectional Soot Model

Introduction

The sectional soot model proposed in this study is first described in Section 3.1. To illustrate the effects of the proposed changes to the reference model, comparisons to the reference model and to academical experiments are presented in Section 3.2.

3.1 Soot modeling

The soot model introduced in the present study is based on the approach of Mauss [81, 128] followed by the more recent work of Netzell *et al.* [55, 78], Marchal [56, 77] and Vervisch-Kljakic [57]. This section describes its governing equations and the evolutions brought to the source terms estimation.

The soot particles population is evaluated by using a sectional method. The soot particles are separated with respect to their volume into discrete sections. In contrast to Fraioli *et al.* [72] where soot particles are considered as chemical species, the present approach considers that soot particles are solid and modeled as a distinct dispersed phase, interacting with the gaseous phase. In the turbulent reactive flow, each section i, representing the soot particles of a given volume range, is governed by a standard transport equation for the soot mass fraction in this section, $\widetilde{Y}_{soot,i}$:

$$\frac{\partial \overline{\rho}\widetilde{Y}_{soot,i}}{\partial t} + \nabla \cdot (\overline{\rho}\tilde{u}\widetilde{Y}_{soot,i}) = \nabla \cdot (\overline{\rho} D_{t,soot} \nabla \widetilde{Y}_{soot,i}) + \overline{\rho}\widetilde{\dot{\omega}}_{soot,i} \tag{3.1}$$

with $\overline{\rho}$ the gas phase density, $\tilde{u}$ the gas velocity, $D_{t,soot}$ the turbulent diffusion coefficient of soot and $\widetilde{\dot{\omega}}_{soot,i}$ the soot source term for section i.

We start with the presentation of the particle volume discretization and of the variables used to represent soot particles in each section. Then, the different physical phenomena involved in the soot formation process are described. These phenomena are illustrated in Fig. 3.1 and are introduced in the following order:

- First, collisional source terms: particle inception, condensation and coagulation.
- Secondly, surface chemistry source terms: surface growth and oxidation.

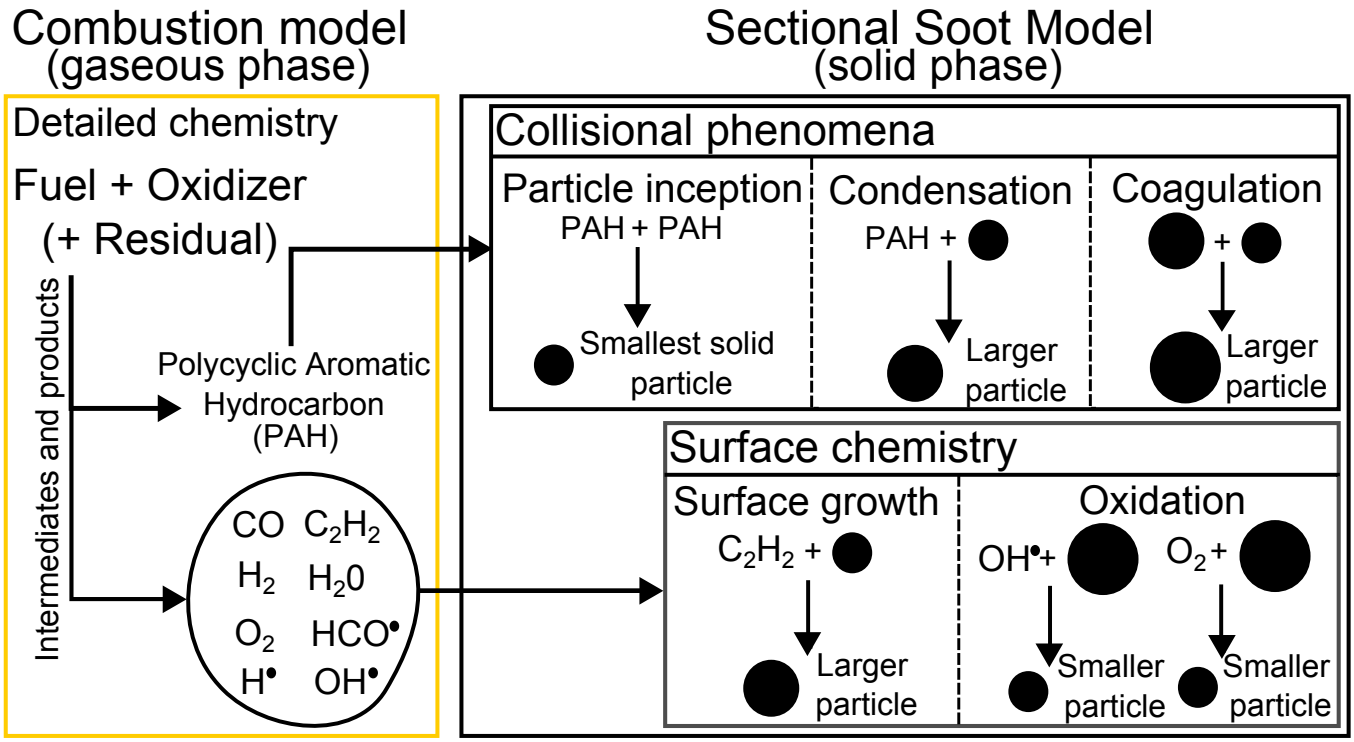

Figure 3.1: Illustration of the five phenomena representing soot formation and evolution with the involved gaseous species.

3.1.1 Volume discretization

In this model, a fixed interval of volume $[V_{MIN}; V_{MAX}]$ is divided into n_{sect} sections. The smallest volume of the considered particles is V_{MIN} and is equal to the carbon-equivalent volume of the number of carbon atoms of two soot precursors and two acetylene molecules. Carbon-equivalent volume for two atoms of carbon is given by:

$$V_{C_2} = \frac{2M_C}{\mathcal{N}_A \rho_{soot}} \tag{3.2}$$

where M_C is the molar mass of carbon, $\mathcal{N}_A$ the Avogadro number and ρ_{soot} the soot density which is assumed constant at a value of $1.86 \cdot 10^3$ kg.m^{-3} [55, 56].

Using pyrenyl ($C_{16}H_9$) as precursor as in [55, 56, 58, 78, 77], V_{MIN} becomes equal to $18V_{C_2}$ with a value of $3.857 \cdot 10^{-28}$ m^3 which is approximately the volume of a 0.9 nm diameter sphere. In the case of a complete solid-gas coupling between the soot model and a kinetic solver, all hydrogen atoms taken from the gas phase are then sent to H_2 to close the hydrogen balance since all volumes exchanged between phases are given with respect to the exchanged number of carbon atoms.

The largest modeled particles have a volume V_{MAX} corresponding to the volume of a $d_{MAX} = 10\,\mu$m diameter sphere. In Diesel engines, the particles produced are one or two orders of magnitude smaller than this value d_{MAX} in diameter [72, 129, 130, 131]. This V_{MAX} value ensures that carbon mass will not accumulate in the last section.

The first section represents soot particles of a constant volume range going from V_{MIN} to $V_{MIN} + V_{C_2}$. The following sections are defined to fill the represented volume interval with $n_{sect} - 1$ sections

with a geometrical progression:

$$V_{max,i} = (V_{MIN} + V_{C_2}) \left(\frac{V_{MAX}}{V_{MIN} + V_{C_2}} \right)^{(i-1)/(n_{sect}-1)} \quad \forall\, i \in [\![2; n_{sect}]\!] \tag{3.3}$$

3.1.2 Model variables

The source terms given by the soot model are written as volume fraction source terms. The i^{th} section soot particles volume normalized by the total volume of both gas and solid phase is the soot volume fraction Q_i. Assuming the volume of all soot particles is negligible with respect to the volume of the gas, Q_i can be deducted from $\widetilde{Y}_{soot,i}$:

$$Q_i = \frac{\overline{\rho}}{\rho_{soot}} \widetilde{Y}_{soot,i} \tag{3.4}$$

Accordingly, the soot mass fraction source term in Eq. (3.1) is given by:

$$\overline{\rho}\widetilde{\dot{\omega}}_{soot,i} = \rho_{soot}\dot{Q}_i = \rho_{soot}(\dot{Q}_{nucl,i} + \dot{Q}_{cond,i} + \dot{Q}_{sg,i} + \dot{Q}_{ox,i} + \dot{Q}_{coag,i}) \tag{3.5}$$

where $\dot{Q}_{nucl,i}$, $\dot{Q}_{cond,i}$, $\dot{Q}_{coag,i}$, $\dot{Q}_{sg,i}$ and $\dot{Q}_{ox,i}$ are respectively the volume fraction source terms of the i^{th} section due to nucleation, condensation, coagulation, surface growth and oxidation respectively.

The soot volume fraction density q_i is assumed to be constant in a given section i [55]:

$$q_i = \frac{Q_i}{V_{max,i} - V_{min,i}} \tag{3.6}$$

As soot density ρ_{soot} is assumed constant, the mass density is also constant in a section. The particle number density $n_i(v)$ is deduced from q_i:

$$n_i(v) = \frac{q_i}{v} \; \forall\, v \in [V_{min,i}; V_{max,i}] \tag{3.7}$$

Finally, the volume number of particles in section i, N_i, is:

$$N_i = \int_{V_{min,i}}^{V_{max,i}} n_i(v)dv = \frac{Q_i}{V_{max,i} - V_{min,i}} ln\left(\frac{V_{max,i}}{V_{min,i}}\right) \tag{3.8}$$

It has been shown by Netzell [55] that considering n_i or q_i constant in a section has a very low influence on the predicted SNDF. The knowledge of the number of particles in each section given by Eq. (3.8) allows to calculate the SNDF. Knowing $\tilde{Y}_{soot,i}$ for each section i then gives an instantaneous access to the SNDF or any soot variable distributions at each time step and every location as illustrated in Fig. 3.2.

3.1.3 Collisional source terms

Particle inception, condensation and coagulation are collisional phenomena. They are represented by the Smoluchowski equation [62]. In the continuous form, it reads:

$$\dot{F}_a(t) = \frac{1}{2}\int_0^a (\beta_{a-b,b} F_b(t) F_{a-b}(t))db - \int_0^\infty (\beta_{a,b} F_a(t) F_b(t))db \tag{3.9}$$

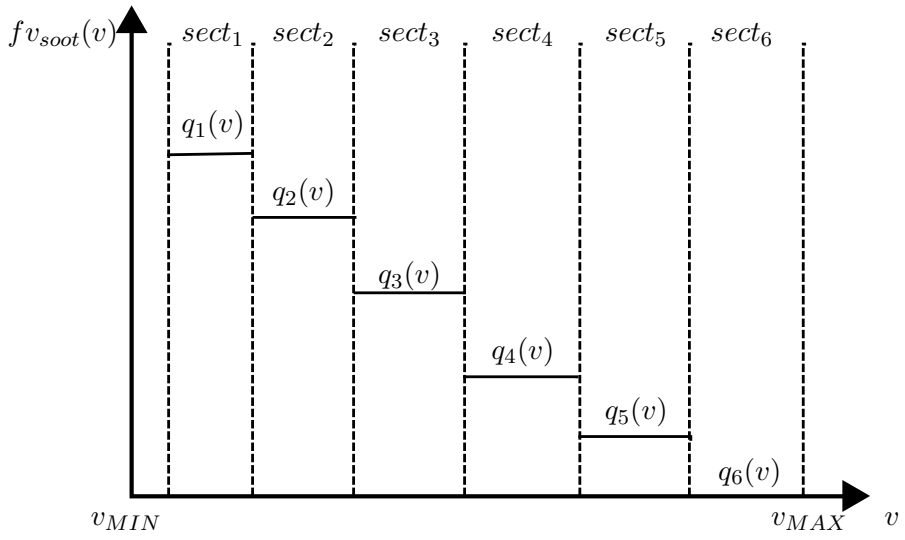

Figure 3.2: Exemple of soot volume fraction distribution in size reconstruction

where $F_x(t)$ is the number of particles of size x, $\dot{F}_x(t)$ its variation rate and $\beta_{x,y}$ the collision frequency between particles of size x and y.

The collision frequencies are obtained using the theory of aerosol science [64], applied to soot formation by Kazakov and Frenklach [65]. These frequencies are evaluated for three different regimes based on the value of the Knudsen number Kn defined as:

$$Kn(d) = \frac{\lambda_{gas}}{d} \tag{3.10}$$

where d is the particle diameter and λ_{gas} the gas mean free path, computed for the bath gas N_2.

3.1.3.a Inception and Condensation

Inception and condensation are the two phenomena related to precursors collisions. There can either be collisions between precursors to create the smallest considered soot particles (particle inception), or between precursors and soot particles to increase soot particles volume (condensation). The precursor species used in these phenomena is a virtual species called PAH (for Polycyclic Aromatic Hydrocarbons). PAH is the product of the pyrenyl radical polymerization by acetylene:

$$C_{16}H_9 + C_2H_2 \xrightarrow{k_{pol}} PAH + H_2 \tag{3.11}$$

where k_{pol} is the rate constant of reaction for this polymerization reaction.

The volume fraction reaction rate of PAH, r_{PAH}, reads:

$$r_{PAH} = \mathcal{N}_A k_{pol} [C_{16}H_9] [C_2H_2] V_{PAH} \tag{3.12}$$

where V_{PAH} is the volume of a precursor (18 carbon atoms).

Considering N_{PAH} the volume number of PAH particles, volume fraction variation rate of the smallest modeled soot $\dot{Q}_{Nucl}$ comes from the Smoluchowski equation (3.9) coupled with Eq. (3.6) and Eq. (3.7):

$$\dot{Q}_{Nucl} = 2V_{PAH}\beta^{fm}_{PAH,PAH}N^2_{PAH} \tag{3.13}$$

where $\beta^{fm}_{PAH,PAH}$ is the molecular collision frequency for two precursors.

It is then possible to express the global volume amount of precursors that collide with all soot particles per unit time $\dot{Q}^{PAH}_{Cond}$:

$$\dot{Q}^{PAH}_{Cond} = V_{PAH} N_{PAH} \sum_{i=1}^{i_{max}} \int_{V_{min,i}}^{V_{max,i}} \beta^{fm}_{PAH,i} n_i(v) dv \tag{3.14}$$

where $\beta^{fm}_{PAH,i}$ is the molecular collision frequency between precursors and soot particles of section i.

N_{PAH} is calculated using a steady state assumption between the formation of PAH through reaction (3.11) and its consumption by collision due to nucleation and condensation over all the sections [55]:

$$r_{PAH} = \underbrace{2 V_{PAH} \beta^{fm}_{PAH,PAH}}_{k_{Nucl}} N^2_{PAH} \quad + \quad \underbrace{\left(V_{PAH} \sum_{i=1}^{i_{max}} \int_{V_{min,i}}^{V_{max,i}} \beta^{fm}_{PAH,i} n_i(v) dv \right)}_{k_{Cond}} N_{PAH} \tag{3.15}$$

The positive roots of this polynomial equation are:

$$N_{PAH} \quad = \quad \frac{-k_{Cond} + \sqrt{k^2_{Cond} + 4 r_{PAH} k_{Nucl}}}{2 k_{Nucl}} \tag{3.16}$$

It is important to note that the inception reaction rate is directly read from Eq. (3.13) while for condensation, the volume fraction computed from Eq. (3.14) represents the global volume fraction transferred from gas phase to solid soot phase. This global volume fraction source term due to condensation has therefore to be distributed correctly towards different sections as explained below.

Condensation reaction rates

The total amount of condensed soot in section i, $\dot{Q}^{BD}_{Cond,i}$ (BD for *Before Distribution*), which has to be distributed into the SNDF reads:

$$\dot{Q}^{BD}_{Cond,i} = N_{PAH} \int_{V_{min,i}}^{V_{max,i}} \beta^{fm}_{PAH,i} \left(V_{PAH} + v \right) n_i(v) dv \tag{3.17}$$

It can be split in two terms. The first term is the flux $\dot{Q}^{out}_{Cond,i}$ of particles in section i that are collided by the precursors:

$$\dot{Q}^{out}_{Cond,i} = N_{PAH} \int_{V_{min,i}}^{V_{max,i}} \beta^{fm}_{PAH,i} n_i(v) v dv \tag{3.18}$$

The second term is the volume of soot precursors colliding with particles of a given section i per unit time $\dot{Q}^{PAH}_{Cond,i}$ obtained by:

$$\dot{Q}^{PAH}_{Cond,i} = V_{PAH} N_{PAH} \int_{V_{min,i}}^{V_{max,i}} \beta^{fm}_{PAH,i} n_i(v) dv \tag{3.19}$$

This term is used previously to evaluate N_{PAH}. In the previous versions of the model [55, 56, 57], $\dot{Q}^{PAH}_{Cond,i}$ (Eq. (3.19)) was directly attributed to section $i+1$ with a quantity of soot transferred between sections i and $i+1$ calculated to ensure mass and number conservation.

Finally, $\dot{Q}^{BD}_{Cond,i}$ is distributed in the sections intersecting with the interval $[V_{min,i}+V_{PAH}; V_{max,i}+V_{PAH}]$. Because the volume range represented by this interval is $V_{max,i}-V_{min,i}$, condensation only makes particles larger and because the sections volume range is growing geometrically, only two cases are possible:

- the volume interval is completely included in one section which will receive the complete condensation reaction rate from section i,
- the interval intersects two different sections which will receive a part of the condensation reaction rate from section i. In this case, section i can be one of those two sections.

Figure 3.3 illustrates these two steps to distribute the condensed mass of soot in the right sections of the distribution. At first, the global amount of condensed soot in section i, $\dot{Q}^{BD}_{Cond,i}$, is evaluated. Then it is distributed with respect to particles volumes towards one or two sections. As a consequence, the rate of volume fraction of soot received by a section j from the condensation over section i, $\dot{Q}^{i\to j}_{Cond}$, is the product of the volume fraction rate of soot distributed from section i, $\dot{Q}^{BD}_{Cond,i}$ (including both the soot received from the gaseous phase and the one taken from the section i), by a pre-tabulated matrix G_{cond} (defined in Section 3.1.3.c) representing the part of section i condensation received by section j:

$$\dot{Q}^{i\to j}_{Cond} = G_{cond}\,(i,j)\,\dot{Q}^{BD}_{Cond,i} \tag{3.20}$$

Finally, the condensation source term in section i is the sum of the volume fraction rates received from all sections, with the volume fraction rate taken from section i ($\dot{Q}^{out}_{Cond,i}$) being withdrawn:

$$\dot{Q}_{Cond,i} = -\dot{Q}^{out}_{Cond,i} + \sum_{j=1}^{n_{sect}} G_{cond}\,(j,i)\,\dot{Q}^{BD}_{Cond,j} \tag{3.21}$$

It is to be noticed that this method keeps the number of particles constant, as the condensation phenomenon should. Indeed, the added volume fraction of soot is consistent with the transfer of soot to the larger size of the distribution, thus conserving the number of particles computed with Eq. (3.7).

3.1.3.b Coagulation

Coagulation is the collision between particles leading to larger particles. It is modeled with the same two steps as condensation: first the global amount of volume fraction which coagulates is evaluated, secondly this amount is distributed towards other sections with a distribution matrix. In contrast with the condensation, it links any two sections i and j, sources of the colliding particles, with a third section k receiving the coagulated particles. Since the volume density of particle number is known for each section and that this value is used in the governing Eq. (3.9), coagulation is solved in volume density of particle number.

The first step to model coagulation consists in evaluating the number of particles of section i and j which collide. This comes directly from the Smoluchowski equation Eq. (3.9), which reads as follows:

$$\dot{N}^{out}_{ij} = \iint_{\Delta v_i \Delta v_j} \beta_{ij} n_i(v_i) n_j(v_j) dv_i dv_j \tag{3.22}$$

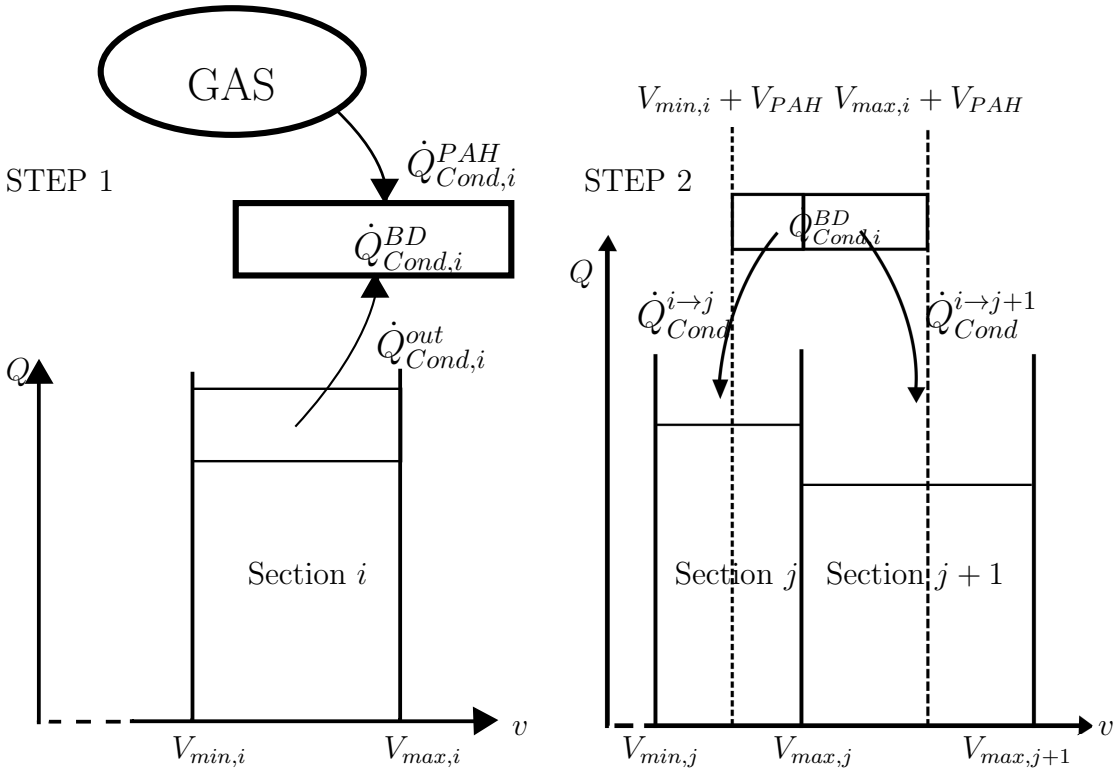

Figure 3.3: Illustration of condensation over section i. STEP 1: computation of $\dot{Q}^{BD}_{Cond,i}$, the sum of the condensed carbon from gaseous phase over section i and the volume fraction of section i colliding with precursors. STEP 2: distribution of $\dot{Q}^{BD}_{Cond,i}$ in other sections.

where $\dot{N}^{out}_{ij}$ is the volume number rate of collisions between particles of sections i and j, $\Delta v_i = v_{max,i} - v_{min,i}$ the volume range represented by section i, and β_{ij} the coefficient frequency defined by Kazakov *et al.* [65] and assumed constant for each pair of sections.

As for condensation, the second step in the coagulation modeling is to distribute the collided particles in the interval $[V_{min,i} + V_{min,j}; V_{max,i} + V_{max,j}]$. A 3-D pre-tabulated matrix $G_{coag}(i,j,k)$ links two sections i and j to a third section k receiving a part of their collided particles. More details on this matrix are given in Section 3.1.3.c.

Accordingly, the particle number rate received by a section k from sections i and j is the product of the volume density of collision between particles of sections i and j, $\dot{N}^{out}_{ij}$, by the matrix G_{coag}:

$$\dot{N}^{i,j\to k}_{Coag} = G_{coag}\,(i,j,k)\,\dot{N}^{out}_{ij} \tag{3.23}$$

As a consequence, the particle number rate in section i is equal to the particle rate received by section i from all smaller sections $\dot{N}^{j,k\to i}_{Coag}$ minus the rate of collision between particles of sections i and all other sections. Using Eq. (3.8), the coagulation source term of section i reads:

$$\dot{Q}_{Coag,i} = \left(\sum_{j,k}^{i} \dot{N}^{j,k\to i}_{Coag} - \sum_{j=1}^{n_{sect}} \dot{N}^{out}_{ij} \right) \frac{V_{max,i} - V_{min,i}}{ln\left(\frac{V_{max,i}}{V_{min,i}}\right)} \tag{3.24}$$

The previous version of the model [55, 56, 57] used a similar approach with a simpler distribution matrix G_{coag} only equal to 1 if the receipting section volume interval included the middle of $[V_{min,i} + V_{min,j}; V_{max,i} + V_{max,j}]$ and equal to 0 otherwise.

3.1.3.c Distribution tensors

Distribution matrix of condensation.

As it is explained in Section 3.1.3.a, the total source term due to condensation of section i, $\dot{Q}^{BD}_{Cond,i}$, is distributed into the different receiving sections through a distribution matrix of condensation. This matrix G_{cond} contains values resulting from Eq. (3.18) and Eq. (3.19) with a integration domain splits in order to keep only the part representing volumes included in the receiving section (here section j). It reads:

$$G_{cond}\left(i,j\right) = \begin{cases} 1 & \text{if} \begin{pmatrix} V_{min,i} + V_{PAH} \geq V_{min,j} \\ \text{and} \\ V_{max,i} + V_{PAH} \leq V_{max,j} \end{pmatrix} \\ 0 & \text{if} \begin{pmatrix} V_{min,i} + V_{PAH} \geq V_{max,j} \\ \text{or} \\ V_{max,i} + V_{PAH} \leq V_{min,j} \end{pmatrix} \\ \alpha & \text{if} \begin{pmatrix} V_{min,i} + V_{PAH} \leq V_{max,j} \\ \text{and} \\ V_{max,i} + V_{PAH} \geq V_{max,j} \end{pmatrix} \\ 1-\alpha & \text{if} \begin{pmatrix} V_{min,i} + V_{PAH} \leq V_{min,j} \\ \text{and} \\ V_{max,i} + V_{PAH} \geq V_{min,j} \end{pmatrix} \end{cases} \tag{3.25}$$

with:

$$\alpha = \frac{\displaystyle\int_{V_{min,i}}^{V_{max,j}-V_{PAH}} \beta^{fm}_{PAH,i}\left(v+V_{PAH}\right) n_i(v) dv}{\displaystyle\int_{V_{min,i}}^{V_{max,i}} \beta^{fm}_{PAH,i}\left(v+V_{PAH}\right) n_i(v) dv} \tag{3.26}$$

Assuming $\beta^{fm}_{PAH,i}$ constant for all volumes in section i leads to an expression of G_{cond} only depending on the volume discretization. This discretization being constant during a computation, G_{cond} can be pre-tabulated during the computation initialization, allowing the use of this more detailed distribution method with almost no supplementary computational cost.

Distribution tensor of coagulation.

Similarly to condensation, the total source term due to coagulation issued from two sections i and j is distributed into the potential receiving sections by a precalculated tensor. In the case of coagulation, one more variable is required compared to condensation. The composition of this tensor is based on some observations used to simplify its equations. As for condensation, assuming the collision frequency $\beta_{i,j}$ constant for all volumes in sections i and j respectively allows to simplify the expression of G_{coag} and makes it only dependent on volumes. The simplified expression of G_{coag} is directly given here for the sake of clarity.

The volume interval represented by each section grows with the number of the section. According to that, the interval $[V_{min,i}+V_{min,j}; V_{max,i}+V_{max,j}]$ cannot be larger than the volume range of two

consecutive sections equal or larger than both sections i and j. Thus, half of the volume range represented by this interval cannot be larger than the range of a section representing volume larger than the one of sections i and j. Then, considering l the section number of the section including the middle of the volume interval $[V_{min,i} + V_{min,j}; V_{max,i} + V_{max,j}]$, the particles coagulated from sections i and j belong to sections $l-1$, l and $l+1$. G_{coag} can be written as follows:

$$G_{coag}(i,j,k) = \begin{cases} 0 & \text{if } \begin{pmatrix} k \geq l+2 \\ \text{or} \\ k \leq l-2 \end{pmatrix} \\ \dfrac{\int_{V_{min,i}}^{MIN(V_{max,i};V_{max,k}-V_{min,j})} n_i(v) \left(\int_{V_{min,j}}^{V_{max,k}-v_i} n_j(v) dv_j \right) dv_i}{\iint_{\Delta_i \Delta_j} n_i(v) n_j(v) dv_i dv_j} & \text{if } (k = l-1) \\ \dfrac{\int_{\Delta_i} n_i(v) \left(\int_{MAX(V_{min,j};V_{min,k}-v_i)}^{MIN(V_{max,j};V_{max,k}-v_i)} n_j(v) dv_j \right) dv_i}{\iint_{\Delta_i \Delta_j} n_i(v) n_j(v) dv_i dv_j} & \text{if } (k = l) \\ \dfrac{\int_{MAX(V_{min,i};V_{min,k}-V_{max,i})}^{V_{max,i}} n_i(v) \left(\int_{V_{min,k}-v_i}^{V_{max,j}} n_j(v) dv_j \right) dv_i}{\iint_{\Delta_i \Delta_j} n_i(v) n_j(v) dv_i dv_j} & \text{if } (k = l+1) \end{cases} \tag{3.27}$$

3.1.4 Surface chemistry source terms

The HACA cycle (*Hydrogen Abstraction Carbon Addition*) developed by Frenklach [26] represents the growth and oxidation of PAH. In the present work, surface chemistry of soot is modeled using a variation of this cycle proposed by D'Anna and Kent [76]. This surface chemistry has been chosen since it has been designed for engine conditions and previously validated by Fraioli *et al.* [72]. The surface chemistry phenomena are described using eight gaseous species (H, H_2, OH, H_2O, C_2H_2, O_2, CO and HCO) in six reactions (given in table Tab.3.1) with the rate constants taken from [76]: where A_i represents stable aromatic soot particles of section i, R_i represents radical soot particles of section i, A_k^p represents stable aromatic soot particles product of a reaction that exchanges p carbon atoms with the gaseous phase, and k_n^i is the rate constant of n^{th} reaction on particles of section i.

3.1.4.a Reaction rates

To evaluate the oxidation and surface growth reaction rates given by the surface chemistry reactions, the total amount of particles in each section is first converted into a concentration ($[A_i] + [R_i]$) proportional to its surface S_i. This value can be obtained from:

$$[A_i] + [R_i] = \int_{v_{min,i}}^{v_{max,i}} \alpha_{\text{HACA}} \frac{\lambda_{soot}}{\mathcal{N}_A} S_i(v) n_i(v) dv \tag{3.28}$$

where λ_{soot} is the number of reactive sites per unit surface of soot and α_{HACA} is the proportion of these sites which are active.

$$
\begin{aligned}
\mathrm{A}_i &\overset{k_1^i}{\leftrightarrow} \mathrm{R}_i + \mathrm{H} \\
\mathrm{A}_i + \mathrm{H} &\overset{k_2^i}{\leftrightarrow} \mathrm{R}_i + \mathrm{H_2} \\
\mathrm{A}_i + \mathrm{OH} &\overset{k_3^i}{\leftrightarrow} \mathrm{R}_i + \mathrm{H_2O} \\
\mathrm{R}_i + \mathrm{C_2H_2} &\overset{k_4^i}{\longrightarrow} \mathrm{A}_k^2 + \mathrm{H} \\
\mathrm{A}_i + \mathrm{OH} &\overset{k_5^i}{\longrightarrow} \mathrm{A}_k^{-1} + \mathrm{HCO} \\
\mathrm{R}_i + \mathrm{O_2} &\overset{k_6^i}{\longrightarrow} \mathrm{A}_k^{-2} + 2\mathrm{CO}
\end{aligned}
$$

Table 3.1: Reactions governing the soot surface chemistry [76].

The value of α_{HACA} is often correlated to temperature [44, 132]. Because temperature dependent expressions of α_{HACA} are not completely validated today, we rather choose a constant value as done in [55, 56] for instance. We choose $\alpha_{\mathrm{HACA}} = 0.27$ which corresponds to the average value of the correlation given by Markatou *et al.* [132] for a temperature interval of 1250K to 3000K. Considering soot particles as spheres and considering that the smallest solid soot particle has only one reactive site ($\lambda_{soot} S_1 = 1$), as in [55, 56], the following relation appears:

$$\lambda_{soot} S_i = \lambda_{soot} S_1 \left(\frac{v_i}{V_{c_2}} \right)^{\frac{2}{3}} = \left(\frac{v_i}{V_{c_2}} \right)^{\frac{2}{3}} \tag{3.29}$$

The previous relation relies on the assumption of spherical particles, however a fractal dimension should be introduced to correct the amount of soot surface available for reaction as in Forrest and Witten [133]. The value and evolution depending on particle size, the fractal dimension of soot is still uncertain [129, 130, 134, 135]. In this paper, a variable fractal dimension depending on particle size has been chosen, as in [55], for all the Diesel surrogate calculations. For the calculations presented here, $\theta = 2.0$ for all particles with a diameter smaller than a given threshold and $\theta = 2.25$ for all particles with a diameter larger than a second threshold and the fractal dimension evolves linearly in between. These thresholds are adapted depending on the fuel used in the simulation, since the growth of soot particles can be based on absorption of different sizes carbon species (PAH or acetylene) depending on the burned fuel. Using Eq. (3.29) and the fractal dimension, the total soot concentration becomes:

$$[\mathrm{A}_i] + [\mathrm{R}_i] = \int_{V_{min,i}}^{V_{max,i}} \alpha_{\mathrm{HACA}} \frac{n_i(v)}{\mathcal{N}_A} \left(\frac{v}{V_{c_2}} \right)^{\frac{\theta}{3}} dv \tag{3.30}$$

As in [55, 56], a steady state assumption on active radical sites allows to write $[\mathrm{R}_i]$ as a function of $[\mathrm{A}_i]$:

$$[\mathrm{R}_i] = \frac{k_{1,i,f} + k_{2,i,f}\,[\mathrm{H}] + k_{3,i,f}\,[\mathrm{OH}]}{k_{1,i,b}\,[\mathrm{H}] + k_{2,i,b}\,[\mathrm{H_2}] + k_{3,i,b}\,[\mathrm{H_2O}] + k_{4,i}\,[\mathrm{C_2H_2}] + k_{6,i}\,[\mathrm{O_2}]}\,[\mathrm{A}_i] \tag{3.31}$$

The volume fraction reaction rates for surface growth ($\dot{Q}^{gas}_{SG,i}$) and oxidation ($\dot{Q}^{gas}_{Ox,i}$) in section i are evaluated as in [55, 56]. These reaction rates represent the mass exchange between the gaseous

phase and the solid phase. They read:

$$\dot{Q}^{gas}_{SG,i} = \mathcal{N}_A K_{SG,i} V_{C_2} \tag{3.32}$$

$$\dot{Q}^{gas}_{Ox,i} = \mathcal{N}_A K_{Ox,i} V_{C_2} \tag{3.33}$$

where $K_{SG,i} = k_{4,i}\left[C_2H_2\right]\left[R_i\right]$ and $K_{Ox,i} = k_{6,i}\left[O_2\right]\left[R_i\right] + k_{5,i}\left[OH\right]\left[A_i\right]/2$.

These reaction rates respectively represent global surface growth and oxidation over all sections and as for condensation and coagulation, they have to be distributed over the SNDF to complete the modeling of the phenomena. In the previous versions of the model [55, 56, 57], $\dot{Q}^{gas}_{SG,i}$ and $\dot{Q}^{gas}_{Ox,i}$ were directly attributed to section $i+1$ and $i-1$ respectively with a quantity of soot transferred between sections i and $i+1$ or $i-1$ calculated to ensure mass and number conservations.

3.1.4.b Surface growth

Surface growth is the carbon addition to soot particles from the gaseous phase. Its volume fraction reaction rate is associated to a reference volume V_{C_2} to be consistent with the number of carbons added by acetylene, which is the adsorbed species in the HACA mechanism. This phenomenon implies only consecutive sections since it leads to a size variation of V_{C_2} which is the volume range of the smallest section. Thus, the volume fraction rate of soot particles in section i which are growing enough to switch to section $i+1$, $\dot{Q}^{out}_{SG,i}$, needs to be modeled:

$$\dot{Q}^{out}_{SG,i} = \mathcal{N}_A K_{SG,i} \int_{V_{max,i}-V_{C_2}}^{V_{max,i}} (v + V_{C_2}) \frac{1}{v} \left(\frac{v}{V_{c_2}}\right)^{\frac{\theta}{3}} dv \tag{3.34}$$

In Eq. (3.34), the volume is $(v + V_{C_2})$ since the concerned particle has already received the volume fraction from the gaseous phase and $(1/v)\left(\frac{v}{V_{c_2}}\right)^{\frac{\theta}{3}}$ represents the available reaction surface variation depending on the volume. The integration over the considered volumes in Eq. 3.34 can be pre-tabulated as the ones for condensation, coagulation and the similar expression given next for oxidation.

Finally, the surface growth source terms applied to each section write:

$$\dot{Q}_{SG,1} = -\dot{Q}^{out}_{SG,1} + \dot{Q}^{gas}_{SG,1} \tag{3.35}$$

$$\dot{Q}_{SG,i} = \dot{Q}^{out}_{SG,i-1} - \dot{Q}^{out}_{SG,i} + \dot{Q}^{gas}_{SG,i} \qquad \forall i \in [\![2; n_{sect}-1]\!] \tag{3.36}$$

$$\dot{Q}_{SG,n_{sect}} = \dot{Q}^{out}_{SG,n_{sect}-1} + \dot{Q}^{gas}_{SG,n_{sect}} \tag{3.37}$$

3.1.4.c Oxidation

The oxidation of soot particles is also part of the surface kinetic scheme where reactions with dioxygen and hydroxyl take carbon from soot particles. Its modeling is similar to surface growth, except that the concerned particle size is reduced by the associated volume V_{C_2}. The volume fraction rate of soot transferred from section i to section $i-1$ reads:

$$\dot{Q^{out}_{Ox,i}} = \mathcal{N}_A K_{Ox,i} \int_{V_{min,i}}^{V_{min,i}+V_{C_2}} (v - V_{C_2}) \frac{1}{v} \left(\frac{v}{V_{c_2}}\right)^{\frac{\theta}{3}} dv \tag{3.38}$$

As for surface growth, the oxidation source terms applied to each section write:

$$\dot{Q}_{Ox,1} = \dot{Q}^{out}_{Ox,2} - \dot{Q}^{gas}_{Ox,1} \tag{3.39}$$

$$\dot{Q}_{Ox,i} = \dot{Q}^{out}_{Ox,i+1} - \dot{Q}^{out}_{Ox,i} - \dot{Q}^{gas}_{Ox,i} \qquad \forall i \in [\![2; n_{sect} - 1]\!] \tag{3.40}$$

$$\dot{Q}_{Ox,n_{sect}} = -\dot{Q}^{out}_{Ox,n_{sect}} - \dot{Q}^{gas}_{Ox,n_{sect}} \tag{3.41}$$

3.2 Homogeneous reactor and premixed flames validations

In order to validate the proposed changes to the sectional soot model, the current version of the model has been compared to the reference version proposed by Vervisch-Kljakic [57]. These comparisons are done on a homogeneous variable volume reactor and 1-D premixed flames. The reactor allows to ensure the mass balance is closed during the interactions between the gaseous phase and the solid soot phase. The flames are computed to verify the ability of the new model to predict SNDF in these academical cases as the reference model. In order to ensure a comparison of the two modeling approaches, these simulations have been ran using the HACA-RC cycle version used by Vervisch-Kljakic [57].

3.2.1 Homogeneous reactor

This section presents the results obtained from the simulation of a homogeneous variable volume reactor of n-heptane / air mixture at an equivalence ratio of $\Phi = 2,5025$. This simulation has been run using the CLOE (*CLosed hOmogeneous rEactor*) code from the IFP-Kinetics package [136] which includes the reference soot module and the proposed one.

The kinetic scheme proposed by Blanquart *et al.* [50] of 148 species and 928 reactions is used to model the n-heptane combustion kinetic. The reactor volume law is a reciprocating motion law defined by the engine-like conditions. The reactor initial conditions and the geometric parameters defining the volume law are given in Table 3.2 with P_0 and T_0 the initial pressure and temperature, RPM the rotating speed, V_{TDC} the volume at the Top Dead Center (TDC) and τ the compression ratio. The computation is done using 30 soot sections.

P_0 $[MPa]$	T_0 $[K]$	RPM	V_{TDC} $[cm^{-3}]$	τ
$0,1$	600	1640	$3,026.10^{-5}$	$17,8$

Table 3.2: Variable volume homogeneous reactor conditions.

Some modifications to the reference model, such as the addition of the exchanged hydrogen to H_2, are made in order to ensure mass conservation. Comparisons between the current version of the model and the reference one have been done on the previously introduced homogeneous closed reactor to illustrate the progress in mass conservation. Atoms balance are done to evaluate the mass changes due to hydrogen or carbon loss. Even if the species interacting with the soot phase include oxygen atoms, oxygen is not absorbed by soot in any of the HACA-RC cycle reaction. Thus, only hydrogen and carbon mass have to be checked. These results are presented in the following.

3.2.1.a Carbon atoms balance

To verify if the amount of soot predicted by the model is coherent with the gas phase composition, carbon mass exchanges between the gaseous and solid phases have to be checked. The gas phase to soot coupling being only partial in the reference model, it has been completed in the proposed version. Figure 3.4 shows the ability of the proposed version of the model to reproduce the reference soot volume fraction in variable volume homogeneous reactor and underlines the difference in the amount of gaseous carbon consumed between the two versions. In this soot model, the expression used to describe soot particle number and soot volume fraction are written considering that soot particles are composed of carbon. Thus, the soot volume fraction is a direct indicator of the amount of carbon contained in the solid phase as illustrated in Fig. 3.4 with the opposite evolutions predicted by the proposed model of soot volume fraction and gaseous carbon mass (normalized by the initial amount of gaseous carbon).

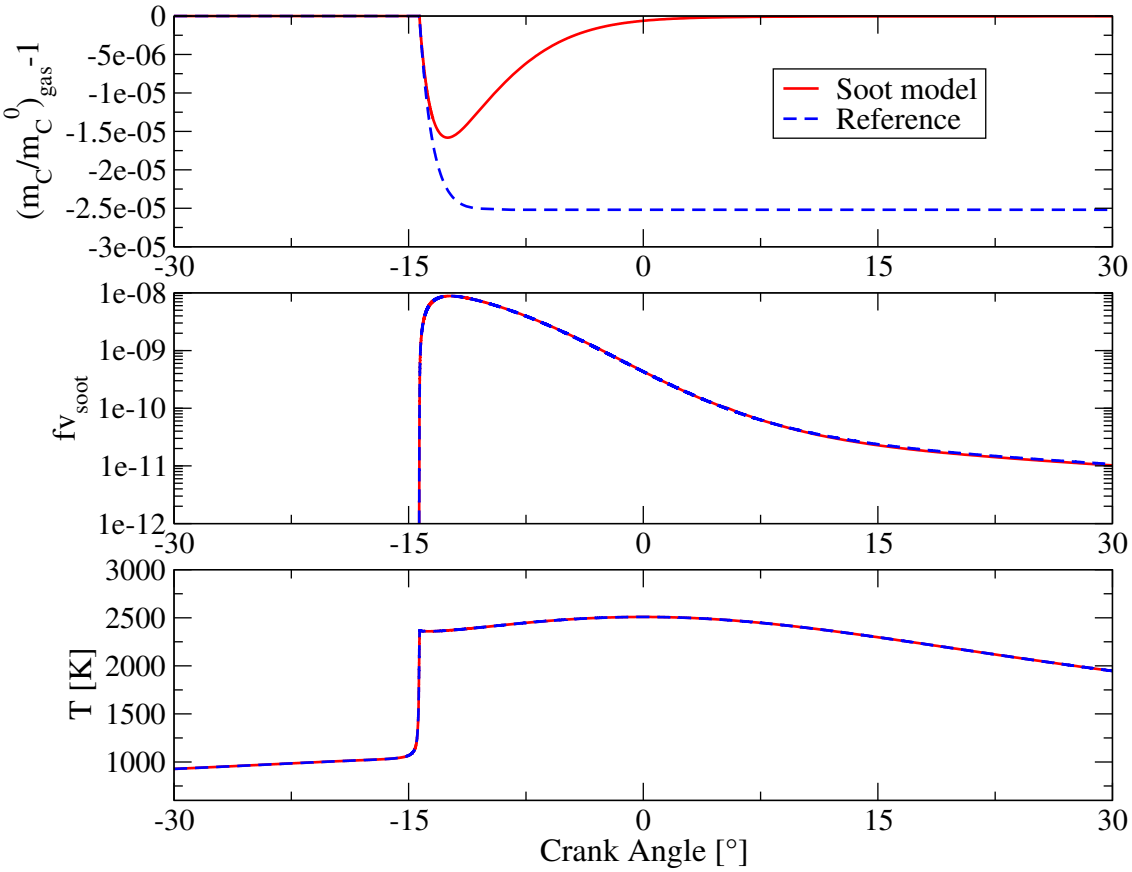

Figure 3.4: Comparisons between the current version of the model and the reference one for the number of carbon atoms missing in the gaseous phase normalized by the initial number of gaseous carbon atoms (top), the sot volume fraction (middle) and the temperature (bottom).

The ability of both versions of the model to predict a coherent evolution of soot is also illustated in Fig. 3.4. The soot volume fraction increases strongly during the ignition at -15 CAD before an oxidation to its final value. The peak value and the final value of soot volume fraction are similar for both versions of the model. This stresses the fact that only the soot size distribution is

modified. The absorption of carbon, and thus the evolution of the soot volume fraction (SVF), is only indirectly modified by the different available surface due to different distribution in size.

A more detailed analysis of the carbon loss is given with Fig. 3.5. The difference between the solid carbon mass in the soot model and the carbon mass lost by the gaseous phase is plotted along with the SVF as indicator of the evolution of the solid phase depending on crank angle. The balance between the gaseous and solid phase carbon of the proposed model is illustrated by the negligible loss of carbon mass, more than three orders of magnitude smaller than the involved carbon mass shown on Fig. 3.4. This loss cannot be null in this case because the gaseous and solid solver are separated which will lead to a numerical error due the distinct resolutions of the two systems. Using only one solver could prevent these errors in this specific case but this is not possible by the code used for 3-D RANS simulation. Thus, the presented results are the ones obtained with two solvers to validate an approach similar to the one used in 3-D RANS simulation.

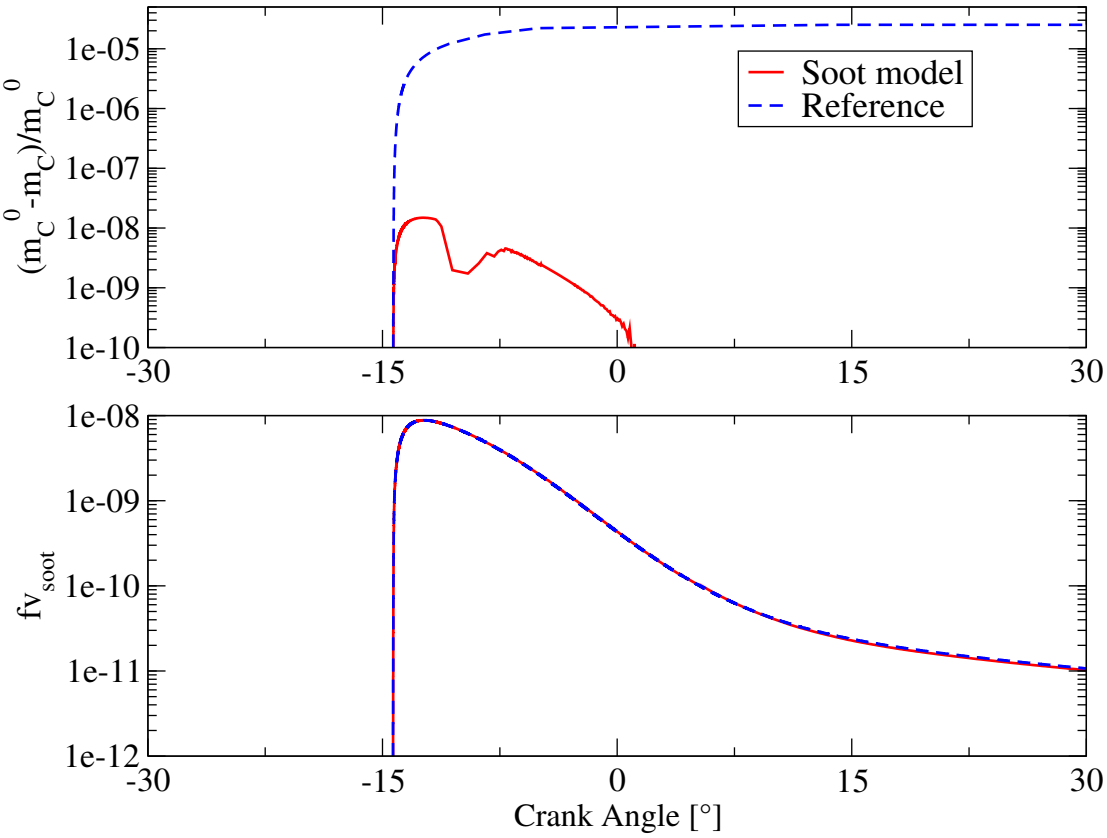

Figure 3.5: Carbon mass lost by the total system normalized by the initial mass of carbon (top) and soot volume fraction (bottom) as a function of crank angle.

3.2.1.b Hydrogen atoms balance

Hydrogen mass balance validation has also been done on the same homogeneous reactor case. The results are given in Fig. 3.6 with the hydrogen mass lost by the gaseous phase normalized by the initial hydrogen mass and the SVF as indicator of the evolution of solid phase depending on crank angle.

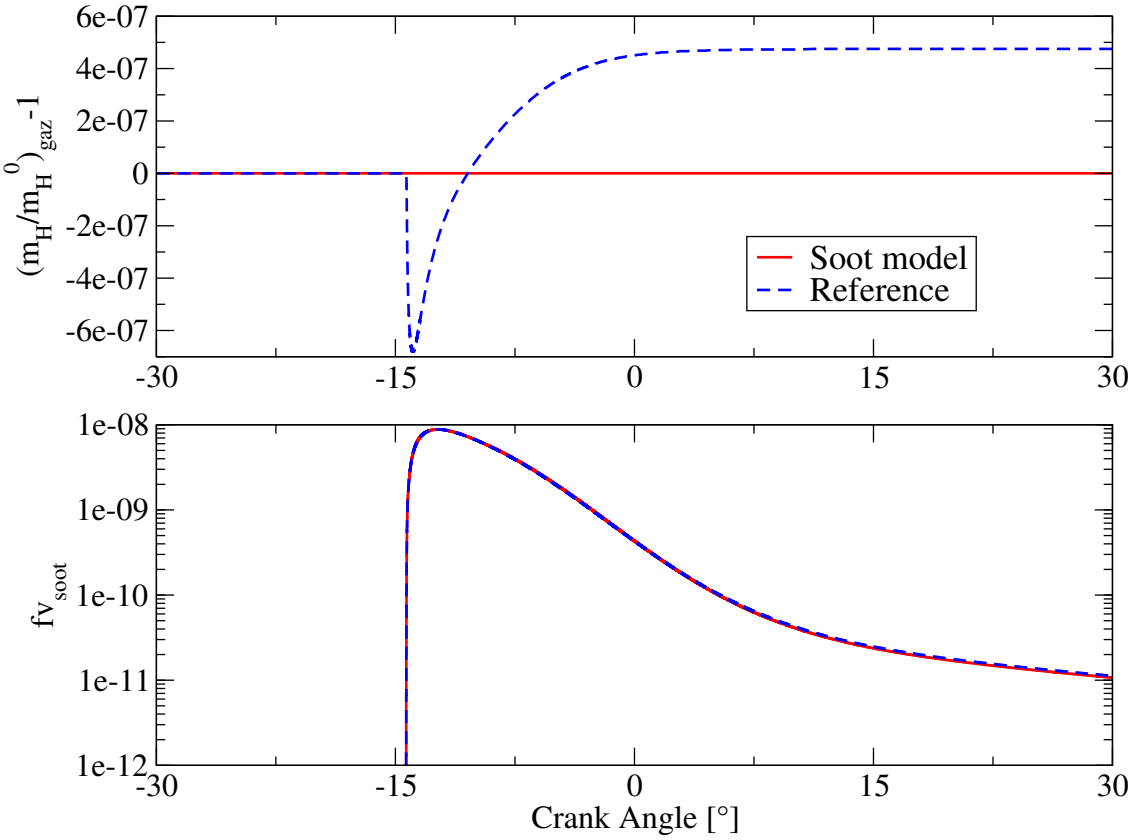

Figure 3.6: Hydrogen mass lost by the gaseous phase (top) and soot volume fraction (bottom) as a function of crank angle.

Since the soot particles are considered as composed only of carbon, the gaseous hydrogen mass should be constant in time during this simulation. This behavior is reproduced by the proposed model. The variation of the gaseous hydrogen mass predicted by the reference model illustrates the fact that soot is composed of hydrogen, as represented by the reactions modeling the formation of precursor and the soot surface chemistry. This hydrogen is neglected in the evaluation of soot volume and mass by both the reference and the proposed model. Considering this hydrogen could lead to a different behavior of soot surface chemistry depending on the availability of hydrogen at soot surface. It is to be noticed that the proposed solution is only a first step allowing mass conservative simulations while the problem of soot surface chemistry is not solved.

3.2.2 Laminar premixed flames

The laminar premixed flames measured by Zhao *et al.* [137] have been chosen to compare the proposed model to the reference one [57]. These are laminar premixed flames of ethylene at an equivalence ratio of 1.92. The fresh gases are diluted by nitrogen or argon. The molar composition are given in Tab. 3.3. Different dilutants were used in order to reach different maximum temperatures for a similar equivalence ratio and fresh gases velocity. The fresh gases velocity was also used as a factor to control the maximum temperature. The conditions of the four flames simulated are given in Tab. 3.4. These various flame temperatures lead to different SNDF by changing the dominance of collisional or chemical phenomena.

C_2H_4 (% mol.)	O_2 (% mol.)	Dilutant (% mol.)
24.2	37.9	37.9

Table 3.3: Fresh gases composition of Zhao *et al.* [137] experiments.

Flamme	Dilutant	Fresh gases velocity $[cm/s]$	T_{max} $[K]$
A1	Ar	7.0	1790
A3	Ar	10.0	1920
B1	N_2	8.0	1790
B3	Ar	8.0	1840

Table 3.4: Dilutant species, fresh gases velocities and maximum temperature of Zhao *et al.* [137] experiments flames.

These flames have been chosen because they were previously studied with the reference model. The simulations were run with the 1-D laminar flame code STELLA from IFP-KINETICS library [136], using the temperature profile, fresh gases composition and velocity as input parameters. The kinetic scheme used to model ethylene combustion chemistry is the one proposed by Mauss [128] including 82 species and 457 reactions, also used in the study with the reference model. The simulations ran with the proposed model used the same set of modeling parameters as the ones ran with the reference model to ensure that the differences were only due to the new modeling.

3.2.2.a Predicted SNDF

Figures 3.7 and 3.8 show the SNDF predicted by both models and compare them to the experimental measurements for the two lower temperature flames A1 and B1. The difference between the two versions can be seen with large soot predicted closer to the burner by the reference model for flame A1 with SNDF 5 mm and 7 mm above the burner in Fig. 3.7. It illustrates the difference of distribution of surface growth and condensation for similar gaseous phase conditions. The predictions from the proposed model are better at 5 mm and 7 mm above the burner for flame B1 as shown in Fig. 3.8 and also at 5 mm above the burner for flame A1 as shown in Fig. 3.7.

However, the predicted SNDF by both models at 10 mm and 12 mm above the burner for flames A1 and B1 are very similar in these cases while the way the SNDF is formed closer to the burner is different. As illustrated in Fig. 3.7 and Fig. 3.8, these predicted SNDF are also very different from the measured ones at 10 mm and 12 mm above the burner. The modeling errors are assumed to

be due to the representation of chemistry in these cases [57] and also to the fact that the collisional particle inception mechanism is not dominant in these low temperature flames [137]. These aspects impact as well the reference model and the proposed one abilities to predict SNDF for flames A1 and B1 since the difference between these models only lies on the way the particles are distributed towards the sections.

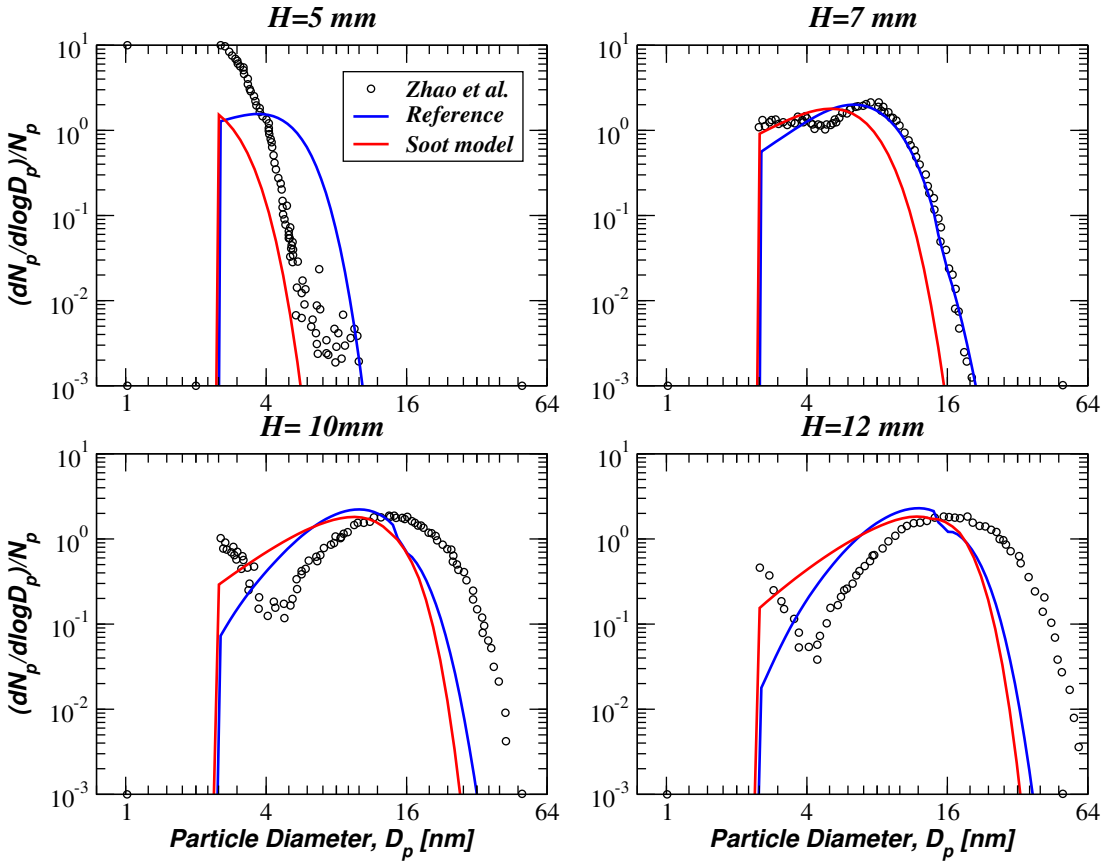

Figure 3.7: Comparison between experimental measurements of Zhao *et al.* [137], reference model predictions and current model predictions for flame A1; SNDF at four different heights above the burner.

The SNDF predicted by the two models for the flame A3 are compared to those measured by Zhao *et al.* [137] in Fig. 3.9. The final SNDF, at 12 mm above the burner, was reproduced well by both the reference model and the proposed model. Even if there are slight differences between the predicted SNDF at 5 mm, 7 mm and 10 mm above the burner by the two models, they all reproduce well the measured SNDF as shown in Fig. 3.9.

Finally, comparisons between the SNDF predicted by the two models and the experimental measurements for the flame B3 are presented in Fig. 3.10. Even if the presence of too large particles is predicted by the current model at 7 mm after the burner, the global behavior of the SNDF with respect to the height above the burner is well reproduced by the proposed model. The predicted size of the larger particles at 5 mm and 12 mm above the burner are similar to the measured ones. A clear progress also appears for the description of small particles at 10 mm and 12 mm above the burner compared to the reference model. This case illustrates the benefit of using a more accurate

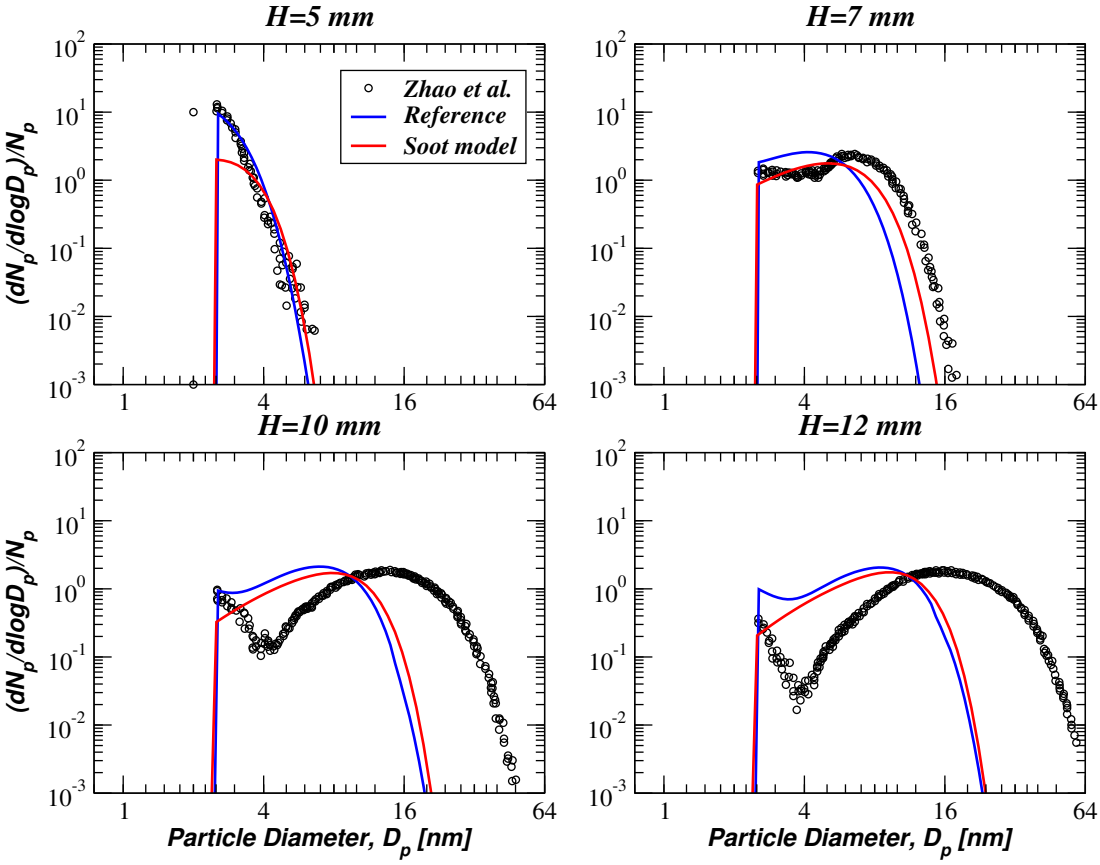

Figure 3.8: Comparison between experimental measurements of Zhao *et al.* [137], reference model predictions and current model predictions for flame B1; SNDF at four different heights above the burner.

distribution of soot source terms towards the sections.

Globally, the proposed model results are at least equivalent to the reference ones on those flames. Progresses are made in some specific cases but the flames A1 and B1 are still not well reproduced by the sectional soot model. This emphasizes the role of the gaseous phase chemistry and the choice of the soot surface chemistry. It illustrates the fact that gas phase modeling is crucial for soot modeling.

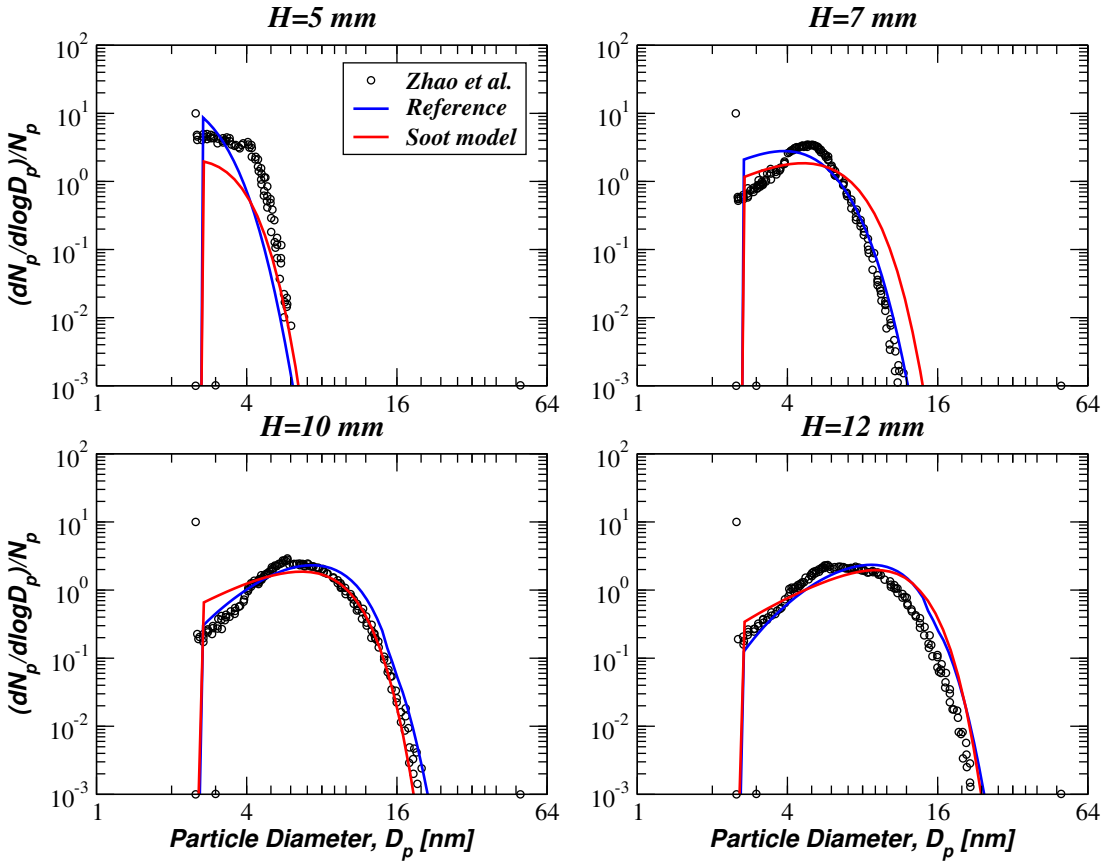

Figure 3.9: Comparison between experimental measurements of Zhao *et al.* [137], reference model predictions and current model predictions for flame A3; SNDF at four different heights above the burner.

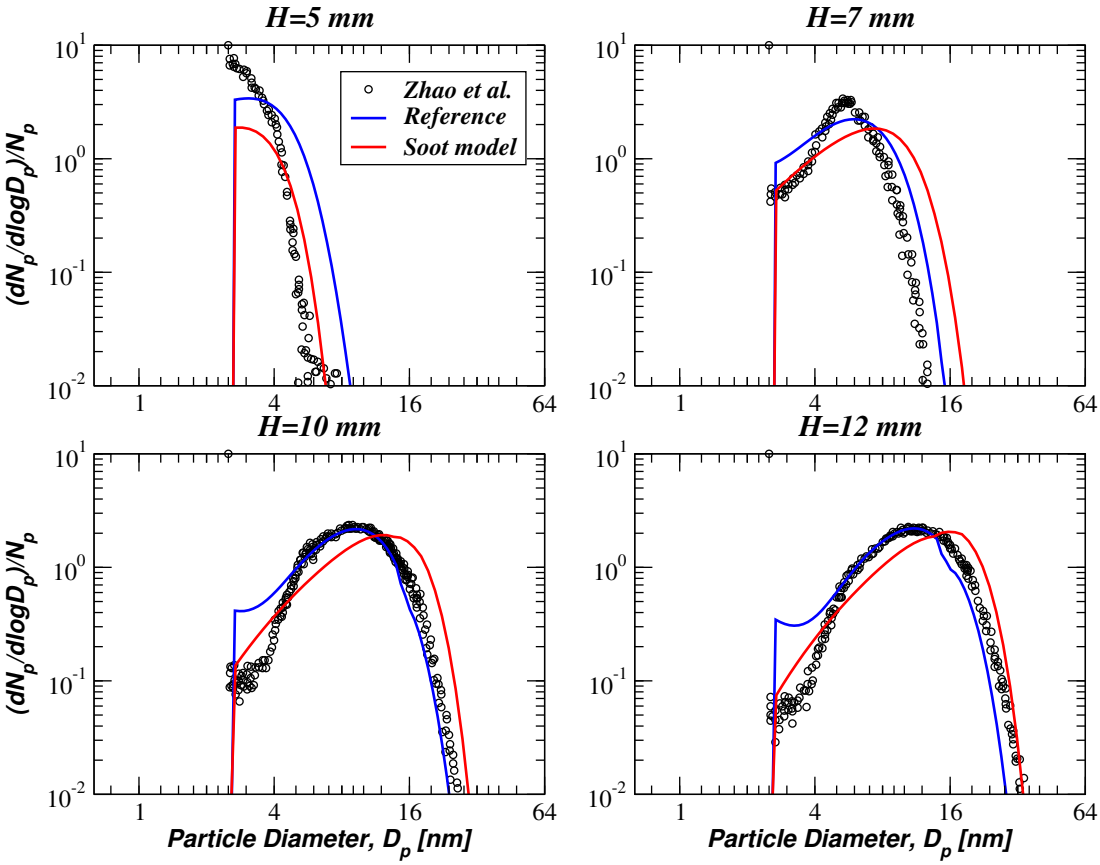

Figure 3.10: Comparison between experimental measurements of Zhao *et al.* [137], reference model predictions and current model predictions for flame B3; SNDF at four different heights above the burner.

Chapter 4

Diesel RANS simulations

This chapter is composed of the article "Sectional soot model coupled to tabulated chemistry for Diesel RANS simulations" submitted to *Combustion and Flames* the 30^{th} of July 2014. It includes a description of the sectional soot model, followed by a description of the combustion model used to represent the gaseous phase in 3D RANS simulation of Diesel engines. Section 4.3 was kept in the article in order to save the article structure but it only contains a description of the sectional soot model previously introduced in Chapter 3. The combustion model introduced in Section 4.4 is the reference combustion model of this thesis. It is only replaced by a more advanced combustion model in Chapter 5 in order to obtain a better prediction of lift-off in Diesel sprays simulations. This reference model coupling with the proposed soot model is then validated on various cases. First, the prediction of this combustion model is validated against a kinetic solver reference in Section 4.5. In order to realize these comparisons in relevant conditions, specifically designed homogeneous reactors have been proposed. These reactors, called ECFM3Z-0D reactors, reproduce conditions similar to Diesel engines ones while being simple enough to be simulated with a detailed kinetic solver, allowing the comparison between the reference combustion model and the kinetic solver. Finally, the model is validated against experimental measurements in Section 4.7. For this purpose, a database of Diesel operating conditions is described. Then, the comparisons between experimental measurements and simulations are shown and analyzed.

However, this chapter contains a modified version of the article. In fact, more details are given about the mass and enthalpy closure used in the tabulated approach in Section 4.4.2.c. Section 4.7.2.c is also improved with in-cylinder iso-surfaces of different gaseous species, soot source terms and soot section mass fractions used to illustrate the ability of the model to reproduce realistic evolutions of the solid phase. The model validations against experiments in Section 4.7.2.d are completed by time-evolutions of the mean soot mass fraction. Finally, supplementary results concerning the possibility to include a pre-tabulated feedback from soot to the gaseous phase composition are also given in Section 4.6.

4.1 Abstract

In future Euro norms, the soot volume fraction and the soot number density will be regulated. Car manufacturers need therefore accurate soot models for piston engine emissions prediction in order to develop future engine concepts. This paper addresses this question by coupling a sectional soot model with a tabulated combustion model for RANS simulations of Diesel engines. The sectional soot model, based on the work of Netzell *et al.* [K. Netzell, H. Lehtiniemi, F. Mauss, P. Combust.

Inst. 31 (2007), 1143-1155], is implemented in the IFP-C3D RANS CFD code. At each time and location, transport equations are solved for several soot sections, including source terms for collisional and chemical processes. The soot model is coupled to a tabulated combustion model derived from the Engine Approximated Diffusion Flame one (EADF) [J-B. Michel, O. Colin, Int. J. Engine Res. 15 (2013), 346-369]. It allows to represent the minor species required by the soot model with a much lower computational cost than a kinetic solver. In order to evaluate the soot model coupled to the resulting combustion model called Variable Pressure Homogeneous Tabulated Chemistry (VPTHC), it is compared to the same soot model directly coupled to a complex chemistry solver. As this comparison can hardly be performed on a real Diesel engine case due to the very high CPU time involved by the chemical solver, it is performed on a variable volume and fuel/air ratio case which retains the essential features of a Diesel engine. Results show that the proposed coupling recovers with reasonable accuracy the evolution of the soot volume fraction and distribution. Finally, an experimental database of Diesel operating points is simulated. The database includes points with a commercial Diesel fuel and the computed surrogate (30% 1-Methylnaphthalene and 70% Decane in liquid volume) to validate the models against the experiments. Soot yields predictions from the model show an improvement against the current standards and reach industrial target of accuracy for most of the database while the model also provides a good estimation of the soot particles distributions in size.

4.2 Introduction

Soot particles are formed during the combustion of hydrocarbon/air mixtures in most combustion devices related to transportation. They are regulated for Diesel engines since 1993 in Europe, and will soon be for spark-ignition engines (SIE). Today, these regulations concern not only the soot mass emission, but also the number of particles and finally the number of the smallest ones, which have been identified as the most harmful [11]. Diesel engines are today equipped with particle filters. However, even with such devices, there is still a strong interest in reducing soot emission at the source for Diesel and SI engines in order to limit the emission of particles small enough to get through particle filters.

In this context, engine manufacturers need experimental and numerical tools to evaluate the raw engine-out Soot Volume Fraction (SVF) and Soot Number Density Function (SNDF). Besides, due to the scarcity of fossil fuels, the contribution of bio-sourced fuels will increase in the future. A key issue is then to be able to evaluate the impact of fuel composition on soot emissions. Several models can be used to get soot emissions in Diesel engines in Reynolds Averaged Navier Stokes (RANS) calculations [138], which are the most used 3-D simulations for combustion chamber designers. Among them, the semi-empirical models [80, 139] are the most popular ones. This type of model is also used for soot-turbulence interactions as in Bolla *et al.* [91]. It is usually based on two equations giving access to a limited number of informations (total mass, mean diameter ...) whereas most advanced models based on sectional [78, 61] or moment [108, 109, 97] methods are able to describe the SNDF. However, only a few comparisons against experiments have been performed in 3-D cases with either the sectional or the moment methods. Using the method of moments, 3-D RANS Diesel sprays simulations have been presented by Karlsson *et al.* [113] and full engine simulations by Priesching *et al.* [114] but without quantitative comparisons against the experimental measurements. Marchal *et al.* [125] presented a single Diesel engine case simulation including a decent prediction of the exhaust soot yield with respect to the experimental measurement using a sectional soot model.

Fraioli *et al.* [72] simulated four Diesel cases with a sectional soot model coupled to a detailed kinetic scheme. In this work, the sectional version [78, 124, 77] of models developed by Mauss and co-workers [113, 112, 114] in previous studies is retained. This model accounts for inception, condensation, surface growth, coagulation and oxidation processes and directly predicts the SNDF at each time and location, in contrast to moment methods for which a post-processing is necessary.

The soot model requires the knowledge of local and instantaneous concentrations of the soot precursor and the chemical species involved in the oxidation and surface growth processes. Kinetic schemes able to correctly predict these concentrations under the whole range of thermodynamic and chemical conditions encountered in Diesel engines are detailed chemical schemes including hundreds of species and thousands of reactions [140, 141, 142, 143, 144]. As a consequence, transporting all the species and solving the complete chemistry totally coupled with turbulent reactive flow balance equations is very costly. It has been shown by Fraioli *et al.* [72] that a 3D RANS Diesel calculation including a full kinetic scheme and soot sections (132 species and 2206 reactions) can take more than a month which is simply unrealistic for industrial use. To overcome these difficulties we propose in the present work a soot modeling strategy split into two parts as illustrated in Fig. 4.1:

- First, a tabulated combustion model is developed to compute the gaseous phase composition, including the concentrations of soot precursor and of all other species involved in the soot formation process.

- Then, the sectional soot model uses these data to estimate the different source terms related to soot formation and destruction to determine the soot mass and SNDF.

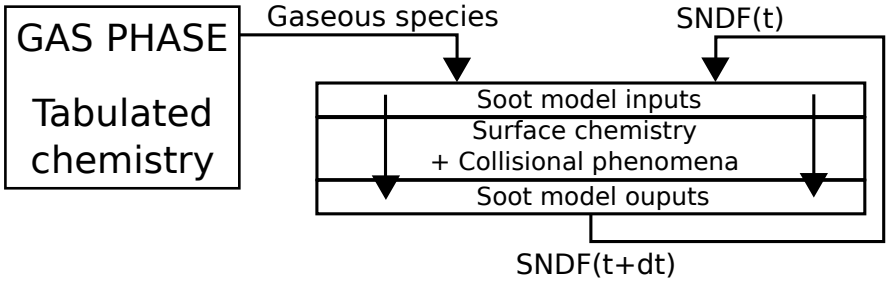

Figure 4.1: Illustration of interactions between a combustion model with detailed chemistry and the soot model.

The advantage of this tabulated strategy is clearly its very reduced CPU time compared to direct chemistry resolution. On the other hand, its major limitation is that the exchange of mass between solid and gaseous phases cannot be accounted for, which is equivalent to say that the impact of the solid phase chemistry on the gaseous composition is negligible. Although this hypothesis is strong, it cannot be avoided in a simple manner as soon as a tabulated approach is considered. The results presented on an academic case and a Diesel engine in this paper show a posteriori that this hypothesis seems acceptable for the practical cases of application targeted here.

In order to study the impact of fuel composition and chemical structure on the soot emissions, one should introduce a complex chemistry mechanism in the turbulent combustion model used for the gaseous phase. In this study, a simplification of the Engine Approximated Diffusion Flame (EADF) combustion model [145] is proposed. Indeed, in EADF, homogeneous variable pressure

trajectories are first tabulated using complex chemistry. Then these trajectories are used in approximate diffusion flame calculations at variable pressure to generate the final EADF table. This way, EADF is able to account for both variable pressure and strain rate effects. For soot description, additional minor species need to be added to the table, which would lead to a very large table which is difficult to handle. Besides the EADF table generation itself requires a large CPU time. For this reason, only the first homogeneous variable pressure table generated by EADF is retained here. The simplified model using this table is called Variable Pressure Tabulated Homogeneous Chemistry (VPTHC). In order to account for the local heterogeneity of mixture fraction, this homogeneous table is inserted in the three Dirac mixture fraction description of the 3-Zones Extended Coherent Flame Model (ECFM3Z) [146]. As this approach cannot account for the effect of strain on chemistry, it must be considered as a first step towards a future coupling between EADF and the soot model.

The aim of this work is to present the complete modeling approach including the tabulated chemistry model and the sectional soot model and to assess the ability of the resulting approach to predict the soot emissions and size distributions of Diesel engine configurations. Since calculations of 3D Diesel engine cases are too costly [72], comparisons based on these cases cannot be done between tabulated chemistry and detailed kinetic solver results. For this reason, we propose a comparison using a dedicated variable volume heterogeneous model reactor called ECFM3Z-0D. This reactor is based on the three mixture fraction description of ECFM3Z and allows to mimic the combustion process observed in a Diesel engine by imposing the mixing time-scale. In the mixed zone of the reactor where combustion takes place, chemistry can be described using either VPTHC or a kinetic solver. This finally allows a direct comparison between the two approaches using identical mixing trajectories. Finally, a dedicated experimental Diesel engine database is used to evaluate the potential of the proposed models. The database is described in Aubagnac-Karkar *et al.* [147] along with an experimental validation of the proposed surrogate against commercial Diesel fuel and a brief presentation of the 3-D simulations results obtained with the model detailed and validated in this paper. It has been chosen because it provides SNDF measurements at exhaust for eleven cases. This type of measurements being very complex, such databases of engine cases only exist at exhaust for metal engines so far, restraining the validation to the exhaust SNDF and soot yields.

Section 4.3 describes the soot model and its adaptations to Diesel conditions. Then, Section 4.4 introduces the turbulent combustion model and its coupling with the soot model. The soot model is validated in Section 4.5 on the ECFM3Z-0D test case. It is finally evaluated on the engine database in Section 4.7.

4.3 Soot modeling

The soot model introduced in the present contribution is based on the previous work of Netzell *et al.* [55, 78]. This section briefly describes its governing equations and the evolutions brought to the source terms estimation.

The soot particles population is evaluated by using a sectional method. The soot particles are separated with respect to their volume into discrete sections. In contrast to Fraioli *et al.* [72] where soot particles are considered as chemical species, the present approach considers that soot particles are solid and modeled as a distinct dispersed phase, interacting with the gaseous phase. In the turbulent reactive flow, each section i, representing the soot particles of a given volume range, is

governed by a standard transport equation for the mass fraction of soot in this section, $\tilde{Y}_{soot,i}$:

$$\frac{\partial \overline{\rho}\widetilde{Y}_{soot,i}}{\partial t} + \nabla \cdot (\overline{\rho}\tilde{u}\widetilde{Y}_{soot,i}) = \nabla \cdot (\overline{\rho}D_{t,soot}\nabla\widetilde{Y}_{soot,i}) + \overline{\rho}\widetilde{\dot{\omega}}_{soot,i} \tag{4.1}$$

with $\overline{\rho}$ the gas phase density, $\tilde{u}$ the gas velocity, $D_{t,soot}$ the turbulent diffusion coefficient of soot and $\tilde{\dot{\omega}}_{soot,i}$ the soot source term for section i.

We start with an explanation of the particle volume discretization and of the variables used to represent soot particles in each section. Then, the different physical phenomena involved in the soot formation process are described. These phenomena are illustrated in Fig. 4.2 and are introduced in the following order:

- First, collisional source terms: particle inception, condensation and coagulation.
- Secondly, surface chemistry source terms: surface growth and oxidation.

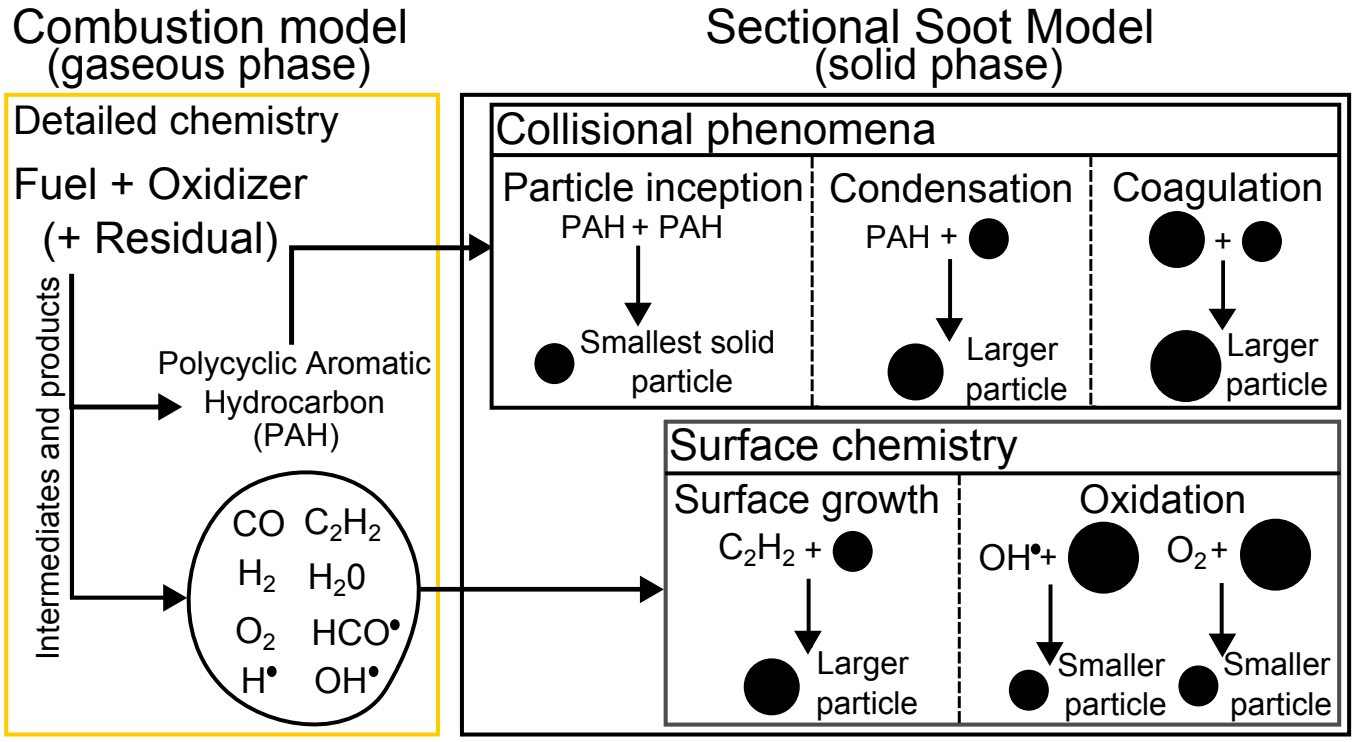

Figure 4.2: Illustration of the five phenomena representing soot formation and evolution with the involved gaseous species.

4.3.1 Volume discretization

In this model, a fixed interval of volume $[V_{MIN}; V_{MAX}]$ is divided into $n_{sections}$ sections. The smallest volume of the considered particles is V_{MIN} and is equal to the carbon-equivalent volume of the number of carbon atoms of two soot precursors and two acetylene molecules. Carbon-equivalent volume for two atoms of carbon is given by:

$$V_{C_2} = \frac{2M_C}{\mathcal{N}_A \rho_{soot}} \tag{4.2}$$

where M_C is the molar mass of carbon, $\mathcal{N}_A$ the Avogadro number and ρ_{soot} the soot density which is assumed constant at a value of $1.86 \cdot 10^3$ kg.m^{-3} [55, 56].

Using pyrenyl ($C_{16}H_9$) as precursor as in [55, 56, 58, 78, 77], V_{MIN} becomes equal to $18V_{C_2}$ with a value of $3.857 \cdot 10^{-28}$ m^3 which is approximately the volume of a 0.9 nm diameter sphere. In the case of a complete solid-gas coupling between the soot model and a kinetic solver, all hydrogen atoms taken from the gas phase are then sent to H_2 to close the hydrogen balance since all volumes exchanged between phases are given with respect to the exchanged number of carbon atoms.

The largest modeled particles have a volume V_{MAX} corresponding to the volume of a $d_{MAX} = 10\,\mu$m diameter sphere. In Diesel engines, the particles produced are one or two orders of magnitude smaller than this value d_{MAX} in diameter [72, 129, 130, 131]. This V_{MAX} value ensures that carbon mass will not accumulate in the last section.

The first section represents soot particles of a constant volume range going from V_{MIN} to $V_{MIN} + V_{C_2}$. The following sections are defined to fill the represented volume interval with $n_{sections} - 1$ sections with a geometrical progression:

$$V_{max,i} = (V_{MIN} + V_{C_2}) \left(\frac{V_{MAX}}{V_{MIN} + V_{C_2}} \right)^{(i-1)/(n_{sections}-1)} \quad \forall\, i \in [\![2; n_{sections}]\!] \tag{4.3}$$

All simulations presented in this paper have been realized with 30 sections. This value has been chosen from the convergence study done with a similar model by Vervisch [57]. This value is a compromise which allows a limited CPU over-cost of the sectional model while giving an accuracy close to a high resolution of typically 100 sections. It has been checked that these results were reproduced by the proposed model. Moreover, 30 or 35 sections are commonly used in 3-D simulations using soot sectional methods [57, 79, 84].

4.3.2 Model variables

The source terms given by the soot model are written as volume fraction source terms. The section i soot particles volume normalized by the total volume of both gas and solid phase is the soot volume fraction Q_i. Assuming the volume of all soot particles is negligible with respect to the volume of the gas, Q_i can be deducted from $\tilde{Y}_{soot,i}$:

$$Q_i = \frac{\overline{\rho}}{\rho_{soot}} \tilde{Y}_{soot,i} \tag{4.4}$$

Accordingly, the soot mass fraction source term in Eq. (4.1) is given by:

$$\tilde{\dot{\omega}}_{soot,i} = \frac{\rho_{soot}}{\overline{\rho}} \dot{Q}_i = \frac{\rho_{soot}}{\overline{\rho}} (\dot{Q}_{nucl,i} + \dot{Q}_{cond,i} + \dot{Q}_{sg,i} + \dot{Q}_{ox,i} + \dot{Q}_{coag,i}) \tag{4.5}$$

where $\dot{Q}_{nucl,i}$, $\dot{Q}_{cond,i}$, $\dot{Q}_{coag,i}$, $\dot{Q}_{sg,i}$ and $\dot{Q}_{ox,i}$ are respectively the volume fraction source terms of section i due to nucleation, condensation, coagulation, surface growth and oxidation.

The soot volume fraction density q_i is assumed to be constant in a given section i [55]:

$$q_i = \frac{Q_i}{V_{max,i} - V_{min,i}} \tag{4.6}$$

As soot density ρ_{soot} is assumed constant, the mass density is also constant in a section. The particle number density $n_i(v)$ is deduced from q_i:

$$n_i(v) = \frac{q_i}{v} \; \forall\, v \in [V_{min,i}; V_{max,i}] \tag{4.7}$$

Finally, the volume number of particles in section i, N_i, is:

$$N_i = \int_{V_{min,i}}^{V_{max,i}} n_i(v)dv = \frac{Q_i}{V_{max,i} - V_{min,i}} ln\left(\frac{V_{max,i}}{V_{min,i}}\right) \tag{4.8}$$

It has been shown by Netzell [55] that considering n_i or q_i constant in a section has a very low influence on the predicted SNDF. The knowledge of the number of particles in each section given by Eq. (4.8) allows to calculate the SNDF as illustrated in Fig. 4.35. Knowing $\widetilde{Y}_{soot,i}$ for each section i gives an instantaneous access to the SNDF at each time step and every location.

4.3.3 Collisional source terms

Particle inception, condensation and coagulation are collisional phenomena. They are represented by the Smoluchowski equation [62]. In the continuous form, it reads:

$$\dot{F}_a(t) = \frac{1}{2}\int_0^a (\beta_{a-b,b}F_b(t)F_{a-b}(t))db - \int_0^\infty (\beta_{a,b}F_a(t)F_b(t))db \tag{4.9}$$

where $F_x(t)$ is the number of particles of size x, $\dot{F}_x(t)$ its variation rate and $\beta_{x,y}$ the collision frequency between particles of size x and y.

The collision frequencies are obtained using the theory of aerosol science [64], applied to soot formation by Kazakov and Frenklach [65]. These frequencies are evaluated for three different regimes based on the value of the Knudsen number Kn defined as:

$$Kn(d) = \frac{\lambda_{gas}}{d} \tag{4.10}$$

where d is the particle diameter and λ_{gas} the gas mean free path, computed for the bath gas N_2. In the present work, collision frequencies of soot precursors (either two soot precursors or a soot precursor and a soot particle) are considered to occur in the molecular collision regime. The soot particles collision regime is chosen as in Kazakov and Frenklach [65].

4.3.3.a Inception and Condensation

Inception and condensation are the two phenomena related to precursors collisions. It can either be collisions between precursors to create the smallest considered soot particles (particle inception), or between precursors and soot particles to increase soot particles volume (condensation). The precursor species used in these phenomena is a virtual species called PAH (for Polycyclic Aromatic Hydrocarbons). PAH is the product of the pyrenyl radical polymerization by acetylene:

$$C_{16}H_9 + C_2H_2 \xrightarrow{k_{pol}} PAH + H_2 \tag{4.11}$$

where k_{pol} is the rate constant of reaction for this polymerization reaction.

The volume fraction reaction rate of PAH r_{PAH} reads:

$$r_{PAH} = \mathcal{N}_A k_{pol} [C_{16}H_9] [C_2H_2] V_{PAH} \tag{4.12}$$

where V_{PAH} is the volume of a precursor (18 carbon atoms).

Considering N_{PAH} the volume number of PAH particles, volume fraction variation rate of the smallest modeled soot $\dot{Q}_{Nucl}$ comes from the Smoluchowski equation (4.9) coupled with Eq. (4.6) and Eq. (4.7):

$$\dot{Q}_{Nucl} = 2V_{PAH}\beta^{fm}_{PAH,PAH}N^2_{PAH} \tag{4.13}$$

where $\beta^{fm}_{PAH,PAH}$ is the molecular collision frequency for two precursors.

It is then possible to express the global volume amount of precursors that collide with all soot particles per unit time $\dot{Q}^{PAH}_{Cond}$:

$$\dot{Q}^{PAH}_{Cond} = V_{PAH}N_{PAH}\sum_{i=1}^{i_{max}}\beta^{fm}_{PAH,i}\int_{V_{min,i}}^{V_{max,i}} n_i(v)dv \tag{4.14}$$

where $\beta^{fm}_{PAH,i}$ is the molecular collision frequency between precursors and soot particles of section i.

N_{PAH} is calculated assuming a steady state assumption between the formation of PAH through reaction (4.11) and its consumption by collision due to nucleation and condensation over all the sections [55]:

$$r_{PAH} = \underbrace{2V_{PAH}\beta^{fm}_{PAH,PAH}}_{k_{Nucl}}N^2_{PAH} \quad + \quad \underbrace{\left(V_{PAH}\sum_{i=1}^{i_{max}}\beta^{fm}_{PAH,i}\int_{V_{min,i}}^{V_{max,i}} n_i(v)dv\right)}_{k_{Cond}}N_{PAH} \tag{4.15}$$

The positive roots of this polynomial equation being:

$$N_{PAH} \quad = \quad \frac{-k_{Cond} + \sqrt{k^2_{Cond} + 4r_{PAH}k_{Nucl}}}{2k_{Nucl}} \tag{4.16}$$

It is important to note that the inception reaction rate is directly read from Eq. (4.13) while for condensation, the volume fraction computed from Eq. (4.14) represents the global volume fraction transferred from gas phase to solid soot phase. This global condensation volume fraction has therefore to be distributed correctly towards different sections as explained below.

Condensation reaction rates

The total amount of condensed soot in section i which has to be distributed into the SNDF $\dot{Q}^{BD}_{Cond,i}$ (BD for *Before Distribution*) reads:

$$\dot{Q}^{BD}_{Cond,i} = N_{PAH}\int_{V_{min,i}}^{V_{max,i}}\beta^{fm}_{PAH,i}\left(V_{PAH}+v\right)n_i(v)dv \tag{4.17}$$

It can be split in two terms. The first term is the flux $\dot{Q}^{out}_{Cond,i}$ of particles in section i that are collided by the precursors:

$$\dot{Q}^{out}_{Cond,i} = N_{PAH}\int_{V_{min,i}}^{V_{max,i}}\beta^{fm}_{PAH,i}n_i(v)vdv \tag{4.18}$$

The second term is the volume of soot precursors colliding with particles of a given section i per unit time $\dot{Q}^{PAH}_{Cond,i}$ obtained by:

$$\dot{Q}^{PAH}_{Cond,i} = V_{PAH} N_{PAH} \int_{V_{min,i}}^{V_{max,i}} \beta^{fm}_{PAH,i} n_i(v) dv \tag{4.19}$$

This term is used previously to evaluate N_{PAH}. In the previous versions of the model [55, 56], $\dot{Q}^{PAH}_{Cond,i}$ (Eq. (4.19)) was directly attributed to section $i+1$ with a quantity of soot transferred between sections i and $i+1$ calculated to ensure mass and number conservation.

Finally, $\dot{Q}^{BD}_{Cond,i}$ is distributed in the sections intersecting with the interval $[V_{min,i}+V_{PAH}; V_{max,i}+V_{PAH}]$. Because the volume range represented by this interval is $V_{max,i} - V_{min,i}$, condensation only makes particles larger and because the sections volume range is growing geometrically, only two cases are possible:

- the volume interval is completely included in one section which will receive the complete condensation reaction rate from section i,
- the interval intersects two different sections which will receive a part of the condensation reaction rate from section i. In this case, section i can be one of those two sections.

Figure 4.3 illustrates these two steps to distribute the condensed mass of soot in the right sections of the distribution. At first, the global amount of condensed soot in section i, $\dot{Q}^{BD}_{Cond,i}$, is evaluated. Then it is distributed with respect to particles volumes towards one or two sections. As a consequence, the rate of volume fraction of soot received by a section j from the condensation over section i, $\dot{Q}^{i\to j}_{Cond}$, is the product of the volume fraction rate of soot distributed from section i, $\dot{Q}^{BD}_{Cond,i}$ (including both PAH received from the gaseous phase and soot taken from the section i), by a matrix G_{cond} (defined in Section 3.1.3.c) representing the part of section i condensation received by section j:

$$\dot{Q}^{i\to j}_{Cond} = G_{cond}\,(i,j)\,\dot{Q}^{BD}_{Cond,i} \tag{4.20}$$

Finally, the condensation source term in section i is the sum of the volume fraction rates received from all sections, with the volume fraction rate taken from section i ($\dot{Q}^{out}_{Cond,i}$) being withdrawn:

$$\dot{Q}_{Cond,i} = -\dot{Q}^{out}_{Cond,i} + \sum_{j=1}^{n_{sections}} G_{cond}\,(j,i)\,\dot{Q}^{BD}_{Cond,j} \tag{4.21}$$

It is to be noticed that this method keeps the number of particles constant, as the condensation phenomenon should. Indeed, the added volume fraction of soot is consistent with the transfer of soot to the larger size of the distribution, thus conserving the number of particles computed with Eq. (4.7).

4.3.3.b Coagulation

The evaluation of the volume number rate of collisions between particles of sections i and j, $\dot{N}^{out}_{ij}$, is done using the method proposed in [55, 56]. It is based on the collision frequency β_{ij} of sections i and j defined by Kazakov and Frenklach [65].

As for condensation, the second step in the coagulation modeling is to distribute the collided particles in the interval $[V_{min,i}+V_{min,j}; V_{max,i}+V_{max,j}]$. A 3-D matrix $G_{coag}(i,j,k)$ links two sections

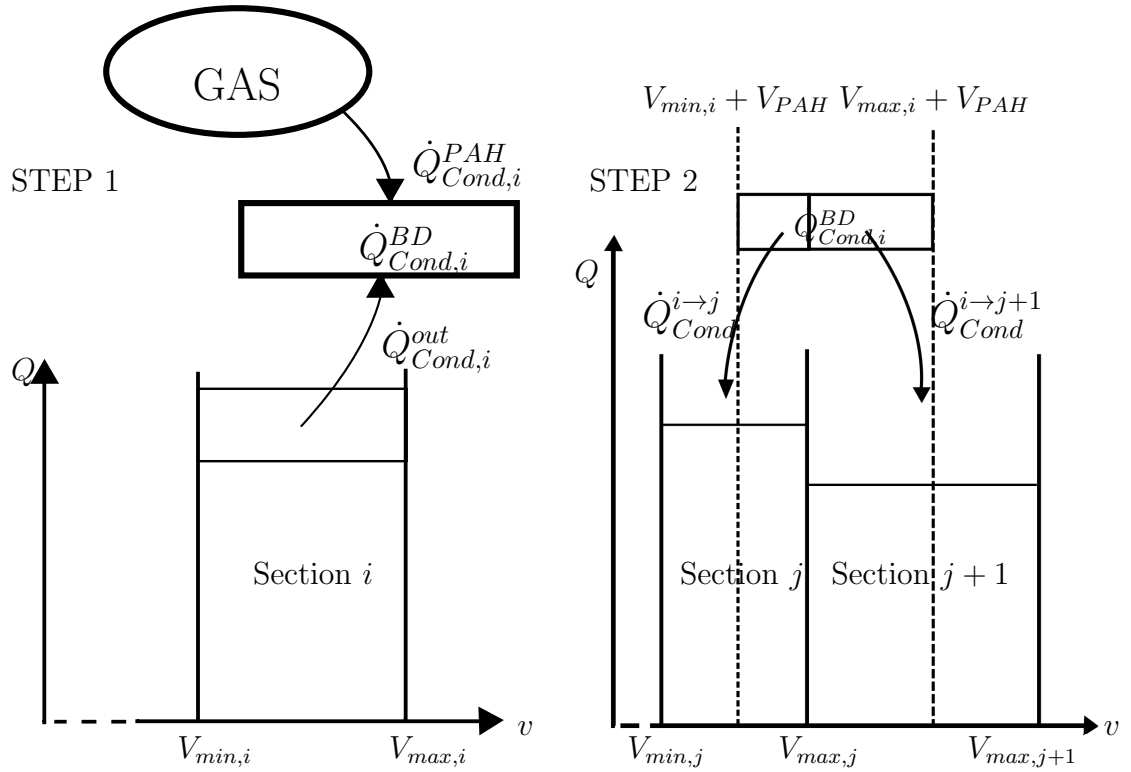

Figure 4.3: Illustration of condensation over section i. STEP 1: computation of $\dot{Q}^{BD}_{Cond,i}$, the sum of the condensed carbon from gaseous phase over section i and the volume fraction of section i colliding with precursors. STEP 2: distribution of $\dot{Q}^{BD}_{Cond,i}$ in other sections.

i and j to a third section k receiving a part of their collided particles. More details on this matrix are given in the Section 3.1.3.c.

Accordingly, the particle number rate received by a section k from sections i and j is the product of the volume density of collision between particles of sections i and j, $\dot{N}^{out}_{ij}$, by the matrix G_{coag}:

$$\dot{N}^{i,j\to k}_{Coag} = G_{coag}\,(i,j,k)\,\dot{N}^{out}_{ij} \tag{4.22}$$

As a consequence, the particle number rate in section i is equal to the particle rate received by section i from all smaller sections $\dot{N}^{j,k\to i}_{Coag}$ minus the rate of collision between particles of sections i and all other sections. Using Eq. (4.8), the coagulation source term of section i reads:

$$\dot{Q}_{Coag,i} = \left(\sum_{j,k}^{i} \dot{N}^{j,k\to i}_{Coag} - \sum_{j=1}^{n_{sections}} \dot{N}^{out}_{ij} \right) \frac{V_{max,i} - V_{min,i}}{ln\left(\frac{V_{max,i}}{V_{min,i}}\right)} \tag{4.23}$$

4.3.4 Surface chemistry source terms

The *Hydrogen Abstraction Carbon Addition - Ring Closure* cycle (HACA-RC) developed by Frenklach [26] represents the growth and oxidation of PAH. In the present work, surface chemistry of soot is modeled using a variation of this cycle proposed by D'Anna and Kent [76]. This surface chemistry has been chosen since it has been designed for engine conditions and previously validated by Fraioli *et al.* [72]. The surface chemistry phenomena are described using eight gaseous species

(H, H_2, OH, H_2O, C_2H_2, O_2, CO and HCO) in six reactions (given in table Tab.3.1) with the rate constants taken from [76].

$$\begin{aligned}
\mathrm{A}_i &\overset{k_1^i}{\leftrightarrow} \mathrm{R}_i + \mathrm{H} \\
\mathrm{A}_i + \mathrm{H} &\overset{k_2^i}{\leftrightarrow} \mathrm{R}_i + \mathrm{H}_2 \\
\mathrm{A}_i + \mathrm{OH} &\overset{k_3^i}{\leftrightarrow} \mathrm{R}_i + \mathrm{H}_2\mathrm{O} \\
\mathrm{R}_i + \mathrm{C}_2\mathrm{H}_2 &\overset{k_4^i}{\longrightarrow} \mathrm{A}_k^2 + \mathrm{H} \\
\mathrm{A}_i + \mathrm{OH} &\overset{k_5^i}{\longrightarrow} \mathrm{A}_k^{-1} + \mathrm{HCO} \\
\mathrm{R}_i + \mathrm{O}_2 &\overset{k_6^i}{\longrightarrow} \mathrm{A}_k^{-2} + 2\mathrm{CO}
\end{aligned}$$

Table 4.1: Reactions governing the soot surface chemistry [76].

where A_i represents stable aromatic soot particles of section i, R_i represents radical soot particles of section i, $\mathrm{A}_k^{\mathrm{p}}$ represents stable aromatic soot particles product of a reaction that exchanged p carbon atoms with the gaseous phase, and k_n^i is the rate constant of reaction n on particles of section i.

4.3.4.a Reaction rates

To evaluate the oxidation and surface growth reaction rates given by the surface chemistry reactions, the total amount of particles in each section has to be converted into a concentration $[\mathrm{A}_i] + [\mathrm{R}_i]$ proportional to its available reactive surface. A steady state assumption on active radical sites allows to distinguish $[\mathrm{R}_i]$ from $[\mathrm{A}_i]$. These steps are realized as in [55, 56] to evaluate the volume fraction reaction rates for surface growth $\dot{Q}_{SG,i}^{gas}$ and oxidation $\dot{Q}_{Ox,i}^{gas}$ in section i. These reaction rates represent the mass exchange between the gaseous phase and the solid phase.

These reaction rates respectively represent global surface growth and oxidation over all sections and as for condensation and coagulation, they have to be distributed over the SNDF to complete the modeling of the phenomena.

4.3.4.b Surface growth

Surface growth is the carbon addition to soot particles from the gaseous phase. Its volume fraction reaction rate is associated to a reference volume V_{C_2} to be consistent with the number of carbon added by acetylene, which is the adsorbed species in the HACA mechanism. This phenomenon only implies consecutive sections since it leads to a size variation of V_{C_2} which is the volume range of the smallest section. Thus, the volume fraction rate of soot particles in section i which are growing enough to switch to section $i+1$, $\dot{Q}_{SG,i}^{out}$, needs to be modeled:

$$\dot{Q}_{SG,i}^{out} = \mathcal{N}_A K_{SG,i} \int_{V_{max,i}-V_{C_2}}^{V_{max,i}} (v + V_{C_2}) \frac{1}{v} \left(\frac{v}{V_{c_2}} \right)^{\frac{\theta}{3}} dv \tag{4.24}$$

where $K_{SG,i} = k_{4,i} [\mathrm{C}_2\mathrm{H}_2] [\mathrm{R}_i]$ and $K_{Ox,i} = k_{6,i} [\mathrm{O}_2] [\mathrm{R}_i] + k_{5,i} [\mathrm{OH}] [\mathrm{A}_i] / 2$.

In Eq. (4.24), the volume is $(v + V_{C_2})$ since the concerned particle already received the volume fraction from the gaseous phase and $(1/v)(v/V_{c_2})^{\theta/3}$ represents the available reaction surface variation depending on the volume.

Finally, the surface growth source terms applied to each section write:

$$\dot{Q}_{SG,1} = -\dot{Q}^{out}_{SG,1} + \dot{Q}^{gas}_{SG,1} \tag{4.25}$$

$$\dot{Q}_{SG,i} = \dot{Q}^{out}_{SG,i-1} - \dot{Q}^{out}_{SG,i} + \dot{Q}^{gas}_{SG,i} \qquad \forall i \in [\![2; n_{sect} - 1]\!] \tag{4.26}$$

$$\dot{Q}_{SG,n_{sect}} = \dot{Q}^{out}_{SG,n_{sect}-1} + \dot{Q}^{gas}_{SG,n_{sect}} \tag{4.27}$$

4.3.4.c Oxidation

The oxidation of soot particles is also part of the surface kinetic scheme used where reactions with dioxygen and hydroxyl take carbon from soot particles. Its modeling is similar to surface growth, except that the concerned particle size is reduced by the associated volume V_{C_2}. The volume fraction rate of soot transferred from section i to section $i-1$ reads:

$$\dot{Q^{out}_{Ox,i}} = \mathcal{N}_A K_{Ox,i} \int_{V_{min,i}}^{V_{min,i}+V_{C_2}} (v - V_{C_2}) \frac{1}{v} \left(\frac{v}{V_{c_2}} \right)^{\frac{\theta}{3}} dv \tag{4.28}$$

As for surface growth, the oxidation source terms applied to each section write:

$$\dot{Q}_{Ox,1} = \dot{Q}^{out}_{Ox,2} - \dot{Q}^{gas}_{Ox,1} \tag{4.29}$$

$$\dot{Q}_{Ox,i} = \dot{Q}^{out}_{Ox,i+1} - \dot{Q}^{out}_{Ox,i} - \dot{Q}^{gas}_{Ox,i} \qquad \forall i \in [\![2; n_{sect} - 1]\!] \tag{4.30}$$

$$\dot{Q}_{Ox,n_{sect}} = -\dot{Q}^{out}_{Ox,n_{sect}} - \dot{Q}^{gas}_{Ox,n_{sect}} \tag{4.31}$$

4.4 Turbulent Combustion Modeling

As mentioned in Section 4.2, a turbulent combustion model able to represent detailed chemistry in non-premixed combustion is required to compute the species needed by the sectional soot model, including soot precursors. In the present work, this is done by coupling the ECFM3Z model [146] and a specifically developed tabulated chemistry model, VPTHC, to the IFP-C3D RANS code [148, 149]. IFP-C3D, also used for the 3-D Diesel simulations and described in Section 4.7, is used to simulate homogeneous cases in this section in order to validate the tabulated approach against a reference solution provided by a detailed kinetic solver computation. The following section contains a description of the mentioned models.

4.4.1 The ECFM3Z model

A detailed description of the model standard version is available in [146] for compression ignition operating conditions. In order to represent the local mixing process, the ECFM3Z model includes a description of the local mixture stratification by considering three homogeneous sub regions (see Fig. 4.4): one region contains only pure fuel (region F), the second region contains fresh air plus any

additional EGR (region A) and the third region contains a mixture of the latter two (region M). During injection, the evaporation of the spray droplets leads to a source of mass in region F. The fuel and air (+EGR) from regions F and A mix to form region M. The mixing model is introduced via the transport equation of region A oxygen and region F fuel tracers:

$$\frac{\partial \bar{\rho}\widetilde{Y}^F_{Fu}}{\partial t} + \nabla.(\bar{\rho}\tilde{u}\widetilde{Y}^F_{Fu}) = \nabla.(\bar{\rho}(D_t)\nabla\widetilde{Y}^F_{Fu}) + \bar{\rho}\widetilde{\dot{S}}_{Fu} + \bar{\rho}\widetilde{\dot{E}}^{F\to M}_{Fu} \tag{4.32}$$

$$\frac{\partial \bar{\rho}\widetilde{Y}^A_{O_2}}{\partial t} + \nabla.(\bar{\rho}\tilde{u}\widetilde{Y}^A_{O_2}) = \nabla.(\bar{\rho}(D_t)\nabla\widetilde{Y}^A_{O_2}) + \bar{\rho}\widetilde{\dot{E}}^{A\to M}_{O_2} \tag{4.33}$$

where $\bar{\rho}$ is the mean density, $\tilde{u}$ the Favre mean velocity, D_t the turbulent diffusivity, $\tilde{Y}^F_{Fu}$ the fuel tracer, $\tilde{Y}^A_{O_2}$ the oxygen tracer, $\widetilde{\dot{S}}_{Fu}$ the source term of gaseous fuel mass fraction (from the evaporation of liquid fuel droplets), $\widetilde{\dot{E}}^{F\to M}_{Fu}$ and $\widetilde{\dot{E}}^{A\to M}_{O_2}$ the mixing source terms respectively from region F to region M and from region A to region M.

$\widetilde{\dot{E}}^{F\to M}_{Fu}$ and $\widetilde{\dot{E}}^{A\to M}_{O_2}$ evolutions are based on a characteristic mixing time τ_m:

$$\widetilde{\dot{E}}^{F\to M}_{Fu} = -\frac{1}{\tau_m}\tilde{Y}^F_{Fu}\left(1-\tilde{Y}^M_{Fu}\right) \tag{4.34}$$

$$\widetilde{\dot{E}}^{A\to M}_{O_2} = -\frac{1}{\tau_m}\tilde{Y}^A_{O_2}\left(1-\tilde{Y}^M_{O_2}\right) \tag{4.35}$$

where $\tilde{Y}^M_{Fu}$ and $\tilde{Y}^M_{O_2}$ are respectively the fuel and oxygen mass fractions in region M. This mixing time-scale τ_m is considered proportional to the turbulent time-scale given by the $k-\epsilon$ model, $\tau_m^{-1} = \frac{\epsilon}{k}C$ where C is a constant set to 0.6.

Potential EGR species are followed by tracers and their mixing is governed by that of oxygen [146].

Finally, the auto-ignition and combustion in region M is described by the VPTHC approach described in the following, as illustrated in Fig. 4.4.

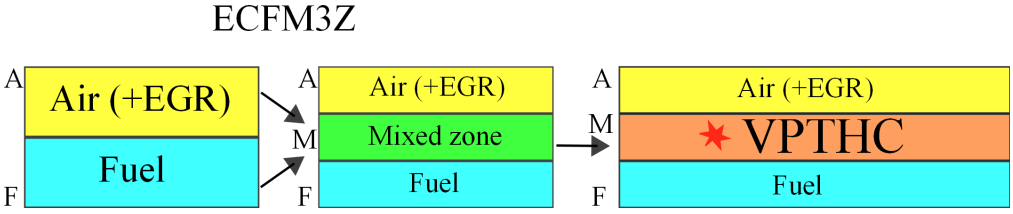

Figure 4.4: Scheme of ECFM3Z coupled with the VPTHC combustion model.

4.4.2 The tabulated chemistry approach

In the EADF approach [145], approximated diffusion flames at variable pressure are used to generate the look-up table. In this work, the turbulent mixing between fuel and air is described by the ECFM3Z model and the look-up table is based on homogeneous reactors calculations at variable pressure in the same manner as in [150]. This strategy allows the use of homogeneous tables which are less demanding in terms of memory requirements compared to the EADF tables. This

tabulated chemistry approach is used in the mixed zone of ECFM3Z and gives a direct access to the species evolutions. The resulting model is called VPTHC (Variable Pressure Tabulated Homogenous Chemistry) and is very close to the model proposed by Jay and Colin [150] where variable volume reactors were used instead of variable pressure reactors. As in [145], this model uses two different tables generated respectively from constant pressure homogeneous reactors (HR) and variable pressure reactors (VPR) computations. Both the HR and VPR are computed with the IFP-Kinetics library solver [136] which is also used as the reference detailed chemistry solver to validate the approach.

4.4.2.a Table generation

HR Table. The constant pressure table is used to represent the auto-ignition phase. It is built from the calculation of a constant pressure HR database for several initial pressures P_0, initial temperatures T_0, mixture fractions Z and mass fractions of dilutant Y_{EGR} as coordinates of the database. The results are stored as a function of the progress variable which quantifies the transition from fresh to burnt gases. This quantity is estimated here as $c = Y_c/Y_{eq}$ where $Y_c = Y_{\mathrm{CO}} + Y_{\mathrm{CO_2}} + Y_{\mathrm{H_2O}}$ and Y_{eq} is the value of Y_c when the equilibrium at constant pressure and enthalpy is reached. It has been verified that Y_c grows bijectively with time in all reactors.

VPR Table. This table describes chemistry in the expansion phase. It is built from a database of VPR at the same initial conditions as the HR table, with two additional coordinates which are the progress variable at the beginning of the expansion Y_{c_0} and the pressure time derivative $\dot{p}$. These reactors are constant pressure reactors until the progress variable reaches the value Y_{c_0} when the pressure is forced to decrease with a constant rate $\dot{p}$. Figure 4.5 illustrates how pressure evolves depending on Y_{c_0} and $\dot{p}$, with the expansion trajectory from the initial pressure P_0 to the final pressure P_F (here, 1 bar). This methodology allows tabulating species evolution in a model trajectory which is close to the expansion trajectory encountered in a piston engine.
The parameters discretization of the HR and VPR tables are given in Tab.4.2.

Quantity		Number of points	Variation
c		100	$[0; 1]$
Z		25	$[0; 0.5]$
P_0	[bar]	13	$[1; 200]$
T_0	[K]	41	$[600; 1200]$
Y_{EGR}		3	$[0; 0.5]$
$\dot{p}$	[bar.s^{-1}]	5	$[-100; -100000]$
c_0		3	$[0.05; 0.95]$

Table 4.2: Discretizations of the tables used in this study.

4.4.2.b Model implementation

To compute species mass fractions in the combustion zone from the ones stored in the look-up table, the input parameters described above need to be calculated. These parameters are the progress variable Y_c and the initial parameters of the reactors: $\tilde{Z}$, $\mathrm{P_0}$, $\mathrm{T_0}$, Y_{EGR}, $\dot{p}$ and Y_{c_0}. These parameters

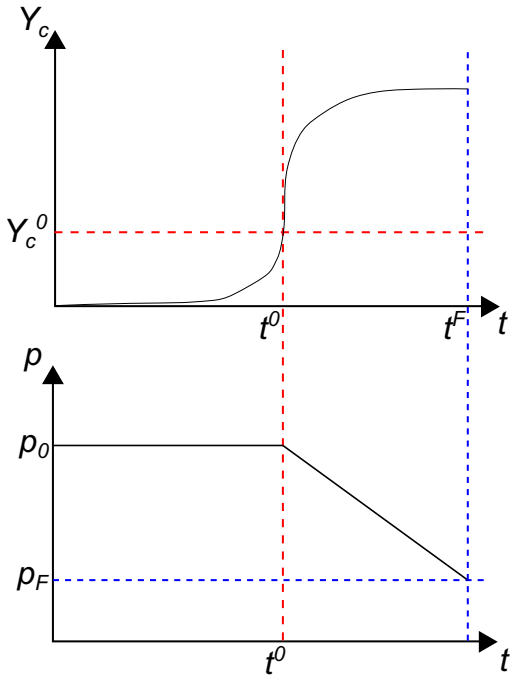

Figure 4.5: Illustration of the pressure time evolution depending on Y_{c_0} and $\dot{p}$ in a VPR [145].

are computed as in [145], their derivations being omitted here for the sake of clarity. The tabulated species are transported in the CFD code as follows:

$$\frac{\partial \overline{\rho}\tilde{Y}_i}{\partial t} + \nabla \cdot (\overline{\rho}\tilde{u}\tilde{Y}_i) = \nabla \cdot (\overline{\rho}D_t \nabla \tilde{Y}_i) + \overline{\rho}\tilde{\dot{\omega}}_i \tag{4.36}$$

In the VPTHC model, the species reaction rate $\tilde{\dot{\omega}}_i$ is modeled by the expression proposed by Michel *et al.* [151]. It reads:

$$\tilde{\dot{\omega}}_i = \frac{\tilde{Y}_i^{Tbl}(\tilde{Z}, \mathrm{P}_0, \mathrm{T}_0, Y_{\mathrm{EGR}}, \dot{p}, Y_{c_0}, \tilde{Y}_c + \delta\tilde{Y}_c) - \tilde{Y}_i}{\tau} \tag{4.37}$$

where τ is a time-scale representing species relaxation towards the homogeneous reactor conditions. It was shown in [151] that as long as τ is chosen small enough compared to the progress variable time-scale, the tabulated trajectory is correctly followed. Here, we choose $\tau = 3dt$ where dt is the CFD time-step. The mean progress variable $\tilde{Y}_c + \delta\tilde{Y}_c$ is deduced from the tabulated progress variable source term $\tilde{\dot{\omega}}_{Y_c}^{Tbl}$ and is given by:

$$\delta\tilde{Y}_c = \tau\tilde{\dot{\omega}}_{Y_c}^{Tbl}(\tilde{Z}, \mathrm{P}_0, \mathrm{T}_0, Y_{\mathrm{EGR}}, \dot{p}, Y_{c_0}, \tilde{Y}_c) \tag{4.38}$$

4.4.2.c Enthalpy balance equation

In the CFD code, only thirteen species are extracted from the look-up table: fuel (here the sum of mass fractions of 1-Methylnaphthalene and Decane), O_2, CO_2, H_2O, CO, H, H_2, O, OH, C_2H_2, CH, HCO and $C_{16}H_9$. To conserve mass and enthalpy, atomic balances on C, H and O are done as well as an enthalpy balance.

The atomic balance of C and the enthalpy balance are closed by a pair of virtual carboneous species C1 and C2. The atomic balances of H and O are closed by virtual species H_2b and O_2b (b standing for balance) which have the same thermodynamic behaviors as their respective real species. The balance of H includes the hydrogen from C1 and C2.

The merging of a two species surrogate fuel into a single species with a specific enthalpy defined as the average specific enthalpy of both fuels in the initial proportion introduces a strong enthalpy loss. Indeed, the proportion of each fuel evolves in time during combustion as illustrated in Fig. 4.6. 1-Methylnaphthalene being consumed faster than Decane, the fuel enthalpy becomes equal to the Decane enthalpy beyond a given point of the reaction while it will be considered as equal to the mixture enthalpy by the CFD code. This justifies the use of a fourth balance species to close the enthalpy balance as well as the mass balance.

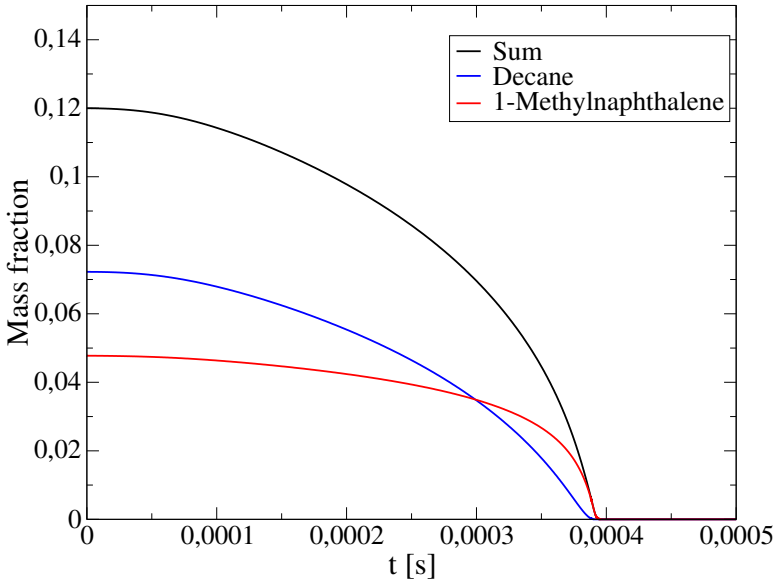

Figure 4.6: Time-evolution of 1-Methylnaphthalene (red), Decane (blue) and their sum mass fraction (black) in a constant pressure homogeneous reactor at 70 bar, with an initial temperature of 1000 K and an initial fuel mass fraction of 0.12

The two carboneous balance species are created with the atomic composition and the sensible enthalpy of C_2H_3. Their specific enthalpies of formation have been chosen in order to conserve the global mixture enthalpy by changing the ratio of C1 and C2 in the carbon mass required to complete the atomic carbon balance. They are fixed as $3 \cdot 10^6$ J.mol^{-1} for C1 and $-6 \cdot 10^5$ J.mol^{-1} for C2. At every time step in every computed homogeneous reactors used to generate the look-up table, CFD-like atomic balances are made with the species stored in the look-up table, H2b, O2b and a virtual C_2H_3b species. From these balances and using the different enthalpies of formation of C1 and C2, the mass fractions Y_{C1} and Y_{C2} are evaluated considering that $Y_{C_2H_3b} = Y_{C1} + Y_{C2}$ and by closing the equation of enthalpy Eq. (4.39) by using a ratio $x = \frac{Y_{C1}}{Y_{C_2H_3b}}$:

$$\mathrm{H} = h_s^{tot} + \sum_{i \in \Omega} Y_i h_0^i + Y_{O_2b} h_0^{O_2} + Y_{H_2b} h_0^{H_2} + Y_{C_2H_3b} h_0^{C2} + x Y_{C_2H_3b} \left(h_0^{C1} - h_0^{C2} \right) \tag{4.39}$$

where H is the enthalpy of the mixture, h_s^{tot} the sensible enthalpy of all tabulated species and of

the species used in atomic balances, Ω the ensemble of all tabulated species and h_0^i the formation enthalpy of species i.

x can be computed from Eq. (4.39). Thus, C1 is stored as C1 $= xY_C$ in the look-up table. For every point of the table, the C2 computed to close the carbon atomic balance in the CFD code is going to close the balance of enthalpy since the value of C1 has been computed in order to do this on the homogeneous reactors.

This type of closure is required to predict auto-ignition with this surrogate. As illustrated in Fig. 4.7, the enthalpy loss due to the error on the fuel enthalpy leads to a strong temperature decrease. Auto-ignition still occurs in this constant pressure simulation because the conditions read by the model in the look-up table are fresh gases conditions, which are not changed in a constant pressure homogeneous reactor. In variable volume reactors or 3-D simulations, this type of enthalpy loss would stop auto-ignition by switching the followed trajectory to a trajectory which does not auto-ignites.

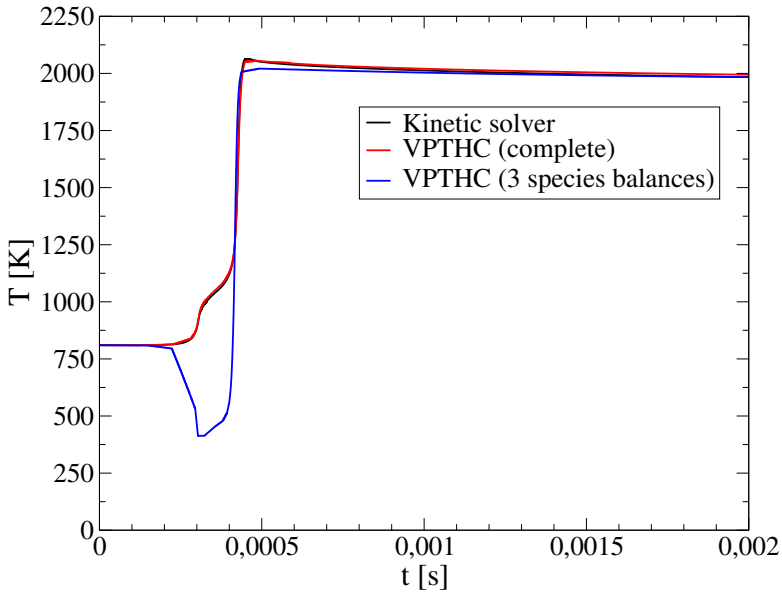

Figure 4.7: Temperature time-evolution in a constant pressure homogeneous reactor at 70 bar, with an initial temperature of 810 K and an initial fuel mass fraction of 0.14, for a solved chemistry (black), a classical 3 species balances closure (blue) and the proposed 4 species balances closure (red)

4.5 Validation of the tabulated chemistry approach

As explained in the introduction, the soot and VPTHC models are first compared to complex chemistry on a simplified model reactor called ECFM3Z-0D, which is implemented in the IFP-C3D code. This kind of reactor allows to use both the VPTHC tabulated model and a kinetic solver, which allows a direct comparison of both approaches. For the present calculations, a mechanism of 590 species and 3890 reactions taken from the Model Fuels Consortium (MFC) thermo-kinetic database [152] is used to build the VPTHC table and to run the detailed kinetic solver computations. The fuel considered for these calculations is a Diesel surrogate composed of 30% 1-Methylnaphthalene

and 70% Decane (in liquid volume) which is also used for the 3D RANS simulation in Section 4.7. The kinetic solver code coupled with IFP-C3D for these calculations comes from the IFP-Kinetics package [136] as the code used to build the look-up tables.

In the following section, the principle of ECFM3Z-0D reactors is described first. Then, a reference computation result of an ECFM3Z-0D reactor run with a detailed kinetic solver is given. Finally, ECFM3Z-0D reactors results obtained with the tabulated approach and the detailed kinetic solver are compared on various conditions.

4.5.1 ECFM3Z-0D reactors description

The global ECFM3Z-0D reactor is a variable volume reactor following piston motion equations. Initially, fuel and air are separated in their respective zones. At a chosen crank angle CA_{start}, the mixing begins. This crank angle corresponds to the beginning of injection in a real Diesel engine computation. The mass flux from zone A (pure air) to zone M (homogeneous combustion zone) is piloted by a time-scale τ_m^A which represents the macro-scale mixing of air with the reactive gaseous jet in a Diesel engine. In order to get a realistic fuel/air ratio in zone M during the mixing of zones A and F, the mixing rate τ_m^F of zone F is defined by fixing equivalence ratio Φ_M in zone M to an imposed value Φ_{force}, a free parameter of the reactor. This mixing is illustrated in Fig. 4.8. When the crank angle reaches CA_{start}, the ECFM3Z governing equations Eq. (4.34) and Eq. (4.35) become:

$$\widetilde{\dot{E}}_{Fu}^{F\to M} = \left(\frac{Y_{Fu}}{Y_{O_2}}\right)_{st} \Phi_{force} \widetilde{\dot{E}}_{O_2}^{A\to M} \tag{4.40}$$

$$\widetilde{\dot{E}}_{O_2}^{A\to M} = \frac{1}{\tau_m} \tilde{Y}_{O_2}^{A} \tag{4.41}$$

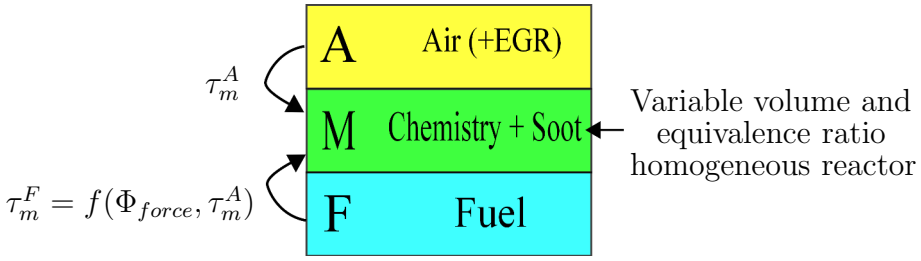

Figure 4.8: Scheme of ECFM3Z-0D reactors.

With this ECFM3Z-0D mixing model, region M can be seen as a variable-volume homogeneous reactor. The reactor composition evolution is illustrated in Fig. 4.9. It shows how air is transferred from zone A to zone M according to a constant time-scale τ_m^A. The unmixed O_2 (O_2 in zone A) decrease starts when the crank angle reaches $CA_{start} = -15$ CAD. Meanwhile, the fuel from zone F (unmixed) mixes in order to keep $\Phi_M = \Phi_{force} = 4.1$ as long as there is fuel in zone F. When the fuel contained in zone F is depleted, Φ_M decreases to the average equivalence ratio of the reactor here equal to 0.906 due to the mixing of O_2 from zone A. Mixed quantities of O_2 and fuel are limited by their consumption from combustion.

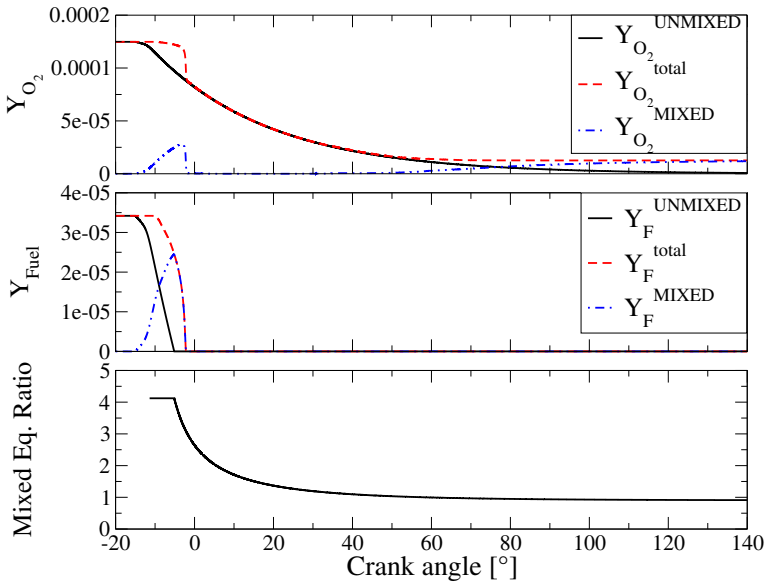

Figure 4.9: Evolution of species mass fraction and fuel/air equivalence ratio in zone M during an ECFM3Z-0D calculation. Mass fractions of O_2 (top), Fuel (middle) with unmixed region in black (solid line), region M in blue (dotted line), global in red(dashed line), and equivalence ratio of region M (bottom) for $CA_{start} = -15$ CAD, $\tau_m^A = 2.10^{-3}$ s, $\Phi_{force} = 4.123$ and an average equivalence ratio $\Phi = 0.906$.

4.5.2 ECFM3Z-0D coupled to a kinetic solver

The homogeneous kinetic solver of the IFP Kinetics library was introduced in zone M to describe chemical reactions [136]. This provides a reference solution which can be compared to the tabulated approach VPTHC.

The species mass fractions Y_k^M in zone M evolve in time due to the chemical source term $\dot{\omega}_k$ given by the kinetic solver and due to the introduction of fuel and air coming from zones A and F:

$$\frac{dY_F^M}{dt} = \dot{\omega}_F + \widetilde{\dot{E}}_{Fu}^{F\to M} \tag{4.42}$$

$$\frac{dY_{O_2}^M}{dt} = \dot{\omega}_{O_2} + \widetilde{\dot{E}}_{O_2}^{A\to M} \tag{4.43}$$

$$\frac{dY_k^M}{dt} = \dot{\omega}_k + \frac{Y_k^A}{Y_{O_2}^A}\widetilde{\dot{E}}_{O_2}^{A\to M} \quad \text{for } k \neq O_2, F \tag{4.44}$$

Like for a standard ECFM3Z computation, the average species mass fractions $\tilde{Y}_k$ are deduced from conditional mass fractions in zones A, F and M [146]. This allows to define the average species reaction rate and the energy source term in the sensible energy equation $\tilde{e}_s$. Finally, the average temperature $\tilde{T}$ is obtained by inversion of $\tilde{e}_s$.

Figure 4.10 presents the evolutions of fuel, oxygen, temperature and soot mass fraction in zone M for the case presented in Fig.4.9. Fuel and oxygen are mixed into zone M after the CA_{start} crank angle. Then, they are consumed when the conditions allowing auto-ignition are reached with an increase of temperature and a soot production peak. As the average mixture is lean ($\Phi = 0.902$), an

excess of oxygen is obtained at the end of the mixing process. This explains the partial oxidation of soot at the beginning of the expansion stroke. Due to this expansion, temperature decreases strongly which eventually leads to a freezing of all reactions, including soot oxidation.

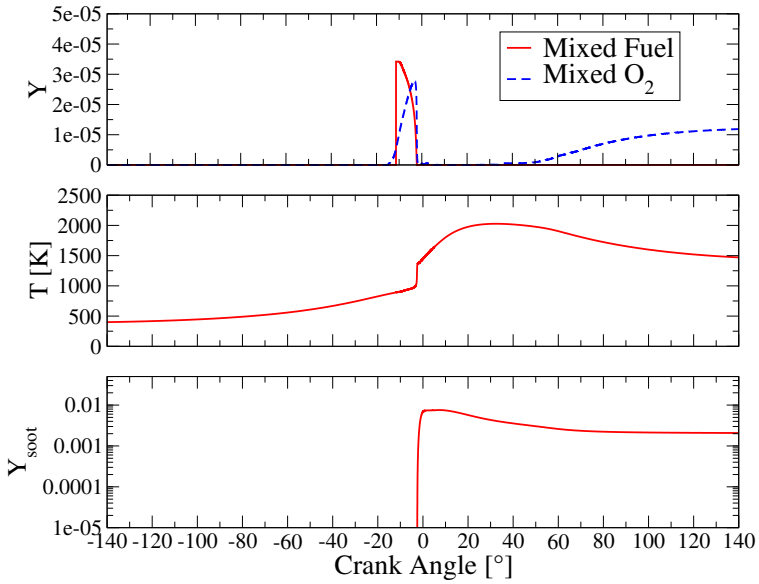

Figure 4.10: ECFM3Z-0D computation with the kinetic solver. Zone M fuel and oxygen mass fractions (top), temperature (middle) and soot mass fraction (bottom) evolutions using $CA_{start} = -15$ CAD, $\tau_m^A = 2.10^{-3}$ s, $\Phi_{force} = 4.123$ and an average equivalence ratio of 0.906.

4.5.3 Comparison between tabulated chemistry and kinetic solver

In order to compare results obtained with the tabulated approach and the detailed kinetic solver, four cases are presented in Tab.4.3, allowing three parametric studies. These calculations start at -140 CAD with an initial pressure of 2 bar and an initial temperature of 400 K and run to $+140$ CAD. More parameter variations (EGR, initial temperature and pressure, rpm) have also been tested with similar results (not presented here).

Case	τ_m $[s]$	Φ_{force}	average equivalence ratio
1 (ref)	2.10^{-3}	4.123	0.906
2	10^{-3}	4.123	0.906
3	2.10^{-3}	2.311	0.906
4	2.10^{-3}	4.123	1.151

Table 4.3: Conditions of the ECFM3Z-0D reactors studied for the parametric evaluation of VPTHC.

Pressure, temperature and soot mass fraction evolutions of the reference case 1 are given in Fig. 4.11. The VPTHC approach shows a very good agreement with the kinetic solver for the evolutions of temperature and pressure which confirms that tabulated chemistry can be used to represent auto-ignition in variable volume environment. Soot mass fraction evolution is also qualitatively well predicted by VPTHC. Quantitatively, VPTHC underpredicts soot mass fraction by

a factor two approximately. We consider this error as acceptable for two reasons at least. First, the model trajectory followed by VPTHC (constant pressure and then constant expansion rate) does not reproduce exactly the piston engine law followed by the kinetic solver. This induces small differences in minor species relevant to soot formation which have a large impact on the final soot yield. This error cannot be reduced as long as such a model trajectory is used. The solution would be otherwise to employ directly the kinetic solver with the inconvenience of a very high CPU cost. Secondly, as shown in the sectional soot model presentation, soot chemistry is still an open topic of research today with large uncertainties on reaction constants, especially concerning inception. In this context, a factor two of error added by the combustion model can be considered acceptable as the uncertainty on chemistry is at least of the same order of magnitude on minor species required for inception [77].

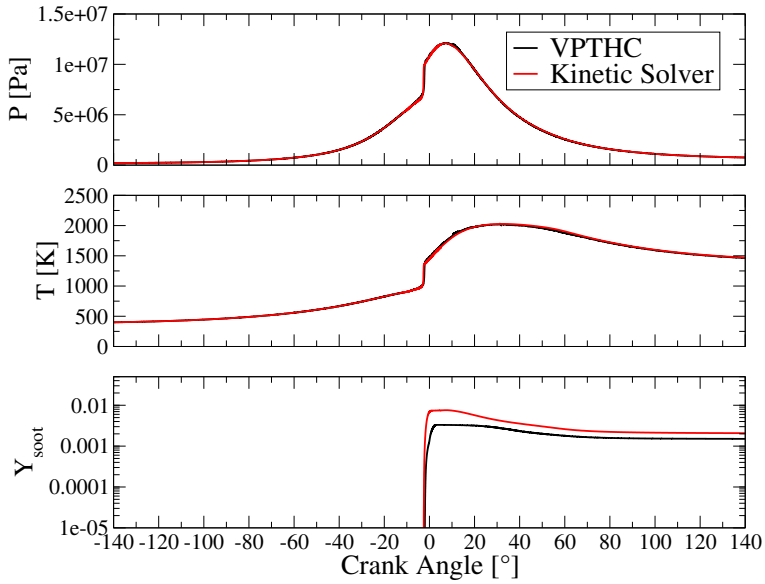

Figure 4.11: Pressure (top), temperature (middle) and soot mass fraction (bottom) evolutions on the reference ECFM3Z-0D reactor with VPTHC tabulated chemistry (black) and the kinetic solver (red) for the reference case.

Similar pressure and soot mass fraction evolutions have been computed for the three other test cases and are given in Fig. 4.12 and Fig. 4.13. The agreement between tabulated and kinetic solver chemistry is still good for pressure both for the auto-ignition delay and the maximum pressure. The gap observed on soot mass fraction evolutions is still acceptable for soot modeling for every case. Globally, soot sensitivity to parametric variations is well reproduced.

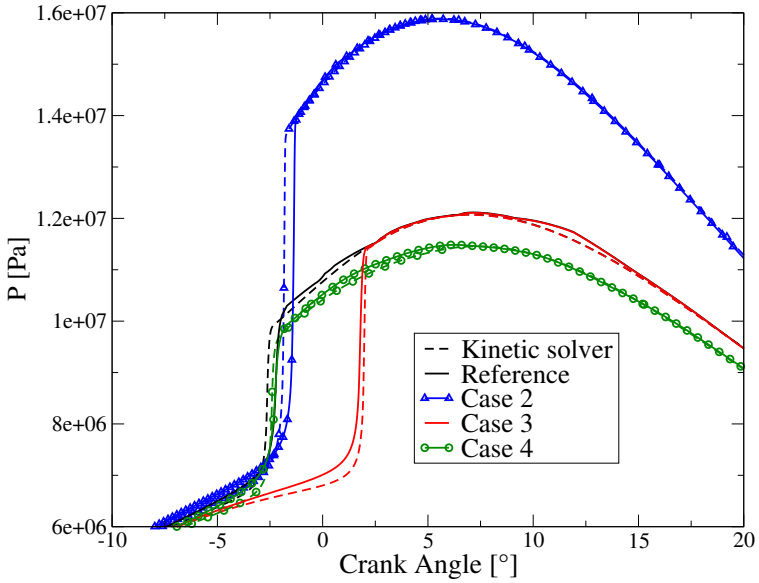

Figure 4.12: Pressure evolution for reference case (black), case 2 (τ_m^{input} variation, triangle symbols), case 3 (Φ_{force} variation, red) and case 4 (average equivalence ratio variation, circle symbols) using both the VPTHC approach (solid line) and the kinetic solver (dashed line).

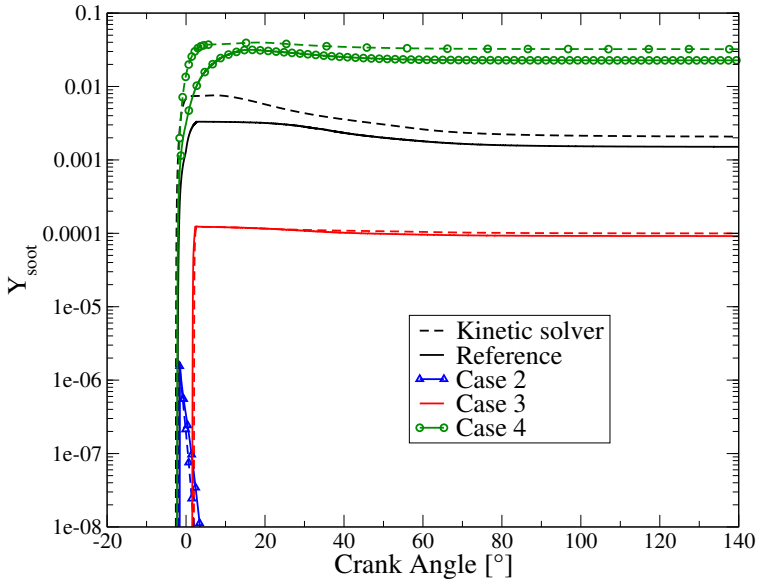

Figure 4.13: Soot mass fraction evolution for reference case (black), case 2 (τ_m^{input} variation, triangle symbols), case 3 (Φ_{force} variation, red) and case 4 (average equivalence ratio variation, circle symbols) using both the VPTHC approach (solid line) and the kinetic solver (dashed line).

Finally, the SNDF predicted by the VPTHC approach and the detailed kinetic solver have been compared. These results are shown in Fig. 4.14 for the reference case. The evolution of the SNDF is found consistent between both approaches. The peak location of the SNDF predicted with the VPTHC approach is slightly smaller than the one predicted using the detailed kinetic solver and the number density at the peak is similar for both cases. The large deviation at -2 CAD is easily explained by the fact that this angle is very close to the auto-ignition one. As auto-ignition starts at -2.7 CAD for the detailed kinetic solver and -2.3 CAD for VPTHC, the soot development at -2 CAD is very different in both simulations and only reflects the difference in auto-ignition delays between the two simulations.

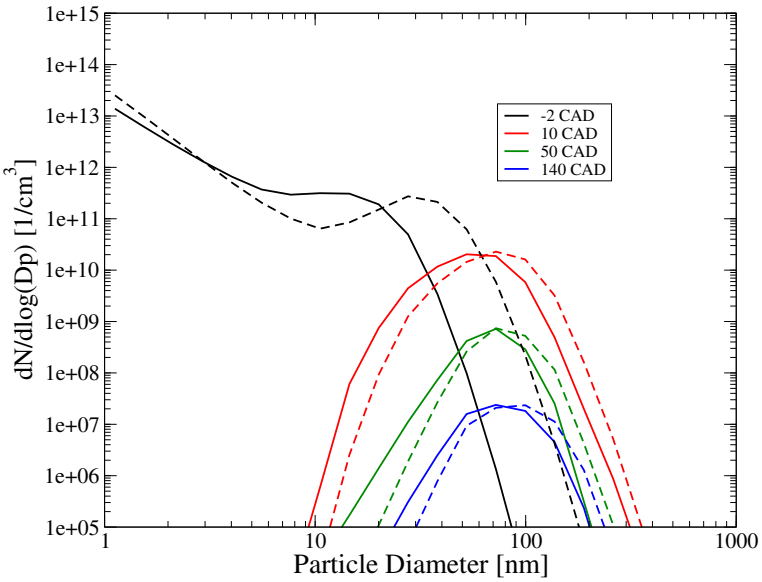

Figure 4.14: SNDF predicted by the VPTHC approach (solid line) and the detailed kinetic solver (dashed line) at the reference case for four crank angles : -2 CAD(black), 10 CAD (red), 50 CAD (green) and 140 CAD (blue)

4.6 Soot impact on gaseous composition

The main limit of this approach is the absence of a feedback from the solid soot phase to the gaseous phase. To address this issue, a possible solution is to include pyrene and acetylene consumption from the pyrene polymerization reaction (3.11) in the homogeneous reactors used to build the VPTHC look-up table. This reaction does not depend on the quantity of soot and is thus usable to represent this part of the gaseous species consumption in reactors which do not account for soot evolution as the ones used to build the VPTHC look-up table. On the contrary, the consumption of C_2H_2 by the HACA mechanism depends on soot mass and distribution, which makes its introduction in the look-up table generation impossible. We therefore propose here to address the impact of a feedback on pyrene only by comparing VPTHC results obtained with two different look-up tables: one with and the other without pyrene polymerization reaction (3.11). These results are presented in Fig. 4.15 for case 2. The decrease of the pyrene mass fraction, between the standard VPTHC model and the one using a modified look-up table including pyrene consumption, is similar to the one between the

kinetic solver simulations with and without feedback from the soot phase. This shows that this modification of the table generation succeeds in reproducing the impact of precursor consumption by the inception process. It also appears that the acetylene mass fraction is not influenced by this feedback in this case, even with a full feedback from the soot phase in the simulation run with a kinetic solver.

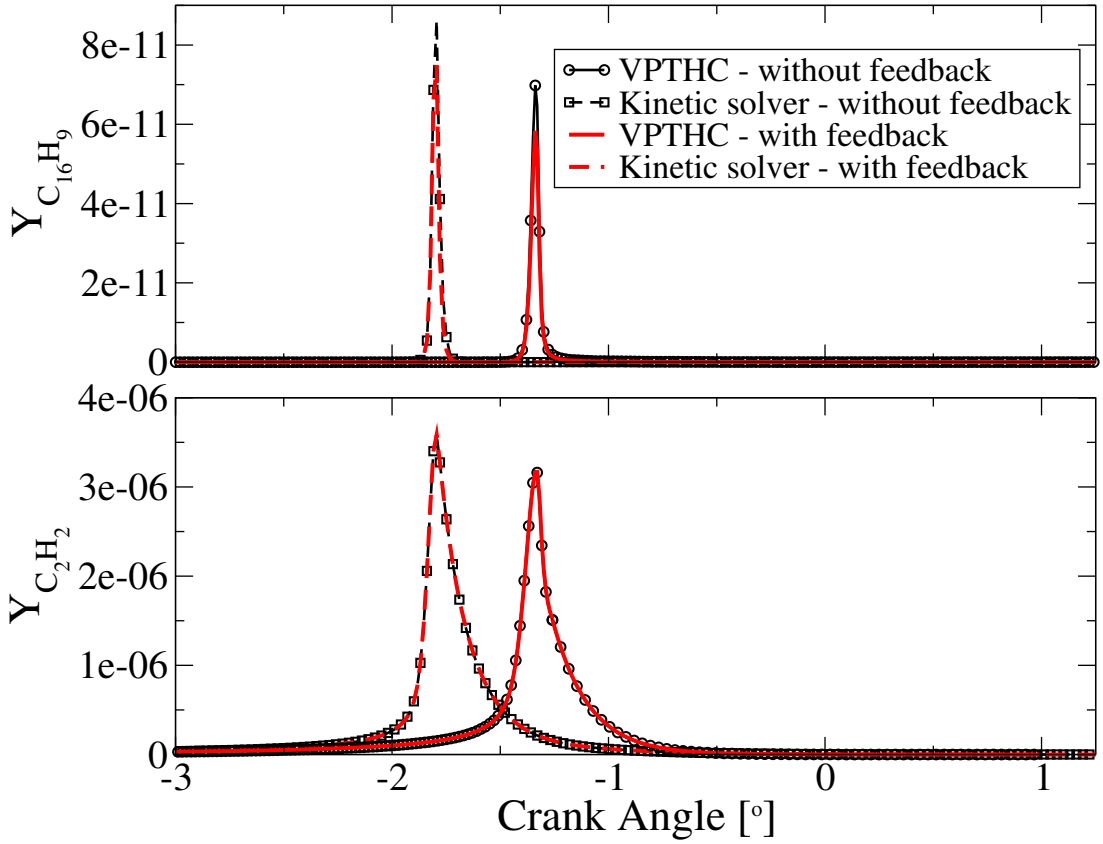

Figure 4.15: Pyrene (top) and acetylene (bottom) mass fraction evolutions for case 2 with the soot model coupled to the standard VPTHC model (black), a kinetic solver without feedback from the solid phase (black dashed lines), the VPTHC model including pyrene and acetylene consumption (red) and a kinetic solver with feedback from the solid phase (red dashed lines).

Similar results are obtained for the soot mass fraction evolution on the same case presented in Fig.4.16. As for the pyrene mass fraction, the decrease of the soot mass fraction between simulations with and without feedback is similar when using VPTHC or a kinetic solver. These first results show the potential of this method to include the effect of soot particles on the gaseous phase in simulations. It also underlines the dominance of the particle inception and condensation source terms over the surface growth due to the HACA mechanism in this case. Indeed, including the effect of particle inception and condensation over the gaseous phase in the tabulation approach allows to evaluate the decrease of soot production correctly. These results must be considered specific to this case and cannot be generalized at this point. To validate this modified table generation method, the impact of oxidation and surface growth on the gaseous phase should also be evaluated for various conditions. For this reason we preferred not to include this modified table generation in this study.

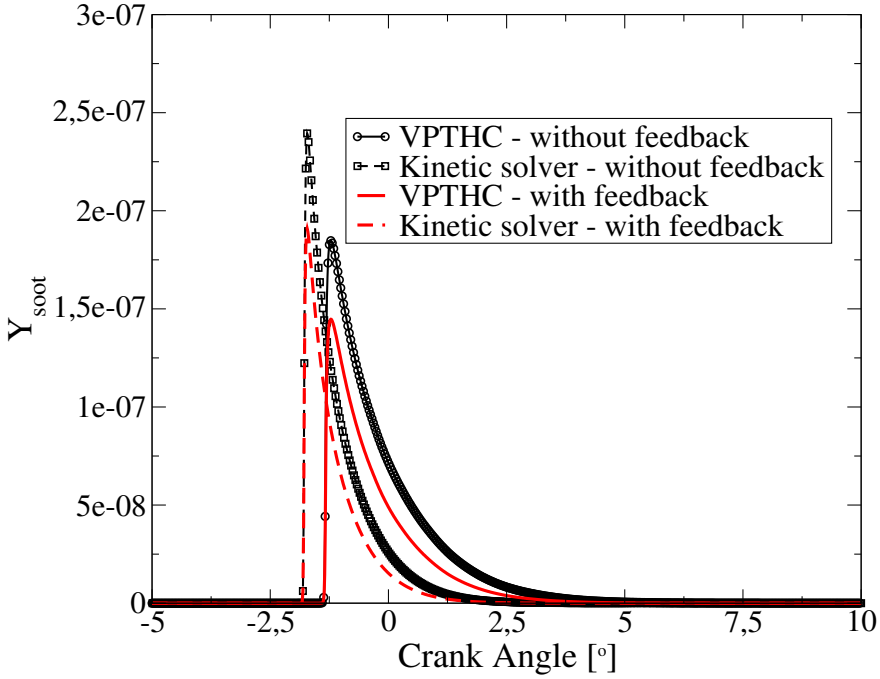

Figure 4.16: Soot mass fraction evolution for case 2 with the soot model coupled to the standard VPTHC model (black), a kinetic solver without feedback from the solid phase (black dashed lines), the VPTHC model including pyrene and acetylene consumption (red) and a kinetic solver with feedback from the solid phase (red dashed lines).

The composition of the fuel which includes aromatic species might favor particle inception and condensation compared to fuels composed of linear alkanes such as n-heptane. Finally, neglecting the feedback of soot particles on the gaseous phase leads to an error of approximatively 25 % at the soot peak on the present homogeneous case. This error is considered acceptable with respect to the current accuracy of soot models. Although these effects were neglected in the present study, very encouraging results were obtained on Diesel engine operating points, as seen in the next Section.

4.7 Evaluation on a Diesel engine

In order to evaluate the combustion and soot models, a complete database has been built at IFPEN for a commercial and a surrogate Diesel fuel [147]. This surrogate fuel is the one presented in the previous section. Using both fuels allows:

- to assess experimentally the difference in soot yield and SNDF between a real Diesel fuel and a surrogate;
- to compare experiments and simulations using exactly the same surrogate fuel, thus avoiding the error caused by the approximation of the real Diesel fuel by a surrogate.

The surrogate Diesel fuel is first validated against the commercial Diesel fuel for the pressure evolutions, soot yields and SNDF at exhaust. Then, a detailed analysis of the simulations is presented. It focuses on the time-evolution of soot distribution and source terms allowing a better understanding of the model behavior in a real engine application.

4.7.1 Numerical set-up

Engine tests are performed on a single-cylinder Diesel engine of 500 cm^3 with a compression ratio of 16:1. A fast analyzer DMS 500 from Cambustion [153] is used to perform both particle size and particle number measurements. The database includes two reference operating points from which variations of Exhaust Gas Recirculation (EGR) rate (from 0% to 30%), injection duration (t_{inj}), injection pressure (P_{inj}) have been performed, both for the standard and the surrogate Diesel fuel. The two reference operating points and all variations are reported in Tab. 4.4. The injection pressure variation is performed around the reference case at 2200 rpm at partial load. It allows addressing the effect of the spray characteristics on soot production. It is realized at constant equivalence ratio, thus the injection duration is changed to keep the fuel injected mass constant between the three cases. The EGR variation is also performed on the same reference case. It isolates the effect of the EGR concentration on the soot yield and SNDF at exhaust for a constant mass of injected fuel. Finally, the last variation concerns the equivalence ratio around the full load 4000 rpm reference case.

The simulations are performed with the IFP-C3D RANS code [148, 149], a fully parallelized code developed by IFP Energies Nouvelles for simulating compressible reactive flows. It solves the Navier Stokes equations using the Arbitrary Lagrangian Eulerian formalism as described by Bohbot *et al.* [148]. It integrates Lagrangian spray and liquid film models [154, 155] and a renormalization group (RNG) $k-\epsilon$ model for turbulence description [156]. A turbulent wall law and a heat transfer law are also required. Kays and Crawford law is used as proposed by Angelberger *et al.* [157]. Moving-mesh strategies are integrated with all physical models needed to simulate internal combustion engines [148, 149].

Before setting the initial conditions for the RANS simulations, the experimental data have been verified with the set of tools presented in Martinez *et al.* [95]. The 3-D simulations start after intake valve closing (IVC) and stop just before the exhaust valve opening (EVO) so that the combustion chamber is closed during the computation. The field at 160 CAD before TDC is initiated with the experimental pressure, recalculated temperature and species concentrations. The initial swirl number is set to 1.9 based on previous studies on this engine (not presented here). The gas composition depends on the equivalence ratio, the internal gas recirculation (IGR) rate, the EGR rate and the air mass flow rate. The IGR mass ratio is set to 5% of the trapped mass. Equivalence

Case	Variation	Speed	IMEP	EGR	t_{inj}	P_{inj}	Equivalence ratio	Legend
1	Reference	2200 rpm	8.29 bar	0%	636 μs	800 bar	0.48	■
2	EGR rate	-	8.23 bar	10%	636 μs	800 bar	0.53	●
3	EGR rate	-	8.14 bar	20%	636 μs	800 bar	0.58	◀
4	EGR rate	-	7.99 bar	30%	636 μs	800 bar	0.65	★
5	P_{inj}	-	8.18 bar	0%	685 μs	700 bar	0.48	▲
6	P_{inj}	-	8.36 bar	0%	602 μs	900 bar	0.48	◆
7	Reference	4000 rpm	22.21 bar	0%	1300 μs	1600 bar	0.85	◆
8	T_{inj}	-	21.58 bar	-	1226 μs	-	0.80	■
9	T_{inj}	-	20.83 bar	-	1100 μs	-	0.75	▲
10	T_{inj}	-	19.95 bar	-	1020 μs	-	0.70	●
11	T_{inj}	-	18.96 bar	-	925 μs	-	0.65	◀

Table 4.4: Main characteristics of the Diesel operating points simulated.

ratio and mass flow rates are directly taken from experimental measurements. Only the following species are present at the beginning of the simulation: O_2, N_2, CO_2 and H_2O. Their mass fractions are determined assuming a perfect combustion at the selected equivalence ratio. The injection rates are defined with a linear increase during 100 μs before a constant phase and finally a linear decrease during 115 μs. The linear evolutions durations are based on previous studies on this engine (not presented here). The constant phase duration and its amplitude are set for the total injection duration and injected mass to be equal to the experimental ones given in Tab.4.4.

Wedge type calculations are performed (wedge is 51.43 degrees wide corresponding to a 7 holes injector nozzle) thanks to the internal automatic mesh generation tool that uses 11 meshes with a characteristic mesh size of 0.75mm. The number of nodes is 112500 at IVC (103377 cells) and 15408 (13260 cells) at TDC. An example of mesh used is given in Fig. 4.17.

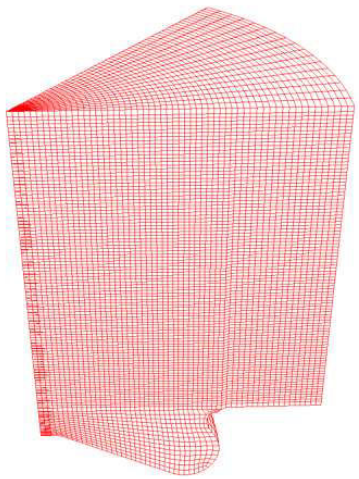

Figure 4.17: Visualization of the computational mesh at 30 CAD

The same numerical and modeling parameters have been used for all points allowing to consider these calculations as real blind tests to evaluate the model predictivity. These calculations have been run on 8 processors and were 4 hours to 6 hours long.

4.7.2 Results

4.7.2.a Surrogate validation

A comparison of the experimental soot emissions obtained with the surrogate and commercial Diesel fuel is given in Fig. 4.18 using the Filter Smoke Number (FSN) as an estimator of the emitted soot mass. It shows that the surrogate offers a good estimation of the soot emissions. In addition, it has been verified that this surrogate gives pressure evolutions very close to those of the Diesel fuel (not shown here). Finally, the soot distribution at exhaust is very similar between the surrogate and the commercial Diesel fuel as shown further in this section. In conclusion, these results show that this surrogate composition constitutes a good approximation of a commercial Diesel fuel both in terms of combustion properties (ignition delay and rate of heat release) and pollutants (soot).

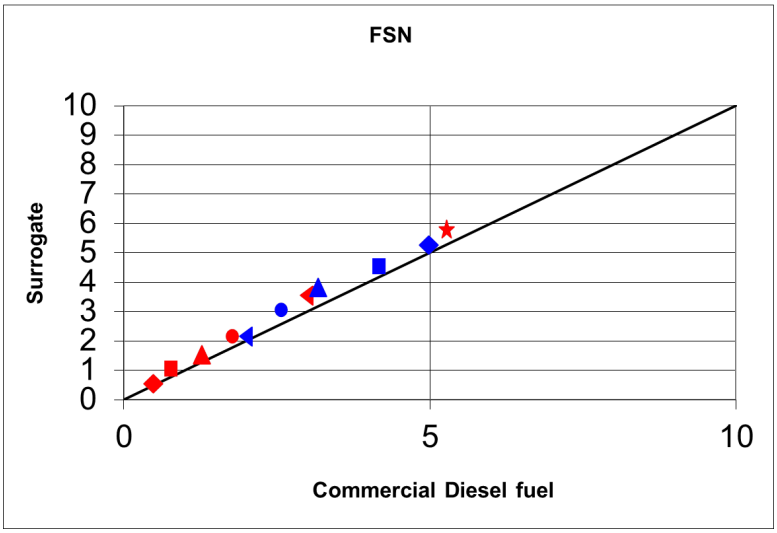

Figure 4.18: Comparison of FSN obtained with the surrogate and commercial fuel. See Tab. 4.4 for the legend.

4.7.2.b Mean cylinder pressure

Mean cylinder pressure results for some partial load operating points (cases 1 to 3) are presented in Fig. 4.19 and compared with the surrogate fuel measurements. The results show a good prediction of the pressure evolution for cases 1 to 3 (0% to 20% EGR) with a slight overestimation of the maximum pressure but a good agreement between experiments and simulations for the crank angle of maximum pressure. The apparent Heat Release Rate (HRR) is also well reproduced with less than 5% of error on the integral of the apparent heat release rate between the measurements and the simulations. The normalized apparent heat release rates are given in Fig. 4.20. The start of HRR and the peak of HRR have been used to define the auto-ignition delay. These delays are presented in Fig. 4.21 for all points. This figure shows that the auto-ignition delay defined as the start of

HRR is very well captured by the simulations, while the one defined by the peak value shows an over-prediction close to 2.5 CAD in all cases. The shape and amplitude of the predicted HRR are in good overall agreement with the experiment.

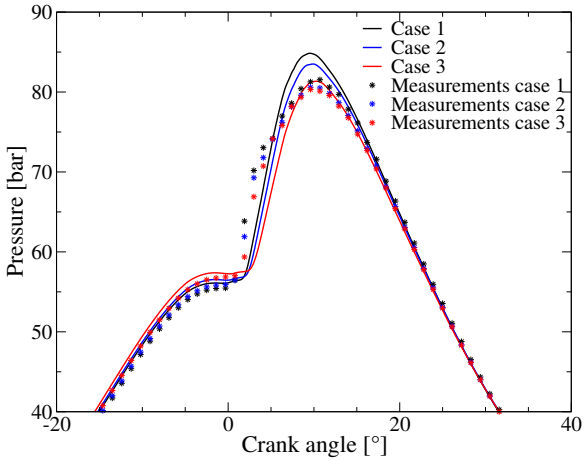

Figure 4.19: Mean cylinder pressure evolutions of operating cases at 2200 rpm for reference (black), 10% EGR (blue) and 20% EGR (red) operating points (cases 1, 2 and 3 respectively). Solid line: soot model. Symbols: measurements with surrogate fuel.

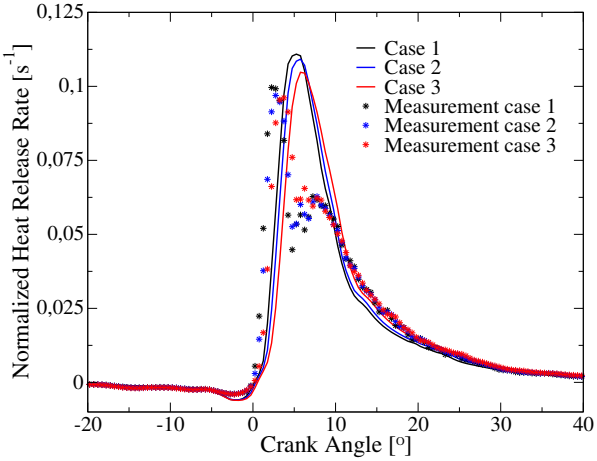

Figure 4.20: Normalized Heat Release Rate evolutions of operating cases at 2200 rpm for reference (black), 10% EGR (blue) and 20% EGR (red) operating points (cases 1, 2 and 3 respectively). Solid line: soot model. Symbols: measurements with surrogate fuel.

It can though be noticed that the initial premixed burn phase is under-predicted by the model leading to a smoother increase of the HRR at first. As a consequence, the experimental decrease of the HRR after the premixed burn phase is not captured by the simulations. This difference was also observed with the ECFM3Z simulations of Martinez *et al.* [95]. The predicted peak HRR auto-ignition delay is also 2.5 CAD late compared to the measured one for case 4 with the highest EGR rate as illustrated with the normalized apparent Heat Release Rates of cases 1 and 4 in Fig. 4.22.

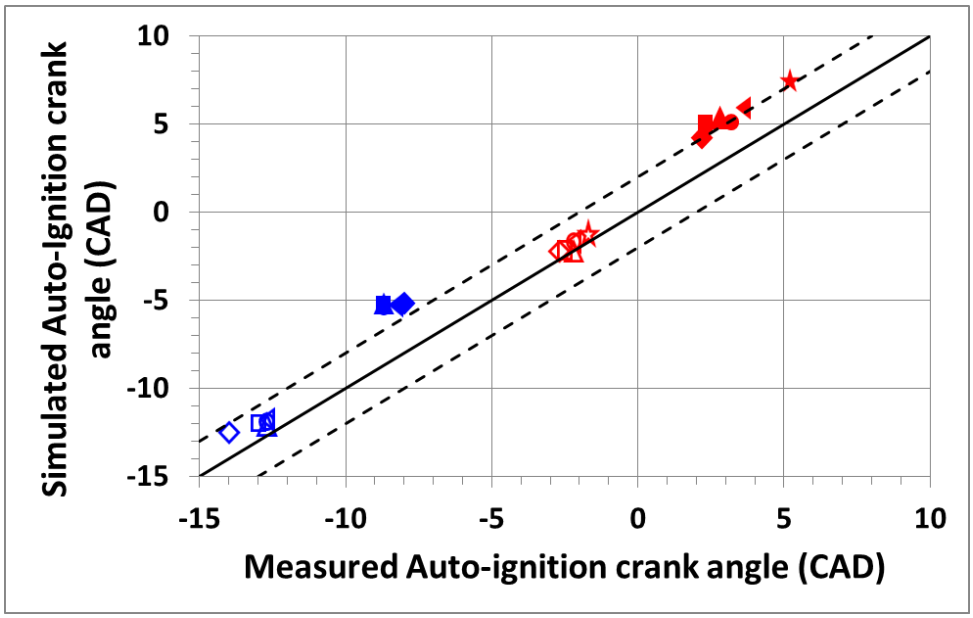

Figure 4.21: Comparison of the experimental and simulated auto-ignition crank angle (CAD, dashed line: +2 CAD and −2 CAD). See Tab. 4.4 for the legend, full symbol represent peak HRR delays and blank symbol represent start of HRR delays.

Again, the integral of the apparent Heat Release Rate is well reproduced with less than 5% of error. However, the error on the auto-ignition delay combined to a later ignition in case 4 leads to a slower pressure increase and a larger error on the crank angle of maximum pressure as illustrated by the mean cylinder pressure evolution of cases 1 and 4 in Fig. 4.23.

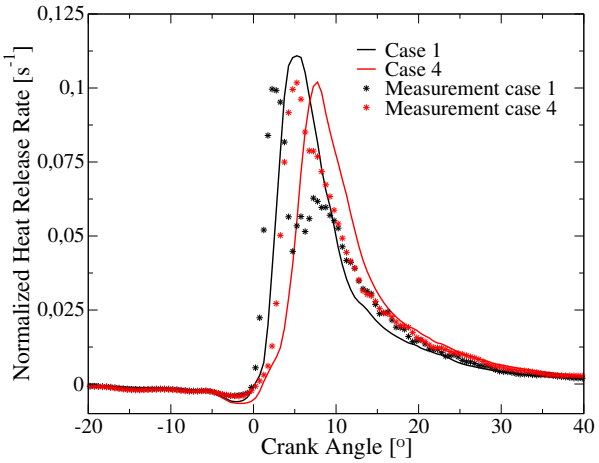

Figure 4.22: Normalized Heat Release Rate evolutions of operating cases at 2200 rpm for reference (black) and 30% EGR (red) operating points (cases 1 and 4 respectively). Solid line: soot model. Symbols: measurements with surrogate fuel.

The over-prediction of the auto-ignition delay based on the HRR peak for all cases can be

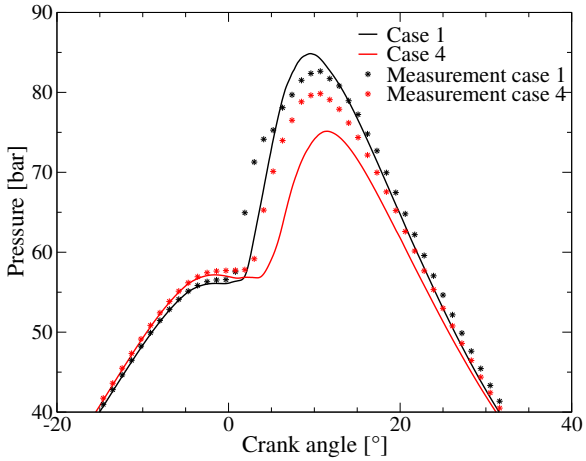

Figure 4.23: Mean cylinder pressure evolutions of operating cases at 2200 rpm for reference (black) and 30% EGR (red) operating points (cases 1 and 4 respectively). Solid line: soot model. Symbols: measurements with surrogate fuel.

explained by many causes. To our opinion, the most important one is the error on the complex chemistry mechanism, as evidenced by the large variability of the auto-ignition delay and auto-ignition reaction rate between different mechanisms as evidenced by the results obtained at ECN for dodecane [158]. Besides, the kinetic scheme used to generate the look-up table, as all schemes proposed for this fuel composition to our knowledge, has not been validated by its authors at the high EGR rate, pressure and temperature characteristic of this operating point. Then the error on spray modeling and turbulent mixing cannot be assumed negligible. It directly impacts the temperature and mixture fraction in the reactive zone and consequently the auto-ignition delay. It also impacts the amount of fresh gases that undergo the initial premixed burn phase, which directly pilots the amplitude of the initial HRR. An experimental engine characterization of the spray and mixing was not possible in the metal engine used in these experiments. It was therefore not possible to assess the model prediction in this respect. Another error is the absence of strain effect in the ECFM3Z model. As illustrated in Michel *et al.* [159], the absence of scalar dissipation in mixture fraction space on an auto-igniting mixing layer leads to a restricted auto-ignition region close to the most reactive mixture fraction. As ECFM3Z does not include scalar dissipation, this finding can explain the fact that the amount of fresh gases undergoing the initial premixed-burn is under-predicted with ECFM3Z compared to the experiment. Finally, the error cause by the EGR rate composition in the homogeneous reactors used to generate the look-up table might also play a role, but to a lesser extent as illustrated by the experiments of Colban *et al.* [160] and Kashdan and Thirouard [161].

Cases 5 to 6 represent a variation in injection pressure for 2200 rpm partial load operating points and cases 7 to 11 correspond an injection duration variation for 4000 rpm full load operating points. The simulations of these cases also show a good prediction of the auto-ignition delay, which is presented in Fig. 4.21, and a good estimation of the maximum pressure (not presented here).

4.7.2.c In-cylinder soot fields

Global evolutions. Figure 4.24 shows soot mass fraction fields in the vertical plane containing the spray axis. Four soot diameters are represented (1 nm, 20 nm, 100 nm and 260 nm) along with the fields of the conditional fuel/air equivalence in region M and mean temperature. The first crank angle shown in Fig. 4.24 is 0 CAD since it is the first angle at which a notable amount of 100 nm particles has been created.

At 10 CAD, all soot formation mechanisms are active as illustrated with the 2D fields of the soot mass fraction source terms in Fig. 4.25. Coagulation is not plotted since its sum over all sections is null. Particle inception and condensation add carbon mass in the high equivalence ratio area around the spray where the equivalence ratio is larger than two approximately. At the same time, in a larger zone surrounding the spray and where temperature is still larger than 1700 K and the equivalence ratio is lower than 1.5, oxidation reduces the amount of soot and limits its diffusion in the combustion chamber. The surface growth source term is spread in a wider area around the spray than particle inception and condensation because it is based on acetylene which is a species more distributed in the combustion chamber than the soot precursor. As shown in Fig. 4.24, 100 nm diameter particles are present in these oxidazing areas but not 1 nm and 20 nm diameter ones because these smaller particles are created next to the spray and are going to grow by condensation, coagulation and surface growth as they move away from it.

After 35 CAD in the expansion phase, 1 nm and 20 nm diameter particles are no more present close to the axis of the spray. This is due to the fact that fuel oxidation being almost finished in this area, the inception reaction rate becomes null. Particles created previously have undergone oxidation and coagulation, and have been convected outside the axis of the spray by the swirl motion. Fig. 4.26 presents the different soot source terms at 35 CAD ATDC. Soot mass is still created by surface growth but it is also limited by oxidation in the high temperature areas where soot already exists and surface chemistry is still active. The fields corresponding to diameters of 100 nm and 260 nm at 35 CAD and 57 CAD in Fig. 4.24 show large amounts of soot in rich areas with lower temperature and less soot in the stoichiometric or lean areas with the highest temperature where the conditions are favorable to oxidation. As mentioned previously, particle inception and condensation are null in the 2D views of Fig. 4.26 but these phenomena still exist in other areas of the combustion chamber at 35 CAD. This last point also explains the presence of some small particles at 57 CAD.

The mean source terms evolutions are depicted in Fig. 4.27 for the reference 4000 rpm case (case 7). These evolutions split soot formation and evolution process into three main steps:

- First, the solid phase evolution is triggered by a large amount of small particles formed during the ignition from -10 CAD and -5 CAD.
- Then, a transition phase occurs with a competition between the mass addition from precursors (particle inception and condensation) in rich areas and the oxidation of particles which have been transported to leaner areas as illustrated from -5 CAD and 30 CAD. This behavior is also illustrated in Fig. 4.25.
- Finally, after 30 CAD, the soot production source terms vanish as the combustion ends. Oxidation source term also decreases with the temperature decrease due to the expansion, even if, as illustrated in Fig. 4.26, temperature is still high enough in some areas at 35 CAD to oxidize particles. Once the temperature is too low to allow oxidation, the SNDF evolution is only caused by coagulation.

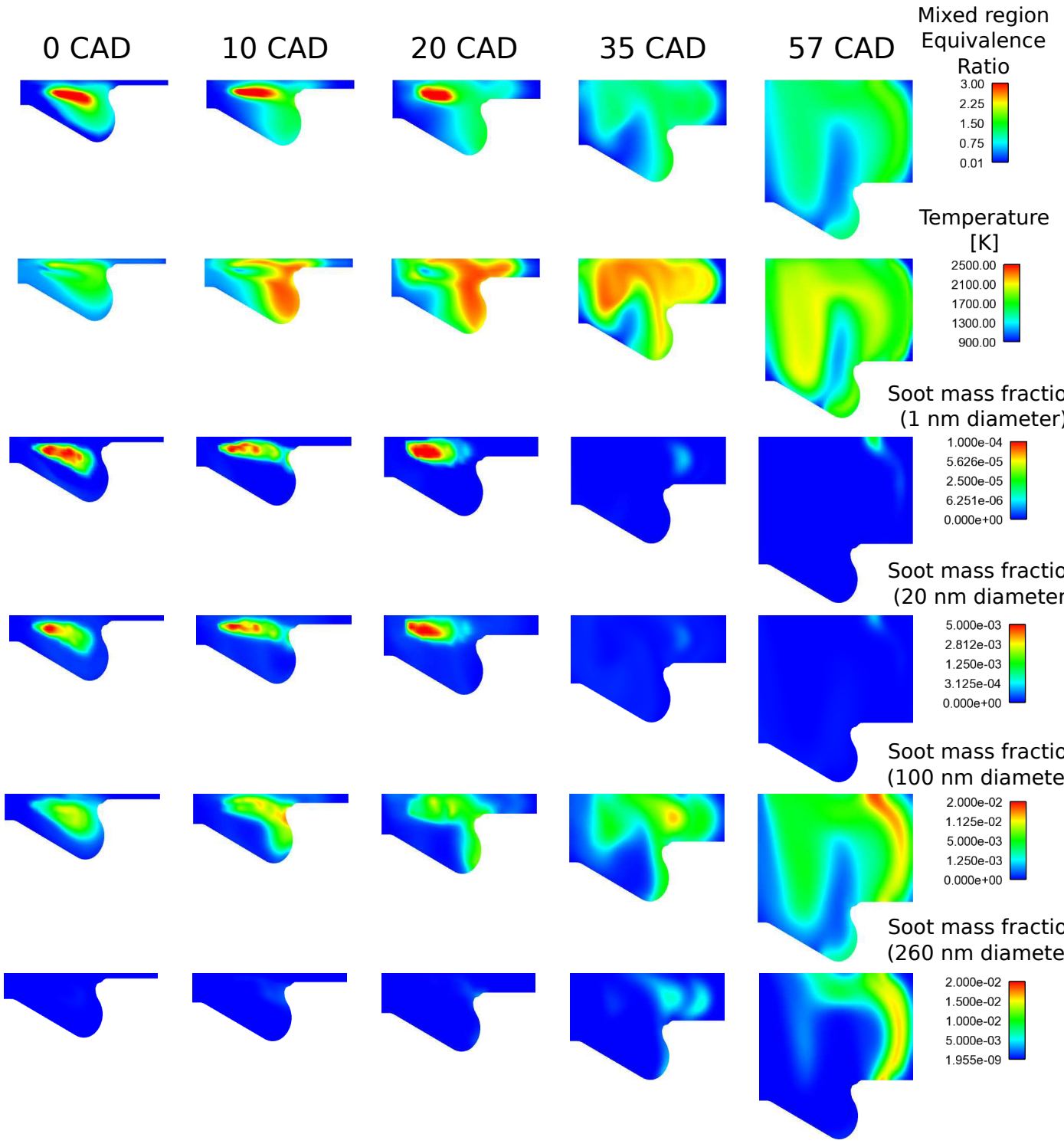

Figure 4.24: 2D fields in the vertical plane containing the spray axis for the reference 4000 rpm case (case 7). From top to bottom : fields of mixed region equivalence ratio, temperature and soot mass fraction of four different diameters (1 nm, 20 nm, 100 nm and 260 nm) at five different crank angles (from left to right, 0 CAD, 10 CAD, 20 CAD, 35 CAD and 57 CAD).

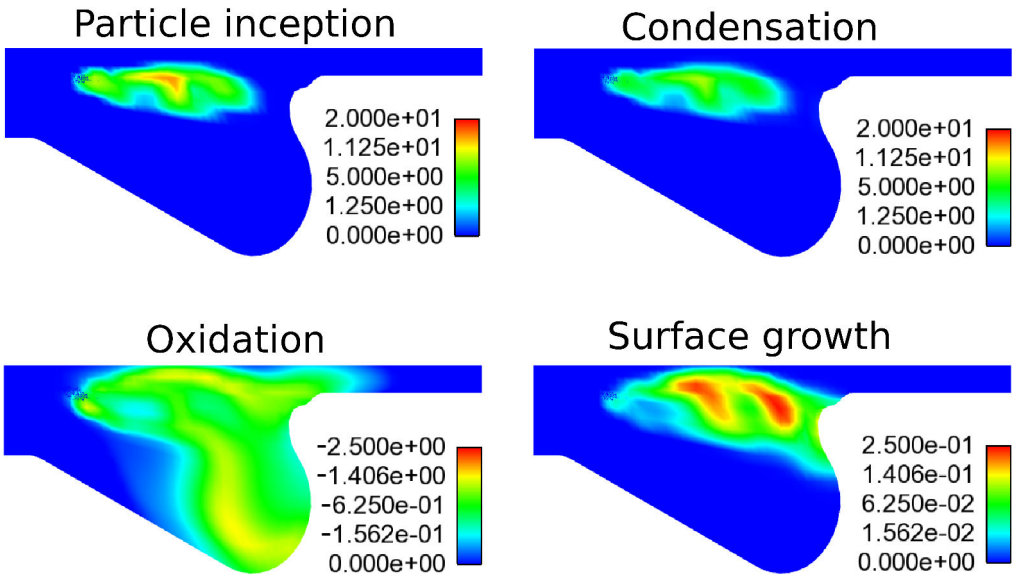

Figure 4.25: 2D fields in the vertical plane containing the spray axis for the reference 4000 rpm case (case 7) at 10 CAD. Soot mass fraction source terms (s^{-1}) for all sections: particle inception (top left), condensation (top right), oxidation (bottom left), surface growth (bottom right).

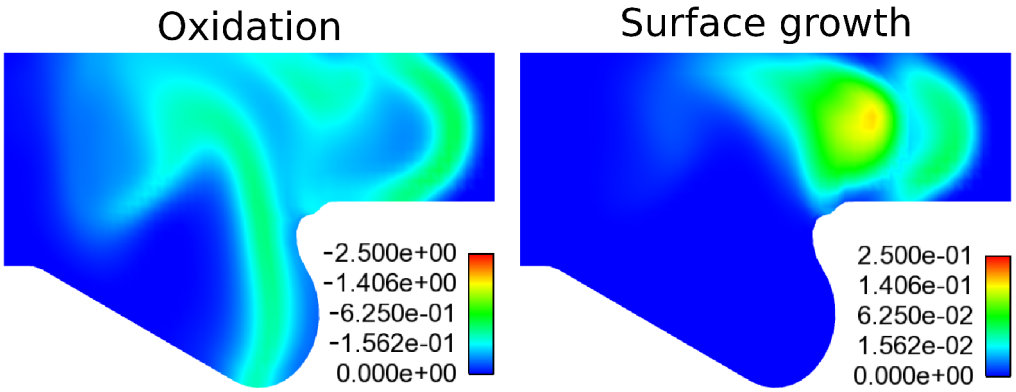

Figure 4.26: 2D fields in the vertical plane containing the spray axis for the reference 4000 rpm case (case 7) at 35 CAD. Soot mass fraction source terms (s^{-1}) for all sections: oxidation (left), surface growth (right).

Relative locations of species and soot particles. The location of the more important species involved in soot formation and oxidation (pyrene, acetylene and hydroxyl) is shown in Fig. 4.28. Carbon based species (pyrene and acetylene) are located in regions surrounding the spray initially. The pyrene existence region is less spread than the acetylene one. These regions are then convected by the swirl in the cylinder as illustrated in Fig. 4.28 with iso-surfaces from 10 CAD to 35 CAD. Hydroxyl is located around the rich regions indicated by pyrene and acetylene. It exists in the regions combining high temperatures with sufficiently oxidizing conditions.

The dispersed soot phase interacts with this gaseous composition and its location is very similar as illustrated in Fig. 4.29. The particle inception location follows the pyrene one because pyrene

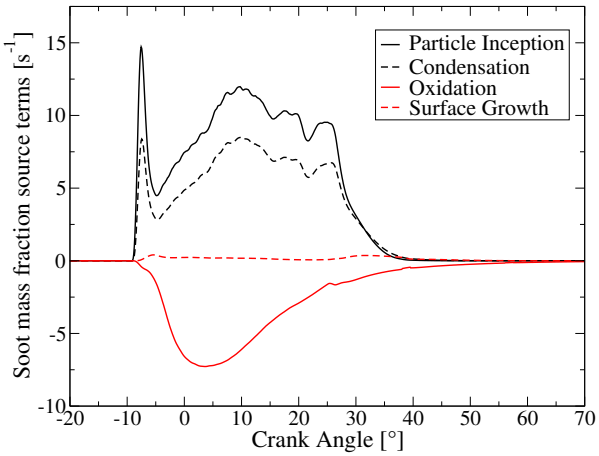

Figure 4.27: Global soot mass fraction source terms (s^{-1}) for the reference 4000 rpm case (case 7): particle inception (solid, black), condensation (dashed, black), oxidation (solid, red), surface growth (dashed, red).

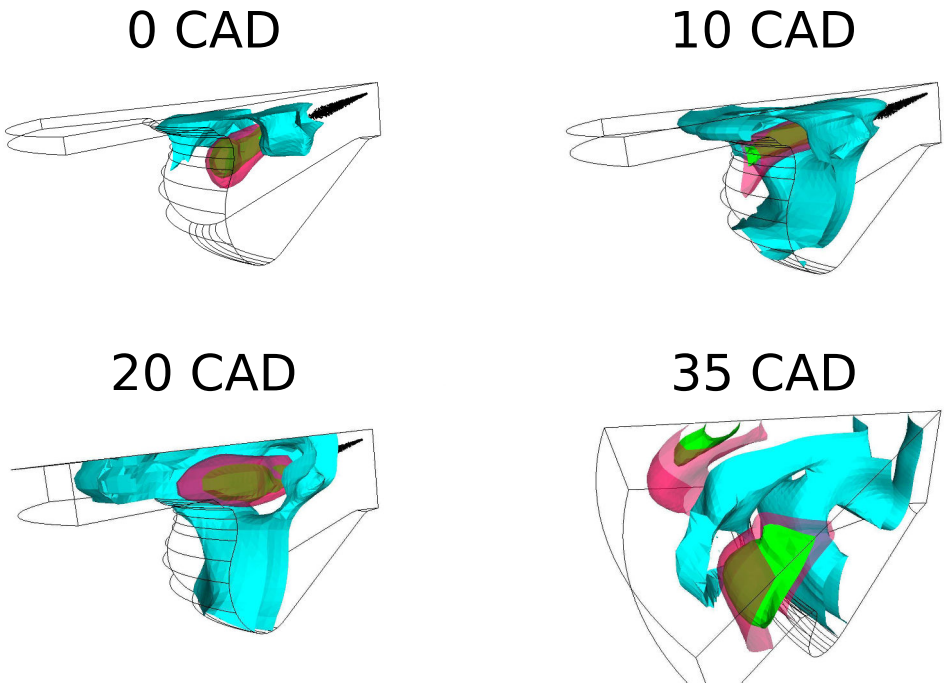

Figure 4.28: Iso-surfaces taken at the half of the value range for pyrene (green), acetylene (pink) and hydroxyl (blue) mass fractions at four different crank angles (0 CAD, 10 CAD, 20 CAD and 35 CAD)

is limiting reactant in its reaction with acetylene leading to particle inception. The soot volume fraction appears to be further to the spray than the region where particle inception occurs. This illustrate the ability of the model to reproduce a growth of soot in a reactive flow with particles

convected during their growth. Moreover, an oxidation region surrounds and limits the expansion of the region where soot particles are.

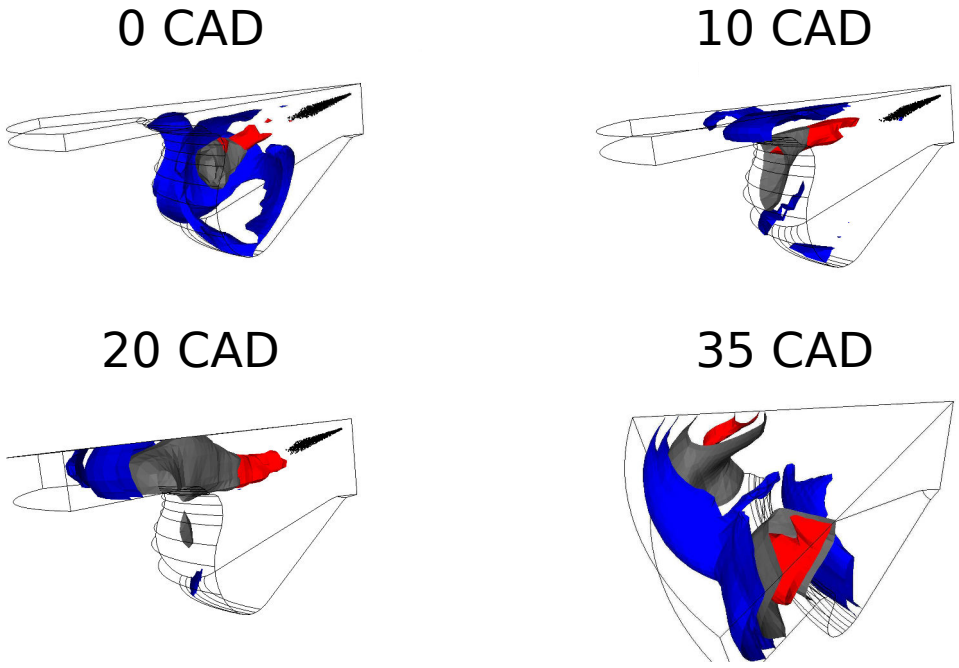

Figure 4.29: Iso-surfaces taken at the half of the value range for particle inception (red) and oxidation (blue) source terms and soot volume fraction (grey) at four different crank angles (0 CAD, 10 CAD, 20 CAD and 35 CAD)

Finally, the growth of soot particles within time and space is illustrated with iso-surface of different particles sizes mass fraction in Fig. 4.30. At 0 CAD, the structure can be seen clearly with the smallest particles next to the spray and the particles being further and further from the spray as they grow before meeting the high oxidation reaction rate region. At contact between the particles and the cylinder walls is predicted at 10 CAD. It results from the same contact of the carbon species and the cylinder wall at the same time. However, interactions between the soot dispersed phase and walls is not yet taken into account in this model. After 20 CAD, a new behavior appears for large particles. Indeed, the 100 nm particles high density region (inside the volume limited by the iso-surface) is further from the spray than the one of 260 nm particles. It illustrates a particle size decrease predicted by the model along the trajectory followed by soot particles.

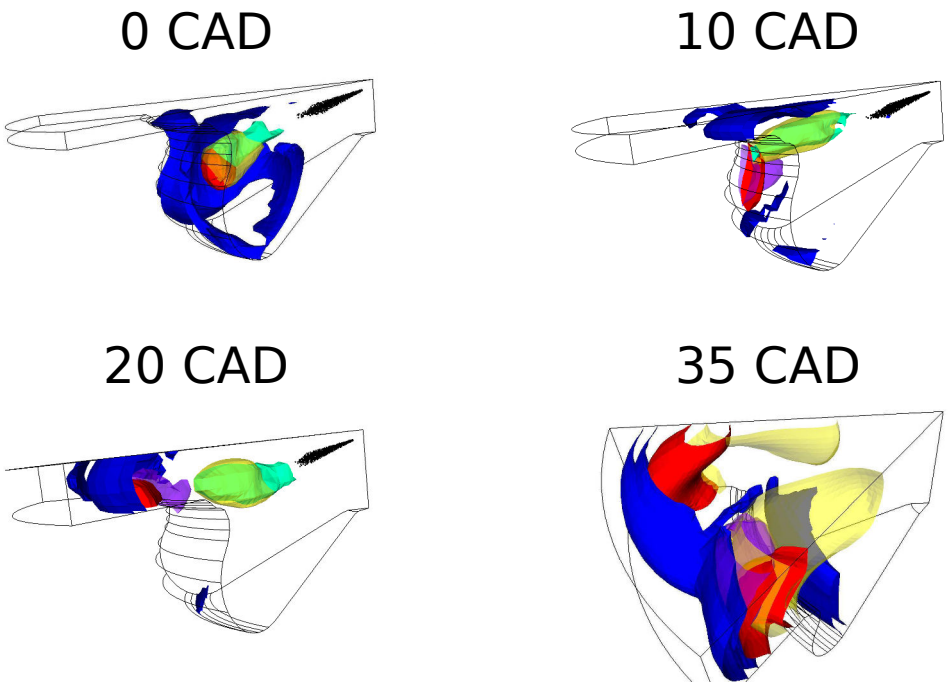

Figure 4.30: Iso-surfaces taken at the half of the value range for the oxidation source term (blue) and the mass fractions of particles diameters 1 nm (light blue), 20 nm (yellow), 100 nm (red) and 260 nm (purple) at four different crank angles (0 CAD, 10 CAD, 20 CAD and 35 CAD)

4.7.2.d Soot model validation

In order to validate the soot model, a comparison of experimental (with surrogate fuel) and numerical soot yield at EVO is first presented along with the predicted time-evolution of the soot mass in the cylinder. Then, the numerical and experimental PSDF at EVO are compared.

Soot yield. The simulation results of soot emissions are presented in Fig. 4.31 and compared to the measurements. These results show a good agreement with the experiments. Except for case 6, all calculations predict the total mass with a relative error within -50% and $+100\%$. The chosen validation interval, of $+100\%/-50\%$ is a common target used by engine manufacturers in the field of soot modeling on piston engines. The variations of soot emissions with the injection duration (blue symbols, cases 7 to 11) and with the EGR (red symbol, cases 1 to 4) are well predicted. For partial load cases, the sensitivity to the injection pressure (red symbols, cases 1, 5 and 6) is underpredicted. This could be explained by the fact that the soot model relies on species and temperature given by the spray, evaporation, mixing and combustion models which do not represent the influence of the injection pressure with a sufficient accuracy.

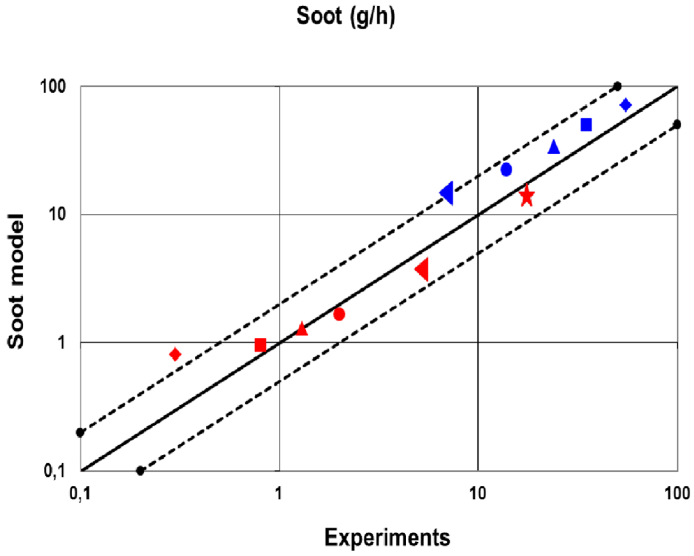

Figure 4.31: Comparison of the experimental and simulated soot emissions rate (g/h, dashed line: +100% and -50%). See Tab. 4.4 for the legend.

The time-evolutions of the soot mass predicted by the sectional soot model (SSM) are shown in Fig. 4.32 for cases 1, 7 and 11. The time-evolution of soot mass for case 1 only shows a first formation phase from ignition at 1.5 CAD to 9 CAD after TDC before an oxidation phase leading to the stabilized soot mass after 50 CAD after TDC. The soot mass evolutions are different for cases 7 and 11. The longer injection durations required to reach higher equivalence ratios (respectively 0.85 and 0.65 for cases 7 and 11) lead to a second phase of formation after the first soot production phase due to the premixed auto-ignition. The differences in injection durations and injected fuel masses between cases 7 and 11 induce the difference of duration of the second phase of soot formation. The soot formation being longer and the rotating speed of the engine being faster, the soot oxidation is still effective at the EVO in case 7.

Figure 4.33 shows the results obtained for the same cases with the Phenomenological Soot Kinet-

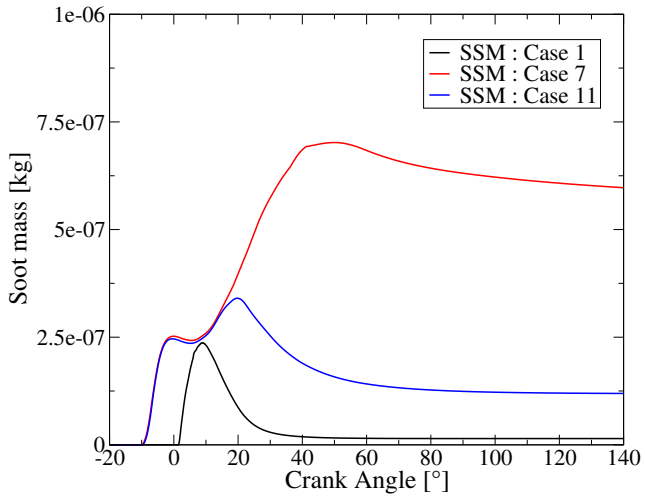

Figure 4.32: Soot mass (kg) evolutions predicted by the SSM function of the crank angle for cases 1 (black), 7 (red) and 11 (blue).

ics (PSK) model [80, 94], a semi-empirical two-equations model usually used for engine simulations [95]. In comparison with Fig. 4.31, it illustrates the significant improvement obtained by the use of a sectional approach. The injection duration variation at full load does not affect the soot mass emission rate for the three lowest values before leading to a too important variation for the two largest values. On the contrary, this effect is well reproduced with the sectional soot model with a slight overestimation for all cases but with a relative variation close to the experimental ones. For all the partial load cases, the PSK model strongly underestimates the soot yield unlike the sectional soot model.

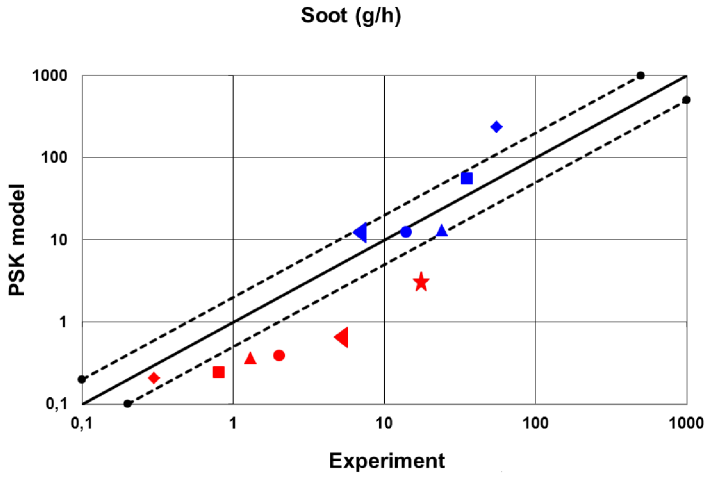

Figure 4.33: Comparison of the experimental and simulated with the PSK model soot emissions rate (g/h, dashed line: +100% and -50%). See Tab. 4.4 for the legend.

These differences between the predictions of the PSK model and the SSM are illustrated with

the soot mass time evolutions of cases 1, 7 and 11 presented in Fig. 4.34. Although the soot mass variations predicted by the PSK model are more important, the soot mass time evolutions are qualitatively similar to the ones predicted by the SSM with one peak of soot production for case 1 and two peaks for cases 7 and 11. These discrepancies can be first explained by the lack of information on particles sizes in PSK. Indeed, in PSK, surface chemistry is based on an averaged surface for all soot particles. The importance of this aspect is underlined by the inability of PSK to predict the mean soot diameter for both cases. The second source of discrepancy is the simplified treatment of chemistry in PSK where soot inception is based on ethylene instead of a PAH like pyrene. Ethylene is itself given by a reduced four step mechanism and OH by an equilibrium computation instead of complex chemistry in the present study [94].

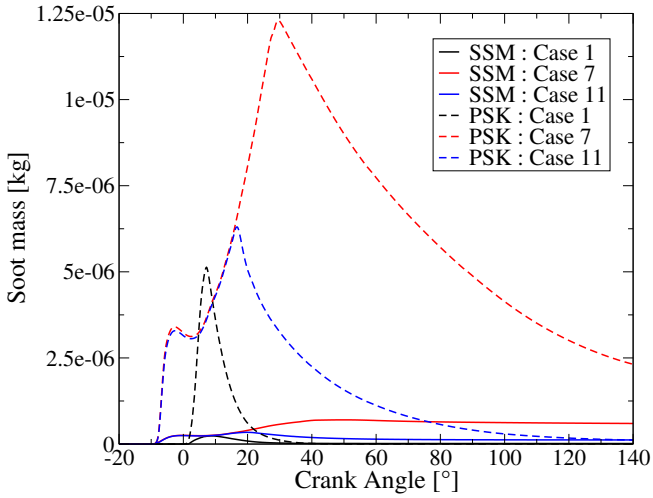

Figure 4.34: Soot mass (kg) evolutions predicted by the SSM (solid lines) and the PSK model (dashed lines) function of the crank angle for cases 1 (black), 7 (red) and 11 (blue).

Predicted SNDF. SNDF simulation results at exhaust for the two reference cases 1 and 7 are given in Fig. 4.35 and Fig. 4.36 respectively and compared to the experiments performed with the surrogate fuel and to the average particle diameter predicted at exhaust by the PSK model. These results are promising as the global amount of soot (in number) is predicted within an order of magnitude compared to the experiments and the peak location of the size distribution is also well reproduced. Some differences between the experiments and the simulations might come from the fact that measurement of particles is quite difficult and could be strongly modified depending on particle composition. However, the predicted SNDF offers a realistic view of the accumulation mode at exhaust, matching the experiment on the median diameter and on the global shape of the distribution for particle diameters larger than the 23 nm cut-off used for the definition of EU emission standards. Note that the double peak of the SNDF observed experimentally for large particles in Fig. 4.36 is certainly an artifact of the soot meter.

The average diameters predicted by the PSK model, 60 nm for case 1 and 6 nm for case 7, illustrate the importance of modeling the SNDF. The large under-prediction on the average particle diameter for case 7 is suspected to lead to an overestimation of the available reactive surface for soot growth and oxidation. This value is here only compared to the SNDF at exhaust, because there

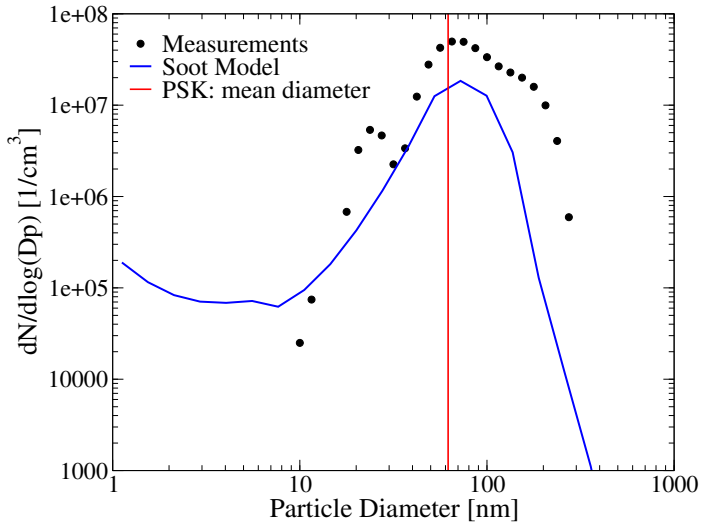

Figure 4.35: SNDF at exhaust for the reference 2200 rpm case (case 1): simulation results (blue line), compared to the SNDF measured (black dots) and the average diameter predicted by the PSK model (red line).

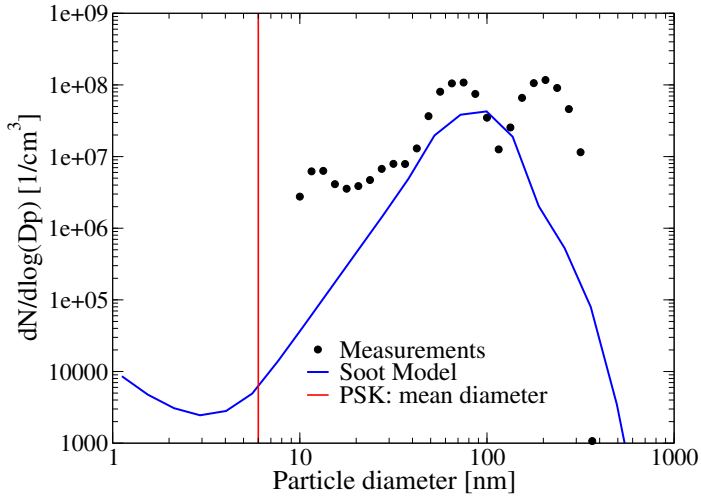

Figure 4.36: SNDF at exhaust for the reference 4000 rpm case (case 7): simulation results (blue line), compared to the SNDF measured (black dots) and the average diameter predicted by the PSK model (red line).

is no measurement inside the cylinder. However, the error on the predicted mean diameter in case 7 at exhaust coupled to the difference of soot mass time-evolutions between the PSK model and the SSM predictions point this diameter (and indirectly, the available reaction surface) as the main source of improvement of the SSM compared to the PSK model.

The time evolution of the mean SNDF computed over the complete chamber can also be extracted from the simulations. Fig. 4.37 and Fig. 4.38 present these mean SNDF for the two reference points

(cases 1 and 7). At the ignition crank angle, the particle inception effect on the mean SNDF shape is clearly represented with a large amount of very small particles. It is followed by a transfer of small size particles to larger size particles due to coagulation. Finally, the established distribution is partially oxidized which can be observed through the reduction of the soot peak concentration (from 60 CAD up to the exhaust). A clear difference on the duration (in crank angles) of particle inception can be seen between Fig. 4.37 and Fig. 4.38 with small soot disappearing earlier on the 2200 rpm reference case compared to the 4000 rpm reference case.

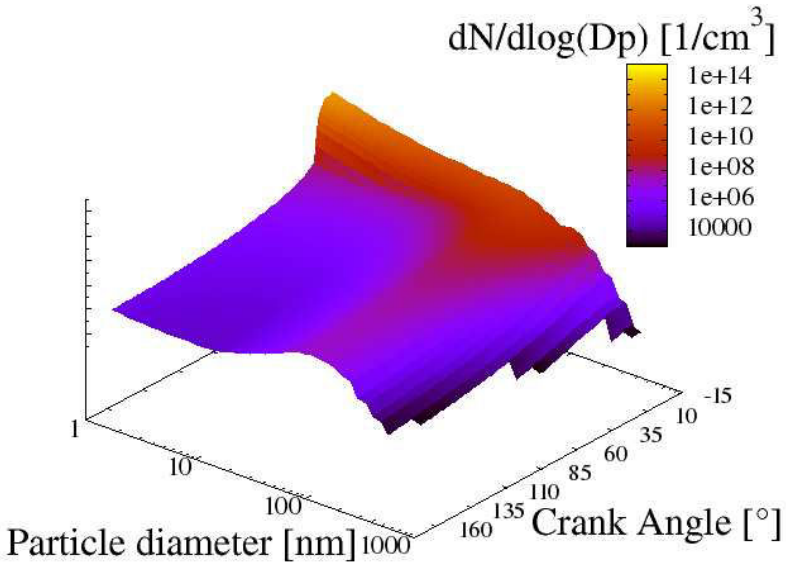

Figure 4.37: Particle volume number density depending on particle diameter and crank angle colored by volume number density for the reference 2200 rpm case (case 1).

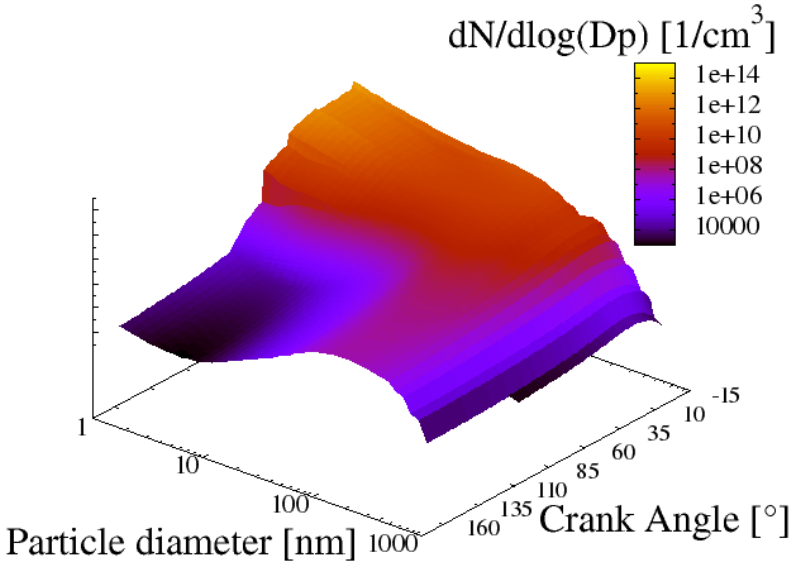

Figure 4.38: Particle volume number density depending on particle diameter and crank angle colored by volume number density for the reference 4000 rpm case (case 7).

4.8 Conclusions

In this article, improvements brought to a sectional soot model are presented as well as its coupling with the ECFM3Z [146] turbulent combustion model using a novel chemistry tabulation method called VPTHC.

The sectional soot model is based on the description proposed in [77, 78, 124]. Two modifications have been proposed in this work. First, a more accurate distribution of source terms through the modeled SNDF is described. Secondly, a version of the HACA-RC cycle adapted to engine calculations is employed [72].

This soot model requires as input parameters minor species mass fractions which are not available using simplified kinetics. For this reason, a specific combustion model is proposed that allows to describe these minor species. This model is based on the three mixing zones description of ECFM3Z [146] and on the tabulated reaction rate model VPTHC. VPTHC (Variable Pressure Tabulated Homogeneous Chemistry) is in fact a simplified version of the EADF combustion model [145]. It consists in the tabulation of species mass fractions and progress variable reaction rate using constant and variable pressure homogeneous reactors. These outputs are used to calculate species reaction rates in the reactive zone of ECFM3Z. VPTHC thus allows to include a complex chemistry description at a low computational cost.

The ability of the VPTHC model to reproduce the detailed chemistry required by the soot model is first evaluated on heterogeneous variable volume reactors (ECFM3Z-0D) specifically developed to mimic Diesel combustion. Results show that the soot mass evolution during combustion is qualitatively reproduced by VPTHC, even though a factor between two and three is found between the tabulated method and the kinetic solver. This error is attributed to the VPTHC model trajectory which only approximates the real engine trajectory: as minor species are extremely sensitive to this trajectory, their prediction is much more difficult than for major combustion products like CO_2. For the time being, this error is considered acceptable because of the very large uncertainty linked to the inception and surface chemistry and because the present model is devoted to an industrial usage for which the limitation of the CPU cost is a major requirement. Clearly, the species description proposed in VPTHC shall be improved in the future.

The soot and combustion models are finally evaluated on a Diesel engine database which includes two operating points with parametric variations on EGR rate, injection pressure and duration. This database [147] was acquired both for a commercial and a surrogate Diesel fuel which is also used in the simulations (30% 1-Methylnaphthalene and 70% Decane in volume). Measurements provide soot particle distributions at exhaust and soot yield. The main conclusions of this comparison are:

- The present surrogate offers a good representation of the commercial Diesel fuel for the rate of heat release and for soot production (in terms of mass and distribution);
- The ECFM3Z/VPTHC model developed in this study reproduces with good accuracy the auto-ignition delay and heat release rate for all the database;
- the soot yield obtained with the proposed model (sectional soot model coupled with ECFM3Z/VPTHC) shows a good agreement with the experiments for the reference cases at 2200rpm and 4000rpm and for the EGR and injection duration variations. In contrast, the effect of injection pressure on the soot yield is underestimated.
- The soot particle distributions at exhaust correctly match the measurements in terms of distribution peak location and number density.

The underestimation of injection pressure influence on soot yield is yet an open topic. These simulations have been run with the standard modeling parameters of IFP-C3D without any calibration between the operating points. It is well-known that spray models are not fully predictive yet. The different sets of the $k-\epsilon$ model coefficients used by the different laboratories simulating the Engine Combustion Network (ECN) Spray A (a Diesel-like spray in a constant volume vessel) illustrate this fact. These coefficients are available in [158]. The inability of the spray model to reproduce a small variation of injection pressure can be suspected to lead to the final error. Giving actual evidence of this is difficult in this context because no data are available from this metal engine to validate the spray model. Another possible explanation is the absence of strain effect in the ECFM3Z mixing model: as the injection pressure is increased, larger gaseous velocities are expected, leading to larger strain rates. As the strain rate increases, minor species concentrations like the soot precursor can be strongly impacted as evidenced in the DNS of Bisetti *et al.* [73].

Future work will be devoted to improving the gaseous species description given by the VPTHC model. This task might include the introduction of a feed-back model in the table representing the impact of soot chemistry on the gaseous composition, and the introduction of specific transport equations for minor species as proposed in Bisetti *et al.* [73].

Chapter 5

Diesel spray RANS simulation

This chapter is based on the current version of the article entitled "Combustion and soot modeling of a high pressure and temperature Dodecane spray" to be submitted in November 2014. It contains a description the Approximated Diffusion Flame (ADF) model which is coupled to the sectional soot model for RANS simulations of Diesel sprays in a constant volume vessel. These simulations provide a second validation of the model after the Diesel engines cases presented in the previous chapter, using a more detailed combustion model and a different fuel. They also allow a more detailed analysis of the soot formation and evolution predicted by the model.

First, the simulations were ran with the to ECFM3Z model coupled to the VPTHC model to represent chemistry in the mixing region. However, this method is based on a simplified mixture fraction stratification and it does not include strain effects. Even if the auto-ignition delay predictions were acceptable with this approach, the lift-off lengths variations were underestimated. Since one of the objectives of the Spray A simulations was to validate the ability of the model to predict soot particles location, an approach able to predict the lift-off variations had to be used. Therefore, the ADF model has been used for these simulations because it takes into account the strain effects on the flame. These effects appeared to be necessary to represent the flame lift-off lengths. The lift-off lengths predicted by the ADF model had a better agreement with the experimental ones. Thus, the study of the soot particles location based on the gaseous phase predicted by the ADF model was possible.

The sectional soot model used in the Spray A simulations is slightly different than the one described in Chapter 3. The first simulations underestimated oxidation rates with very low variations with respect to the temperature or dilutant mass fraction. This behavior was due to the value of the coefficient from the quasi-steady state approximation in Eq. 3.31. It limited the oxidation by hydroxyl and its variations. Therefore, a simpler method has been used. The reaction rates of surface growth by acetylene and oxidation by oxygen and hydroxyl were directly obtained from the surface chemistry reactions as in [73, 109]. These three reactions used for the Spray A simulations are the same as the ones used for the other simulations of this work [76].

5.1 Abstract

Diesel engines are known to be one of the main sources of soot particle emission in the atmosphere. The norms to restrain these emissions have created a need of accurate soot models for piston engine emissions prediction in the automotive industry. This paper addresses this question by coupling a sectional soot model with a tabulated combustion model for RANS simulations of the Engine

Combustion Network (ECN) Spray A [L.M. Pickett, C.L. Genzale, G. Bruneaux, L-M. Malbec et al. SAE Int. J. Engines 3 (2010) 156-181], a high pressure Dodecane spray with conditions very similar to Diesel engines ones. The sectional soot model, which has already been used in Diesel engines RANS simulations with a simpler combustion model in Aubagnac-Karkar *et al.* [D. Aubagnac-Karkar, J-B. Michel, O. Colin, N. Darabiha, Combust. Flame (2015), In Press], is implemented in the IFP-C3D RANS CFD code. At each time and location, transport equations are solved for several soot sections, including source terms for collisional and chemical processes. The soot model is here coupled to the Approximated Diffusion Flame - Presumed Conditional Moment model (ADF-PCM) [J-B. Michel, O. Colin, D. Veynante, Flow Turb. Comb. 83 (2009), 33-60] which is a tabulated combustion model. It allows to represent the minor species required by the soot model with a much lower computational cost than a kinetic solver and includes complex turbulence-chemistry interactions.

The predictions of these models agree with the experimental measurements for most of the Spray A cases, for flame structure and soot production. These results show that detailed soot models can be coupled to tabulated combustion models with good results in turbulent flames.

5.2 Introduction

A better understanding of soot particles formation and evolution is required to respond to the stringent worldwide regulations on their emissions in the ground transport sector. In Europe, for instance, EURO norms regulate particles emissions for Diesel engines since 1993 and will soon also regulate them for spark-ignition engines (SIE). Even if Diesel engines are today equipped with particle filters, being able to predict soot particles number and size is still important to car manufacturers. Indeed, some emitted particles are small enough to get through particle filters and the norms on particles number will take them into account in the future. Moreover, particle filters are expensive and a reduction of the raw-engine soot emissions would lead to a reduction of particle filters sizes and costs.

In this context, engine manufacturers need experimental and numerical tools to evaluate the raw engine-out Soot Volume Fraction (SVF) and Soot Number Density Function (SNDF). These tools have to be implemented in RANS (Reynolds Averaged Navier Stokes) simulation codes, the most used method for industrial combustion chamber simulation. Two main methods are used for the prediction of SVF and SNDF in 3-D RANS simulations, the sectional method [61, 78, 162] or the moment method [97, 108, 109]. In this work, a sectional soot model [162] derived from models developed by Mauss and co-workers [112, 113, 114] is retained. It accounts for inception, condensation, surface growth and oxidation processes and directly predicts the SNDF at each time and location, in contrast to moment methods for which a post-processing is necessary.

Computing the local and instantaneous concentration of the soot precursors and the chemical species involved in soot surface chemistry is required by detailed soot models, such as the one used in the present paper. Kinetic schemes able to correctly predict these concentrations under the whole range of thermodynamic and chemical conditions encountered in Diesel engines are detailed chemical schemes including hundreds of species and thousands of reactions [140, 141, 142, 143, 144]. As a consequence, transporting all the species and solving the complete chemistry totally coupled with turbulent reactive flow balance equations is very costly. Thus, less expensive approaches have to be used. Tabulated chemistry approaches have a very reduced CPU time compared to direct chemistry resolution. Moreover, the sectional soot model has already been coupled to a tabulated turbulent

combustion model derived of the Engine Approximated Diffusion Flame (EADF) [145] and used to predict soot in RANS simulations of a Diesel engine with encouraging results [162]. In the present work, a more complex model, the ADF-PCM model [151, 163], is used in order to include flame structure effects to the gas phase modeling.

Relevant validation cases are required for these models. The closest academical set-up to Diesel engines conditions is high pressure spray. In this study, the ability of the proposed sectional soot model coupled to the ADF-PCM turbulent combustion model to predict SVF is evaluated against measurements from the Dodecane Spray A [164, 165, 166] of the Engine Combustion Network (ECN). The ECN Spray A is here retained because:

- it is a high pressure and temperature spray with conditions representative of those of a real Diesel engine,
- Dodecane is a heavy fuel as Diesel fuel for which detailed chemical mechanisms are available,
- ECN provides large experimental databases with all variations required to validate a model.

The aim of this work is to assess the ability of the proposed combustion and soot models to predict flame structure and soot production on the ECN Spray A cases. Section 5.3 describes the ADF-PCM model used to compute the gaseous phase quantities and the sectional soot model representing the soot particles formation and evolution. Then, the numerical configuration and simulations results are given in Section 5.4.

5.3 Models

As mentioned in the introduction, a turbulent combustion model able to represent detailed chemistry in non-premixed combustion is required to compute the species involved in the soot formation process, including minor species such as soot precursors. In the present work, the ADF-PCM model is used for that purpose. The two ADF-PCM and sectional soot models are described in the following section.

5.3.1 Turbulent combustion model: ADF-PCM

In the ADF-PCM approach [151, 159, 163], approximated diffusion flames at various initial conditions are used to generate a look-up table from which the species reaction rates are evaluated by the CFD code. The generation of this look-up table splits into three parts:

- First, a chemistry database of autoigniting adiabatic homogeneous reactors is generated with the IFP-Kinetics solver [136]. It allows the representation of pressure, temperature and dilutant gases effects.
- Then, the flamelet equation of Peters [167] is solved for the progress variable only using the chemical source terms extracted from the previous table in order to create a database of 1-D approximated diffusion flames (ADF) which includes strain rate and temperature stratification effects.
- Finally, the mixture fraction stratification is modeled with presumed pdf which are integrated and stored in the ADF look-up tables.

This method allows the representation of a detailed chemistry, required by the soot model, at a very low computational cost. A similar approach was used for LES modeling of Diesel sprays with good results in Tillou *et al.* [168].

5.3.1.a Homogeneous reactor table

This first table is built from the calculation of constant pressure autoigniting homogeneous reactors for several pressures P, fresh gas temperatures T^0, mixture fractions Z and mass fractions of dilutant Y_{EGR} as coordinates of the database. The results are stored as functions of the progress variable which quantifies the transition from fresh to burnt gases. This quantity is here estimated as $c = Y_c/Y_{eq}$ where $Y_c = Y_{\mathrm{CO}} + Y_{\mathrm{CO_2}} + Y_{\mathrm{H_2O}}$ and Y_{eq} is the value of Y_c when the equilibrium at constant pressure and enthalpy is reached. It has been verified that Y_c evolves bijectively with time in all computed reactors.

5.3.1.b Approximated diffusion flames calculations

In the ADF approach [151, 159, 163], the local and instantaneous structure of the reaction zone is represented by autoigniting strained laminar diffusion flames which are tabulated. These flames are defined by:

- A fresh gases mixture composition $Y_{i,F}$ and temperature T^0_F at the fuel saturated mixture fraction $Z = Z_S$
- A fresh gases mixture composition $Y_{i,A}$ and temperature T^0_A at mixture fraction $Z = 0$

The fresh gases composition and enthalpy evolve linearly with mixture fraction, thus defining the fresh gases temperature though the flames.

The flamelet equation of Peters [167] is solved for the progress variable Y_c:

$$\frac{\partial Y_c}{\partial t} = \chi \frac{\partial^2 Y_c}{\partial Z^2} + \dot{\omega}_{Y_c} \tag{5.1}$$

where χ is the scalar dissipation rate defined as:

$$\chi = D \left|\nabla Z\right|^2 \tag{5.2}$$

where D is the diffusion coefficient. The strain rate, a, is used to characterize the scalar dissipation rate, using the following relation for a counterflow diffusion flame [169]:

$$\chi = \frac{a Z_s}{2\pi} \exp\left(-2\left[\mathrm{erf}^{-1}\left(1 - 2\frac{Z}{Z_s}\right)\right]^2\right) = aF(Z) \tag{5.3}$$

The progress variable reaction rate $\dot{\omega}_{Y_c}$ in the flamelet equation (5.1) is extracted from the homogeneous reactors table in the ADF approach. Then, a database of flamelets computed with this method can be generated for different values of T^0_F, T^0_A and a as well as the values of Y_{EGR} and P of the homogeneous reactors database.

5.3.1.c Integration over a probability density function

Finally, the mixture fraction stratification is represented by a presumed β-PDF $P(Z, \widetilde{Z}, \widetilde{Z''})$ (here written $P(Z)$) depending on the Favre average mixture fraction $\widetilde{Z}$ and its variance described in this work with its segregation factor $S_z = \widetilde{Z''}/(\widetilde{Z}(Z_s - \widetilde{Z}))$. This presumed β-pdf is then applied to the ADF progress variable source term and species computations to obtain the final table.

$$\widetilde{\dot{\omega}}_{Y_c}^{ADF-PCM}(\widetilde{Z}, \mathrm{P}, \mathrm{T}_F^0, \mathrm{T}_A^0, Y_{\mathrm{EGR}}, a, S_z, t) = \int_{Z=0}^{Z_s} \dot{\omega}_{Y_c}^{flamelet}(Z, \mathrm{P}, \mathrm{T}_F^0, \mathrm{T}_A^0, Y_{\mathrm{EGR}}, a, t) P(Z) dZ \quad (5.4)$$

$$\widetilde{Y}_i^{ADF-PCM}(\widetilde{Z}, \mathrm{P}, \mathrm{T}_F^0, \mathrm{T}_A^0, Y_{\mathrm{EGR}}, a, S_z, t) = \int_{Z=0}^{Z_s} Y_i^{flamelet}(Z, \mathrm{P}, \mathrm{T}_F^0, \mathrm{T}_A^0, Y_{\mathrm{EGR}}, a, t) P(Z) dZ \quad (5.5)$$

where $\dot{\omega}_{Y_c}^{flamelet}$ and $Y_i^{flamelet}$ are defined as:

$$\dot{\omega}_{Y_c}^{flamelet}(Z, \mathrm{P}, \mathrm{T}_F^0, \mathrm{T}_A^0, Y_{\mathrm{EGR}}, a, t) = \dot{\omega}_{Y_c}^{HR}(Z, \mathrm{P}, \mathrm{T}_F^0, \mathrm{T}_A^0, Y_{\mathrm{EGR}}, c(Z, t, a)) \quad (5.6)$$

$$Y_i^{flamelet}(Z, \mathrm{P}, \mathrm{T}_F^0, \mathrm{T}_A^0, Y_{\mathrm{EGR}}, a, t) = Y_i^{HR}(Z, \mathrm{P}, \mathrm{T}_F^0, \mathrm{T}_A^0, Y_{\mathrm{EGR}}, c(Z, t, a)) \quad (5.7)$$

where $c(Z, t, a) = Y_c(Z, t, a)/Y_c^{eq}(Z)$ is obtained from the flamelet equation solved for the progress variable and the equilibrium value of the progress variable from the homogeneous reactor table.

Finally, $\widetilde{\dot{\omega}}_{Y_c}^{ADF-PCM}$ and $\widetilde{Y}_i^{ADF-PCM}$ are stored in the final ADF-PCM table depending on the flamelets initial conditions and $\tilde{c}(Z, t, a) = \widetilde{Y}_c(Z, t, a)/\widetilde{Y}_c^{eq}(Z)$.

5.3.1.d Model implementation

To extract species mass fractions in the combustion zone from the look-up table, the input parameters described above need to be calculated. These parameters are the progress variable $\widetilde{Y}_c$ and the initial parameters of the reactors: $\widetilde{Z}$, P, T_F^0, T_A^0, Y_{EGR}, a and S_z. The thermodynamic parameters P, T_F^0, T_A^0 and Y_{EGR} derivations are detailed in [145]. The flame structure parameters $\widetilde{Z}$, a and S_z derivations are given in [163]. The tabulated species are transported in the CFD code as follows:

$$\frac{\partial \overline{\rho} \widetilde{Y}_i}{\partial t} + \nabla \cdot (\overline{\rho} \tilde{u} \widetilde{Y}_i) = \nabla \cdot (\overline{\rho}(D + D_t) \nabla \widetilde{Y}_i) + \overline{\rho} \widetilde{\dot{\omega}}_{Y_i} \quad (5.8)$$

where $\overline{\rho}$ is the mean density, D an averaged diffusion coefficient and D_t the turbulent diffusivity.

It has been shown [151] that directly imposing species reaction rates from the look-up table leads to uncontrolled deviations from the look-up table trajectories. Thus, another formulation [170, 171] has been proposed by Michel *et al.* [151] for tabulated models species reaction rate $\widetilde{\dot{\omega}}_{Y_i}$. It reads:

$$\widetilde{\dot{\omega}}_{Y_i} = \frac{\widetilde{Y}_i^{ADF-PCM}(\widetilde{Y}_c + \delta \widetilde{Y}_c) - \widetilde{Y}_i}{\tau} \quad (5.9)$$

where τ is a time-scale representing species relaxation towards the homogeneous reactor conditions. It was shown in [151] that as long as τ is chosen small enough compared to the progress variable time-scale, the tabulated trajectory is correctly followed. Here, we choose $\tau = 3dt$ where dt is the CFD time-step. The mean progress variable $\widetilde{Y}_c + \delta \widetilde{Y}_c$ is deduced from the tabulated progress variable source term $\widetilde{\dot{\omega}}_{Y_c}^{ADF-PCM}$ and is given by:

$$\delta \widetilde{Y}_c = \tau \widetilde{\dot{\omega}}_{Y_c}^{ADF-PCM}(\widetilde{Z}, \mathrm{P}, \mathrm{T}_F^0, \mathrm{T}_A^0, Y_{\mathrm{EGR}}, a, S_z, \tilde{c}) \quad (5.10)$$

where $\tilde{c} = \widetilde{Y}_c / \widetilde{Y}_c^{eq}$ with $\widetilde{Y}_c$ here defined from the transported species.

In the CFD code, only thirteen species are extracted from the look-up table: $n-C_{12}H_{26}$, O_2, CO_2, H_2O, CO, H, H_2, O, OH, C_2H_2, CH, HCO and $C_{16}H_9$. Therefore, the kinetic scheme intermediary species atoms are missing. Three additional species are added to close the atomic balances in carbon, hydrogen and oxygen: C_2H_3, H_2b and O_2b (b standing for balance) which have the same thermodynamic properties as their respective real species as in [145, 162, 168].

5.3.2 Sectional soot model

The present soot model is identical to the one proposed in Aubagnac-Karkar *et al.* [162], which is itself derived from the work of Netzell *et al.* [55, 78]. The present approach considers that soot particles are solid and modeled as a distinct dispersed phase, interacting with the gaseous phase. The soot particles population is evaluated by using a sectional method. The soot particles are separated with respect to their volume into discrete sections. In the turbulent reactive flow, each section i, representing the soot particles of a given volume range $[V_{min,i}; V_{max,i}]$, is governed by a standard transport equation for the mass fraction of soot in this section, $\widetilde{Y}_{soot,i}$:

$$\frac{\partial \overline{\rho} \widetilde{Y}_{soot,i}}{\partial t} + \nabla \cdot (\overline{\rho} \tilde{u} \widetilde{Y}_{soot,i}) = \nabla \cdot (\overline{\rho} D_{t,soot} \nabla \widetilde{Y}_{soot,i}) + \overline{\rho} \widetilde{\dot{\omega}}_{soot,i} \tag{5.11}$$

with $\overline{\rho}$ the gas phase density, $\tilde{u}$ the gas velocity, $D_{t,soot}$ the turbulent diffusion coefficient of soot here equal to the turbulent diffusivity D_t and $\widetilde{\dot{\omega}}_{soot,i}$ the soot source term for section i.

$\widetilde{\dot{\omega}}_{soot,i}$ is defined as the sum of five source terms describing the main processes of soot formation and evolution. These different physical phenomena are described next. They are illustrated in Fig. 5.1 and are introduced in the following order:

- Collisional source terms: particle inception, condensation and coagulation.
- Surface chemistry source terms: surface growth and oxidation.

5.3.2.a Collisional source terms

Particle inception, condensation and coagulation are collisional phenomena. They are represented by the Smoluchowski equation [62]. In the continuous form, it reads:

$$\dot{F}_a(t) = \frac{1}{2} \int_0^a (\beta_{a-b,b} F_b(t) F_{a-b}(t)) db - \int_0^\infty (\beta_{a,b} F_a(t) F_b(t)) db \tag{5.12}$$

where $F_x(t)$ is the number of particles of size x, $\dot{F}_x(t)$ its variation rate and $\beta_{x,y}$ the collision frequency between particles of size x and y. The collision frequencies are obtained using the theory of aerosol science [64], applied to soot formation by Kazakov and Frenklach [65].

Coagulation: Coagulation is the collision between particles, leading to larger particles. Its reaction rate is directly evaluated from Eq. (5.12) and distributed among the sections.

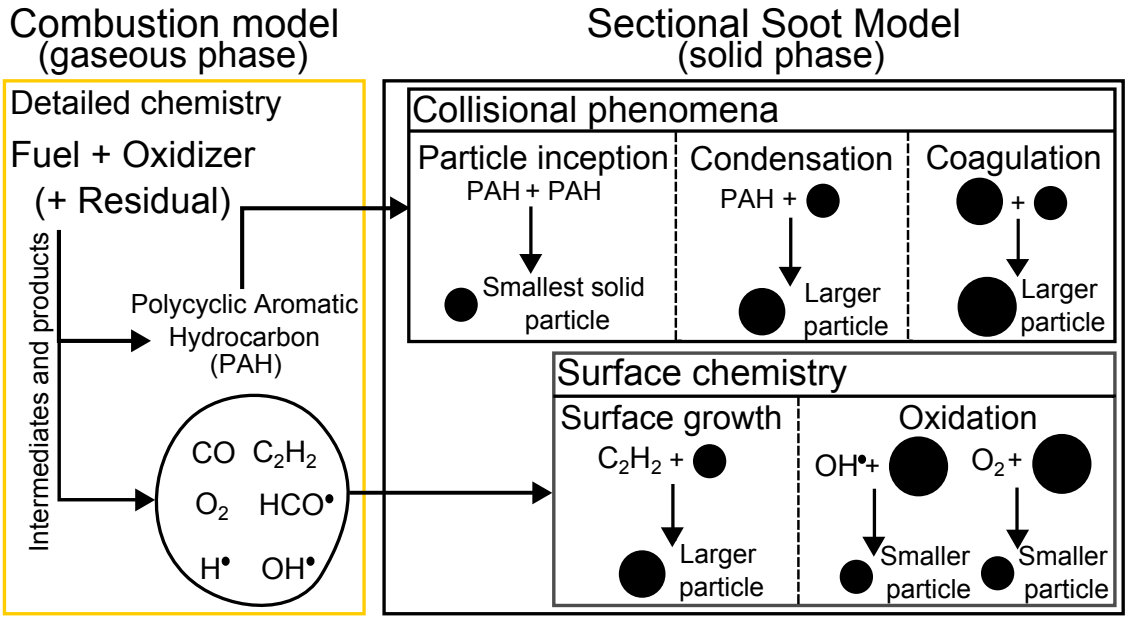

Figure 5.1: Illustration of the five phenomena representing soot formation and evolution with the involved gaseous species.

Inception and condensation; Inception and condensation are the two phenomena related to precursors collisions. It can either be collisions between precursors to create the smallest considered soot particles (particle inception), or between precursors and soot particles to increase soot particles volume (condensation). The precursor species used in these phenomena is a virtual species called PAH (for Polycyclic Aromatic Hydrocarbons). PAH is the product of the pyrenyl radical ($C_{16}H_9$), a usual soot precursor [55, 56, 58, 78, 77], polymerization by acetylene as in [56, 77, 78, 162]:

$$C_{16}H_9 + C_2H_2 \xrightarrow{k_{pol}} \text{PAH} + H_2 \tag{5.13}$$

where k_{pol} is the rate constant of reaction for this polymerization reaction.

This precursor formation rate is balanced with its consumption rate by particle inception and condensation which are evaluated using Eq. (5.12). This balance equation closes the problem of particle inception and condensation by giving the number density of virtual precursors PAH, thus leading to the final reaction rate of particle inception and condensation to be distributed in the sections.

5.3.2.b Surface chemistry

Although the HACA-RC cycle (*Hydrogen Abstraction Carbon Addition - Ring Closure*) developed by Frenklach [26] is commonly used to model soot surface chemistry [56, 75, 76, 78], the constants for soot modeling in turbulent flame are still unsure [73]. Accordingly, considering only reaction rates taken from literature for surface growth by acetylene addition, oxidation by hydroxyl radical and oxidation by molecular oxygen is sufficient is turbulent combustion cases [73, 109]. In the present work, these three surface chemistry reaction rates are taken from a variation proposed by D'Anna and Kent [76] of the HACA-RC cycle. This surface chemistry scheme has been chosen as a reference since it has been used with a similar sectional model in Diesel engine simulation [162]

and was designed for Diesel engine conditions and previously validated by Fraioli *et al.* [72]. The surface chemistry phenomena are described using six gaseous species (H, OH, C_2H_2, O_2, CO and HCO) in three reactions (given in table Tab.5.1) with the rate constants taken from [76]. In Tab.5.1, C_i represents soot particles of section i, C_k^p represents stable aromatic soot particles product of a reaction that exchanged p carbon atoms with the gaseous phase, and k_n^i is the rate constant of reaction n on particles of section i.

$$\begin{aligned} C_i + C_2H_2 &\xrightarrow{k_4^i} C_i^2 + H \\ C_i + OH &\xrightarrow{k_5^i} C_i^{-1} + HCO \\ C_i + O_2 &\xrightarrow{k_6^i} C_i^{-2} + 2CO \end{aligned}$$

Table 5.1: Reactions governing the soot surface chemistry [76].

To evaluate the oxidation and surface growth reaction rates given by the surface chemistry reactions, the total amount of particles in each section is first converted into a concentration ($[C_i]$) also proportional to the surface $S_i(v)$ of particles of volume v included in section i. This value can be obtained from:

$$[C_i] = \int_{v_{min,i}}^{v_{max,i}} \alpha_{\text{HACA}} \frac{\lambda_{soot}}{\mathcal{N}_A} S_i(v) n_i(v) dv \tag{5.14}$$

where $\mathcal{N}_A$ is the Avogadro number, $n_i(v)$ is the number density of soot particle of volume v included in section i, λ_{soot} is the number of reactive sites per unit surface of soot and α_{HACA} is the proportion of these sites which are active.

The value of α_{HACA} is often correlated to temperature [44, 132]. Because temperature dependent expressions of α_{HACA} are not completely validated up to now, we rather choose a constant value as done in [55, 56]. We choose $\alpha_{\text{HACA}} = 0.27$ which corresponds to the average value of the correlation given by Markatou *et al.* [132] for a temperature interval of 1250K to 3000K as in [55, 77, 78, 162].

The number of reactive sites available for reaction ($\lambda_{soot} S_i$) is evaluated as in [55, 56]. Considering that the smallest solid soot particle has only one reactive site ($\lambda_{soot} S_1 = 1$), the number of reactive sites only depends on particles volume. Finally, the variation of the available surface with particle volume is represented by correcting the surface of a sphere of equivalent volume by a fractal dimension θ. For the calculations presented here, $\theta = 2.0$ for all particles with a diameter smaller than 20 nm and $\theta = 2.25$ for all particles with a diameter larger than 60nm and the fractal dimension evolves linearly in between as in [55, 77, 78, 162].

5.4 Results

5.4.1 Experimental database

The Spray A is a high-pressure Dodecane spray designed to reproduce Diesel sprays. In the Spray A set-up [164], Dodecane is injected in a high-pressure constant volume vessel of 1150 cm^3. The initial composition of ambient gas is known as well as its thermodynamical conditions.

A large database of variations are available for the Spray A including different injection pressures and ambient gas densities, compositions (with different molar fractions of oxygen) and temperatures.

This allows experimental studies on the effect of each of these parameters and offers validation cases for models in conditions that are close to actual Diesel engines conditions and well documented.

Two of those variations include soot measurements and all the available cases of these variations have been simulated. These different cases are summarized in Tab. 5.2 with the ambient temperature T_{amb}, the ambient pressure P_{amb}, the molar fraction of oxygen X_{O_2} and the mass fraction of dilutant Y_{EGR}. For all these cases, the fuel injection pressure difference to the ambient gas pressure is 150 bar, the injected fuel temperature is 363 K and the ambient gas density is 22.8 kg.m^{-3} (the pressure is adapted to keep this density on the temperature sweep). The injections are 6.1 ms long and 14 mg of Dodecane are injected. For each value of X_{O_2}, a specific composition is provided including CO_2 and H_2O. This justifies a non-zero value of Y_{EGR} for case 3 with 21% in mole of oxygen, the dilutant mass fraction being evaluated with respect to pure air.

Case	Variation	T_{amb}	P_{amb}	X_{O_2}	Y_{EGR}
1	Ref.	900 K	60 bar	15%	0.294
2	X_{O_2}	900 K	60 bar	13%	0.387
3	X_{O_2}	900 K	60 bar	21%	0.018
4	T_{amb}	750 K	49.3 bar	15%	0.294
5	T_{amb}	800 K	52.5 bar	15%	0.294
6	T_{amb}	850 K	56.1 bar	15%	0.294
7	T_{amb}	1000 K	66.2 bar	15%	0.294
8	T_{amb}	1100 K	73 bar	15%	0.294
9	T_{amb}	1200 K	79.4 bar	15%	0.294

Table 5.2: Main characteristics of the Spray A simulated cases.

5.4.2 Numerical configuration

The computations have been ran on a 1500000 hexahedral cells mesh illustrated in Fig 5.2. The geometry is a cube of 1150 cm^3, the volume of the experimental vessel, with a characteristic length in the spray axis of 0.48 mm and 0.52 mm in the transverse directions at the injector nozzle. As shown in Fig.5.2 with the OH mass fraction 5 ms after the beginning of injection (SOI) on the reference case, the mesh has a better resolution area to correctly describe the spray.

The Dodecane chemistry is represented by a kinetic scheme proposed by Narayanaswamy *et al.* [141] of 255 species and 1509 reactions used to generate the look-up table. The table is discretized in order to cover all the simulated cases given in Tab.5.2 with:

- 7 couples of initial air temperature T_A^0 and pressure P, one per point in the temperature sweep (respectively 750 K/ 49.3 bar, 800 K/ 52.5 bar, 850 K/ 56.1 bar, 900 K/ 60 bar, 1000 K/ 66.2 bar, 1100 K/ 73 bar, 1200 K/ 79.4 bar);

- a fuel temperature T_F^0 of 300 K and a saturated mixture fraction Z_S constant at the value of 0.5 obtained from a previous study of a single droplet evaporation [172] and usually used with this model for Diesel spray simulations [145, 168, 95]. Moreover, combustion indicators sensitivity to the value of Z_S have been tested and is very low.

- 3 values of dilutant gases mass fraction Y_{EGR}, 0.387, 0.294 and 0 computed to reproduce the

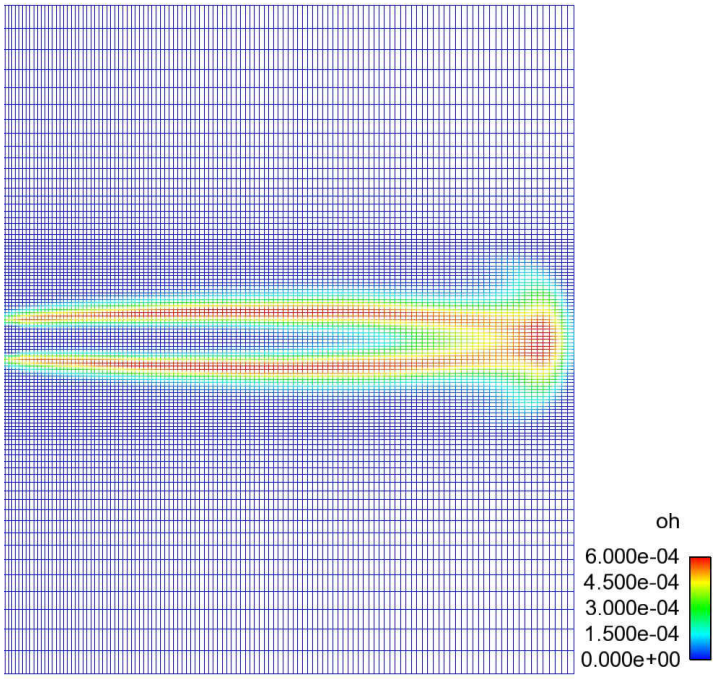

Figure 5.2: Visualization of the computational mesh in the plane containing the axis of the spray colored by OH mass fraction 5.5 ms after the start of injection (SOI) on the reference case.

initial gaseous composition for the 3 values of ambient oxygen molar fractions respectively 13%, 15% and 21%;

- 30 progress variable c ranging from 0 to 1, 21 strain rates a from 0 s^{-1} to 20000 s^{-1}, 100 average mixture fractions from 0 to 0.5 and 8 mixture fraction segregation factors S_z from 0 to 0.3 to described the possible flame structures with enough accuracy.

The sectional soot and the ADF-PCM models are implemented in the IFP-C3D RANS code [148, 149], which is a fully parallelized code developed by IFP Energies Nouvelles for simulating compressible reactive flows. It integrates Lagrangian spray and liquid film models [154, 155], and a standard k-ϵ model for turbulence description. The simulations using the IFP-C3D RANS code were 8 to 18 hours long on 128 processors with a CFD maximum time-step of 10^{-6} s and a temporal subcycling for the soot sections.

5.4.3 Non-reactive case

First, a non reactive case has been simulated with ambient gas molar composition of 89.71% of N_2, 6.52% of CO_2 and 3.77% of H_2O, its other properties being identical to those of the reference reactive case. This ensures that the IFP-C3D RANS code provides an acceptable representation of the spray and its evaporation which is required by the combustion and soot models. The liquid and vapor fuel penetrations are given in Fig. 5.3 and Fig. 5.4 respectively. Both predicted penetrations agree with the experiments.

The fuel mass fraction axial and radial profiles are given in Fig. 5.5 and Fig. 5.6. The stabilized axial profile of fuel mass fraction is compared to the mean experimental one in Fig. 5.5. The

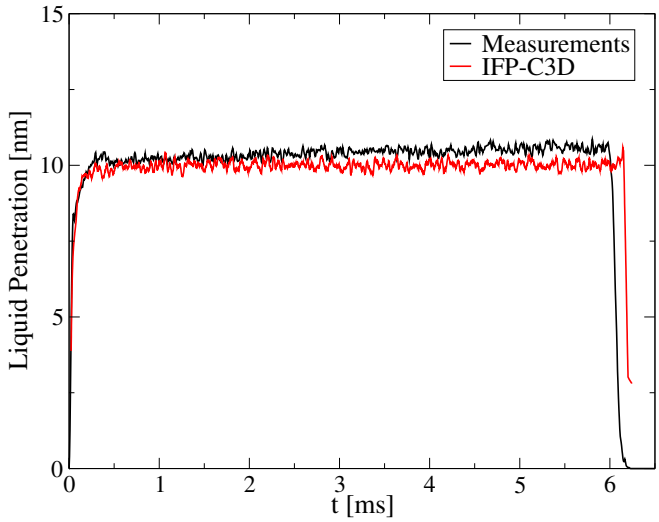

Figure 5.3: Temporal evolution of the experimental and simulated liquid penetrations for the non-reactive case.

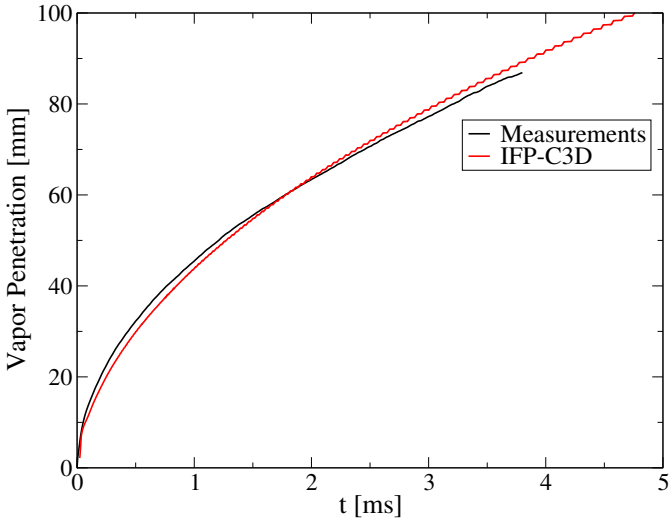

Figure 5.4: Temporal evolution of the experimental and simulated vapor penetrations for the non-reactive case.

measured mean mass fraction uncertainties are given and the predicted fuel mass fraction along the axis of the spray is in the uncertainties interval. Fig. 5.6 shows the fuel mass fraction radial profiles simulated and measured at two distances from the injector orifice. The predicted profiles are slightly wider than the measured ones but this error remains acceptable. The shapes of radial profiles agree with the axial ones. Indeed, the angle of the gaseous phase of the spray is slightly too large, which lowers the fuel mass fraction value along the spray axis and widens the radial profiles.

Globally, the agreement with the experiments in the range of distance from injector where it is available is sufficient to allow further simulations in reactive cases.

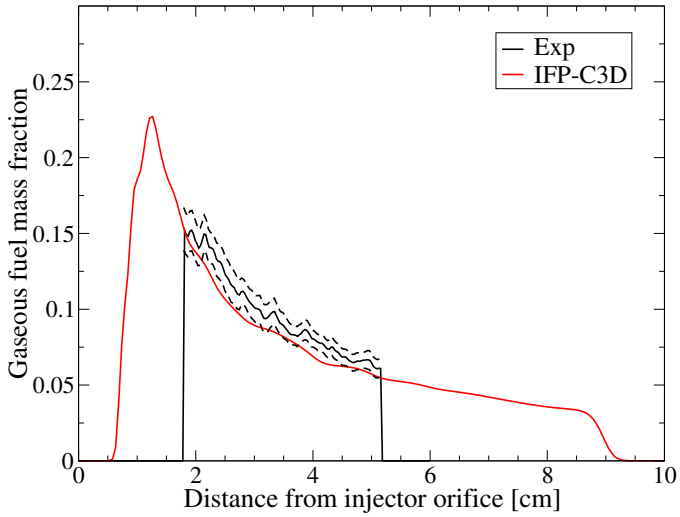

Figure 5.5: Comparison between experimental (black with standard deviation in dashed line, available in a limited range of distances from injector orifice) and simulated gaseous fuel mass fraction along the spray axis depending on the distance from the injector orifice.

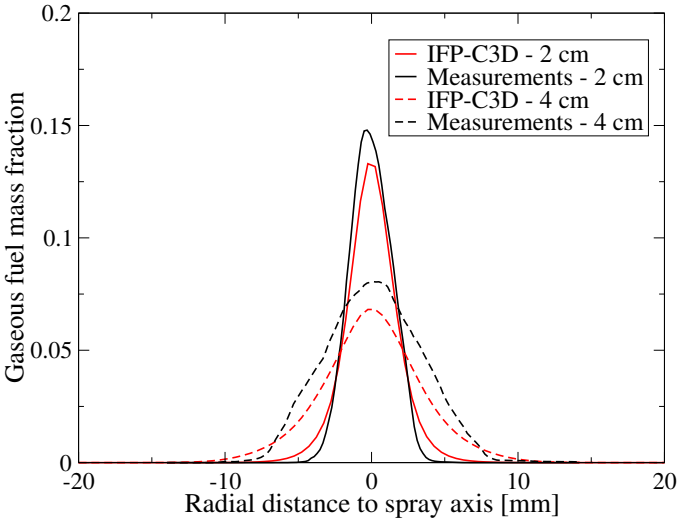

Figure 5.6: Comparison between experimental and simulated fuel mass fraction at two distances from the injector orifice depending on the distance from the spray axis.

5.4.4 Reference case

The ability to reproduce the global behavior of a Diesel spray is shown here by the study of the heat release rate, lift-off length and soot production of the ECN Spray A reference case. The comparison of experimental and simulated heat release rates is given in Fig. 5.7. The predicted shape corresponds to the usual heat release rates obtained on Diesel sprays with a first peak during the autoignition of premixed gases around the spray before a constant heat release rate during the diffusion controlled combustion phase. As evidenced by the error on the location of the peak of heat release in Fig. 5.7, the predicted ignition delay is longer than the experimental one, 0.49 ms predicted against 0.4 ms measured. This error is attributed to the uncertainties on the ignition kinetics of Dodecane, even more at high pressure. These uncertainties are discussed further in this study in Section 5.4.5.b. The experimental heat release rates and ignition delays are obtained following the method proposed by Higgins *et al.* [173] using both pressure and luminosity data.

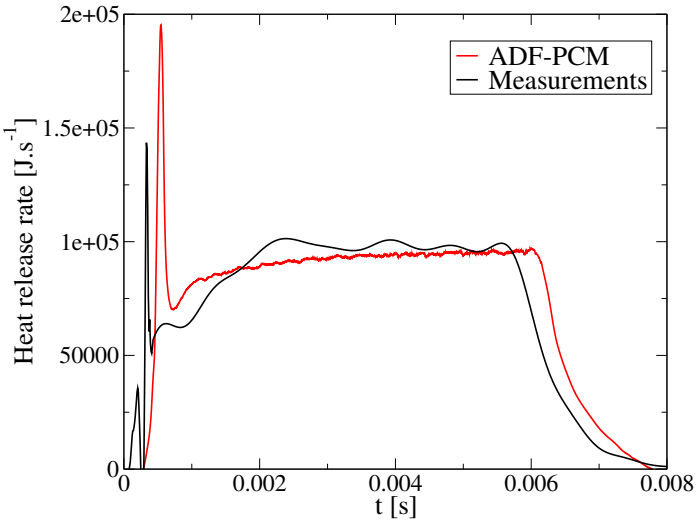

Figure 5.7: Comparison between experimental and simulated heat release rates time-evolution for the reference case.

Flame lift-off length measurements have been obtained using the method described by Higgins and Siebers [174]. In a quasi-steady spray, the measured OH and OH* signal intensities in the spray axis depending on distance to injector can be split into two phases. First, they present a strong gradient at the location where the reaction begins. Then, this gradient decreases and takes a constant value further downstream from the injector. A transition typical to this type of spray is located between these two regions. This evolution depending on the distance from the injector orifice is illustrated in Fig. 5.8 for the simulated OH mass fraction. To obtain a representation similar to the one provided by a chemiluminescence signal, the OH mass fraction presented in Fig. 5.8 is the integral mass at a distance z from the injector over the plan perpendicular to the spray axis in the x and y directions:

$$I(z) = \iint_D Y_{\mathrm{OH}}(x, y) dx dy \tag{5.15}$$

where D is the plane defined by directions x and y.

The lift-off length definition is based on OH evolutions of the same type as the one presented in Fig. 5.8. Arbitrary thresholds are defined to evaluate the experimental lift-off lengths in the strong gradient area. A value of 50% of the chemiluminescence signal at the "knee" has been used in experiments and the same threshold applied to OH mass fraction is used in the present study. For the reference case, the measured lift-off length is 16.1 mm and the predicted one is 16.7 mm. These results are illustrated in Fig.5.9 with OH mass fraction fields in the plane containing the spray axis at four different times after SOI, also illustrating the ability of the model to reproduce a quasi-steady flame structure. The experimental lift-off length is indicated by the vertical white line to illustrate the global good prediction of the flame location.

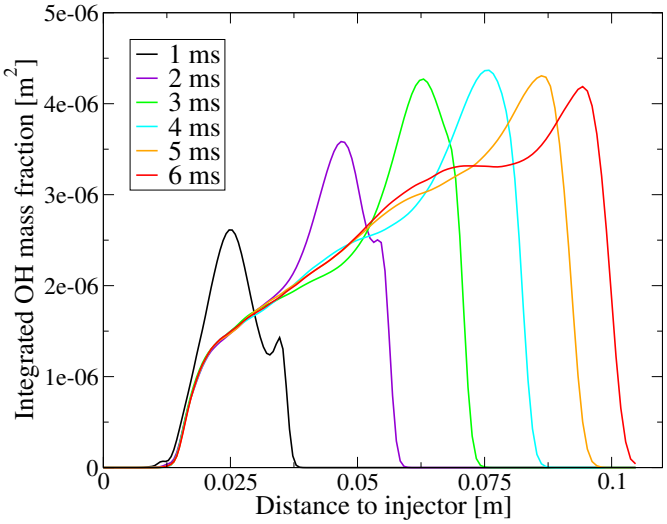

Figure 5.8: OH mass fraction integrated in a plane perpendicular to the spray axis depending on the distance from the injector for the reference case.

Soot volume fraction (SVF) fields are also available from the experimental database. A 2-D field of SVF in the plane containing the spray axis is available for this case, based on the integration during the quasi-steady spray of SVF measured by soot optical extinction [165] or Laser Induced Incandescence [166]. The soot mass contained in an experimental window going from a distance of 2 cm from the injector to 6.5 cm from the injector is also available. The evolution of this soot mass is shown in Fig. 5.10 along with the model predicted soot mass in the given experimental windows. The soot mass experimental measurement shows that soot processes are also in a quasi-steady state from 3 ms after SOI through the end of injection at 6 ms after SOI. This quasi-steady state is well reproduced by the model with a similar mass of soot. The very slow increase of soot between 4 ms and 6 ms observed in this figure is due to a slight imbalance between the four source terms during this period. These source terms are based on phenomena such as particle inception which are not well defined yet. Therefore, this result is considered very acceptable for a complex case such as the Spray A. Nevertheless, the initial peak of soot production is not predicted by the model. This can be explained by two reasons. First, the RANS approach has a low ability to represent the steep mixture fraction gradient observed experimentally and in LES [175, 176]: in the experiments, the fluctuations from shot to shot of the position of this front lead to a smooth mean gradient as seen in Fig.5.11. RANS recovers this mean gradient and represents the fluctuations with a fluctuations modeling. Secondly, these mixture fraction fluctuations are included in ADF-PCM but they are

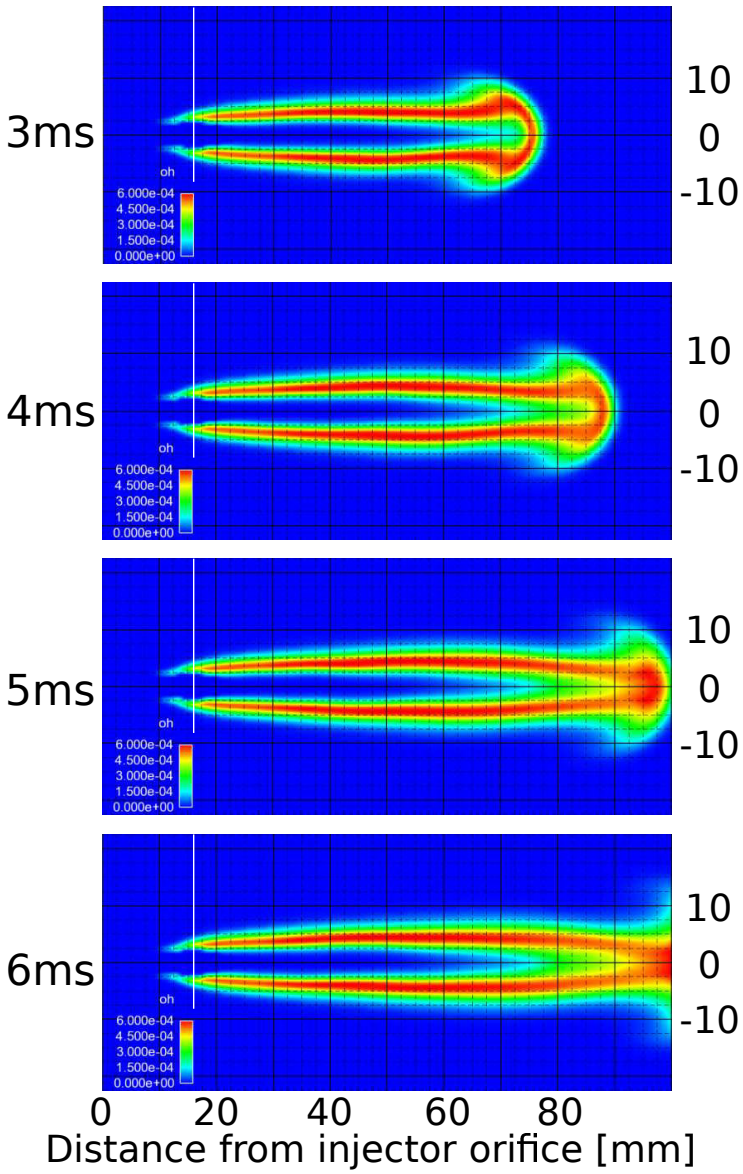

Figure 5.9: OH mass fraction fields in the plane containing the spray axis at four different times after SOI (3 ms, 4 ms, 5 ms, 6 ms) for the reference case, with an indication of the experimental lift-off length.

mostly interpreted in this model as a local heterogeneity of mixture fraction. On the contrary, LES has the ability to represent this intermittency thanks to the simulation of many realizations of the spray injection [176]. Last, even if the combustion model includes a fluctuations representation of the mixture fraction distribution, the soot model itself is homogeneous. Thus, the soot phase evolution is driven by the mean species concentrations read by the soot model. This impedes to represent the strong production of soot within the real instantaneous gradient. This also explains why the quasi-steady state soot mass predicted by the model occurs later than the experimental one, the initial amount of soot being formed during a longer time.

The predicted SVF at four different times after SOI are compared with the time-averaged ex-

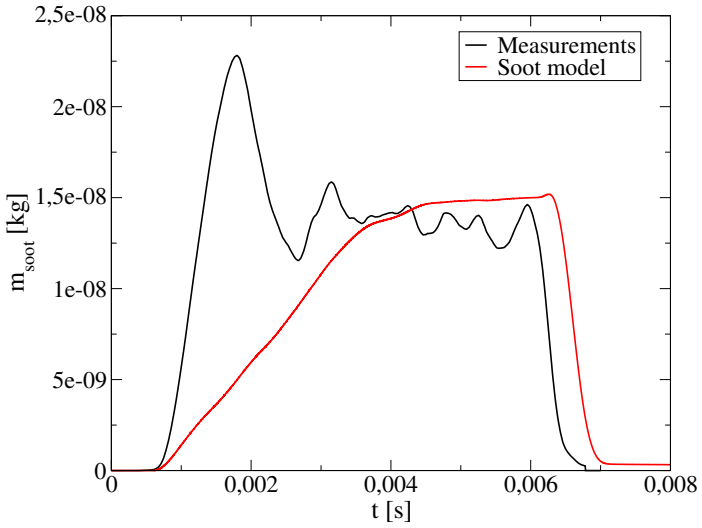

Figure 5.10: Comparison between the experimental and predicted soot mass integrated over the experimental measurement windows as a function of time for the reference case.

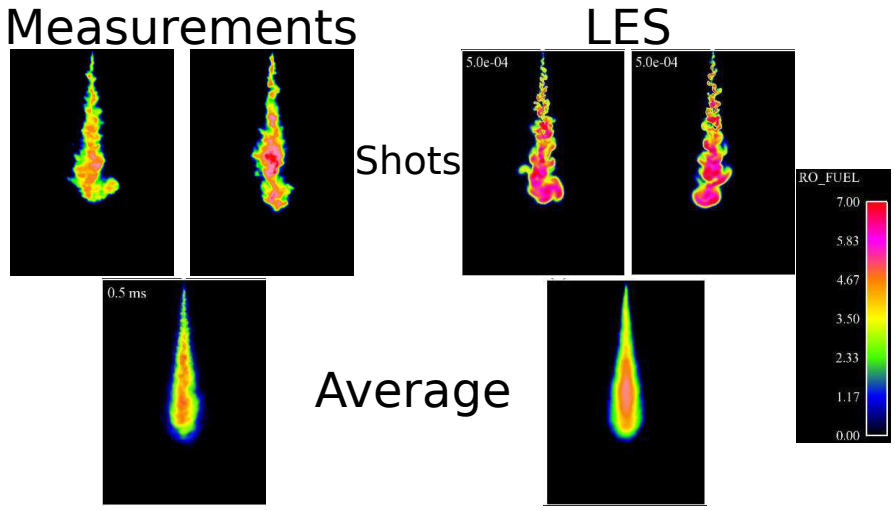

Figure 5.11: Comparisons of experimental measurements (left) and LES predictions (right) of mixture fractions in a Diesel-like spray 0.5 ms after the beginning of injection with two individual shots of each (top) and the averaged value over 30 realizations (bottom) [176].

perimental SVF in Fig. 5.12. The predicted SVF are stabilized after 4 ms as indicated by the soot mass. The stabilized predicted SVF location and width are similar to those of the experiments. The absolute values of the SVF fields cannot be compared since the experimental one is averaged from 1.8 ms to 5.8 ms [165], including a first long duration without soot in the regions where negligible SVF is observed, thus lowering the measured SVF. The predicted SVF fields in the plane containing the spray axis are shaped by the balance between a strong soot production in the rich regions next to the spray axis and oxidation in the regions with a large amount of hydroxyl on the side of the spray and further from the injector nozzle as illustrated in Fig. 5.13. The shape of the particle inception

and condensation source terms are explained by the fact that these phenomena are controlled by pyrene and acetylene which maxima are not located in the same regions of the spray as shown in Fig.5.14.

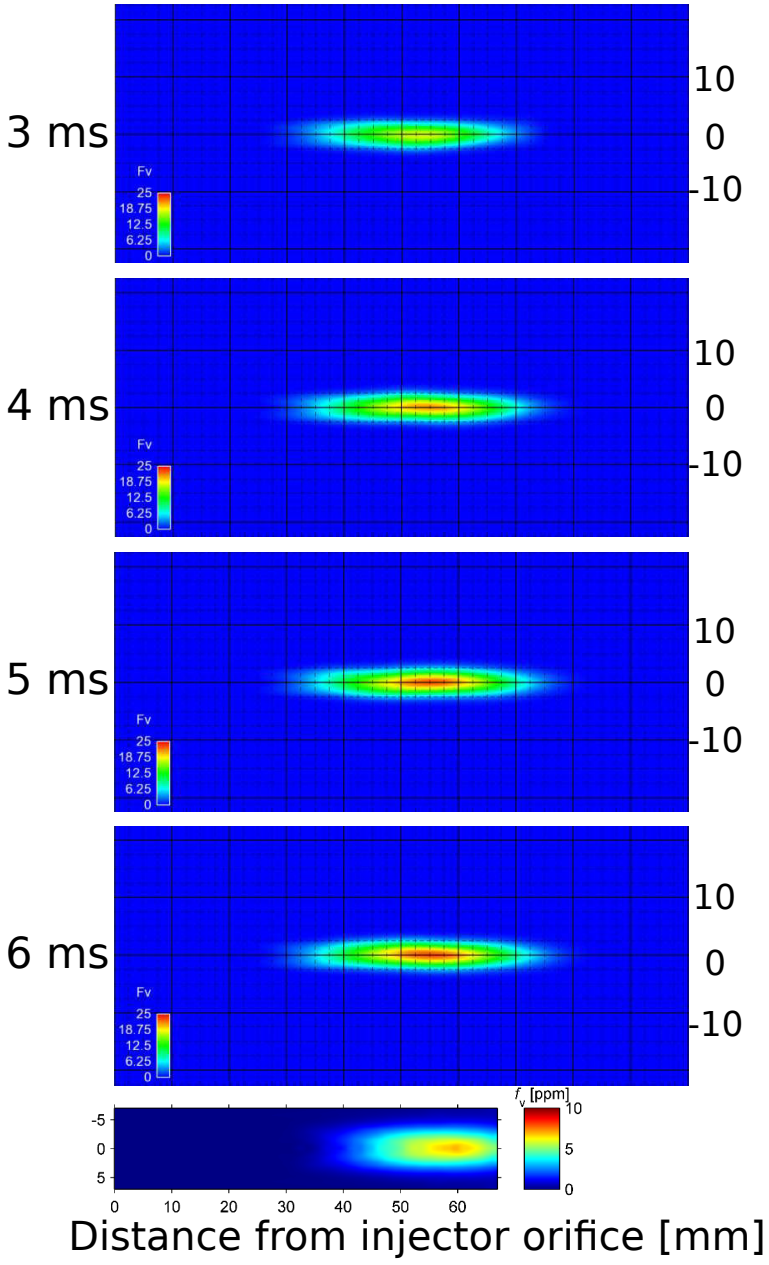

Figure 5.12: SVF fields in the plane containing the spray axis at four different times after SOI (3 ms, 4 ms, 5 ms, 6 ms) compared to the time-averaged experimental SVF for the reference case

Finally, the dynamics of the soot production is analysed using the global source terms evolutions presented in Fig. 5.15. The quasi-steady state corresponds to a balance between the surface growth and condensation, in the one hand, and oxidation source term, in the other hand, for this spray while particle inception only triggers the soot production processes. Further studies, for instance

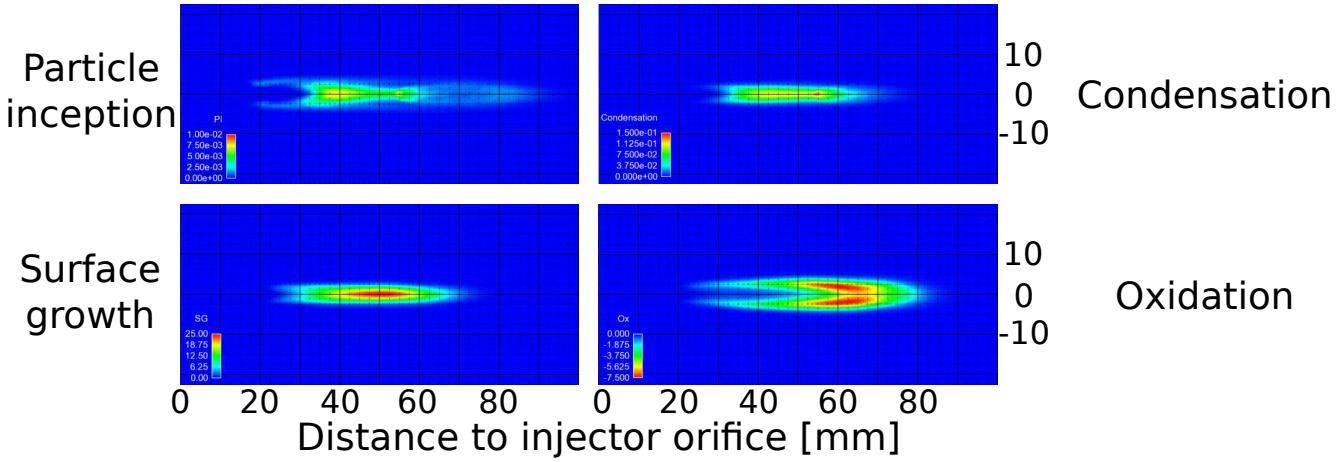

Figure 5.13: Soot mass fraction source terms (s^{-1}) fields in the plane containing the spray axis predicted by the soot model for the reference case 5.5 ms after SOI, including particle inception (top left), condensation (top right), surface growth (bottom left) and oxidation (bottom right).

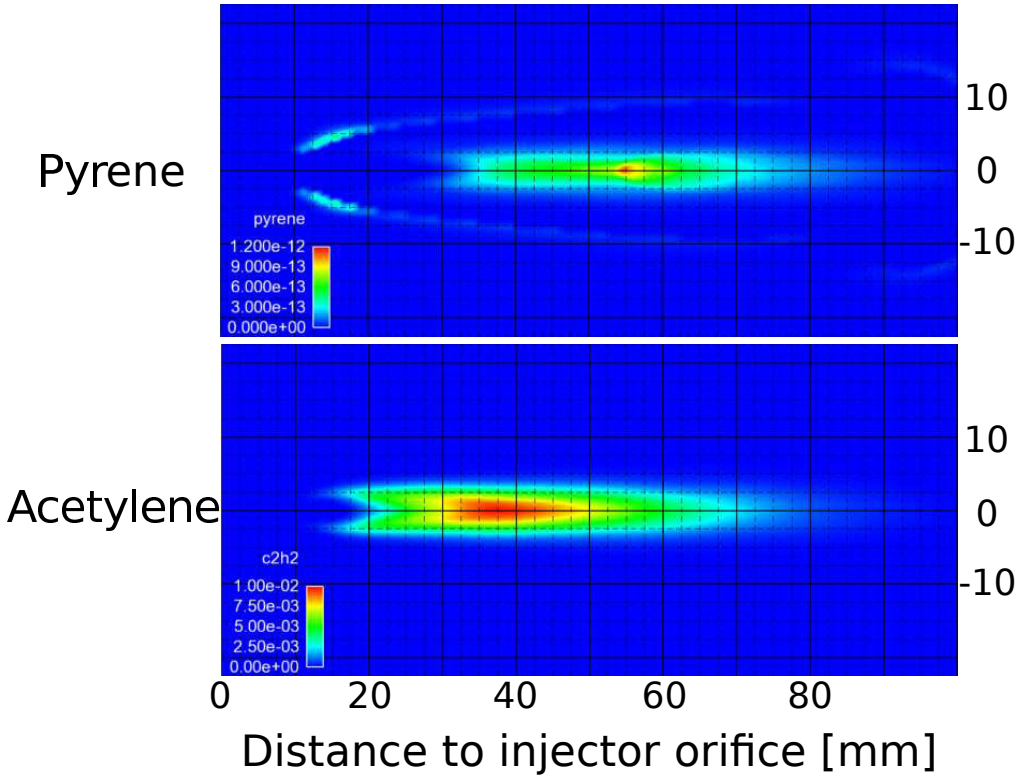

Figure 5.14: Pyrene (top) and acetylene (bottom) mass fractions fields in the plane containing the spray axis predicted by the ADF-PCM model for the reference case 5.5 ms after SOI.

on the version of Spray A with a fuel containing some aromatics species, could allow to figure out if this balance is specific to these conditions and to Dodecane or if they are more universal. Indeed,

Dodecane is a heavy fuel but it does not contain aromatic species which are directly involved in soot precursors kinetics.

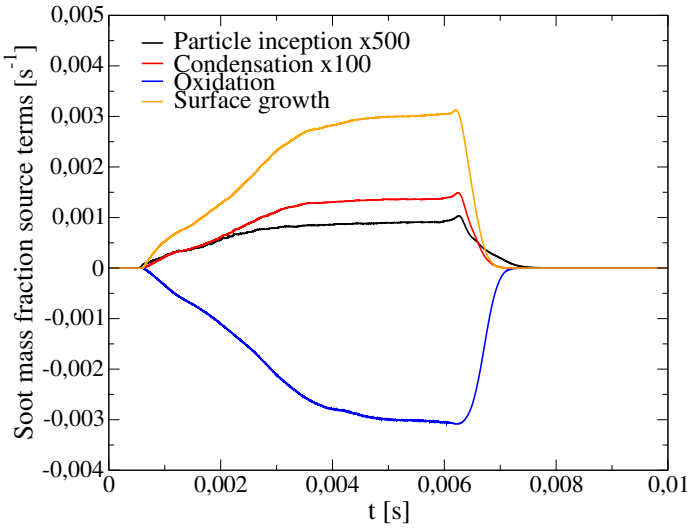

Figure 5.15: Time-evolution of the particle inception, condensation, surface growth and oxidation source terms for the reference case.

5.4.5 Variations

In the ECN database, the variations of dilutant mass fraction and of ambient gas temperature include soot measurements. All the available variations have been simulated in this study and the results are given in this section. These results underline the ability of the proposed models to reproduce the effects of dilutant and ambient temperature on flame structure and soot production. The limits of this modeling approach are also presented and discussed.

5.4.5.a EGR sweep

Combustion indicators. Figure 5.16 illustrates the ability of the ADF-PCM model to reproduce lift-off lengths in the Spray A conditions for different dilutant mass fractions. The trends are well reproduced with an acceptable error smaller than 1 mm between the experimental measurements and the predicted lift-off lengths.

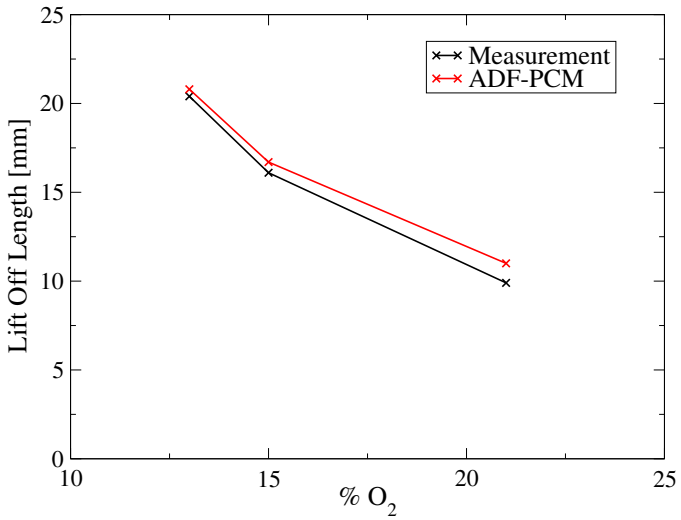

Figure 5.16: Evolution of the lift-off lengths with the oxygen molar fractions (cases 1 to 3).

Prediction of ignition delays for the same variations are showed in Fig. 5.17. As for the reference case, the ignition delays for the two other initial compositions are too long. However, the global trend is reproduced with predicted ignition delays which increase with the mass fraction of dilutant.

Soot production. The evolution of soot production is illustrated in Fig. 5.18 with the soot mass time-evolution for the three different dilutant mass fractions. The model reproduces the apex of the stabilized soot mass value for the reference case compared to the two other values of dilutant mass fractions, which are 0.387 and 0.018 for cases 2 and 3 against 0.294 for the reference case. This evolution depends on the dilutant mass fraction because of the competition between the soot growth phenomena and oxidation as shown in Fig. 5.19. For case 3 where the dilutant mass fraction is the lowest, the particle inception reaction rate increases due to the higher temperature reached, which provides more particles in the surface growth regions compared to the two cases. The surface growth is also increased by these conditions with twice the value of the reference case for a similar mass of soot. However, this does not lead to a larger mass of produced soot particles because the

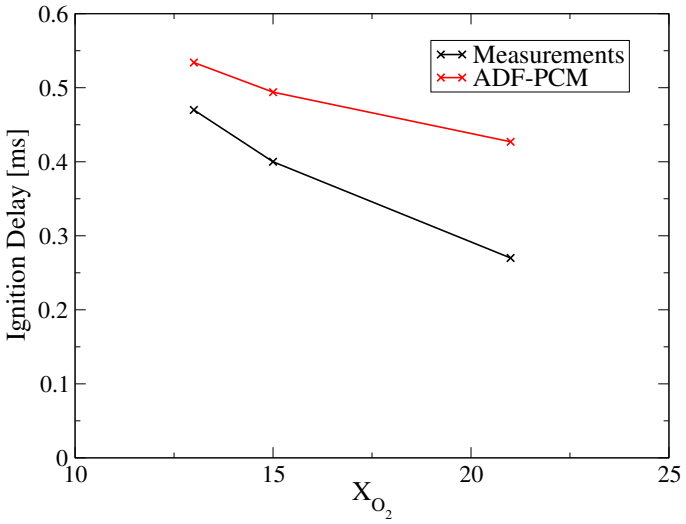

Figure 5.17: Evolution of the ignition delays with the oxygen molar fractions (cases 1 to 3).

high temperature combined to a more oxidizing gaseous composition also allows a higher oxidation reaction rate. With the increase of the dilutant mass fraction, the reaction rates of these two phenomena decrease. The oxidation is more limited than the soot growth phenomena between cases 1 and 3. This leads to an increase of the soot production as the dilutant mass fraction increases. However, the evolution is different between cases 1 and 2 where the dilutant mass fractions are higher. The main reason of this difference is that the soot particles, following the lift-off lengths, get further downstream as the dilutant mass fraction increases. This locates a part of the soot mass outside of the experimental measurement windows as illustrated for case 1 in Fig. 5.12 where a part of the SVF is located outside of the measurement windows.

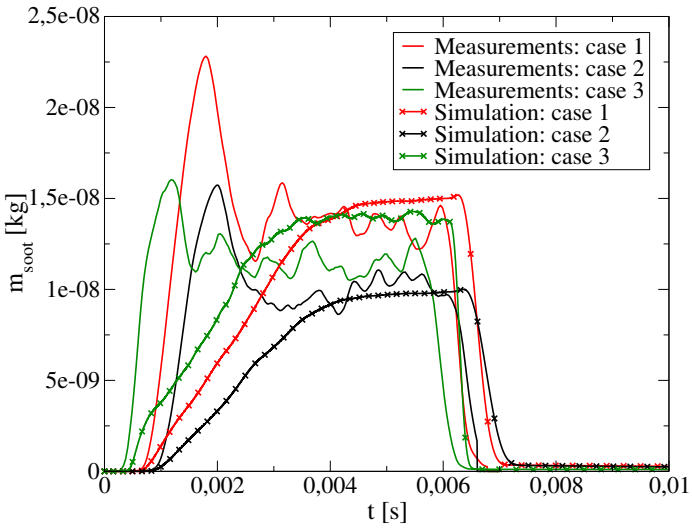

Figure 5.18: Comparison between experimental and predicted soot mass time-evolution with three different dilutant mass fractions (cases 1 to 3).

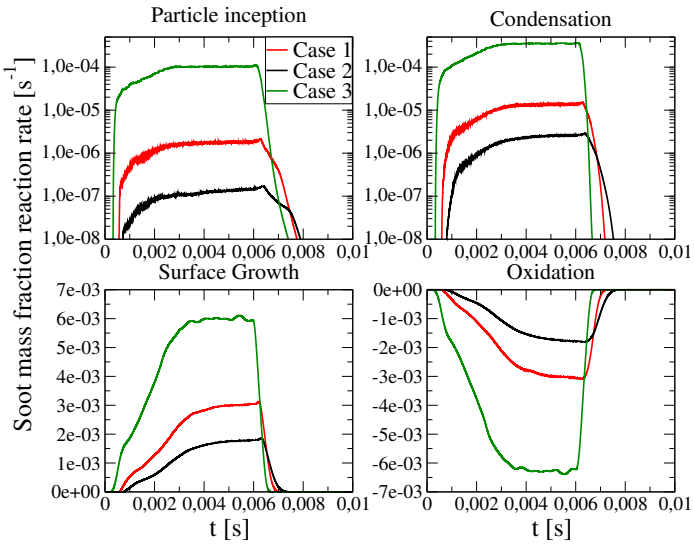

Figure 5.19: Comparison between the time-evolution of the space-averaged soot reaction rates of particle inception (top left), condensation (top right), surface growth (bottom left) and oxidation (bottom right) with three different dilutant mass fractions (cases 1 to 3).

5.4.5.b Ambient temperature sweep

Combustion indicators. The predicted lift-off lengths and ignition delays depending on ambient gas temperatures are given in Fig. 5.20 and Fig. 5.21. The predicted lift-off lengths and ignition delays for low temperature cases are well reproduced. The variation between the reference case and case 7 is not correctly reproduced for the ignition delay as for the lift-off length. The most probable explanation for this error is the lack of accuracy in the description of the NTC region by the detailed mechanism. This point is detailed next.

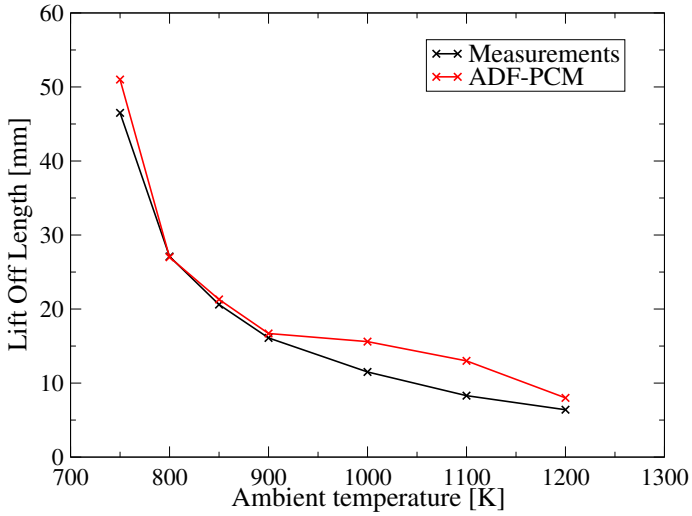

Figure 5.20: Lift-off lengths depending ambient gas temperatures.

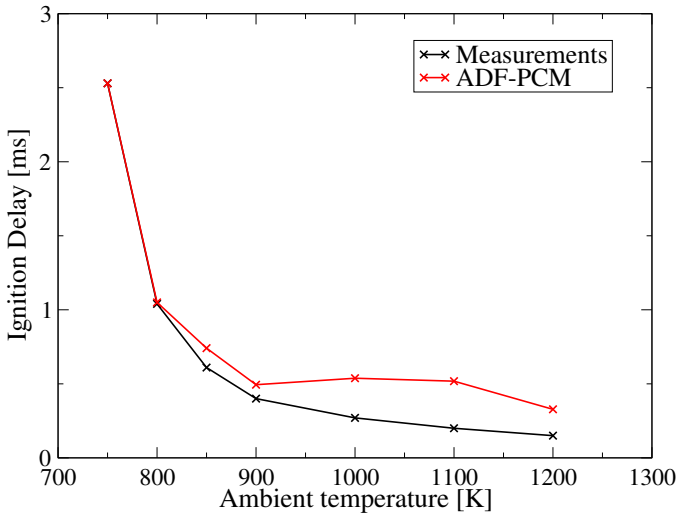

Figure 5.21: Ignition delays depending ambient gas temperatures.

Dodecane ignition delay measurements in shock tubes are available in Vasu *et al.* [177]. These measurements are compared with predicted ignition delays of constant volume reactors simulated with the IFP-Kinetics library solver [136], using the kinetic scheme used to generate the look-up table, proposed by Narayanaswamy *et al.* [141], and two other kinetic schemes which are the JetSurF2.0 [178] and the scheme proposed by Malewicki and Brezinsky [179]. These results, given in Fig. 5.22, cannot be taken as direct indications whether the ignition delay should be shorter or longer at a given temperature since these cases are homogeneous and at initial pressures and temperatures much lower than in the Spray A case. Still, they illustrate a chemical effect of dodecane combustion. A very strong NTC occurs in a temperature range which is the one where the ADF-PCM combustion model, based on source terms taken from homogeneous chemistry, provides less accurate results for the Spray A simulations. Similar results are obtained by Pei *et al.* [180] for shock tubes simulations as well as Spray A simulations using different kinetic schemes and combustion models. They also illustrate the challenge that the Spray A modeling constitutes with high pressures and temperatures conditions and a heavy fuel which combustion properties are not yet well modeled.

Soot production. Experimental soot mass time-evolutions are only available for cases 6 and 7 of the temperature sweep. A comparison between the predicted soot mass time-evolutions and the measurements is given in Fig. 5.23. It shows that the effect of ambient temperature on the soot yield is well reproduced from 850 K to 900 K but not from 900 K to 1000 K. This behavior was predictable for case 7 at 1000 K. Indeed, this case is located in the NTC region of the employed mechanism. As the lift-off length and auto-ignition delay are poorly reproduced at this temperature, it can be inferred that the gaseous temperature and minor species are also poorly reproduced. In this situation, one can not expect the soot model to predict correct soot profiles. This case illustrates the importance of the gaseous phase representation in advanced soot modeling, and thus the importance of the combustion model the soot model is coupled with.

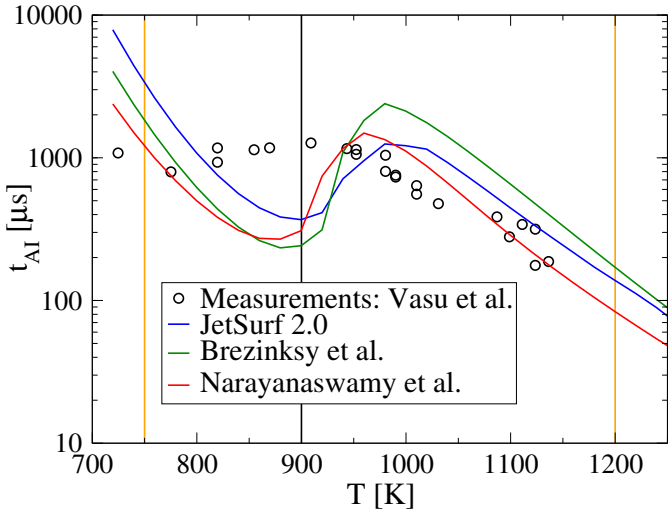

Figure 5.22: Ignition delays of stoichiometric Dodecane/Air mixture depending on the initial temperatures for constant volume homogeneous reactors at an initial pressure of 20 bar using different kinetic schemes compared to shock tube ignition delays measurements. The reference Spray A temperature (vertical black line) and the Spray A experiments temperature range (vertical orange lines) are indicated.

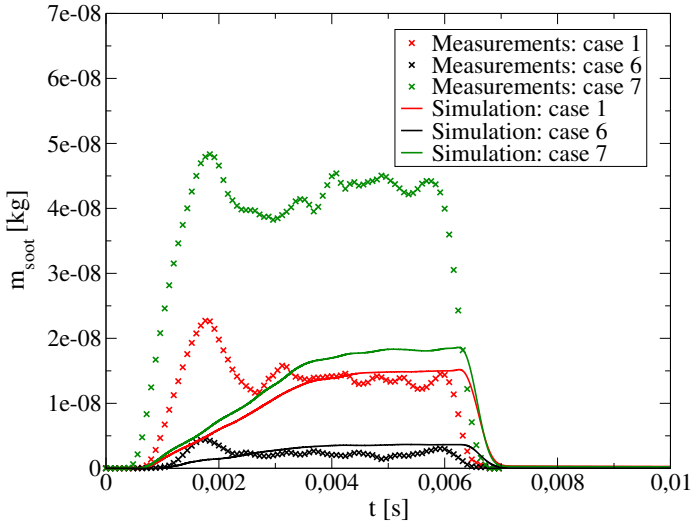

Figure 5.23: Comparison between experimental and predicted soot mass time-evolution with three different dilutant mass fractions (cases 1 to 3).

5.5 Conclusion

In this article, the coupling of a sectional soot model with the ADF-PCM model is evaluated against experimental measurements for the Spray A [164, 165, 166] of the Engine Combustion Network (ECN), a high pressure Dodecane spray. The ability of the ADF-PCM model to reproduce the flame structure is studied as well as the sectional soot model predictions for Soot Volume Fraction (SVF) and total soot mass. The sectional soot model is based on the description proposed in [77, 78], adapted to CFD in [162].

This soot model requires as input parameters minor species mass fractions which are not available using simplified kinetics. For this reason, it can only be coupled with a combustion model which describes these minor species. The ADF-PCM model [151, 163, 159] has been chosen since it allows the representation of minor species at a low computational cost by tabulating very detailed kinetic schemes (here the one proposed by Narayanaswamy *et al.* [141] of 255 species and 1509 reactions) and also takes into account the diffusion flame structure and mixture fraction heterogeneities (thanks to a probability density function).

In order to validate this approach in Diesel-like conditions, the ECN Spray A has been chosen as a validation case. This choice is justified by the fact that a large experimental database, including soot measurements, is available for this Dodecane spray in a constant volume vessel at high pressure.

Two parametric variations around the Spray A reference case have been simulated, representing nine different cases including five cases with soot measurements. The results of these simulations are promising with a good ability to reproduce both the main combustion indicators and the stabilized soot production for most of these cases. The effects of dilutant mass fraction on the stabilized soot mass are well reproduced. Initial temperature effects are also predicted with a good agreement outside of the interval of 900 K to 1000 K. This interval corresponds to the NTC region of Dodecane which seems to be over-predicted by the kinetic scheme used in the present study. However, the predicted soot mass evolutions in time lack the first peak measured experimentally. They also raise two fundamental issues of Diesel spray modeling:

- Heavy fuel chemistry is still uncertain and even if current schemes allow a good representation of stabilized combustion, they still have a limited ability to model some transient effects such as the ignition delays in high pressure cases.
- Soot chemistry is not yet fully understood and more work on soot modeling and coupling with turbulent combustion models is required to represent the initial production of soot in sprays.

Future work will be devoted to the application of the present soot model to LES of the same experiment possibly allowing to quantify the importance of spray intermittency on the soot average production.

Chapter 6

Conclusions and perspectives

6.1 Conclusions

The current concern on the effect of particulate matter on environment and public health has forced the car industry to study not only the way to treat these particles in the exhaust pipe but also their formation in the combustion chamber. Indeed, the arising question of the number and size of soot particles cannot be solved by considering only the exhaust after-treatment systems. The present work addresses the numerical aspect of this issue by proposing models to simulate the raw-engine soot yield and size distribution that will allow engine manufacturers to develop cleaner engine technologies.

After a detailed presentation of the industrial issue which includes global statistics as well as the basics of the physical and technological topics involved, a state-of-the-art of the soot particles modeling is presented. This review illustrates the complexity of modeling soot particles yield and size distribution in the industrial context. Indeed, it requires:

- a detailed representation of the fuel cracking and carbon species evolutions during combustion reactions;
- a detailed soot model which can interact with a detailed gas phase chemical reactions and represent the soot size distribution evolutions;
- the ability to apply the two previously mentioned aspects in 3-D turbulent simulations to take into account the spatial heterogeneities;
- a coupling of all these factors which provides results with an industrially reasonable CPU time.

6.1.1 Soot modeling

The sectional method appeared to be the method that best fits these objectives. Thus, a reference sectional soot model previously validated on simulations of C_2 fuels laminar flames was used as a basis for this PhD work. Evolutions on the distribution of source terms among the sections were proposed. These evolutions were validated against the same experiments as the reference model, giving satisfactory results to allow further use of the modified model. Finally, a different set of surface chemistry constants, taken from literature and previously used in Diesel engine simulations, was used with this model for the 3-D RANS simulations.

6.1.2 Diesel engine simulations

6.1.2.a Specific developments

After these soot model developments, the major development work achieved in this thesis concerns the coupling of the soot model with the gaseous phase description, that is, with the turbulent combustion model. For this purpose, a tabulated approach dedicated to variable pressure combustion was used and adapted from a previous work proposed by IFPEN [145]. This model allows a correct description of essential minor species involved in the soot source terms. This constitutes a major progress compared to available descriptions of the literature that always consider constant pressure tabulations, thus leading to very important errors on the soot source terms during the expansion stroke.

The soot model was also coupled to a kinetic solver to simulate a reference case for a first validation of the coupling with the tabulated approach. This validation was done in specifically developed variable volume and mixture fraction reactors which reproduce Diesel-like conditions while allowing the reference simulation with the kinetic solver at a reasonable CPU time.

6.1.2.b Experimental validations

A database of Diesel engine operating conditions including measurements of soot size distributions at exhaust was used. This database also allowed the validation of the Diesel surrogate because all the conditions were done with a commercial Diesel fuel as well as the modeled surrogate (30% 1-Methylnaphthalene and 70% Decane in liquid volume) to ensure experimentally that the heat release, soot yield and soot size distribution were similar. Then, the database was simulated using the RANS code IFP-C3D. The soot modeling results, soot yields as well as soot size distributions, showed a very good agreement with the experimental results on 9 of the 11 operating conditions with only the variation in injection pressure which was not correctly predicted. These results were also obtained with a very low CPU time (one operating conditions obtained in 4 to 8 hours on 8 processors) thanks to the tabulated chemistry which allows to include the results from kinetic schemes with hundreds of species and thousands of reactions in 3-D RANS simulations.

6.1.3 Diesel Spray

A high pressure and temperature Diesel-like spray in a constant volume vessel was simulated. The Spray A, a well documented spray operated by the various laboratories involved in the Engine Combustion Network has been chosen as a reference. Among the variations performed on the Spray A, variations of ambient gas temperature and composition included soot measurements.

6.1.3.a Specific developments

The first simulations were run using the same combustion and soot model as these of the Diesel engine. However, the VPTHC coupled to ECFM3Z model underestimated the flame lift-off variations. To validate the ability of the soot model to predict soot location, the flame lift-off predictions had to match the experimental measurements. Thus, the soot model was coupled to the ADF model [151], a more detailed tabulated model, which takes into account a more detailed mixture fraction stratification and strain while being able to predict the minor species required by the soot model.

Moreover, the sectional soot model used in the Diesel engine simulations did not predict correctly the variations of the oxidation by hydroxyl reaction rate. This was shown to be due to the quasi-steady state approximation used to couple the HACA mechanism to the sectional method to represent soot surface chemistry. Thus, the surface chemistry reaction rates have been read directly from the constants of the HACA mechanism. This solution provided a more physical evolution of hydroxyl reaction rate in the spray.

6.1.3.b Experimental validations

After a validation of the ability of IFP-C3D to reproduce non-reactive spray characteristics, the two variations including soot measurements were simulated. The predictions of the models were good. First, the ADF model used to model the gas phase evolution predicted the main combustion indicators (lift-off lengths and ignition delays) with a good accuracy. This stands as another validation of this model. Then, the sectional soot model predictions of soot volume fraction and total soot mass showed a good agreement with the experimental measurements. These results validate both the sectional soot model and the ability of the ADF model to predict species involved in soot formation and oxidation. However, the predicted total soot mass evolutions in time lacked the first peak measured experimentally. This difference was shown to be due to the RANS approach which is unable, unlike LES, to predict the steep mixture fraction front at the leading point of the gaseous jet.

6.2 Perspectives

The proposed sectional soot model and its coupling with two versions of a tabulated chemistry combustion model provided satisfactory results against experiments. However, these two experimental validations also pointed out the fact that soot modeling is a real challenge and many aspects of soot particle formation and oxidation processes still have to be understood to obtain a universal model.

6.2.1 Soot modeling

This study illustrated the uncertainties concerning some phenomena involved in soot formation and oxidation. Indeed, the reaction constants of pyrene polymerization used for the simulations of the two experimental validations are different. The fractal dimensions used to link soot particles surfaces to their volumes were also slightly different between the two experimental validations. Their minimum and maximum values were the same but the threshold which separates them was different. These differences are mostly attributed to the difference in the fuel components. Indeed, the fuel molecular composition influences:

- The particle inception physics: the presence of aromatic species in the fuel might change the balance between the physical phenomena involved in particle inception by facilitating different reaction pathways to larger PAH. These new pathways might not include the specific species (radical pyrene) used by the model as an indicator of soot particle inception, thus requiring to change the rate of particle inception with respect to the radical pyrene concentration.

- The particles structure: the growth of particles should be different as pointed by Fig.4.27 for the engine case and Fig.5.15 for the Spray A. With a fuel composition including aromatics, the gain of carbon in the solid phase is mainly due to PAH (particle inception and condensation)

while for a pure alkane fuel it is mainly due to acetylene addition. The addition of a species containing 18 carbon atoms should lead to different particle shape than the addition of a species containing 2 carbon atoms. This difference is not yet taken into account by this model and can only be guessed with the fractal dimension imposed as a parameter.

- The kinetic scheme used to represent chemistry: this indirect effect is due to the uncertainties in the chemistry of large aromatics which can be predicted with orders of magnitude of difference by two kinetic schemes for the same case. These uncertainties explain why ad-hoc parameters are still required in the soot models to compensate these incertitudes. As most of the time kinetic mechanisms are only validated for a reduced number of fuel species, this implies to change the kinetic mechanism when changing the fuel formulation or to merge existing mechanisms.

6.2.2 Chemistry-turbulence interactions

Detailed experiments of the Spray A have also pointed out that the coupling between the sectional soot model and the turbulent reactive flow could be improved. In the proposed model, the dispersed soot phase is homogeneous inside a mesh cell. Even if the combustion model takes into account the mixture fraction stratification, the inputs of the model are also averaged on a cell. Some studies already exist to treat these issues using the method of moments:

- Balthasar *et al* [111] proposed to include the soot moments involved in the PDF transport approach computing the flow scalars. A similar approach has recently been used in LES [109, 110, 115] showing that even in LES the subfilter interactions between soot particles and the small turbulence structures influence the soot phase evolution.

- The resolution of the soot moments as conditionally-averaged scalars in a Conditional Moment Closure (CMC) approach is also possible to take into account the soot evolution depending on the mixture fraction. This approach, which is commonly used with semi-empirical approaches [91, 181, 182], has recently been used with the method of moment by Lehtiniemi *et al.* [183].

These approaches can include differential diffusion effects on the soot phase. Indeed, large aromatic species involved in particle inception have a large sensitivity to these effects according to recent DNS results [73, 118]. Taking into account the mixture fraction stratification requires assumption about the maximum mixture fraction. It is considered constant in the present work, but a more detailed representation can be integrated, thus influencing the mixture fraction stratification and the scalar dissipation rate, as in Netzell *et al.* [78].

6.2.3 Multi-physics modeling

All other phenomena involved in devices using combustion have to be modeled with a good accuracy to capture soot particles formation and oxidation. This includes the ability to represent a detailed chemistry in 3-D turbulent combustion which has been studied here and for which the use of tabulated chemistry showed to be a viable solution.

It also means that the representation of the fluctuations, of mixture fraction and temperature mostly, has to be accurate because the species involved in soot particle inception are very sensitive

to these parameters. Otherwise, improvements of the chemistry-turbulence interactions modeling would not improve the final ability to predict the soot phase variations.

Finally, the mixture fraction heterogeneities also depend on the ability of the two-phase flow models to predict the spray shape and variations with essential parameters. Most devices concerned with soot norms employ a fuel injector located close to the combustion region which make the ability to predict the spray a crucial need for properly modeling soot in industrial systems.

6.3 Future works

The previous perspectives indicate that pursuing the present modeling effort for Diesel engines is a necessary task. In this direction, a PhD is today starting at IFPEN on the modeling of PAH and particle inception.

In the field of gas turbines, the soot models used today in the industry are very similar to those used for Diesel engines. For this reason, the model developed in this work will be adapted to the LES of gas turbines in another PhD.

Bibliography

[1] T. Poinsot and D. Veynante. *Theoretical and Numerical Combustion*. 2012.

[2] U.S. Energy Information Administration. International energy outlook. 2010.

[3] S.C. Davis, S.W. Diegel, and R.G. Boundy. Transportation energy data book : Edition 33. 2014.

[4] CCFA. L'industrie automobile française. In *Analyse et statistiques*, 2014.

[5] F. Pischinger, H. Schulte, and J. Hansen. Grundlagen und entwicklungslinien des dieselmotorischen brennverfahren. In VDI-Berichte, editor, *Die Zukunft des Dieselmotors*, pages 61–93, Düsseldorf, 1988.

[6] S. Barbusse and G. Plassat. Les particules de combustion automobile et leurs dispositifs d'élimination. In *ADEME : Données et références*, 2005.

[7] M. Ba and J. Colosio. Qualité de l'air : une surveillance accrue des particules, mais des concentrations à réduire d'ici l'an 2005. *IFEN, les données de l'environnement*, 58:1–5, 2000.

[8] *Les dossiers du CCFA : Automobile et qualité de l'air*, 2005.

[9] G. T. O'Connor, L. Neas, B. Vaughn, M. Kattan, H. Mitchell, E. F. Crain, R. Evans, R. Gruchalla, W. Morgan, J. Stout, G. K. Adams, and M. Lippmann. Acute respiratory health effects of air pollution on children with asthma in US inner cities. *The Journal of allergy and clinical immunology*, 121:1133–1139, 2008.

[10] T. Nicolai, D. Carr, S.K. Weiland, H. Duhme, O. Von Ehrenstein, C. Wagner, and E. Von Mutius. Urban traffic and pollutant exposure related to respiratory outcomes and atopy in a large sample of children. *European Respiratory Journal*, 21:956–963, 2003.

[11] K. Donaldson, L. Tran, L.A. Jimenez, R. Duffin, D.E. Newby, N. Mills, W. MacNee, and V. Stone. Combustion-derived nanoparticles: A review of their toxicology following inhalation exposure. *Part. Fibre Toxicol.*, 2:10, 2005.

[12] S. Kamm, O. Möhler, K.-H. Naumann, H. Saathoff, and U. Schurath. The heterogeneous reaction of ozone with soot aerosol. *Atmospheric Environment*, 33:4651–4661, 1999.

[13] M. Shiraiwa, Y. Sosedova, A. Rouvière, H. Yang, Y. Zhang, J. P. D. Abbatt, M. Ammann, and U. Pöschl. The role of long-lived reactive oxygen intermediates in the reaction of ozone with aerosol particles. *Nature Chemistry*, 3:291–295, 2011.

[14] M. Jacobson. Control of fossil-fuel particulate black carbon and organic matter, possibly the most effective method of slowing global warming. *J. Geophys. Res.*, 107(D19):4410, doi:10.1029/2001JD001376, 2002.

[15] K. Adachi, S. H. Chung, and P. R. Buseck. Shapes of soot aerosol particles and implications for their effects on climate. *J. Geophys. Res.-Atmos.*, 115(D15), 2010.

[16] T.C. Bond. Can warming particles enter global climate discussions? *IOP Publishing*, 2, 2007.

[17] Union Européenne. REGLEMENT (CE) No 715/2007 DU PARLEMENT EUROPEEN ET DU CONSEIL du 20 juin 2007 relatif à la réception des véhicules à moteur au regard des émissions des véhicules particuliers et utilitaires légers (Euro 5 et Euro 6) et aux informations sur la réparation et l'entretien des véhicules. In *Journal officiel de l'Union Européenne*, 2007.

[18] J. Andersson, G. Barouch, R. Munoz-Bueno, E. Sandbach, and P. Dilara. Particle measurement programme (pmp) light-duty inter-laboraty correlation exercice (ilce-ld) final report. Technical report, European Commission - Joint Research Centre, 2007.

[19] A. Robert, S. Richard, O. Colin, L. Martinez, and L. De Francqueville. Les prediction and analysis of knocking combustion in a spark ignition engine. *Proc. Combust. Inst.*, In Press, 2014.

[20] A. Favre. Equations des écoulements turbulents compressibles. *Journal de mécanique*, 1965.

[21] J. Boussinesq. *Théorie de l'écoulement tourbillonnant et tumultueux des liquides dans les lits rectilignes à grande section.* 1897.

[22] V. Yakhot, S.A. Orszag, S. Thangam, T.B. Gatski, and C.G. Speziale. Development of turbulence models for shear flow by a double expansion technique. *Phys. Fluids*, 4(7):1510–1520, 1992.

[23] W.P. Jones and B.E. Launder. The prediction of the laminarization with 2-equations model of turbulence. *Int. J. Heat Mass Transfer*, (15), 1972.

[24] M. Gradzinski, H. Hercman, M. Nowak, and P. Bella. Age of black coloured laminae within speleothems from Domica Cave and its significance for dating of prehistoric human settlement. *Geochronometria*, 28:39–45, 2007.

[25] F. Ospitali, D. C. Smith, and M. Lorblanchet. Preliminary investigations by Raman microscopy of prehistoric pigments in the wall-painted cave at Roucadour, Quercy, France. *Journal of Raman Spectroscopy*, 36:1063–1071, 2006.

[26] M. Frenklach. Reaction mechanism of soot formation in flames. *Phys. Chem. Chem. Phys.*, 4:2028–2037, 2002.

[27] J. A. Cole, J. D. Bittner, J. P. Longwell, and J.B. Howard. Formation mechanisms of aromatic compounds in aliphatic flames. *Combust. Flame*, 56:51–70, 1984.

[28] M. Frenklach, D. W. Clary, W.C Jr Gardiner, and S. E. Stein. Detailed kinetic modeling of soot formation in shock-tube pyrolysis of acetylene. *Proc. Combust. Inst.*, 20:887–901, 1985.

[29] J.A. Miller and C. F. Melius. Kinetic and Thermodynamic Issues in the Formation of Aromatic Compounds in Flames of Aliphatic Fuels. *Combust. Flame*, 91:21–39, 1992.

[30] R. D. Kern and K. Xie. Shock tube studies of gas phase reaction preceding the soot formation process. *Prog. Energ. Combust.*, 17:191–210, 1991.

[31] C. F. Melius, M. E. Colvin, N. M. Marinov, W. J. Pitz, and S. M. Senkan. Reaction mechanisms in aromatic hydrocarbon formation involving the C5H5 cyclopentadienyl Moiety. *Proc. Combust. Inst.*, 26:685–692, 1996.

[32] E. Ikeda, R. S. Tranter, J. H. Kiefer, R. D. Kern, H.G. Singh, and Q. Zhang. The pyrolysis of methylcyclopentadiene : isomerization and formation of aromatics. *Proc. Combust. Inst.*, 28:1725–1732, 2000.

[33] A. Lamprecht, B. Atakan, and K. Kohse-Hoinghaus. Fuel-rich propene and acetylene flames: A comparison of their flame chemistries. *Combust. Flame*, 122:483–491, 2000.

[34] H.A. Gueniche, J. Biet, P.A. Glaude, R. Fournet, and F. Battin-Leclerc. A comparative study of the formation of aromatics in rich methane flames doped by unsaturated compounds. *Fuel*, 88:1388–1393, 2009.

[35] C.L. Rasmussen, Skjøth-Rasmussen M.S., A.D. Jensen, and P. Glarborg. Propargy recombination: estimation of the high temperature, low pressure rate constant from flame measurements. *Proc. Combust. Inst.*, 30:1023–1031, 2005.

[36] Y. Giorgievskii, J.A. Miller, and S.J. Klippenstein. Association rate cconstant for rreaction between resonance-stabilized radicals: $c_3h_3 + c_3h_3$, $c_3h_3 + c_3h_5$, and $c_3h_5 + c_3h_5$. *Phys. Chem. Chem. Phys.*, 9:4259–4268, 2007.

[37] R. S. Tranter, X. Yang, and J. H. Kiefer. Dissociation of c_3h_3i and rates of c_3h_3 combination at high temperatures. *Proc. Combust. Inst.*, 33:259–265, 2011.

[38] A. Nawdiyal, N. Hansen, T. Zeuch, L. Seidel, and F. Mauss. Experimental and modelling study of speciation and benzene formation pathways in premixed 1-hexene flames. *Proc. Combust. Inst.*, In Press, 2014.

[39] T. Bierkandt, T. Kasper, E. Akyildiz, A. Lucassen, P. Oßwald, M. Köhler, and P. Hemberger. Flame structure of a low-pressure laminar premixed and lightly sooting acetylene flame and the effect of ethanol addition. *Proc. Combust. Inst.*, In Press, 2014.

[40] P. Desgroux, X. Mercier, and K. A. Thomson. Study of the formation of soot and its precursors in flames using optical diagnostics. *Proc. Combust. Inst.*, 34:1713–1738, 2013.

[41] M.J. Castaldi, N. M. Marinov, C. F. Melius, J. Huang, S. M. Senkan, W.J. Pit, and C.K. Westbrook. Experimental and modeling investigation of aromatic and polycyclic aromatic hydrocarbon formation in a premixed ethylene flame. *Proc. Combust. Inst.*, 26:693–702, 1996.

[42] N. M. Marinov, M. Castaldi, C. F. Melius, and W. Tsang. Aroflame and polycyclic aromatic hydrocarbon formation in a premixed propane flame. *Combust. Sci. Technol.*, 128:295–342, 1997.

[43] R.P. Lindstedt and K.-A. Rizos. The formation and oxidation of aromatics in cyclopentene and methyl-cyclopentadiene mixtures. *Proc. Combust. Inst.*, 29:2291–2298, 2002.

[44] M. Frenklach and H. Wang. Detailed modeling of soot particle nucleation and growth. *Proc. Combust. Inst.*, 28:1559–1566, 1991.

[45] J. Appel, H. Bockhorn, and M. Frenklach. Kinetic Modeling of Soot Formation with Detailed Chemistry and Physics: Laminar Premixed Flames of C2 Hydrocarbons. *Combust. Flame*, 121:122–136, 2000.

[46] H. Böhm, A. Lamprecht, B. Atakan, and K. Kohse-Höinghaus. Modelling of a fuel-rich premixed propene-oxygen-argon flame and comparison with experiments. *Phys. Chem. Chem. Phys.*, 2:4956–4961, 2000.

[47] B.V. Unterreiner, M. Sierka, and R. Ahlrichs. Reaction pathways for growth of polycyclic aromatic hydrocarbons under combustion conditions, a dft study. *Phys. Chem. Chem. Phys.*, 6:4377–4384, 2004.

[48] V. V. Kislov, N. I. Islamova, A. M. Kolker, S. H. Lin, and A. M. Mebel. Hydrogen Abstraction Acetylene Addition and Diels-Alder Mechanisms of PAH Formation: A Detailed Study Using First Principles Calculations. *J. Chem. Theory Comput.*, 1:908–924, 2005.

[49] B. Shukla and M. Koshi. Comparative study on the growth mechanisms of PAHs. *Combust. Flame*, 158:369–375, 2011.

[50] G. Blanquart, P. Pepiot-Desjardins, and H. Pitsch. Chemical mechanism for high temperature combustion of engine relevant fuels with emphasis on soot precursors. *Combust. Flame*, 158:588–607, 2009.

[51] N.A. Slavinskaya and P. Frank. A modelling study of aromatic soot precursors formation in laminar methane and ethene flames. *Combust. Flame*, 156:1705–1722, 2009.

[52] H. Wang. Formation of nascent soot and other condensed-phase materials in flames. *Proc. Combust. Inst.*, 33:41–67, 2011.

[53] C.A. Schuetz and M. Frenklach. Nucleation of soot: molecular dynamics simulations of pyrene dimerization. *Proc. Combust. Inst.*, 29:2307–2314, 2002.

[54] N.A. Eaves, S.B. Dworkin, and M.J. Thomson. The importance of reversibility in modeling soot nucleation and condensation processes. *Proc. Combust. Inst.*, In Press, 2014.

[55] K. Netzell. *Development and Application of Detailed Kinetic Models for the Soot Particle Size Distribution Function.* PhD thesis, Lund Institute of Technology, 2006.

[56] C. Marchal. *Modélisation de la formation et de l'oxydation des suies dans un moteur automobile.* PhD thesis, Université d'Orléans, 2008.

[57] P. Vervisch-Kljakic. *Modélisation des oxydes d'azote et des suies dans les moteurs Diesel.* PhD thesis, Ecole Centrale Paris, 2011.

[58] S. Sukumaran, Van Huynh C., and Kong SC. Numerical modeling of soot emissions in diesel sprays based on detailed fuel and pah chemistry. *Combust. Sci. Technol.*, 185(11):1696–1714, 2013.

[59] H. Richter and J.B. Howard. Formation of polycyclic aromatic hydrocarbons and their growth to soot - a review of chemical reaction pathways. *Prog. Energ. Combust.*, 26:565–608, 2000.

[60] B. Apicella, A. Carpentieri, M. Alfe, R. Barbella, A. Tregrossi, P. Pucci, and A. Ciajolo. Mass spectrometric analysis of large PAH in a fuel-rich ethylene flame. *Proc. Combust. Inst.*, 31:547–553, 2007.

[61] T. Blacha, M. Di Domenico, P. Gerlinger, and M. Aigner. Soot predictions in premixed and non-premixed laminar flames using a sectional approach for PAHs and soot. *Combust. Flame*, 159:181–193, 2011.

[62] M. V. Smoluchowski. Versuch einer mathematischen Theorie der Koagulationskinetik kolloider Lösungen., 1916.

[63] H. Sabbah, L. Bennier, S. Klippenstein, I.R. Sims, and B.R. Rowe. Exploring the role of pahs in the formation of soot: Pyrene dimerization. *J. Phys. Chem. Lett.*, 1:2962–2967, 2010.

[64] J. H. Seinfeld. *Atmospheric Chemistry and Physics of Air Pollution.* John Wiley & Sons, 1986.

[65] A. Kazakov and M. Frenklach. Dynamic Modeling of Soot Particle Coagulation and Aggregation: Implementation With the Method of Moments and Application to High-Pressure Laminar Premixed Flames. *Combust. Flame*, 114:484–501, 1998.

[66] S.W. Wang and S.K. Friedlander. The self-preserving particle size distribution for coagulation by brownian motion: Ii. small particle slip correction and simultaneous shear flow. *J. Colloid Interface Sci.*, 24:170–179, 1967.

[67] S.E. Pratsinis. Simultaneous nucleation, condensation, and coagulation in aerosol reactors. *J. Colloid Interface Sci.*, 124:416–428, 1988.

[68] D.W. Mackowski, M. Tassopoulos, and D.E. Rosner. *Aerosol Sci. Technol.*, 20:83–99, 1994.

[69] W.J. Menz and M. Kraft. The suitability of particle models in capturing aggregate structure and polydispersity. *Aerosol Sci. Technol.*, 47(7):734–745, 2013.

[70] J. Rissler, M.E. Messing, A.I. Malik, P.T. Nilsson, E.Z. Nordin, M. Bohgard, M. Sanati, and J.H. Pagels. Effective density characterization of soot agglomerates from various sources and comparison to aggregation theory. *Aerosol Sci. Technol.*, 47(7):792–805, 2013.

[71] A. La Rocca, G. Di Liberto, P.J. Shayler, and M.W. Fay. The nanostructure of soot-in-oil particles and agglomerates from an automotive diesel engine. *Tribol. Int.*, 61:80–87, 2013.

[72] V. Fraioli, C. Beatrice, and M. Lazzaro. Soot particle size modeling in 3D simulations of diesel engine combustion. *Combust. Theor. Model.*, 15:863–892, 2011.

[73] F. Bisetti, G. Blanquart, M. Mueller, and H. Pitsch. On the formation and early evolution of soot in tuburlent nonpremixed flames. *Combust. Flame*, 159:317–335, 2012.

[74] A. D'Anna and J.H. Kent. Modeling of particulate carbon and species formation in coflowing diffusion flames of ethylene. *Combust. Flame*, 144:249–260, 2006.

[75] A. D'Anna and J.H. Kent. A model of particulate and species formation applied to laminar, nonpremixed flames for three aliphatic-hydrocarbon fuels. *Combust. Flame*, 152:573 – 587, 2008.

[76] A. D'Anna. Detailed Kinetic Modeling of Particulate Formation in Rich Premixed Flames of Ethylene. *Energy Fuels*, 22:1610 – 1619, 2008.

[77] C. Marchal, Delfau J-L., Vovelle C., G. Moréac, Mounaïm-Rousselle C., and F. Mauss. Modelling of aromatics and soot formation from large fuel molecules. *Proc. Combust. Inst.*, 32:753–759, 2009.

[78] K. Netzell, H. Lehtiniemi, and F. Mauss. Calculating the soot particle size distribution function in turbulent diffusion flames using a sectional method. *Proc. Combust. Inst.*, 31:667–674, 2007.

[79] Q. Zhang. *Detailed modeling of soot formation/oxidation in laminar coflow diffustion flames.* PhD thesis, University of Toronto, 2009.

[80] S. Martinot, P. Beard, J. Roesler, and A. Garo. Comparison and Coupling of Homogeneous Reactor and Flamelet Library Soot Modeling Approaches for Diesel Combustion. *SAE paper*, (2001-01-3684), 2001.

[81] F. Mauss, T. Schäfer, and H. Bockhorn. Inception and Growth of Soot Particles in Dependence on the Surrounding Gas Phase. *Combust. Flame*, 99:697–705, 1994.

[82] M. Frenklach. On surface growth mechanism of soot particles. *Proc. Combust. Inst.*, 26:2285–2293, 1996.

[83] A. Khosousi and S.B. Dworkin. Detailed modelling of soot oxidation by O_2 and oh in laminar diffusion flames. *Proc. Combust. Inst.*, In Press, 2014.

[84] A. Veshkini, S.B. Dworkin, and M.J. Thomson. A soot particle surface reactivity model applied to a wide range of laminar ethylene/air flames. *Proc. Combust. Inst.*, In Press, 2014.

[85] J.C. Kaiser, N. Riemer, and D.A. Knopf. Detailed heterogeneous oxidation of soot ssurface in a particle-resolved aerosol model. *Atmos. Chem. Phys.*, 11:4505–4520, 2011.

[86] I.M. Kennedy. Models of soot formation and oxidation. *Prog. Energy Combust. Sci.*, 23:95–132, 1997.

[87] H.F. Calcote and D.M. Manos. Effect of molecular structure on incipient soot formation. *Combust. Flame*, 49:289–304, 1983.

[88] D.B. Olson, J.C. Pickens, and R.J. Gill. The effect of molecular structure on soot formation ii. diffusion flames. *Combust. Flame*, 62:43–60, 1985.

[89] P. S. Mehta and S. Dast. A correlation for soot concentration in diesel exhaust based on fuel-air mixing parameters. *Fuel*, 71:689–692, 1992.

[90] K.M. Leung, R.P. Lindstedt, and W.P. Jones. A simplified reaction mechanism for soot formation in nonpremixed flames. *Combust. Flame*, 87:289–305, 1991.

[91] M. Bolla, Y.M. Wright, K. Boulouchos, G. Borghesi, and E. Mastorakos. Soot formation modeling of n-heptane sprays under diesel engine conditions using the conditional moment closure approach. *Combust. Sci. Technol.*, 185(5):766–793, 2013.

[92] R. Said, A. Garo, and R. Borghi. Soot Formation Modeling for Turbulent Flames. *Combust. Flame*, 108:71–86, 1997.

[93] J. B. Moss, C. D. Stewart, and K. J. Young. Modeling Soot Formation and Burnout in a High Temperature Laminar Diffusion Flame Burning under Oxygen-Enriched Conditions. *Combust. Flame*, 101:491–500, 1995.

[94] S. Jay, P. Beard, and A. Pires Da Cruz. Modeling coupled processes of co and soot formation and oxidation for conventional and hcci diesel combustion. *SAE Paper*, (2007-01-0162), 2007.

[95] L. Martinez, J-B. Michel, S. Jay, and O. Colin. Evaluation of Different Tabulation Techniques Dedicated to the Prediction of the Combustion and Pollutants Emissions on a Diesel Engine with 3D CFD. *SAE paper*, (2013-01-1093), 2013.

[96] M. Balthasar and M. Kraft. A stochastic approach to calculate the particle size distribution function of soot particles in laminar premixed flames. *Combust. Flame*, 133:289–298, 2003.

[97] M. Balthasar and M. Frenklach. Detailed kinetic modeling of soot aggregate formation in laminar premixed flames. *Combust. Flame*, 140:130–145, 2005.

[98] J. Singh, M. Balthasar, M. Kraft, and W. Wagner. Stochastic modeling of soot particle size and age distribution in laminar premixed flames. *Proc. Combust. Inst.*, 30:1457–1465, 2005.

[99] A. Violi, A. Kubota, T.N. Truong, W. J. Pitz, C.K. Westbrook, and A.F. Sarofim. A fully integrated kinetic monte carlo/molecular dynamics approach for the simulation of soot precursors growth. *Proc. Combust. Inst.*, 29:2343–2349, 2002.

[100] A. Violi. Modeling of soot particle inception in aromatic and aliphatic premixed flames. *Combust. Flame*, 139:279–287, 2004.

[101] A. Violi, G.A. Voth, and A.F. Sarofim. The relative rrole of acetylene and aromatic precursors during soot particle inception. *Proc. Combust. Inst.*, 30:1343–1351, 2005.

[102] M. Celnik, A. Raj, R. West, R. Patterson, and M. Kraft. Aromatic site description of soot particles. *Combust. Flame*, 155:161–180, 2008.

[103] A. Raj, M. Celnik, R. Shirley, M. Sander, R. Patterson, R. West, and M. Kraft. A statistical approach to develop a detailed soot growth model using pah characteristics. *Combust. Flame*, 2009.

[104] M. Celnik, R. Patterson, M. Kraft, and W. Wagner. Coupling a stochastic soot population balance to gas-phase chemistry using operator splitting. *Combust. Flame*, 148:158–176, 2007.

[105] R.I.A. Patterson, W. Wagner, and M. Kraft. Stochastic weighted particle mmethod for population balance equations. *J. Comput. Phys.*, 230:7456–7472, 2011.

[106] R.I.A. Patterson. Convergence of stochastic particle systems underunder advection and coagulation. *Stoch. Anal. Appl.*, 31(5):800–829, 2013.

[107] W.J. Menz, J. Akroyd, and M. Kraft. Stochastic solution of population balance equations for reactor networks. *J. Comput. Phys.*, 256:615–629, 2014.

[108] M.E. Mueller, G. Blanquart, and H. Pitsch. Hybrid Method of Moments for modeling soot formation and growth. *Combust. Flame*, 156:1143–1155, 2009.

[109] M.E. Mueller, G. Blanquart, and H. Pitsch. Modeling the oxidation-induced fragmentation of soot aggregates in laminar flames. *Proc. Combust. Inst.*, 33:667–674, 2011.

[110] P. Donde, V. Raman, M.E. Mueller, and H. Pitsch. Les/pdf based modeling of soot-turbulence interactions in turbulent flames. *Proc. Combust. Inst.*, 34:1183–1192, 2013.

[111] M. Balthasar, F. Mauss, A. Knobel, and M. Kraft. Detailed Modeling of Soot Formation in a Partially Stirred Plug Flow Reactor. *Combust. Flame*, 128:395–409, 2002.

[112] F. Mauss, K. Netzell, and H. Lehtiniemi. Aspect of modeling soot formation in turbulent diffusion flames. *Combust. Sci. Technol.*, 178:1871–1885, 2006.

[113] A. Karlsson, I. Magnusson, M. Balthasar, and F. Mauss. Simulation of soot formation under diesel engine conditions using a detailed kinetic soot model. *SAE paper*, (981022), 1998.

[114] P. Priesching, R. Tatschl, F. Mauss, F. Saric, K. Netzell, W. Bauer, M. Schmid, A. Leipertz, S. S. Merola, and B. M. Vaglieco. Soot particle size distribution - a joint work for kinetic modeling and experimental investigations. *SAE paper*, (2005-24-053), 2005.

[115] M.E. Mueller, Q.N. Chan, N.H. Qamar, B.B. Dally, H. Pitsch, Z.T. Alwahabi, and G.J. Nathan. Experimental and computational study of soot evolution in a turbulent nonpremixed bluff body ethylene flame. *Combust. Flame*, 160:1298–1309, 2013.

[116] M.E. Mueller and H. Pitsch. Large eddy simulation of soot evolution in an aircraft combustor. *Phys. Fluids*, 25(110812), 2013.

[117] M.E. Mueller and H. Pitsch. Large eddy simulation subfilter modeling of soot-turbulence interactions. *Phys. Fluids*, 23:na, 2011.

[118] A. Attili, F. Bisetti, M.E. Mueller, and H. Pitsch. Formation, growth, and transport of soot in a three-dimensional turbulent non-premixed jet flame. *Combust. Flame*, 161:1849–1865, 2014.

[119] H. Richter, S. Granata, W. H. Green, and J.B. Howard. Detailed modeling of PAH and soot formation in a laminar premixed benzene/oxygen/argon low-pressure flame. *Combust. Flame*, 30:1397–1405, 2005.

[120] F. Gelbard, Y. Tambour, and J. H. Seinfeld. Sectional representation for simulating aerosol dynamics. *J. Colloid Interface Sci.*, 76(2):541–556, 1980.

[121] Y. Tambour. Vaporization of polydisperse fuel spray in a laminar boundary layer flow: A sectional approach. *Combust. Flame*, 58:103–114, 1984.

[122] J.B. Greenberg, I. Silverman, and Y. Tambour. On the origin of spray sectional conservation equations. *Combust. Flame*, 93:90–96, 1993.

[123] F. Laurent and M. Massot. Multi-fluid modelling of laminar polydisperse spray flames: origin, assumptions and comparision of sectional and sampling methods. *Combust. Theor. Model.*, 5(4):537–572, 2007.

[124] C. Marchal, G. Moréac, K. Netzell, M. Kasper, and F. Mauss. *The pressure dependence of soot particle size distribution functions.* Proceedings of the European Combustion Meeting, 2007.

[125] C. Marchal, G. Moréac, Vovelle C., Mounaïm-Rousselle C., and F. Mauss. *Soot modelling in automotive engines.* Proceedings of the European Combustion Meeting, 2009.

[126] M. Köhler, K-P. Geigle, T. Blacha, P. Gerlinger, and W. Meier. Experimental characterization and numerical simulation of a sooting lifted turbulent jet diffusion flame. *Combust. Flame*, 159(8):2620–2635, 2012.

[127] D.L. Wright, R. McGraw, and D.E. Rosner. Bivariate extension of the quadrature method of moment for modeling simultaneous coagulation and sintering of particle populations. *J. Colloid Interface Sci.*, 236(2):242–251, 2001.

[128] F. Mauss. *Entwicklung eines kinetischen Modells der Russbildung mit schneller Polymerisation.* PhD thesis, RWTH Aachen, 1998.

[129] H. Burtscher. Physical characterization of particulate emissions from diesel engines: a review. *J. Aerosol Sci.*, 36:896–932, 2005.

[130] S.J. Harris and M.M. Maricq. Signature size distributions for diesel and gasoline engine exhaust particulate matter. *J. Aerosol Sci.*, 32:749–764, 2001.

[131] M.M. Maricq, Podsiadlik D.H., and Chase R.E. Size distributions of motor vehicle exhaust pm: A comparison between elpi and smps measurements. *Aerosol Sci. Technol.*, 33:239–260, 2000.

[132] P. Markatou, H. Wang, and M. Frenklach. A computational study of sooting limits in laminar premixed flames of ethane, ethylene, and acetylene. *Combust. Flame*, 93:467–482, 1993.

[133] S.R. Forrest and T.A. Jr Witten. Long-range correlations in smoke-particle aggregates. *J. Phys. A-Math. Gen.*, 12(5):–, 1979.

[134] R.K. Chakrabarty, H. Moosmüller, W. P. Arnott, M.A. Garro, G. Tian, J.G. Slowik, E.S. Cross, J.-H. Han, P. Davidovits, T.B. Onasch, and D.R. Worsnop. Low fractal dimension cluster-dilute soot aggregates from a premixed flame. *Phys. Rev. Lett.*, 102:235504, 2009.

[135] D. Witkowski, Katsufumi K., Gokul V., and Rothamer D. Evaluation of the sooting properties of real fuels and their commonly used surrogates in a laminar co-flow diffusion flame. *Combust. Flame*, 160:1129–1141, 2013.

[136] A. Velghe, J. Bohbot, and S. Jay. A high efficiency parallel architecture dedicated to internal combustion engine simulation coupled with chemical kinetic solver. 6th European Conference on Computational Fluid Dynamics, 2014. In press.

[137] B. Zhao, H. Yang, Z. Li, M. V. Johnston, and H. Wang. Particle size distribution function of incipient soot in laminar premixed ethylene flames: effect of flame temperature. *Combust. Flame*, 30:1441–1448, 2005.

[138] X.S. Bai, M. Balthasar, F. Mauss, and L. Fuchs. Detailed Soot modeling in turbulent jet diffusion flames. *Proc. Combust. Inst.*, pages 1623–1630, 1998.

[139] K. J. Syed, C. D. Stewart, and J. B. Moss. Modeling soot formation and thermal radiation in buoyant turbulent diffusion flames. *Proc. Combust. Inst.*, pages 1533–1541, 1991.

[140] J. M. Anderlohr, R. Bounaceur, A. Pires Da Cruz, and F. Battin-Leclerc. Modeling of autoignition and no sensitization for the oxidation of ic engine surrogate fuels. *Combust. Flame*, 156:505–521, 2009.

[141] K. Narayanaswamy, G. Blanquart, and H. Pitsch. A consistent chemical mechanism for oxidation of substituted aromatic species. *Combust. Flame*, 157:1879–1898, 2010.

[142] H. P. Ramirez, K. Hadj-Ali, Diévart P., G. Dayma, C. Togbé, G. Moreac, and P. Dagaut. Oxidation of commercial and surrogate bio-diesel fuels (b30) in a jet-stirred reactor at elevated pressure: Experimental and modeling kinetic study. *Proc. Combust. Inst.*, 33:375–382, 2011.

[143] H. P. Ramirez, K. Hadj-Ali, Diévart P., G. Moreac, and P. Dagaut. Kinetics of oxidation of commercial and surrogate diesel fuels in a jet-stirred reactor: Experimental and modeling studies. *Energy Fuels*, 24:1668–1676, 2010.

[144] N.A. Slavinskaya and P. Frank. A modeling study of aromatic soot precursors formation in laminar methane and ethene flames. *Combust. Flame*, 156:1705–1722, 2009.

[145] J-B. Michel and O. Colin. A tabulated diffusion flame model applied to Diesel engine simulation. *Int. J. Engine Res.*, 15:346–369, 2013.

[146] O. Colin and A. Benkenida. The 3-Zones Extended Coherent Flame Model (ECFM3Z) for Computing Premixed/Diffusion Combustion. *Oil Gas Sci. Technol.*, 59:593–609, 2004.

[147] D. Aubagnac-Karkar, J.B. Michel, O. Colin, L. Noel, and N. Darabiha. A sectional soot model for rans simulation of diesel engines. *SAE paper*, (2014-01-1590), 2014.

[148] J. Bohbot, N. Gillet, and A Benkenida. IFP-C3D: an Unstructured Parallel Solver for Reactive Compressible Gas Flow with Spray. *Oil Gas Sci. Technol.*, 64:309–335, 2009.

[149] A. Velghe, N. Gillet, and J. Bohbot. A high efficiency parallel unstructured solver dedicated to internal combustion engine simulation. *Comput. Fluids*, 45:116–121, 2011.

[150] S. Jay and O. Colin. A variable volume approach of tabulated detailed chemistry and its applications to multidimensional engine simulations. *Proc. Combust. Inst.*, 33:3065–3072, 2011.

[151] J-B. Michel, O. Colin, and C. Angelberger. On the formulation of species reaction rates in the context of multi-species CFD codes using complex chemistry tabulation techniques. *Combust. Flame*, 157:701–714, 2010.

[152] Reaction Design. Reaction design concludes model fuel consortium. http://www.reactiondesign.com/news/3/95/Reaction-Design-Concludes-Model-Fuels-Consortium/, November 2012.

[153] Cambustion. Dms 500 fast particle analyser. http://www.cambustion.com/products/dms500.

[154] P.J. O'Rourke and A. A. Amsden. A Particle Numerical Model for Wall Fluid Dynamics in Port-Injected Engines. *SAE paper*, (961961), 1996.

[155] C. Habchi. A Comprehensive Model for Liquid Film Boiling in Internal Combustion Engines. *Oil Gas Sci. Technol.*, 65(2):331–343, April 2010.

[156] Z.Y. Han and R.D. Reitz. Turbulence modeling of internal combustion engines using rng k-epsilon models. *Combust. Sci. Technol.*, 106:267–295, 1995.

[157] C. Angelberger, T. Poinsot, and B. Delhaye. Improving near wall combustion and wall heat transfer modeling in si engine computation. *SAE Paper*, (972881), 1997.

[158] Engine Combustion Network. Ecn workshop proceedings. http://www.sandia.gov/ecn/workshop/ECN3.php, April 2014.

[159] J-B. Michel, O. Colin, and D. Veynante. Modeling ignition and chemical structure of partially premixed turbulent flames using tabulated chemistry. *Combust. Flame*, 152:80–99, 2008.

[160] W.F. Colban, D. Kim, P.C. Miles, S. Oh, R. Opat, R. Krieger, D. Foster, R.P. Durrett, and M.A. Gonzalez. A detailed comparison of emission and combustion performance between optical and metal single-cylinder diesel engines at low temperature combustion conditions. *SAE Paper*, (2008-01-1066), 2008.

[161] J.T. Kashdan and B. Thirouard. A comparison of combustion and emissions behaviour in optical and metal single-cylinder diesel engines. *SAE Paper*, (2009-01-1963), 2009.

[162] D. Aubagnac-Karkar, J.B. Michel, O. Colin, and N. Darabiha. Sectional soot model coupled to tabulated chemistry for diesel rans simulations. *Combust. Flame*, 2015. In Press.

[163] J-B. Michel, O. Colin, and D. Veynante. Comparison of differing formulations of the pcm model by their application to the simulation of an auto-igniting h_2 /air jet. *Flow Turb. Combust.*, 83:33–60, 2009.

[164] L.M. Pickett, C.L. Genzale, G. Bruneaux, L-M. Malbec, L. Hermant, C. Christiansen, and J. Schramm. Comparison of diesel spray combustion in different high-temperature, high-pressure facilities. *SAE Int. J. Engines*, 3:156–181, 2010.

[165] J. Manin, L Pickett, and S. Skeen. Two-color diffused back-illumination imaging as a diagnostic for time-resolved soot measurements in reacting sprays. *SAE Int. J. Engines*, 6:1908–1921, 2013.

[166] E. Cenker, G. Bruneaux, L Pickett, and C. Schulz. Study of soot formation and oxidation in the engine combustion network (ecn), spray a: Effects of ambient temperature and oxygen concentration. *SAE Int. J. Engines*, 6:352–365, 2013.

[167] N. Peters. Laminar diffusion flaflame models in non-premixed turbulent combustion. *Prog. Energ. Combust. Sci.*, 10:319–339, 1984.

[168] J. Tillou, J-B. Michel, C. Angelberger, and D. Veynante. Assessing les models based on tabulated chemistry for the simulation of diesel spray combustion. *Combust. Flame*, 161:525–540, 2014.

[169] N. Peters. *Turbulent Combustion*. Cambridge University Press., 2000.

[170] O. Colin, C. Pera, and S. Jay. *Detailed chemistry tabulation based on a FPI approach adapted and applied to 3-D internal combustion engine calculations*. Proceedings of the European Combustion Meeting, 2007.

[171] C. Pera, O. Colin, and S. Jay. Development of a fpi detailed chemistry tabulation methodology for internal combustion engines. *Oil Gas Sci. Technol.*, 64(3):243–258, 2009.

[172] S. Jay and O. Colin. Modélisation fpi détente en moteur - modélisation de la stratification en température. Technical report, IFP Energies Nouvelles / GSM, 2008.

[173] B. Higgins, D. Siebers, and A. Aradi. Diesel-spray ignition and premixed-burn behavior. *SAE Paper*, (2000-01-0940), 2000.

[174] B. Higgins and D. Siebers. Measurements of the flame lift-off location on di diesel sprays using oh chemiluminescence. *SAE Paper*, (2001-01-0918), 2001.

[175] G. Bruneaux. Mixing process in high pressure diesel jets by normalized laser induced exciplex fluorescence - part i: Free jet. *SAE Paper*, (2005-01-2100), 2005.

[176] C. Habchi and G. Bruneaux. *LES and Experimental investigation of Diesel sprays*. ICLASS 2012, 2012.

[177] S.S. Vasu, D.F. Davidson, Z. Hong, V. Vasudevan, and R.K. Hanson. n-dodecane oxidation at hhigh-pressure: Measurements of ignition delay times and oh concentration time-histories. *Proc. Combust. Inst.*, 32:173–180, 2009.

[178] H. Wang, E. Dames, B. Sirjean, D.A. Sheen, R. Tangko, A. Violi, J.Y.W. Lai, F.N. Egolfopoulos, D.F. Davidson, R.K. Hanson, C.T. Bowman, C.K. Law, W. Tsang, N.P. Cernansky, D.L. Miller, and R.P. Lindstedt. A high-temperature chemical kinetic model of n-alkane (up top n-dodecane), cyclohexane and methyl-, ethyl-, n-propyl and n-butyl-cyclohexane oxidation at high ttemperature, jetsurf version 2.0, September 2010.

[179] T. Malewicki and K. Brezinsky. Experimental and modeling study on the pyrolysis and oxidation of n-decane and n-dodecane. *Proc. Combust. Inst.*, 34:361–368, 2013.

[180] Y. Pei, E.R. Hawkes, S. Kook, G.M. Goldin, and T. Lu. Modelling n-dodecane spray and combustion with the trtransport probability density function method. *Combust. Flame*, 2015. In Press.

[181] Yunardi, R.M. Woolley, and M. Fairweather. Conditional moment closure prediction of soot formation in turbulent, nonpremixed ethylene flames. *Combust. Flame*, 152(3):360–376, 2008.

[182] A. Kronenburg, R.W. Bilger, and J.H. Kent. Modeling soot formation in turbulent methane-air jet diffusion flames. *Combust. Flame*, 121(1-2):24–40, 2000.

[183] H. Lehtiniemi, A. Borg, and F. Mauss. *Conditional Moment Closure with a Progress Variable Approach*. COMODIA 2012, 2012.